EXPERIMENTAL STUDY OF FULL-SCALE ICED-AIRFOIL AERODYNAMIC PERFORMANCE USING SUB-SCALE SIMULATIONS

BY

GREG T. BUSCH

DISSERTATION

Submitted in partial fulfillment of the requirements
for the degree of Doctor of Philosophy in Aerospace Engineering
in the Graduate College of the
University of Illinois at Urbana-Champaign, 2009

Urbana, Illinois

Doctoral Committee:

Professor Michael Bragg, Chair
Professor Eric Loth
Associate Professor Michael Selig
Associate Professor Kenneth Christensen

Abstract

Determining the aerodynamic effects of ice accretion on aircraft surfaces is an important step in aircraft design and certification. The goal of this work was to develop a complete sub-scale wind tunnel simulation methodology based on knowledge of the detailed iced-airfoil flowfield that allows the accurate measurement of aerodynamic penalties associated with the accretion of ice on an airfoil and to validate this methodology using full-scale iced-airfoil performance data obtained at near-flight Reynolds numbers. In earlier work, several classifications of ice shape were developed based on key aerodynamic features in the iced-airfoil flowfield: ice roughness, streamwise ice, horn ice, and tall and short spanwise-ridge ice. Castings of each of these classifications were acquired on a full-scale NACA 23012 airfoil model and the aerodynamic performance of each was measured at a Reynolds number of 12.0 x 10^6 and a Mach number = 0.20. In the current study, sub-scale simple-geometry and 2-D smooth simulations of each of these castings were constructed based on knowledge of iced-airfoil flowfields. The effects of each simulation on the aerodynamic performance of an 18-inch chord NACA 23012 airfoil model was measured in the University of Illinois 3 x 4 ft. wind tunnel at a Reynolds number of 1.8 x 10^6 and a Mach number of 0.18 and compared with that measured for the corresponding full-scale casting at high Reynolds number. Geometrically-scaled simulations of the horn-ice and tall spanwise-ridge ice castings modeled $C_{l,max}$ to within 2% and $C_{d,min}$ to within 15%. Good qualitative agreement in the C_p distributions suggests that important geometric features such as horn and ridge height, surface location, and angle with respect to the airfoil chordline were appropriately modeled. Geometrically-scaled simulations of the ice roughness, streamwise ice, and short-ridge ice tended to have conservative $C_{l,max}$ and C_d. The aerodynamic performance of simulations of these types of accretion was found to be sensitive to roughness height and concentration. Scaled roughness heights smaller than those

found on the casting were necessary to improve simulation accuracy, resulting in $C_{l,max}$ and $C_{d,min}$ within 3% and 5% of the casting, respectively.

Acknowledgments

I would first like to thank my advisor, Professor Mike Bragg, for taking me into his group and providing guidance throughout the course of this investigation. Thanks also go to Profs. Eric Loth, Michael Selig, and Ken Christensen on my doctoral committee for their valuable input, and to Dr. Andy Broeren, who supplied his trouble-shooting expertise in the lab and provided useful advice whenever I needed assistance. My groupmates Ed Whalen and Jason Jacobs frequently lended a helping hand, and many thanks go to them as well. This work was supported through a grant from NASA, and I would like to thank Mr. Gene Addy and Dr. Sam Lee at NASA Glenn Research Center for their help and support during this investigation. Finally, I would like to thank my wife Lisa and my parents for their encouragement over the years.

Table of Contents

List of Tables

List of Figures

Nomenclature

A_{ss}	Wind-tunnel inlet settling-section area
A_{ts}	Wind-tunnel test-section area
b	Airfoil model span
c	Aifoil model chord
C_a	Axial force coefficient
C_d	Drag coefficient
$C_{d,\alpha=0}$	Drag coefficient at $\alpha = 0$ deg.
$C_{d,min}$	Minimum drag coefficient
C_l	Lift coefficient
$C_{l,max}$	Maximum lift coefficient
C_m	Pitching moment coefficient about the airfoil quarter-chord
C_n	Normal force coefficient
C_p	Pressure coefficient
D'	Drag force per unit span
F_A	Axial force
F_N	Normal force
h	Wind-tunnel test-section height
k/c	Ice-shape height, non-dimensionalized by the chord
M	Mach number
M	Pitching moment
P	Static pressure
P_o	Total pressure

q_∞	Freestream dynamic pressure
Re	Reynolds number based on chord length
s/c	Airfoil model surface location, non-dimensionalized by the chord
S	Airfoil model surface area
T	Temperature
U	Uncertainty
u_1	Velocity in a plane far behind the airfoil
U_∞	Test section freestream velocity
u_w	Velocity in the wake
V_A	Scaled axial force voltage
V_M	Scaled pitching moment voltage
V_N	Scaled normal force voltage
W	Wind-tunnel test-section width
w/c	Width of ice-shape base, non-dimensionalized by the chord
x/c	Coordinate parallel to the airfoil model chordline, non-dimensionalized by the chord
x_o	Difference between the quarter-chord location and the balance center in the chordwise direction
y_i	Position of the wake rake probe relative to airfoil model chordline
y/c	Coordinate normal to the airfoil model chordline, non-dimensionalized by the chord
y_o	Difference between the quarter-chord location and the balance center in the direction normal to the chordline
z/b	Coordinate in the airfoil model spanwise direction, non-dimensionalized by the span

Greek Symbols

α	Airfoil model angle of attack
$\Delta C_{d,rms}$	Percent RMS difference in C_d over the linear angle of attack range
ϵ_{sb}	Solid blockage correction factor
ϵ_{wb}	Wake blockage correction factor
θ	Ice horn angle with respect to the chordline
λ_2	Airfoil shape factor
μ	Coefficient of viscosity
ρ	Air density
σ	Streamline curvature correction factor

Acronyms

ESP	Electronically Scanned Pressure
FAA	Federal Aviation Administration
IPS	Ice protection system
IRT	NASA Glenn Icing Research Tunnel
IWT	Goodrich Icing Wind Tunnel
LWC	Liquid Water Content
MVD	Median Volumetric Diameter
NACA	National Advisory Committee on Aeronautics
NASA	National Aeronautics and Space Administration
SG	Simple-geometric simulation
SLD	Supercooled large droplet
UIUC	University of Illinois at Urbana-Champaign

Subscripts

2-D	Two dimensional
3-D	Three dimensional
amb	Ambient conditions
atm	Atmospheric conditions
bal	Force and moment balance measurement
cor	Corrected
ss	Wind-tunnel inlet settling section
ts	Wind-tunnel test section
u	Uncorrected
w	Wake
∞	Freestream conditions (except in the wake drag equations where it represents the edge of the wake)

Chapter 1

Introduction

The effects of ice accretion on aircraft surfaces can substantially reduce aircraft performance, especially if the wing, empennage, or control surfaces are affected. Reductions in airfoil maximum lift of over 50% and increases in minimum drag of more than 400% have been observed for some types of ice accretion.[1,2] It is important to determine the aerodynamic performance penalties that can be expected from a given icing encounter so that aircraft can be designed and certified for flight through icing conditions. These penalties are often determined experimentally using aerodynamic wind tunnels, as flight testing is difficult and expensive and CFD methods typically lack the desired accuracy, especially in highly separated, unsteady flows near maximum lift. However, measuring iced-airfoil aerodynamic performance in a dry-air wind tunnel requires construction of a sub-scale geometric representation of an ice accretion, referred to as a sub-scale simulation or artificial ice shape, as icing tunnels are unsuitable for obtaining high quality aerodynamic performance data. Recently, a major joint NASA/ONERA/Illinois research program developed and validated methods of categorizing and simulating ice accretion on wind tunnel airfoil models.[3] Different types of ice accretion were identified and classified based on key flowfield features,[4] and methods of constructing sub-scale simulations for each of these types of accretion were developed using sub-scale icing and aerodynamic airfoil models at low Reynolds number.[1,5–8] These methods were then validated using iced-airfoil performance data obtained by Broeren et al.[9] and CassouDeSalle et al.[10] on a full-scale airfoil model at near-flight Reynolds numbers.[11,12] This dissertation is part of the larger NASA/ONERA/Illinois project to better understand iced-airfoil aerodynamics and to use this understanding to develop and validate sub-scale simulation methods.

1.1 Classification of Iced-Airfoil Flowfields

Bragg et al.[4] have characterized four main types of iced-airfoil flowfields based on key aerodynamic characteristics: ice roughness, streamwise ice, horn ice, and spanwise-ridge ice. These flowfields were summarized by Bragg et al.[4] and Busch and Bragg.[12] Ice roughness is generally higher than the local boundary-layer thickness, so each roughness element can be analyzed as an isolated flow obstacle in regions where the concentration is low. If the Reynolds number based on roughness height, Re_k, is sufficiently high, the roughness element will cause the boundary layer to undergo bypass transition, a process which is much slower and less energetic than natural transition. This alters the boundary-layer development relative to natural transition and generally results in premature boundary-layer separation near the trailing edge of the airfoil. Streamwise ice also has surface roughness and ice feathers which affect boundary-layer development in a similar manner to ice roughness. Additionally, slope discontinuities at the ice/airfoil junction or on the ice shape itself may cause a short separation bubble to form, similar to that defined by Tani.[13] Short bubbles have only a local effect on the airfoil flowfield and do not grow significantly with angle of attack, but their position on the airfoil may change slightly with changes in angle of attack. The horn-ice flowfield has much in common with that of a backward-facing step flowfield. The tip of the horn generates a strong adverse pressure gradient which triggers boundary-layer separation at a fixed point independent of angle of attack, and a shear layer forms between the inviscid flow over the top of the horn and the recirculatory flow behind the horn. The shear layer entrains high energy flow from the inviscid region and eventually reattaches to the airfoil (if the airfoil is at sufficiently low angle of attack), forming a long separation bubble (also like that defined by Tani[13]). The separation bubble dominates the flowfield and usually causes thin-airfoil stall, as described by McCullough and Gault.[14] For the fourth type of ice shape, spanwise-ridge ice, the boundary layer has time to develop before separation occurs, and may even transition upstream of the ridge. In this sense, the ridge acts as a flow obstacle. As with horn ice, the strong adverse pressure gradient at the tip of the ridge causes a separation bubble to form and the type of separation bubble determines whether the ridge is considered to be tall or short.

In the literature, the accretion classifications rime ice and glaze ice are often encountered as well. These classifications are based on accretion mechanism. Rime ice typically forms in colder conditions. The water droplets that impinge on the wing freeze immediately upon impact, forming opaque, white ice. Due to this immediate freezing, rime-ice accretions generally conform to the shape of the airfoil. The other type of ice, glaze ice, forms at warmer conditions. In this case, the water droplets flow freely over the airfoil surface for a short time and then freeze. This causes the resulting ice to be clear, so it is sometimes also called clear ice. The classification of a given accretion as rime ice or glaze ice does not preclude classification using the definitions of Bragg et al,[4] as these definitions were based on aerodynamic characteristics rather than accretion mechanism. It is possible to have, for example, either glaze ice roughness or rime ice roughness.

Broeren et al.[9,15] measured the aerodynamic performance degradation of a 72-inch chord NACA 23012 airfoil using high-fidelity, full-scale ice castings representative of each type of iced-airfoil flowfield at near-flight Reynolds numbers. Representative data from this testing are shown in Fig. 1.1, which compares the aerodynamic performance degradation of the NACA 23012 with various types of ice shapes. The tall spanwise-ridge ice shape is seen to cause the most severe degradation in $C_{l,max}$, causing a reduction of nearly 75%. It also causes the largest increase in C_d, causing it to increase by over 300% at α = -4 deg. In contrast, the short spanwise-ridge causes the smallest degradation in maximum lift (about 18%). The ice roughness and streamwise ice shapes cause larger penalties to $C_{l,max}$ than does the short ridge, but similar to each other, and also increase the airfoil C_d by comparable amounts. The horn-ice casting causes larger performance penalties than the ice roughness, streamwise-ice, and short ridge castings, but not as large as the tall spanwise ridge. This plot illustrates the wide range of performance penalties that ice accretion may cause and shows why it is important to understand the aerodynamics of each classification of ice shape and to simulate each appropriately.

1.2 Sub-Scale Simulation of Iced-Airfoil Aerodynamics

In theory, full-scale iced-airfoil aerodynamics can be exactly reproduced on a sub-scale airfoil model in a dry-air wind tunnel by exactly reproducing and scaling the ice accretion geometry and matching the Reynolds and Mach numbers. In reality, this is usually impractical. The ice accretion geometry is too complex to fully document and reproduce at a reduced scale, and wind tunnel facilities capable of matching both Reynolds and Mach numbers are difficult to schedule and expensive to run. As a result, there are differences in geometry and usually Re and M between the sub-scale and full-scale cases and accompanying unknown aerodynamic performance uncertainties associated with these differences.

Perhaps the largest of these uncertainties results from differences in geometry between the full-scale and sub-scale cases. Sub-scale simulations usually have simplified geometries compared to the full-scale ice shape, and different types of simulations have different levels of simplification. Typically, simulations with a higher geoemtric fidelity will yield more representative results, but at a higher cost in both time and money. Therefore, it is important to find the lowest fidelity simulation that accurately captures the aerodynamics of the ice shape. The highest fidelity type of simulation is a casting of the original ice shape. Castings model nearly every feature of the shape, from small-scale surface roughness to large-scale spanwise variation. Unfortunately, castings are expensive to produce, require time in an icing wind tunnel, and cannot be easily scaled. These constraints make it advantageous to use simplified simulations instead of castings to model the ice shape aerodynamics. Therefore, sub-scale simulation techniques need to be validated for use on aerodynamic models.

Two of the most common sub-scale simulation types are 2-D smooth simulations and simple-geometry simulations. A 2-D smooth simulation is a constant-cross section extrusion of a two-dimensional tracing of the ice accretion cross-section. The tracing usually needs to undergo a smoothing process to make it suitable for extruding, whereby the number of points used to represent the cross-section is reduced. A simple-geometry simulation uses extruded geometric shapes, such as rectangles and quarter rounds, to represent an ice shape. Simple-geometry simulations are normally two-dimensional, and are considered to be of lower fidelity than 2-D smooth simulations. The low cost and minimal fabrication effort of simple-geometry

simulations makes them ideal for use in parametric studies, such as those of Papadakis et al.,[16] Kim,[17] and Lee.[18] Frequently, surface roughness is added to the two-dimensional simulations in an attempt to provide a better representation of the iced-airfoil flowfield.

Based on the key flowfield characteristics discussed above and the existing performance data obtained using ice accretion simulations, Bragg et al.[4] identified important geometric features on each type of ice shape. For shapes with long separation bubbles, such as horn-ice and spanwise-ridge ice, it was observed that geometric intricacies and surface roughness were not as important to represent as was the gross ice geometry. For smaller, more conformal shapes in which the dominant mechanism for affecting airfoil performance is alteration of the boundary layer, it was observed that changes in surface roughness height, concentration, location, and chordwise extent were important. These conclusions suggest that a simulation which appropriately represented the important geometric features of an accretion would cause similar performance penalties, as long as Reynolds and Mach number effects were small or the parameters kept constant. At the time, little data were available on full-scale iced airfoils to quantify the accuracy with which simulations could reproduce full-scale iced-airfoil aerodynamics.

Building on the knowledge obtained during the study of Bragg et al.,[4] several different types of sub-scale simulations were built by Busch[5] and installed on an 18-inch chord NACA 23012 aerodynamic model to emulate ice accreted on a sub-scale, 18-inch chord NACA 23012 icing model. For that study, the icing conditions were selected to produce ice shapes with gross geometry similar to that which would form on a full-scale airfoil, as it was not possible at the time to actually use a full-scale airfoil for both icing and aerodynamic tests. 2-D smooth simulations (some with additional surface roughness), carefully constructed from tracings representative of the average ice accretion geometry, modeled $C_{l,max}$ to within 2% for all ice shape types. Simple-geometry simulations yielded similar comparisons. The angle of attack at which $C_{l,max}$ occurred was accurately captured to within 1 deg. for all ice shape types except the spanwise-ridge ice, for which the 2-D smooth simulation stalled 2 deg. earlier than did the corresponding casting. C_d was accurately modeled for the ice roughness, streamwise-ice, and horn-ice simulations (again, with the proper addition of surface roughness). However, significant spanwise variation in the flowfield of the 2-D smooth spanwise-ridge ice simulation

made it difficult to determine its ability to accurately model C_d of the casting in this study. These results showed that by accurately capturing the important ice geometry, iced-airfoil aerodynamics at equivalent geometric scale, Reynolds number, and Mach number may in general be accurately modeled using simplified, two-dimensional simulations.

As discussed at the beginning of this section, there are uncertaintes associated with differences in Re and M as well as geometry. The effects of these parameters on ice accretion aerodynamics have been documented in several studies. Broeren et al.[9] found that $C_{l,max}$ changed very little over a Reynolds number range of 4.6 x 10^6 - 16.0 x 10^6 and only slightly more over a Mach number range of 0.10 - 0.28 for most types of ice shapes on a NACA 23012 airfoil. Addy and Chung[19] obtained similar results over a similar Reynolds number range for a 36-inch chord NLF-0414 airfoil. Papadakis et al.[20] varied Reynolds number from 2.0 x 10^6 - 4.0 x 10^6 and from 0.5 x 10^6 - 2.0 x 10^6 on 57-inch chord and 24-inch chord modified NACA 63_A213 airfoil models, respectively. No notable Reynolds number effects were observed on the larger model, but $C_{l,max}$ decreased by about 9% as Reynolds number was increased on the smaller model (note that M was not constant during this study). The exact dependence on Reynolds number in this range may be airfoil and ice shape dependent, as Lee et al.[21] report very little effect of Reynolds number over a range of 0.5 x 10^6 - 1.8 x 10^6 on $C_{l,max}$ of a NACA 23012m with a spanwise-ridge ice shape (M also varied in this study). Regardless, the Reynolds number range of interest in the current study is 1.8 x 10^6 - 12.0 x 10^6, where Reynolds number effects have been shown to be small for most types of ice shape.

These studies suggest that sub-scale simulations could accurately reproduce the aerodynamic effects of a full-scale ice accretion if designed appropriately. Further supporting this idea is the investigation by Papadakis et al.[20] which also used modified NACA 63_A213 airfoil models of different chords to investigate the effects of geometric scaling on the aerodynamic penalties caused by 2-D smooth and simple-geometry horn-ice simulations. Geometrically-scaled ice simulations on 57-inch chord and 24-inch chord models at identical Reynolds number (but different Mach number) yielded similar penalties to $C_{l,max}$, suggesting that geometric scaling may be appropriate for these low fidelity horn-ice simulations.

1.3 Motivation, Objectives, and Approach

The studies summarized above all studied a portion of the sub-scale simulation process. Some compared sub-scale ice simulations and castings at similar Re, some compared sub-scale simulations with full-scale simulations at similar Re, some examined Re and M effects on ice accretion castings and simulations, and others investigated which geometric features were important to represent on sub-scale simulations. In particular, the recent studies by Broeren et al.[9,15] using full-scale ice castings at high Reynolds number are considered to give the highest-fidelity iced-airfoil performance data to date and, in addition to improving the understanding of iced-airfoil flowfields, provides a new opportunity to validate the entire sub-scale simulation process and to quantify the accuracy of simulation methods. The goal of the current study is to develop a complete sub-scale wind tunnel simulation methodology based on knowledge of the detailed iced-airfoil flowfield that allows the accurate measurement of aerodynamic penalties associated with the accretion of ice on an airfoil and to validate this methodology using full-scale iced-airfoil data obtained at near-flight Reynolds numbers. Since each classification of iced-airfoil flowfield has different key aerodynamic characteristics, this work will be based on representative accretions from each classification. The specific objectives of the current work are to

1. Understand how the underlying aerodynamics support ice accretion simulation methods

2. Identify important geometric features which must be appropriately modeled to accurately replicate the aerodynamics of the original ice shape

3. Quantify the accuracy with which sub-scale simulations can be used to simulate the aerodynamics of a full-scale iced airfoil at a higher Reynolds number representative of in-flight conditions

To achieve these objectives, seven ice accretions investigated by Broeren et al.[9,15] were selected as representative examples of each of the classifications of iced-airfoil flowfield: ice roughness, streamwise ice, horn ice, and tall and short spanwise-ridge ice. Based on knowledge obtained in previous studies, sub-scale simulations of each of these flowfields were designed, constructed, and tested in the University of Illinois low-speed wind tunnel using an 18-inch

chord NACA 23012 airfoil model at low Reynolds number. The aerodynamic performance degradation caused by each simulation was then compared to that of the casting to evaluate the accuracy with which that particular simulation method may be used and new knowledge obtained during this process was used to improve the simulation method.

The remainder of this dissertation is divided into four chapters. The next chapter is a Literature Review and discusses the flowfields and important aerodynamic characteristics of each type of ice shape classified by Bragg et al.[4] It then reviews challenges faced when simulating an ice accretion on a sub-scale model at Reynolds numbers below those encountered in flight. The chapter entitled Experimental Methodology explains the experimental details of the tests. It covers how ice accretions were acquired, how the ice shape simulations were constructed, and the data acquisition system used for the aerodynamic tests. It also contains an analysis of the uncertainties associated with this system. The Results and Discussion chapter contains an analysis of the data collected during the aerodynamic tests. Some of the preliminary results of this work were presented by Busch et al.[11] and Busch and Bragg.[12] The final chapter contains a summary of this study as well as the main conclusions derived from this investigation. It also gives some recommendations to be considered for future research.

Chapter 2

Literature Review

Effective ice accretion aerodynamic simulation requires an understanding of the iced-airfoil flowfield. Different types of ice shapes have different key flowfield features, and the proper reproduction of these features is crucial to accurately obtaining the iced-airfoil aerodynamic performance. This chapter provides a brief description of the different types of iced-airfoil flowfield and the key features present in each. When ice simulations are not of the same scale as the original ice shape, scaling effects may be important. Several previous studies have examined the effects of Reynolds and Mach number on iced-airfoil performance and the results of these studies are summarized. Also discussed are the uncertainties associated with sub-scale ice simulations that result from the inability to exactly reproduce and scale ice geometries and some of the uncertainties associated with making airfoil performance measurements in a wind tunnel. Finally, to show that the simulation techniques that will be discussed in Chapters 3 and 4 are applicable to most airfoils, the results of studies which have compared different airfoil geometries with similar ice simulations are presented.

2.1 Types of Ice Shapes

As discussed in the Introduction, Bragg et al.[4] conducted a review and classified four types of iced-airfoil flowfields based on key aerodynamic characteristics: ice roughness, streamwise ice, horn ice, and spanwise-ridge ice. Since this review, Broeren et al.[9] measured the aerodynamic performance of high-fidelity, full-scale simulations of each type of ice shape at flight Reynolds and Mach numbers on a NACA 23012 airfoil. The data set obtained by Broeren et al. is considered to give the true iced-airfoil aerodynamic performance. This section of this dissertation discusses the flowfields and pressure distributions for examples of each type of

ice shape based on data from Bragg et al.'s review and Broeren et al.'s full-scale data. It also reviews which features earlier studies have found to be important to include on sub-scale simulations. When considering the following discussion, it is important to remember that many ice shapes may not fit clearly in one category and may have characteristics common to more than one type of flowfield.

2.1.1 Ice Roughness

Ice roughness initially consists of large isolated elements of varying size and concentration. The roughness elements typically remain close to the leading edge of the airfoil on the upper surface, extending back only a few percent chord for typical icing conditions. At positive angles of attack, roughness frequently extends farther aft on the lower surface than on the upper surface. The stagnation line of the airfoil generally remains relatively smooth and free of roughness. Just downstream of the stagnation region on the upper and lower surfaces the height and concentration of the roughness is usually highest and gradually tapers off in the downstream direction. As the exposure time continues to increase, the roughness size and density may increase and individual roughness elements may eventually coalesce to some degree.

2.1.1.1 Ice Roughness Flowfield

Ice roughness is generally higher than the local boundary-layer thickness, so each roughness element can be analyzed as an isolated flow obstacle in regions where the concentration is low.[4] Around the individual roughness elements are regions of localized flow separation, which causes a reduction in boundary-layer momentum, results in increased airfoil drag, and may alter the flowfield far from the airfoil, where the flow can be considered inviscid. If the Reynolds number based on roughness height, Re_k, is sufficiently high, the roughness element will cause the boundary layer to undergo a different type of transition than on a clean airfoil, referred to as bypass transition, which bypasses the natural transition caused by Tollmein-Schlichting instabilities. The process of bypass transition begins at the roughness element, which initiates a transitional boundary layer. A boundary layer undergoing bypass transition will transition to turbulent much more slowly than in the case of natural transition, with the

speed at which transition occurs depending on the local pressure gradient and Re_k.[22] This process is illustrated in Fig. 2.1. In the figure, $Re_{k,crit}$ represents the critical Reynolds number at which transition would normally occur at the location of the element. No transition wedge is observed for Re_k much less than the $Re_{k,crit}$. For Re_k sufficiently large to cause bypass transition, a transition wedge appears far downstream of the roughness element. As Re_k increases further, the transition wedge moves upstream, closer to the element. The net result of this is a less energetic transition process which causes the boundary layer to be more prone to separation than a naturally transitioning boundary layer. Thus, airfoils with ice roughness contamination are predisposed to trailing-edge separation at lower angles of attack than clean airfoils. This usually causes stall to occur at a reduced angle of attack relative to the clean case.

The effect of a high-fidelity rime ice roughness simulation on the surface pressure distribution of a NACA 23012 airfoil is shown in Fig. 2.2 for two angles of attack: 13.0 deg., just below stall, and 13.5 deg., just above stall. In the $\alpha = 13.0$ deg. C_p distribution, it is clear that the effect of the ice roughness is to reduce the suction peak near the leading edge of the airfoil. The iced-airfoil also is unable to recover pressure back to the freestream as is the clean airfoil; the C_p at the trailing edge of the iced airfoil is negative. This was likely caused by trailing-edge separation, denoted by the region of relatively constant pressure beyond $x/c = 0.80$. When the angle of attack is increased to 13.5 deg., there is a large decrease in suction on the upper surface of the airfoil. C_p is almost constant beyond $x/c = 0.15$, indicative of separated flow. This abrupt change in C_p distribution is characteristic of leading-edge stall,[14] though this particular stall could be described as a combination of leading-edge and trailing-edge stall citebib:mcculloughgault since trailing-edge separation occurred on the airfoil prior to stall.

2.1.2 Important Geometric Features of Ice Roughness

Bragg et al.[4] discuss a study by Brumby[23] which examined the effect of average roughness height on aerodynamic performance. Brumby assembled airfoil data from various sources to show the effect of roughness height and location on $C_{l,max}$ (Fig. 2.3). The trendlines on Brumby's plot show that as roughness height increases, $C_{l,max}$ decreases for a narrow strip of

roughness at a given location. Also, as the strip of roughness moves farther aft on the airfoil surface, it has less of an effect on $C_{l,max}$.

Another characteristic used to define ice roughness is its concentration, or area density, which is defined in this dissertation as the ratio of the area of all individual roughness elements over the total airfoil surface area of the roughness region. On most ice roughness shapes, the stagnation region remains relatively smooth, with large, densely packed regions of roughness on either side. The ice roughness height and concentration generally tend to decrease towards the aft sections of the roughness. Jackson[24] showed that concentration can have a substantial effect on the magnitude of the aerodynamic performance degradation for a NLF-0414 airfoil, and that $C_{l,max}$ is especially sensitive to changes when the roughness concentration is low (Fig. 2.4). At some critical roughness concentration, which appears to be dependent on roughness height, $C_{l,max}$ becomes insensitive to further increases in concentration. This occurs at somewhere between 10% and 20% concentration for k/c= 0.00046 roughness and between 10% and 30% concentration for k/c = 0.0027 roughness extending from x/c = 0 to 7% on the upper and lower surfaces of a NLF-0414 airfoil. These results suggest that to accurately reproduce $C_{l,max}$, roughness concentration is important to represent if below the critical concentration; otherwise, it is less important.

Papadakis et al.[25] used sandpaper roughness of varying grit size and extent to determine the effects of ice roughness on 1/4-th and full-scale models of a business jet tail at Re = 1.36 x 10^6 and Re = 5.1 x 10^6. Two extents were used: the extents predicted by the LEWICE[26] airfoil ice accretion prediction code (approximately from x/c = 0.017 on the suction surface to x/c = 0.025 on the pressure surface) and from x/c = 0.13 on the suction surface to x/c = 0.13 on the pressure surface. Roughness heights ranged from k/c_{mac} = 0.00026 to 0.00137 on the 1/4-scale model and from k/c_{mac} = 0.00009 to 0.00034 on the full-scale model. The effects of roughness extent on aerodynamic performance were small in all cases except for the k/c_{mac} = 0.00137 roughness on the 1/4-scale model, where $C_{l,max}$ was about 5% below its value for the shorter roughness extents. Jackson[24] obtained similar results in testing k/c = 0.00046 sandpaper roughness on a NLF-0414. Very little change in $C_{l,max}$ and only a slight change in C_d was documented for chordwise extents from x/c = 0.04 - 0.10 but a notable decrease in $C_{l,max}$ occurred for roughness extending to x/c = 0.29. These results show that

small changes in roughness extents near the airfoil leading edge usually do not play a large role in affecting airfoil $C_{l,max}$ compared to the effects of roughness height and concentration, but, consistent with Brumby,[23] large changes in roughness extent may reduce $C_{l,max}$.

Busch[5] showed in an earlier study that grit roughness applied to an otherwise clean airfoil can model the aerodynamic performance degradation due to ice roughness reasonably well. A simulation based on glaze ice roughness accreted on a sub-scale, 18-inch chord NACA 23012 icing tunnel model was constructed. Based on measurements of a casting of the accretion, the average roughness height was $k/c = 0.0025$ on the upper surface of the airfoil and $k/c = 0.0012$ on the lower surface. Silicon carbide roughness elements of height $k/c = 0.0026$ were applied to an 18-inch chord NACA 23012 aerodynamic model at the appropriate chordwise extents to represent the ice roughness. The effects of the simulated roughness on C_l, C_m, and C_d were measured and compared with the effects of the casting. These data are shown in Fig. 2.5. General agreement was good between the casting and simulation for the range of α over which the lift curve slope is linear. $C_{l,max}$ of the simulation was within 4% of the casting $C_{l,max}$. However, stall occurred about 1 degree earlier for the ice simulation than for the casting, resulting in differences in both $C_{l,max}$ and C_m at $\alpha = 10$ deg. Agreement in C_d between the simulation and casting is good at positive angles of attack, but below $\alpha = 0$ deg., the simulation has much higher C_d than the casting. The higher C_d of the simulation was likely caused by a larger average roughness height on the lower surface of the simulation than on the casting. No simulation was constructed which had different roughness sizes on the upper and lower surface in this earlier study by Busch,[5] but data acquired in the current study suggest that a smaller roughness size on the lower surface would have likely improved agreement in C_d at negative angles of attack without adversely affecting the agreement at positive angles. In spite of the disagreement in C_d at low angles of attack, the results at positive angles of attack suggest that simple-geometry simulations of the same scale of a casting can reproduce the casting aerodynamics relatively accurately at identical Reynolds and Mach numbers if appropriate grit roughness is used.

2.1.3 Streamwise Ice

Streamwise-ice is usually conformal to the airfoil geometry (unlike horn-ice or spanwise ridge ice), and may even resemble a leading-edge extension. The stagnation region of streamwise-ice shapes usually remains relatively smooth, while ice feathers and nodules (small, highly three-dimensional protuberances) farther aft cause the rest of the shape to be rough.

2.1.3.1 Streamwise-Ice Flowfield

If the ice geometry is not completely conformal to the airfoil, a short separation bubble, as described by Tani,[13] may form (Fig. 2.6) due to the adverse pressure gradient created where the gross ice geometry attaches to the airfoil. A schematic of the time-averaged flow about a short separation bubble is shown in Fig. 2.7. The bubble is formed when the incoming boundary layer separates from the airfoil (or ice) surface and forms an unstable shear layer. Instabilities in the shear layer cause a turbulent transition, which enhances mixing and may allow reattachment to the airfoil surface. The region under the shear layer, labeled the "dead air" region in Fig. 2.7, usually consists of slow moving and recirculatory flow. After the shear layer reattaches to the airfoil surface, a turbulent boundary layer develops, but this boundary layer is much less energetic than if it had transitioned naturally (i.e., if no bubble were present). The location of the separation bubble may move slightly with changes in airfoil angle of attack, but the size of the separation bubble usually remains relatively constant over a range of angle of attack. The short bubble may appear on the airfoil C_p distribution as a constant-pressure plateau, but has only a localized effect.

Another factor contributing to the performance degradation of an airfoil with streamwise ice is the surface roughness of the ice shape, which affects the boundary-layer development in a similar manner as ice roughness. Accordingly, airfoils with streamwise-ice shapes usually have reduced boundary-layer health and tend to experience premature trailing-edge flow separation. In most cases this causes reductions in maximum lift similar to those caused by ice roughness, but some streamwise-ice accretions have been shown to increase $C_{l,max}$ by increasing the airfoil chord and acting as a leading-edge flap.[27,28] Even these accretions, however, increase airfoil drag.

The C_p distribution measured by Broeren[29] on a NACA 23012 airfoil with a streamwise ice accretion is shown in Fig. 2.8. Two angles of attack are shown: the angle of attack of $C_{l,max}$ (12.0 deg.) and the angle of attack 1.0 deg. after $C_{l,max}$ occurs (13.0 deg.). As with the ice roughness accretions, the streamwise-ice causes trailing-edge separation beginning at $x/c = 0.80$ just prior to stall. Also at $\alpha = 12.0$ deg., a second constant pressure plateau is evident in the C_p distribution from $x/c = 0.015$ - 0.05. This region of constant C_p was likely caused by a short separation bubble, though no flow visualization was conducted to confirm this. This separation bubble appears to be approximately the same size at 13.0 deg. as it does at 12.0 deg.; that is, it does not grow significantly with angle of attack. Note also that the stall of the airfoil with the streamwise-ice accretion is fundamentally different from that of the ice roughness accretion in that the post-stall C_p distribution is very similar to the pre-stall C_p distribution. This is characteristic of trailing-edge stall, which tends to result in a much more gradual loss of lift than leading-edge stall.[14]

2.1.4 Important Geometric Features of Streamwise Ice

Busch[5] conducted a study which examined the effects of roughness height and concentration on 2-D smooth and simple-geometry streamwise-ice simulations. The degradation in $C_{l,max}$ with increasing roughness height relative to the $C_{l,max}$ of the 2-D smooth and simple-geometry simulations with no additional grit roughness is shown in Fig. 2.9a. For the two streamwise-ice simulations, the roughness was applied from x/c = -0.004 to 0.01 on the upper surface and from x/c = 0.02 to 0.13 on the lower surface. The airfoil leading edge was free of roughness. As with ice roughness, $C_{l,max}$ for the streamwise-ice simulations tended to decrease as roughness height increased. However, the addition of roughness tended to have a much smaller effect on $C_{l,max}$ relative to the simulation $C_{l,max}$ without roughness than for the ice roughness shape. For the range of roughness heights tested, the sensitivity of $C_{l,max}$ to roughness height was similar between the two streamwise-ice simulations and the ice roughness simulation. Though no smaller roughness heights were tested for the streamwise ice, it is likely that there would be a large increase in the sensitivity of $C_{l,max}$ to roughness height for very small roughness heights, similar to that seen in the case of ice roughness.

To determine the effect of roughness concentration on $C_{l,max}$, Busch[5] applied two different

roughness heights, $k/c = 0.0009$ and $k/c = 0.0026$, to a 2-D smooth simulation at various concentrations, using the same extents as in the roughness height study. For very low concentrations, increasing the concentration caused $C_{l,max}$ to decrease rapidly (Fig. 2.9b). At some critical concentration, $C_{l,max}$ became much less affected by further increases. This trend is very similar to that observed for ice roughness. The similar trends between the ice roughness and streamwise-ice simulations suggest that surface roughness alters the boundary-layer development in a similar way for both types of accretion. This result is not surprising, as conformal streamwise-ice accretions sometimes act as leading-edge extensions.

Another consideration for designing streamwise-ice simulations is that the exact shape and size of the gross leading-edge geometry does not usually have a large impact on the iced-airfoil $C_{l,max}$. For example, Kim and Bragg[27] showed that, for a simple-geometry simulation of a streamwise-ice accretion on a NLF-0414 airfoil, moderate changes in the height of the accretion did not have a large effect on $C_{l,max}$. This is in contrast to a horn-ice accretion, where it has been shown that small changes in horn height do have a large effect on $C_{l,max}$.[30] Though the effect of streamwise-ice height on $C_{l,max}$ is small, Kim and Bragg found that its effect on C_m is significant. In another study, Busch et al.[11] constructed two types of streamwise-ice simulation on a NACA 23012 airfoil, a simple-geometry and 2-D smooth simulation, which had slightly different leading-edge geometries. For a given level of surface roughness, different leading-edge geometries had only a small effect on iced-airfoil aerodynamic performance. It is clear that the presence of a geometry on the leading edge that alters the airfoil profile is important to represent, although these results indicate that its shape is not critical.

2.1.5 Horn-Ice Flowfield

Horn-ice shapes tend to be studied more than any other type of shape because of the large aerodynamic penalties. The height, angle, and location of the horn depend largely on airfoil geometry and icing conditions and have a significant impact on iced-airfoil aerodynamics. Ice horns tend to be fairly two-dimensional in comparison to the feathers on streamwise-ice shapes, but may still exhibit a great deal of three-dimensionality as will be shown later in this dissertation.

A horn-ice flowfield is essentially that of a backward-facing step flow in a pressure gra-

dient.[4] The dominant feature is a long separation bubble[13] generated near the tip of the horn (Fig. 2.10). The bubble results from the strong adverse pressure gradient created by the horn geometry and the separation point tends to be independent of angle of attack and freestream conditions. A shear layer forms between the inviscid flow over the top of the horn and the recirculatory flow inside the bubble. This shear layer eventually becomes turbulent and entrains high energy flow from outside the bubble, promoting pressure recovery. If the airfoil angle of attack is sufficiently low, the shear layer may entrain sufficient high energy flow to reattach to the airfoil surface. As airfoil angle of attack increases, the shear layer must reattach in a stronger adverse pressure gradient, increasing the amount of high energy flow the shear layer must entrain and increasing separation bubble length. At high angles of attack, the separation bubble does not reattach to the airfoil, and the airfoil is considered to be stalled. This type of stall was classified as thin-airfoil stall by McCullough and Gault[14] and is typical for airfoils with horn-ice accretions. This process is highly unsteady, as the separation bubble undergoes changes in size due to shear layer flapping as vorticity is shed downstream. Since the separation bubble changes size, it does not reattach at a single location and reattachment is better defined as a zone than a single chordwise position.

The time-averaged C_p distribution measured by Broeren et al.[9] for a NACA 23012 airfoil with a horn-ice casting is shown in Fig. 2.11 for angles of attack prior to and after stall. Prior to stall, the suction peak near the leading edge is nearly as great as the clean airfoil suction peak. There is a small spike in the C_p distribution at x/c = -0.02. This low pressure was measured by a tap located in the tip of the horn and captured the acceleration of the flow over the tip. This pressure spike is predicted by CFD methods,[31,32] but is not always captured in experimental data due to insufficient pressure tap resolution. Downstream of the spike is a region of constant pressure from x/c = 0.00 - 0.06 which corresponds with the long separation bubble generated by the adverse pressure gradient at the tip of the horn. At α = 8.0 deg., pressure recovery begins just downstream of x/c = 0.06, as the shear layer begins to entrain higher energy flow. Pressure recovery continues all the way to the trailing edge of the airfoil, although the trailing-edge pressure is still lower than in the clean case, indicating poorer boundary-layer health. At α = 9.5 deg., pressure recovery occurs much more slowly and decreases dramatically beyond x/c = 0.40, with C_p almost constant downstream

of this point. This indicates separated flow over much of the airfoil upper surface. The airfoil has experienced thin-airfoil stall, and $C_{l,max}$ decreases gradually as angle of attack is increased further. This C_p distribution shows good qualitative agreement with the time-averaged upper-surface C_p distribution measured by Gurbacki[33] for a different horn-ice shape on a NACA 0012, shown in the middle of Fig. 2.10. In the figure, the separation bubble reattachment zone has been highlighted in gray and was estimated by Gurbacki from surface oil-flow visualization images. As with the NACA 23012 horn-ice studied by Broeren et al., a region of nearly constant pressure is present just downstream of the ice horn, indicative of a separation bubble. Downstream of $x/c = 0.14$, pressure is recovered and the pressure coefficients downstream of $x/c = 0.30$ tend to be of comparable magnitude to those of the clean NACA 0012 airfoil, and, as in the case of Broeren et al., the trailing-edge pressure is slightly lower than for the iced airfoil than for the clean airfoil. Roberts[34] had suggested that the intersection of the clean and iced-airfoil C_p distributions is the approximate mean location of separation bubble reattachment. Fig. 2.10 shows that this method is reasonably accurate, but tends to under-estimate separation bubble size. Another method of approximating the mean separation bubble reattachment location from the C_p distribution is to identify where the slope of the iced-airfoil C_p distribution is the same as that of the clean airfoil.[35] From Fig. 2.10, this technique would put mean reattachment near $x/c = 0.40$, just downstream of the zone measured by Gurbacki.

Particle-image velocimetry (PIV) measurements taken by Jacobs and Bragg[36] using artificial ice shapes provide additional detail about the flowfield around a horn-ice accretion. A contour plot of the mean streamwise velocity behind a 2-D smooth horn-ice simulation is shown in Fig. 2.12. Consistent with the above discussion, a shear layer is visible between the high velocity flow over the top of the horn and the relatively slow-moving recirculatory flow just behind the horn. The shear layer is very thin immediately behind the horn, just after boundary-layer separation, and it is easily seen from Fig. 2.12 that this is a region of very high velocity gradients. Two streamlines are highlighted in this time-averaged view of the horn-ice flowfield, the separation streamline and the stagnation streamline. The separation streamline separates the region of forward flow outside the separation bubble from the region of recirculatory flow inside the separation bubble, and the stagnation streamline is a

streamline with a mean velocity of zero. The streamlines both intersect the airfoil surface at $x/c = 0.12$, indicating that this is the mean separation bubble reattachment location at $\alpha = 0$ deg. Note that the time-averaged shear layer thickness grows as the shear-layer develops downstream of the horn and is thickest just before reattachement.

Figure 2.13 shows the mean streamlines downstream of the ice horn, and a large, primary region of recirculation is clearly evident (Jacobs and Bragg[36] note that this recirculation is in the clockwise direction). A second region of recirculation (with counter-clockwise rotation), usually referred to as a secondary vortex, can also be observed just behind the horn. As α increases, the separation bubble, and these regions of re-circulation, grow non-linearly and the mean reattachment location moves farther aft. This is illustrated in Fig. 2.14, which shows mean separation bubble reattachment location as a function of angle of attack. Jacobs[37] obtained data using both surface oil-flow visualization and PIV at two spanwise stations, and compared it with data from Gurbacki[33] obtained using an 18-inch chord airfoil model at higher Reynolds number. According to Jacobs data, from $\alpha = 0$ to 3 deg., the mean separation bubble reattachment location moves aft by only about 10% chord. From 3 deg. to 6 deg., it moves downstream to about $x/c = 0.43$. Gurbacki's data shows similar trends, though mean reattachment is shown to be consistently farther downstream than for Jacobs's data. Blumenthal[38] and Busch[5] have obtained similar results for different horn-ice simulations on a different airfoil.

The figures referenced above provide a detailed illustration of the time-averaged horn-ice flowfield, but there is a high degree of unsteadiness which may cause the flowfield to look quantitatively different at different points in time. The last image in Fig. 2.10 shows RMS C_p measurements obtained by Gurbacki.[33] Immediately downstream of the ice horn, the RMS fluctuations in C_p are small, only slightly above those measured for the clean airfoil at the same chordwise position. However, RMS C_p increased rapidly with increasing chordwise position, reaching a maxmium value of 0.10 just upstream of the reattachment zone. Gurbacki points out that the location of the peak RMS C_p is consistent with RMS pressures observed in backward facing step flows[39–42] and flows over blunt flat plates.[43,44] Instabilities in the shear layer eventually generate spanwise vortices, which amalgamate to form larger vortical structures. These vortical structures continue to pair-up and grow in

strength, enhancing mixing and entraining higher energy flow into the shear layer. This process eventually promotes pressure recovery and allows the shear layer to reattach to the airfoil. In both horn-ice and backward-facing step flowfields, the high values of RMS C_p just upstream of mean reattachment are concomitant with the shedding of these large-scale vortical structures from the shear layer.[45,46] At and downstream of reattachment, the shear layer approaches the wall and reattaches, resulting in decreasing values of RMS C_p with increasing chordwise distance.

2.1.6 Important Geometric Features of Horn Ice

In an earlier study, Busch et al.[1,6] investigated the level of detail required to accurately represent a horn-ice casting using simulations of varying fidelity and of the same scale as the casting. The iced-airfoil performance measured for each of these simulations was compared to that measured for the casting on an 18-inch chord NACA 23012 airfoil. Both 3-D simulations and 2-D simulations were constructed to determine the importance of representing spanwise variation in the horn geometry. The 3-D simulations were based on measurements of the casting and varied horn height and angle along the span to match the spanwise variation present on the casting. One of the 2-D simulations was a 2-D smooth simulation, which captured the ice geometry at only a single spanwise station, and the other was a simple-geometry "spoiler" type simulation in that a rectangle was used to model only horn height and angle. In this study, the highest fidelity 3-D simulation almost exactly reproduced $C_{l,max}$, C_d, and the surface flowfield of the casting (Fig. 2.15). 2-D smooth and simple-geometry simulations were able to reproduce $C_{l,max}$ accurately and had C_d similar to that of the casting given the large degree of uncertainty resulting from spanwise variation in the wake. This study also showed that it is not necessary to add surface roughness to reproduce the aerodynamic features in the casting flowfield.

While the 2-D simulations were able to reproduce the aerodynamic performance of the casting with reasonably good accuracy, they were not able to reproduce spanwise variation in the surface flowfield matching that of the casting. Gurbacki,[33] Blumenthal,[38] and Busch et al.[6] used fluorescent oil-flow visualization, a technique which relies on surface shear stresses to show flow direction and shear and time-averaged flowfield features such as mean separation

bubble reattachment and transition, to compare the flowfields of castings and 2-D smooth simulations (Fig. 2.16). In the image, flow is from left to right, and the 3-D casting is visible on the left of Fig. 2.16a. The horizontal scales at the top and bottom of the picture correspond to the chordwise station in percent chord, while the vertical scale on the right measures the spanwise station in inches. The speckled region in the figure indicates the mean reattachment zone of the separation bubble, which ranges from $x/c = 0.25$ near the top of the model to $x/c = 0.28$ near the bottom of the model. Inside of the separation bubble is a region of reverse flow, indicated by the oil streaks flowing from right to left. Note that the separation bubble of the casting contains highly three-dimensional cell structures. In contrast, the flowfield behind the 2-D smooth simulation is very two-dimensional (Fig. 2.16b). Jacobs[37] showed that the cellular structures in the flowfield of a 2-D smooth simulation with roughness were formed by discrete, quasi-steady streamwise vortices non-uniformly distributed across the airfoil span. Streamwise vortices were also present behind a 2-D smooth simulation without roughness, but the distribution was much more uniform, resulting in the more two-dimensional flowfield. In studies by Jacobs[37] and Gurbacki,[33] these cell structures were generated on 2-D smooth simulations by adding grit roughness to the horn, but in another study by Busch,[5] the horn-ice flowfield remained two-dimensional even after the addition of grit roughness. Busch also constructed a simple-geometry simulation which varied horn height and angle along the airfoil span to match the variation present in the horn of the casting. Flow visualization for this simulation is compared with that of the casting in Fig. 2.17. The separation bubble reattachment line behind this simulation is three-dimensional and very closely represents that of the casting, suggesting that spanwise variation of the gross horn geometry is necessary to generate the appropriate streamwise vorticity and reproduce the surface flowfield. However, streamwise vorticity does not appear to have a substantial effect on $C_{l,max}$ and is therefore not necessary to exactly represent for most simulation needs.

Since the iced-airfoil flowfield depends mainly on horn height, angle, and location and not the geometric intricacies of the horn, horn-ice can be represented using simple-geometry simulations, which makes it easy to conduct parametric studies to determine the effects of parameters such as horn height, angle, and location. The effects of these parameters have been investigated in the past by Kim[17] and Papadakis et al.[16,47] In Kim's study, simple-

geometry simulations of various heights were installed on a NLF-0414 airfoil model at several chordwise locations, and in the studies of Papadakis et al., spoiler-ice simulations of two different heights were installed at two chordwise locations and several different angles on a NACA 0011 airfoil. All studies found $C_{l,max}$ to decrease as horn height increased for a given positive surface location and horn angle, and Kim showed that $C_{l,max}$ decreased more rapidly with increasing height for farther aft locations to $s/c = 0.034$. In looking at the effects of horn location, Kim observed $C_{l,max}$ to decrease almost linearly as the horn location s/c increased from -0.012 to 0.034 for a constant horn height, with larger horn heights causing $C_{l,max}$ to decrease more rapidly. Papadakis et al. also found $C_{l,max}$ to decrease with increasing s/c. In addition, Papadakis et al. reported that for a given horn height ($k/c = 0.0625$) and location ($x/c = 0.02$), the degradation in $C_{l,max}$ increased as horn angle with respect to the chordline (θ) increased from 10 to 90 deg., but then decreased as θ increased further to 130 deg.

The degradation in $C_{l,max}$ measured in several studies for various horn heights and airfoil geometries are compared in Fig. 2.18 for horns located near $s/c = 0.01$ and 0.02. For each study in which multiple data points are available, such as that of Broeren et al. which looked at the effects of simulated horn-ice on three different airfoil geometries, the degradation in $C_{l,max}$ is seen to increase slightly with increasing horn height. The plot shows that some airfoil geometries, such as the NACA 0012 and 23012, tend to be more sensitive to horn-ice of a given height for a given location. The NLF-0414 and NACA 3415 airfoils have very similar sensitivities to horn-ice for horns located near $s/c = 0.017$, as horns with the same heights and locations caused nearly identical reductions in $C_{l,max}$ on these two airfoils. The sensitivity of $C_{l,max}$ to horn height k/c shown in 2.18 is highly dependent on surface location s/c and may differ for horns at different locations.

Kim and Bragg[27] examined the effect of horn tip radius on $C_{l,max}$ and C_d of a NLF-0414 using simple-geometry simulations and found that for a horn of height $k/c = 0.022$ it had little impact. In contrast, Blumenthal et al.[30] found that decreasing the horn tip radius on a 2-D smooth horn-ice simulation for a similarly sized and located horn ($k/c = 0.027$, $s/c = 0.020$) on a NACA 0012 airfoil reduced $C_{l,max}$ by about 8% and increased C_d at all positive angles of attack. This discrepancy is likely due in part to the increased sensitivity of the NACA 0012 to ice contamination relative to the NLF-0414. For larger horns which caused

larger performance penalties on the NLF-0414, Kim[17] recorded increasing sensitivity to horn tip radius as the horn height increased or the location moved toward the trailing edge of the airfoil. Tip radius had the largest effect on the largest, farthest aft horn ($k/c = 0.067$, $s/c = 0.034$), where decreasing horn tip radius reduced $C_{l,max}$ by 22%. Most horns, however, are smaller and located farther upstream where the sensitivity to tip radius is somewhat less.

Frequently horn-ice accretions have lower surface horns in addition to upper-surface horns. Kim and Bragg[27] and Blumenthal et al.[30] have shown that the presence of a lower surface horn on 2-D smooth and simple-geometry simulations has little effect on iced-airfoil aerodynamics at high angles of attack near $C_{l,max}$. At low lift coefficients, lower-surface horns tend to increase drag (Fig. 2.19), and they may also affect the negative stall angle of attack and decrease the magnitude of negative $C_{l,max}$. Bragg et al.[4] and Kim[17] discuss that the total drag on the iced airfoil with upper and lower horns can be approximated as the linear combination of the drag increments of the upper and lower surface horns:

$$C_{d,total} = C_{d,clean} + (C_{d,upper} - C_{d,clean}) + (C_{d,lower} - C_{d,clean}) \tag{2.1}$$

This is illustrated in Fig. 2.19. The line marked "sum" in the figure uses the formula above to estimate the drag polar of the airfoil with both upper and lower surface horns, and the curve is remarkably similar to the measured drag polar at all angles of attack shown. For simulation of ice accretion at angles of attack of a practical interest, the effect of the lower surface horn is mainly to increase C_d at low angle of attack, and this effect diminishes with increasing angle of attack. This phenomenon has been observed for other types of ice accretion as well, such as spanwise-ridge ice.[15]

To isolate the effects of surface roughness, many studies have compared identical 2-D simulations of horn-ice with and without roughness and documented its effect. In these studies the presence of surface roughness had differing effects. Busch[5] found that $k/c = 0.0037$ roughness caused $C_{l,max}$ to decrease and C_d to increase on a NACA 23012. Jacobs and Bragg[36] observed separation bubble size to decrease with the addition of $k/c = 0.0059$ roughness to a NACA 0012 horn-ice simulation. No performance data were reported in that study, but a decrease in separation bubble size usually corresponds to an increase in $C_{l,max}$

and a decrease in C_d. Blumenthal et al.[30] added $k/c = 0.0037$ roughness to the front face of a horn on a NACA 0012 and found $C_{l,max}$ to decrease and C_d to increase at low angles of attack. Papadakis et al.[20] observed only very small reductions in $C_{l,max}$ with the addition of $k/c = 0.00058$ roughness to a horn on a modified NACA 63A-213 airfoil. Addy et al.[48] found that the addition of $k/c = 0.00078$ roughness to horn ice on a GLC-305 airfoil had no effect on the airfoil $C_{l,max}$ and only a minor effect on C_d. The authors in this study proposed that various methods of applying grit roughness may yield differing results, as there are no standardized methods for determining appropriate roughness sizes or concentrations. Indeed, the non-dimensional roughness heights used in these studies varied greatly, with roughness of height less than $k/c = 0.00078$ having only a small effect on iced-airfoil performance and roughness of height $k/c = 0.0058$ improving performance. Roughness heights in the range between these heights tended to degrade performance. It is likely that the sensitivity of the airfoil to ice accretion is also important, as each of these studies were conducted on different airfoils.

In regards to improving simulation aerodynamic fidelity for horn-ice accretions, surface roughness has not been shown to be universally effective, and if not applied appropriately, may worsen simulation fidelity. Busch[5] compared the aerodynamic performance of a 2-D smooth simulation of a horn-ice accretion with and without surface roughness to its corresponding casting. The aerodynamic performance of the 2-D smooth simulation without roughness was found to better reproduce the performance of the casting, as adding surface roughness resulted in estimates of $C_{l,max}$ and C_d which were too conservative.

2.1.7 Spanwise-ridge Ice

The fourth classification of iced-airfoil flowfield is spanwise-ridge ice, which often results from the use of a thermal ice protection system operating at less than 100% evaporation (especially in SLD conditions). Usually the airfoil leading edge is free or mostly free of ice, and a relatively two-dimensional ridge forms downstream of the heated porion of the leading edge. Broeren et al.[15] sub-classified spanwise ridges based on the types of flowfield they generate as either tall or short. Tall ridges generate long separation bubbles which have a global effect on the airfoil C_p distribution, while short ridges generate short separation bubbles which have only

a local effect on the airfoil C_p distribution. The flowfields and important goemetric features of each type of ridge are now discussed in more detail.

2.1.7.1 Tall Spanwise-Ridge Ice Flowfield

A fundamental difference between the flowfields of horn-ice and tall ridge-ice accretions is that in the latter, the boundary layer has time to develop and may be transitional or turbulent before reaching the ridge. Thus, the ridge acts as a flow obstacle.[4] An adverse pressure gradient exists upstream of the ridge, causing the boundary layer to separate just prior to reaching the ridge. This primary upstream separation zone is illustrated in the flowfield of a ridge-ice simulation in Fig. 2.20, and the recirculatory flow inside of this upstream separation bubble often drives a secondary upstream recirculation zone. Behind the ridge, a long separation bubble forms, and the flowfield downstream of the ridge is similar to that of a horn-ice accretion. The severe adverse pressure gradient at the tip of the ridge causes boundary-layer separation, and a shear layer forms between the recirculatory flow downstream of the ridge and the flow over the top of the ridge. As with horn-ice, this shear layer eventually transitions and entrains higher energy flow, promoting pressure recovery and potentially causing the separation bubble to reattach to the airfoil surface, as shown in Fig. 2.20. Of course, Fig. 2.20 is a simplified time-averaged representation of the ridge-ice flowfield, as the separation bubble is highly unsteady. The pressure recovery process may occur in a much more adverse pressure gradient than it does for a horn-ice accretion due to the aft location of the ridge on the airfoil. Therefore, tall ridges often cause more severe aerodynamic penalties than horns even though they tend to be smaller in size.

Broeren et al.[9] measured the surface pressure distribution of a NACA 23012 airfoil with a tall spanwise-ridge ice casting at Re = 12.0 x 10^6 and M = 0.20. The ridge was located at x/c = 0.05. As shown in Fig. 2.21, the ridge eliminated the leading-edge suction peak present on the clean airfoil. A strong adverse pressure gradient is seen immediately upstream of the ridge, and a very small constant pressure region extending only about 0.5% chord is barely visible just upstream of $x/c = 0.05$. This region corresponds to the primary upstream recirculation zone shown in Fig. 2.20. At $x/c = 0.05$, pressure decreases sharply as the flow accelerates over the top of the ridge, and the magnitude of the pressure decrease is dependent

on airfoil angle of attack. For both angles, a large region of nearly constant pressure is present downstream of the ridge. This region corresponds to the primary downstream recirculation zone. At $\alpha = 4.0$ deg., prior to airfoil stall, pressure recovery begins around $x/c = 0.23$ and persists to the trailing edge, although the trailing edge pressure of the iced airfoil remains lower than that of the clean airfoil. At an angle of attack higher than airfoil stall ($\alpha = 6.1$ deg.), a very slow pressure recovery begins downstream of $x/c = 0.40$, and the trailing edge pressure is much lower than at the lower angle of attack. It is likely that the flow is completely separated behind the ridge at this angle of attack. As was the case with the horn-ice casting of Fig. 2.11, the ridge ice has caused the airfoil to exhibit a thin-airfoil stall.

2.1.8 Important Geometric Features of Tall-Ridge Ice

To determine the sensitivity of iced-airfoil performance to variations in ridge geometry, Lee[18] performed a study analogous to Kim's study of horn-ice geometry.[17] Quarter-round simple-geometry simulations of ridge ice of various heights were placed at various locations on a NLF-0414 and modified NACA 23012 airfoil, both with 18-inch chords. As with horn-ice accretions located at positive s/c (i.e., on the upper surface of the airfoil), the degradation in airfoil $C_{l,max}$ and C_d increased with increasing ridge height. This is shown for the $C_{l,max}$ of the NACA 23012m airfoil in Fig. 2.22. Whalen et al.[49] also found $C_{l,max}$ to decrease with increasing ridge height.

Also shown in Fig. 2.22 is the dependence of $C_{l,max}$ on ridge surface location for a modified NACA 23012 airfoil. Ridges located at $x/c = 0.10$ to $x/c = 0.12$ caused the largest changes in $C_{l,max}$ and in C_m. Lee and Bragg[50] explain that ridges in this region were located just upstream of the maximum adverse pressure gradient on the NACA 23012m airfoil. The large adverse pressure gradient in which the separation bubble formed made it especially difficult for the separated shear layer to entrain sufficient high energy flow to reattach. This resulted in larger separation bubbles and correspondingly large aerodynamic penalties. Lee[18] shows that on a NLF-0414 airfoil, which has only a very slight adverse pressure gradient over much of its chord, $C_{l,max}$ is relatively insensitive to ridge location. Lee et al.[21] note that the ridge location at which C_d was most affected did not exactly correspond with that at which $C_{l,max}$ was most affected. Instead, C_d was increased most by ridges located slightly farther

upstream, near the region of maximum local air velocity ($C_{p,min}$).

The 0.025-inch roughness in Fig. 2.22 corresponds to a strip of $k/c = 0.0014$ roughness with width $s/c = 0.028$ (with no ridge). Unlike the ridges, the roughness had the largest effect on $C_{l,max}$ when located near the leading edge. Lee[18] notes that this is because a ridge affects the airfoil performance through a different mechanism than the roughness. The ridge causes a separation bubble to form which grows with angle of attack, and $C_{l,max}$ occurs when the airfoil is at sufficiently high angle of attack that the separation bubble does not reattach. This is a thin-airfoil type stall. In contrast, roughness causes early boundary-layer transition and extracts momentum. This eventually causes premature trailing-edge separation and ultimately results in trailing-edge stall. Lee reasoned that the momentum loss due to the roughness had the greatest effect when the roughness was located at the leading edge - this is consistent with the results of Brumby (Fig. 2.3). Lee also explains that each ridge, regardless of height, caused similar penalties to $C_{l,max}$ as the roughness when located at the airfoil leading edge. At this location, the ridges were in a favorable pressure gradient. The separation bubble remained small and stable, and the main effect of the ridge was to extract momentum and cause early boundary-layer transition in a manner similar to the roughness (note that a ridge located at the airfoil leading edge would act in a manner similar to a streamwise-ice accretion). Note that these results are very similar to those observed by Kim and Bragg[27] for simple-geometry horn-ice simulations located near the airfoil leading edge.

The trends observed by Lee[18] were in good agreement with an earlier study by Jacobs,[51] who attached two-dimensional spoilers of various heights to a NACA 0012 airfoil at chordwise positions ranging from $x/c = 0.00$ to 0.65. Jacobs tabulated the $C_{l,max}$ data obtained for each spoiler configuration, and the results were very similar to those observed by Lee (Fig. 2.23). For a given chordwise location (and at all locations), $C_{l,max}$ decreased with increasing ridge height. For a given spoiler height greater than $k/c = 0.003$, $C_{l,max}$ increased with increasing chordwise location, except for ridges located at $x/c = 0.05$. At this particular location, $C_{l,max}$ was greatly affected by the spoiler and was much more sensitive to spoiler height, dropping faster with increasing height than at any other chordwise position. This resulted in a $C_{l,max}$ much lower than for any other chordwise position for spoiler heights greater than $k/c = 0.003$. Note that $C_{l,max}$ was also very sensitive to the height of the

$x/c = 0.00$ spoiler, and very small changes in spoiler height caused large changes in $C_{l,max}$ for small spoilers located near the airfoil leading edge; this sensitivity diminshed greatly for larger spoiler heights. This may initially seem to be in conflict with the results of Lee[18] and Kim,[17] which suggest that small changes in leading-edge geometry don't have a large effect on $C_{l,max}$. However, the changes to leading-edge geometry in Jacobs's study were not small – k/c varied from 0.0004 to 0.0125, nearly two orders of magnitude difference. According to Jacobs's plot (Fig. 2.23, variations in spoiler height from $k/c = 0.006$ to 0.014 (the range of leading-edge ice thicknesses investigated by Lee) had very little impact on $C_{l,max}$. Similarly, the spoilers of Kim's study ranged from $k/c = 0.020$ to 0.067, falling in the range of heights where $C_{l,max}$ is not sensitive. Jacobs does not show the effect of lower surface spoilers on airfoil $C_{l,max}$, as it was found that changes in lower surface spoiler height and location had only small effects on maximum lift.

In addition to using surface roughness alone, Lee and Bragg[52] added surface roughness to some of their simple-geometry ridge simulations. It was found that, in general, roughness had a measurable effect on $C_{l,max}$ and C_d. This effect was dependent on the chordwise extent of the roughness. Roughness entirely within the separation bubble upstream or downstream of the ridge caused only a slight decrease in $C_{l,max}$. Roughness extending far upstream of the upstream ridge separation bubble caused a slight increase in $C_{l,max}$. Lee[18] explained that this was likely due to the roughness displacing the boundary layer upwards, reducing the effective ridge height and decreasing separation bubble size. Busch et al.[11] added surface roughness on and downstream of the ridge on 2-D smooth and simple-geometry tall ridge simulations. A slight decrease in $C_{l,max}$ and increase in C_d was measured, consistent with the results of Lee. Whalen[53] measured the aerodynamic performance of NACA 3415 and 23012 airfoils with both 2-D and 3-D simple-geometry simulations. While this study was not conducted to determine the effect of surface roughness alone, the height, shape, and location of the upper surface ridge on the 2-D and 3-D simulations was similar. The trends in this study agreed with those observed by Lee and Busch et al.; $C_{l,max}$ was found to be consistently lower on the 3-D simulations, and C_d was higher at positive angles of attack on the 3-D simulations than on the 2-D simulations.

2.1.8.1 Short Spanwise-Ridge Ice Flowfield

Unlike tall ridges, short ridges tend to have a much smaller effect on the airfoil flowfield. They generate short separation bubbles as opposed to the long separation bubbles of tall ridges. For airfoils with short-ridge ice, the upper-surface suction peak at the leading-edge of the airfoil is largely unaffected by the presence of the ridge. The difference between short and tall ridges is analagous to Tani's[13] definition of short and long separation bubbles – long separation bubbles tend to have a global effect on the airfoil C_p distribution, while short separation bubbles tend to cause only local effects. Short bubbles also do not grow substantially with angle of attack as do long bubbles. This is illustrated in Fig. 2.24, which shows the mean separation bubble reattachment location as a function of angle of attack for short and tall spanwise ridge ice simulations. In the figure, the $k/c = 0.0069$ and 0.0139 ridges are tall ridges and the $k/c = 0.0035$ ridge is a short ridge. For the tall ridges, separation bubble reattachment location rapidly moved downstream with angle of attack, increasing from $x/c = 0.50$ to the trailing edge as α increased from 1 to 5 deg. on the NACA 23012m and from $x/c = 0.33$ to 0.42 from $\alpha = 6$ to 8 deg. on the NACA 3415. In constrast, the separation bubble reattachment location for the short ridge on the NACA 3415 remained at $x/c = 0.20$ for the range of α from 6 to 16 deg.

In addition to the tall ridge discussed above, Broeren et al.[9] also measured NACA 23012 performance with a short ridge casting. A representative C_p distribution for this type of ridge is shown in Fig. 2.25. The ridge caused a sharp decrease in pressure just beyond $x/c = 0.13$ as the flow accelerated over the top of the ridge, similar to that which occurred with the tall ridge casting. However, unlike the tall ridge, the short ridge had a much smaller impact on the pressure distribution over other portions of the airfoil. For example, the tall ridge caused a significant decrease in the magnitude of the leading-edge suction peak, whereas the short ridge caused only a slight reduction. Similarly, the pressure distribution shows only a very small separation bubble behind the ridge (indicated by the short region of nearly constant pressure from $x/c = 0.15$ to 0.16) at $\alpha = 14.0$ deg., as opposed to the long bubble generated by the tall ridge at a much lower angle of attack. Accordingly, in the case of the short ridge, the pressure distribution downstream of $x/c = 0.20$ very closely resembles that of the clean

NACA 23012 airfoil.

2.1.9 Important Geometric Features of Short-Ridge Ice

As with tall ridges, the $C_{l,max}$ of airfoils with short ridges tends to decrease as ridge height increases for a given ridge cross-sectional geometry. Whalen et al.[49] showed this for k/c = 0.0035 - 0.0069 ridges with rectangular cross sections on a NACA 3415 airfoil (Fig. 2.26), and Busch[5] for ridge heights of $k/c = 0.007$ and 0.009 on a NACA 23012 airfoil (also using ridges with rectangular cross-sections). Note that in Fig. 2.26, the $k/c = 0.0052$ and 0.0069 ridges were classified as tall ridges by Broeren et al.[15] based on the airfoil C_p distribution, as they appeared to generate long separation bubbles. In Fig. 2.26, it is evident that $C_{l,max}$ is extremely sensitive to ridge height, at least at this particular location of $x/c = 0.16$ on the NACA 3415 airfoil. For ridge heights from $k/c = 0.0035$ to 0.0069 (0.0625 to 0.125 inches on an 18-inch chord airfoil), $C_{l,max}$ of the NACA 3415 decreases from about 1.48 to 0.95, a 36% decrease. The NACA 3415 with each of the short ridges actually had a 4 deg. higher α_{stall} and $C_{l,max}$ more than 10% greater than the clean NACA 3415. However, the stall was much more abrupt, suggesting leading-edge stall, and Whalen[53] reports that C_d of the iced airfoil was much higher than that of the clean airfoil at angles before clean airfoil stall. Whalen et al.[54] suggest two effects contributing to the increase in $C_{l,max}$ with some short-ridge ice simulations: they produce a short separation bubble which helps energize the boundary layer and postpone trailing-edge separation, and they produce a low-pressure region and secondary pressure recovery which strengthens the leading-edge suction peak and allows lift values beyond those observed for the clean airfoil. Whalen et al. compiled data from other researchers which have observed increases in $C_{l,max}$ with simulated short-ridge geometries and note that the increase usually occurs for ridge heights that are on the order of the local boundary-layer thickness at angles of attack immediately prior to $C_{l,max}$.

Whalen et al.[54] looked at the effect of the chordwise extent of the short ridge on airfoil aerodynamic performance. The results of this study are summarized in Figs. 2.27 and 2.28. Changing the chordwise extents of the ridge had no measurable effect on α_{stall} for k/c = 0.0035 and 0.0069 located at $x/c = 0.05$. Extents had very little effect on $C_{l,max}$ of the k/c = 0.0035 ridge, but did affect $C_{l,max}$ of the $k/c = 0.0069$ ridge when increased from s/c =

0.0069 to 0.014 (0.69% to 1.4%). However, decreases in chordwise extent to $s/c = 0.0035$ or further increases to $s/c = 0.028$ had no further effect on $C_{l,max}$. Whalen et al. showed that, despite the small effects on maximum lift, increasing chordwise extents caused the zero-lift angle of attack to become less negative, indicating that the short ridges with large chordwise extent tended to have more of a de-cambering effect on the airfoil than short ridges of lesser chordwise extents. Fig. 2.28 shows the effect of varying ridge chordwise extent on C_d of the airfoil at $\alpha = 0$ deg ($C_{d,0}$). Generally, increasing chordwise extent caused a decrease in $C_{d,0}$. For the 0.0625-inch ridge ($k/c = 0.0035$) and 0.125-inch ridge ($k/c = 0.0069$) located at $x/c = 0.10$, increasing chordwise extent beyond $s/c = 0.014$ caused only very small changes in C_d. For the 0.125-inch ridge located at $x/c = 0.05$, C_d increased slightly before decreasing again as chordwise extents increased from $s/c = 0.0069$ to 0.028.

Short ridges have an increased sensitivity to cross-sectional geometry relative to tall ridges, which may be represented with simple-geometry simulations with good accuracy, as shown earlier and in Busch et al.[11] Busch[5] attempted to use a simple-geometry simulation with a rectangular cross-section and a 2-D smooth simulation to represent a short ridge on a NACA 23012 airfoil (Fig. 2.29a). The cross-section of the 2-D smooth simulation was representative of the cross-section of a short ridge casting at the spanwise station at which pressure taps were installed. Tracings of the ridge-ice casting were also taken at two additional spanwise stations and are shown in Fig. 2.29b. Comparisons of C_l, C_m, and C_d between the two simulations and the casting are shown in Fig. 2.30, with all data at $Re = 1.8 \times 10^6$ and $M = 0.18$ on an 18-inch chord airfoil model. The 2-D smooth simulation has $C_{l,max}$ reasonably close to that of the casting, but stalled at a 2 deg. lower angle of attack. The simple-geometry simulation, on the other hand, stalled much earlier and had a much lower $C_{l,max}$. Neither simulation modeled C_d of the casting particularly well except at low positive angles of attack. Various sizes of surface roughness were added to the 2-D simulations and were determined to decrease $C_{l,max}$ and increase C_d but did not improve simulation fidelity. This study suggests that the cross-sectional geometry of the ridge is important to model appropriately.

Calay et al.[55] performed a more detailed study on short-ridge geometry using $k/c = 0.035$ simple-geometry simulations on a NACA 0012 airfoil. Three geometries were used: a forward-facing ramp with a back-facing step, a rearward-facing ramp with a front-facing

step, and a double-ramp geometry with the same height and width as the two other ramp geometries (these three geometries are shown in Fig. 2.31). For a given height ($k/c = 0.035$) and chordwise location, Calay et al. found that the rearward-facing ramp caused the largest degradation in $C_{l,max}$ and the forward-facing ramp caused the smallest degradation. The forward-facing ramp also caused the lowest degradation in C_d at $\alpha = 0$ deg. Surprisingly, the double-ramp geometry caused the largest increase in C_d even though it did not cause the largest decrease in $C_{l,max}$.

The summary charts of Fig. 2.31 also show the effect of ridge location on maximum lift and drag at zero angle of attack. For a given ridge geometry and height ($k/c = 0.035$), the penalty to $C_{l,max}$ tended to decrease as the ridge moved aft on the upper surface of the airfoil from $x/c = 0.05$ to 0.25, with a larger decrease occurring from $x/c = 0.05$ to 0.15 than from $x/c = 0.15$ to 0.25. This trend held for all three geometries. The trends in C_d at $\alpha = 0$ deg. were consistent; ridges located farther forward on the upper surface of the airfoil tended to cause larger increases in drag. The incremental increase in drag when a ridge was moved forward by $x/c = 0.10$ was approximately equal for ridges moved from $x/c = 0.25$ to 0.15 and from $x/c = 0.15$ to $x/c = 0.05$. The magnitude of the change was also similar for each ridge geometry.

2.2 General Issues in Sub-scale Ice Accretion Aerodynamic Simulation

As discussed in the Introduction, iced-airfoil performance is usually measured in wind tunnels, since flight testing is expensive and complicated and CFD is not always reliable and accurate for separated, unsteady flows. Some flight testing has been conducted, however, in both natural icing conditions and using icing tankers. Flight testing can be especially useful for validation or evaluating the effectiveness of de-icing systems[56] or the placement of icing probes[57] and is frequently used to support aircraft certification. However, it can only be done seasonally and in certain geographic regions, and the icing conditions aren't as controllable or as uniform as in CFD or icing tunnels. Additionally, flight testing may not always be appropriate depending on the data desired, since physical access to the iced surface may be

limited.

CFD has been used extensively to study iced-airfoil aerodynamics and has been used to provide many valuable insights, but computational methods must be developed further to improve and assure accuracy when applied to iced-airfoils, especially at high angles of attack, which have been shown to have highly unsteady flowfields.[2,58–60] Pan and Loth[61] used a Reynolds-Averaged Navier Stokes (RANS) code to estimate the effect of various ice shapes on the performance of NACA 23012, NACA 3415, and NLF-0414 airfoils. In general, the code had reasonable agreement with experimental data at angles of attack well below stall, but as the airfoil approached stall, agreement worsened considerably. Similar results were obtained by Marongiu et al.[62] for an iced NLF-0414 airfoil. Kumar and Loth[63] and Pan and Loth[64] used Detached Eddy Simulation (DES) to obtain better agreement than was obtained with RANS in the high angle of attack regime, but suggest that further work needs to be done to continue to improve accuracy. Mogili et al.[65] also show that DES is able to better model the near-stall airfoil lift and drag, but note that comparisons of the integrated airfoil performance may be deceiving because the DES did not show good agreement with more detailed flowfield measurements. These studies collectively show that while CFD methods can make substantial contributions to the understanding of iced-airfoil aerodynamics, they are not yet at the level where they can be confidently used to quantitatively evaluate the near-stall performance of an iced airfoil.

To accurately measure iced-airfoil performance, aerodynamic wind tunnels are usually used. Icing tunnels are not generally considered to be suitable for obtaining high quality performance measurements, as mentioned in the Introduction. Addy and Lee[66] conducted aerodynamic performance tests in the NASA Glenn Icing Research Tunnel (IRT), and documented many of the problems they encountered during their tests. Because ice would accrete on the airfoil and cover pressure taps, lift and pitching moment data were acquired using a force-balance. Wake data were acquired with a wake rake after the spray cloud was turned off, but at reduced speeds to minimize ice buildup on the tips of the probes. Because the spray cloud was turned off during performance data acquisition, ice accreted on the airfoil would sublimate over time so multiple icing runs had to be conducted to obtain a complete data set before the ice shape geometry changed, and this significantly lengthened the test

procedure. Also, the icing cloud tended to be concentrated in the center of the test section and was not completely uniform all the way to the walls, but Addy and Lee report that there was good uniformity to within 6 inches of the ceiling and 3 inches of the floor. Finally, the freestream turbulence level in the IRT can be as high as 1%,[67] which is good to enhance mixing and promote icing cloud uniformity but not conducive to making high quality performance measurements.

Addy and Lee[66] compared their aerodynamic performance data using data from an aerodynamic tunnel at the University of Illinois (UIUC) for a casting (a high-fidelity ice simulation discussed further in Section 2.2.2) of ice accreted under the same icing conditions on the same icing model. Comparisons of C_l, C_m, and C_d for two different accretions, 0.5-min ice roughness and 5.0-min horn ice accretions, is shown in Fig. 2.32. The IRT data were obtained at Re = 2.6 x 10^6 and $M = 0.235$, and the LSWT data were obtained at Re 1.8 x 10^6 and $M = 0.18$. For the 0.5-min. ice roughness case, the C_l and C_d data are in good agreement for the two tunnels. However, the C_m curves are not as similar, as the UIUC data show a much larger value of C_m at $\alpha = 10$ deg., just prior to airfoil stall. Agreement in measured aerodynamic performance of the horn-ice accretion is not as good. The IRT data show a much lower value of $C_{l,max}$ (about 13%) and a much higher value of C_d than do the UIUC data. When making these comparisons, it is expected that some differences would exist in the accretion geometry due to the separate icing runs, but the large differences are indicative of the complications inherent in obtaining performance data from icing tunnels.

To perfectly simulate an ice accretion in a dry-air aerodynamic tunnel, one should match Reynolds and Mach numbers and build a simulation of identical (or exactly scaled) geometry to the airfoil plus accretion (to match the boundary conditions of the original ice shape). While the resulting simulation would no doubt reproduce the iced-airfoil aerodynamic performance very accurately, it would be extremely expensive to produce and test. To reduce costs, and since full-scale facilities may not be available, it is usually necessary to use subscale airfoil models. This requires that the ice accretion geometry also be scaled. Frequently, it is very difficult and expensive to document every feature of an accretion, so some of the detail is lost in the documentation process. Even if every feature could be documented, some detail may be lost while fabricating and scaling the simulation. Another tool frequently used

to design sub-scale ice simulations is the LEWICE ice accretion prediction code, which can predict gross 2-D ice geometries on airfoils.[26] However, the code does not predict surface roughness or feather formation. As a result of the inability to exactly reproduce ice accretion geometry, sub-scale ice simulations based on LEWICE predictions usually have much simpler geometries than the accretions they are intended to represent.

In addition to the difficulties inherent in reproducing ice accretion geometry, it is also expensive to match both Reynolds and Mach number on a sub-scale simulation as matching both of these parameters requires a pressure tunnel. Atmospheric tunnels are generally used, so only Mach number or Reynolds number can be matched. Several studies have looked at the effects of varying Reynolds and Mach number on airfoil performance. These studies have shown little variation in aerodynamic performance with Reynolds number but some dependence on Mach number, and are now discussed in additional detail.

2.2.1 Reynolds and Mach number effects on Iced-Airfoil Performance

Reynolds and Mach number effects on clean airfoil performance can be substantial. Typically, $C_{l,max}$ increases as Re increases and decreases as M increases up to about 0.3, but it has been shown that these effects are much less significant on iced airfoils. In Fig. 2.33, the effects of changing Re on $C_{l,max}$ are shown for several airfoils at constant M, and in Fig. 2.34 the effects of changing M at constant Re are shown. In Fig. 2.33, line color and pattern denote the Mach number of the corresponding data set (kept constant) while Re was varied, and in Fig. 2.34 the line color and pattern denote the Reynolds number (kept constant) while M was varied. Symbol type denotes the airfoil configuration (clean or iced) and if iced, what type of ice accretion/simulation was present.

In Fig. 2.33, the trend of increasing $C_{l,max}$ with increasing Re (at constant M) on clean airfoils (closed symbols) is clear in most cases. For Re above about 6.0 x 10^6, $C_{l,max}$ tends to increase gradually with increasing Re. As Re decreases below about 6.0 x 10^6, $C_{l,max}$ tends to decrease more rapidly, and even more rapidly at lower Re. These trends are typical and consistent with published airfoil data.[68–70] As the Reynolds number increases, inertial effects become more dominant over viscous effects, so the boundary layer at higher Re tends to be thinner than the boundary layer at the same conditions but lower Re. This corresponds to

an increase in boundary layer momentum near the airfoil surface, which postpones stall to higher values of $C_{l,max}$ and α_{stall}.

In contrast to the clean airfoils, the $C_{l,max}$ of most iced airfoils exhibits insensitivity to changes in Re, especially horn ice (Fig. 2.33). For ice accretions such as horn ice, the boundary layer has very little time to develop before reaching the horn. The severe adverse pressure gradient at the tip of the horn triggers boundary-layer separation at a fixed location, regardless of Reynolds number. Airfoils with tall ridge ice were generally unaffected by Reynolds number as well, with the exception of two cases in which $C_{l,max}$ increased from about 0.40 to 0.46 from Re = 2.0 x 10^6 to 7.5 x 10^6 and from 0.47 to 0.52 as Re increased from 3.5 x 10^6 to 10.5 x 10^6. These were simple-geometry ridge simulations located at x/c = 0.20, relatively far back on the airfoil upper surface. It is likely that the boundary-layer had more time to develop before reaching these particular ridges, allowing for slightly more Reynolds number sensitivity. Note that for another tall ridge simulation, $C_{l,max}$ decreased as Re increased over a similar range of Re. It is evident that there is not a clear trend of Reynolds number dependence for tall ridge simulations. When analyzing these results, it is also important to keep in mind that the differences in Re shown in Fig. 2.33 tend to be small compared to the initial degradation in clean airfoil $C_{l,max}$ which, for the ridges discussed above, are on the order of 1.0.

Figure 2.33 also shows that two particular ice roughness simulations (using $k/c = 0.0002$ and 0.0006 sandpaper roughness) had $C_{l,max}$ increase by about 0.1 from Re = 2 x 10^6 - 3.5 x 10^6. Beyond Re = 3.5 x 10^6, all roughness simulations showed insensitivity to changes in Re. Papadakis and Gile Laflin[71] measured Re effects below Re = 2.0 x 10^6 on $C_{l,max}$ of airfoils with different sandpaper roughness heights and found that Re effects were significant, though no clear trends were evident and the Mach number varied from 0.05 - 0.17 as Re was changed. Loftin and Smith[72] measured a higher $C_{l,max}$ at Re = 6.0 x 10^6 than Re = 2.0 x 10^6 for airfoils with standard roughness ($k/c = 0.00046$ applied from the leading edge to x/c = 0.08 on the upper and lower surfaces), but the magnitude of this difference was dependent on airfoil geometry and $C_{l,max}$ was not measured for any Re inside of this range. Lynch and Khodadoust[2] showed that the percent reduction in $C_{l,max}$ tends to increase with increasing Re over this range, but this is at least in part caused by the clean airfoil performance dependence

on Re. More research needs to be conducted below Re = 3.5 x 10^6 (especially above Re = 2.0 x 10^6) at constant M on ice roughness simulations to better determine the extent to which Re effects are significant. Streamwise ice accretions, for which surface roughness has a similar effect as on ice roughness accretions, may also show some degree of Reynolds number sensitivity at low Reynolds numbers, but little data are available in this range of Re. Also in Fig. 2.33 is a ridge simulation (a short ridge) with $C_{l,max}$ near 1.5 which shows some sensitivity to variations in Re (at two different values of M), but no clear trend. Re effects have been shown to be significant below Re = 1.7 x 10^6 for short ridge ice accretions.[73]

Figure 2.34 shows the effect of increasing Mach number from M = 0.10 to M = 0.30 at constant Reynolds number on clean airfoil performance. As M increases, clean airfoil $C_{l,max}$ decreases, consistent with other published clean airfoil data.[74,75] At higher values of M, information can not propagate as far upstream as at lower values of M. This causes an increase in streamline curvature near the airfoil leading edge and results in an effective increase in angle of attack. Higher values of M also cause increases in the magnitude of the adverse pressure gradient behind the upper surface suction peak at the leading edge of the airfoil, which causes the flow to separate at a lower value of $C_{l,max}$ than at lower values of M.

The effect of Mach number on iced airfoil $C_{l,max}$ shown in Fig. 2.34 tends to be smaller than the effect on clean airfoil $C_{l,max}$ over the range of M shown. Ice roughness accretions showed very little sensitivity to changes in M, but some streamwise, horn, and ridge-ice accretions experienced a decrease in $C_{l,max}$ on the order of 0.1 as M increased from 0.12 to 0.28. These changes in $C_{l,max}$ with M tended to be larger than changes observed due to variations in Re and were usually much smaller than the degradation in performance due to the presence of ice.

For sub-scale simulation purposes, the trends in Reynolds and Mach number are fortunate, as Mach numbers of 0.2 and Reynolds numbers close to 2.0 x 10^6 can usually be achieved at reasonable cost so most types of accretion can be simulated at sub-scale with confidence. As discussed above, more data are needed for ice roughness, streamwise ice, and short spanwise ridges at Reynolds numbers between 2.0 x 10^6 and 3.5 x 10^6, as little data exist in this range for these types of accretion.

2.2.2 Ice simulation geometry uncertainty

Due to the difficulties in conducting aerodynamic performance tests in icing wind tunnels discussed earlier, aerodynamic tunnels are usually used to acquire iced-airfoil performance data. This requires that simulations of the ice accretion be constructed, and this process may introduce uncertainty into the performance measurements, depending on the type of simulation used. The highest fidelity simulation commonly used is a casting. Castings are usually constructed from molds of ice accreted in an icing wind tunnel. They capture nearly all of the three-dimensional geometry of the accretion, including surface roughness, and are considered to give the "true" aerodynamic penalties associated with the ice accretion. However, the fabrication of castings requires time in an icing wind tunnel and an icing wind tunnel model of a similar scale to the aerodynamic model that will be used. Since aerodynamic models are generally of a smaller scale than the airfoil they represent, this may require scaling of icing conditions. Such scaling is not validated to reproduce ice feathers of the same height k/c as would be accreted on a full-scale icing model.[76,77]

These constraints regarding the use of castings demonstrate the need for simpler, more easily scaled simulations. When designing these simulations, it is convenient to think of ice accretion on an airfoil as affecting the flowfield predominantly in two ways: the gross ice geometry may substantially alter the inviscid flowfield and surface roughness may affect boundary-layer development. With regard to the classifications of ice shapes defined by Bragg et al.,[4] horn-ice and tall spanwise-ridge ice affect the flowfield predominantly through the former mechanism, and ice roughness and streamwise ice mainly through the latter. There may be, of course, significant interaction between these two mechanisms, but for the purposes of simulation it is convenient to consider this difference.

Ice shapes which substantially alter the inviscid flowfield usually do so through the generation of a long separation bubble, as discussed in the Introduction and in Section 2.1.5. This separation bubble results from ice geometry which causes a severe adverse pressure gradient far from the clean airfoil surface relative to the boundary-layer height. For these accretions, the separation point does not move significantly with changes in angle of attack, Mach, or Reynolds numbers. These types of shapes may have a high degree of surface roughness that

may affect boundary-layer development upstream of the separation point, but the roughness does not significantly affect the location of the separation point. Roughness downstream of the separation point is usually located in a separation bubble and also has a relatively small effect on the iced-airfoil flowfield. These trends will be discussed in more detail later in this dissertation.

Ice shapes which affect the iced-airfoil flowfield by altering boundary-layer development usually have gross ice geometries which do not generate long separation bubbles, although they may cause short separation bubbles. Recall that short bubbles do not grow significantly with angle of attack and have only a local effect on the airfoil pressure distribution. For these types of accretion, the effects of surface roughness dominate. The roughness extracts momentum and reduces boundary-layer health compared to the clean airfoil, causing it to separate early. This causes trailing-edge separation to occur at lower angle of attack than for the clean airfoil, and results in trailing-edge stall. In general, roughness of larger size and higher concentration (to a point) causes more severe aerodynamic penalties. The relative effects of surface roughness and gross ice geometry varies by accretion type and must be considered when designing ice accretion simulations. Different types of simulations are now discussed.

Two examples of simulations commonly used to determine iced-airfoil aerodynamics are 2-D smooth and simple-geometry simulations. 2-D smooth simulations are based on tracings of an iced-airfoil cross section. The cross section is extruded along the airfoil span to create a constant cross section, two-dimensional simulation. Frequently, tracings used to make this type of simulation are smoothed prior to simulation construction. Smoothing is a process in which the digitized ice tracing is represented as a spline in which the digitized points become control points. Then a software program, frequently SmaggIce,[78] is used to remove a fraction of the control points (e.g., 50% smoothing removes half of the control points). This process removes some of the most jagged features of the ice tracing but preserves the general ice geometry. Chung et al.[79] investigated the effects of various degrees of smoothing on the aerodynamics of 2-D smooth ice roughness and horn-ice shapes using a computational approach. Figure 2.35 shows the effect of smoothing on the upper and lower surface of the tracing of a horn-ice accretion. As the level of smoothing increases, ice features become

smaller and more rounded. This is especially prevalent on the ice horn, shown at the left of Fig. 2.35, where smoothing the tracing using 25% control points causes a notable decrease in horn height. On the lower surface (right side of Fig. 2.35), using 50% or more control points tends to preserve most of the intricate geometry of the accretion, but rounds it off. Using only 25% control points tends to cause a loss of most of the geometric detail of the surface roughness. In general, Chung et al. showed that as the level of smoothing increased, C_l increased and C_d decreased. This would be expected from the above discussion of the effects of smoothing on ice shape geometry, and is consistent with the trends of other studies discussed below. Note that these results must be intepreted carefully, as the number of control points defined as "100%" depends on the density of points in the digitization of the tracing. Therefore, if a very dense distribution of points is used to digitize a tracing, a higher level of smoothing (e.g., 25%) may provide a more accurate representation of an ice shape than a lower level of smoothing (e.g., 50%) used on a lower point density digitization of an ice tracing.

Simple-geometry simulations are also based on tracings of the ice accretion, but use simple-geometric shapes to capture only the main geometric features of the ice accretion rather than trying to duplicate the tracing exactly. For example, Busch[5] used rectangles to represent the mean horn height and angle of a horn-ice accretion (Fig. 2.36), but did not model any other features of the horn. Simple-geometry simulations tend to have lower cost than 2-D smooth simulations and are better-suited for for use in parametric studies.[16–18,47] Simple-geometry simulations are generally considered to be of a lower geometric fidelity than 2-D smooth simulations. Surface roughness is frequently added to both 2-D smooth and simple-geometry simulations to increase simulation fidelity.

To construct sub-scale 2-D smooth and simple-geometry simulations, ice shapes are usually geometrically-scaled (constant k/c) to create sub-scale simulations. This has worked well in simulating large accretions. Geometric-scaling has been less successful in simulating small accretions or accretions in which surface roughness is important, as important geometric features may be on the order of the height of the local boundary layer. Whalen[53,54] constructed sub-scale simulations of ridge-ice using boundary-layer scaled (constant k/δ) geometries in addition to geometrically-scaled geometries. The boundary-layer scaled geometries were much

larger than the geometrically-scaled geometries and tended to cause increased aerodynamic penalties relative to those of the geometrically-scaled simulations. Broeren et al.[15] showed that the geometrically-scaled simulations were likely already too conservative and that other scaling methods may be necessary to appropriately scale ice geometries which have heights that may be on the order of the local boundary-layer thickness at relevant lift coefficients. However, most simulations to date, including those discussed in this dissertation, have been designed using geometric scaling procedures.

Some studies have used different types of simulations of the same type of ice shape and compared the differences in aerodynamic performance degradation. For example, Gurbacki[33] compared 2-D smooth simulations with and without grit roughness to corresponding castings of horn and streamwise-ice accretions. It was found that the 2-D smooth simulation had a lower $C_{l,max}$ than the casting for the horn ice, but the casting had a lower $C_{l,max}$ than the 2-D smooth simulation for the streamwise ice. Another study by Addy and Chung[19] comparing a horn-ice casting and its 2-D smooth simulation on an NLF-0414 found that the 2-D smooth simulation had a higher $C_{l,max}$ than the casting. Yet another study by Addy et al.[48] on a business jet airfoil found the 2-D smooth simulation to have a lower $C_{l,max}$ than the casting.

The discrepancies observed in these studies prompted additional investigations into the flowfields behind horn-ice castings and 2-D simulations. Gurbacki[33] conducted surface oil-flow visualization experiments, shown in Fig. 2.37, to compare the time-averaged surface flowfields using various types of simulations. On a NACA 0012 airfoill, spanwise non-uniformities were observed downstream of a horn-ice casting and were especially prevalent in the reattachment zone (Fig. 2.37a), but none were observed downstream of the corresponding 2-D smooth simulation (Fig. 2.37b). Additionally, reattachment occurred slightly farther upstream for the casting compared with the 2-D smooth simulation. Based on previous data obtained in flows over backward-facing steps,[80] Gurbacki hypothesized that irregularities in the horn geometry of the casting acted as vortex generators and created additional streamwise vorticity (compared to the 2D smooth simulation) which enhanced mixing in the shear layer, promoting pressure recovery and reattachment.

Jacobs[37] investigated this further using a 2-D smooth horn-ice simulation with added grit roughness, which was observed to cause three-dimensionality in the surface flowfield similar

to that observed by Gurbacki downstream of the horn-ice casting. Also, similar to the study of Gurbacki, Jacobs observed a smaller separation bubble for the 2-D smooth simulation with roughness than for a 2D smooth simulation of the same accretion without roughness. Using particle-image velocimetry, Jacobs identified different distributions of quasi-steady streamwise vorticity downstream of the 2-D smooth simulation with roughness than for the 2-D smooth simulation without roughness. The concentration of this vorticity was highest at spanwise locations which had a high degree of three-dimensionality in the surface flowfield. Jacobs also found that regions of increased surface flowfield three-dimensionality had elevated RMS velocities and Reynolds shear stresses than more two-dimensional regions and suggested that the shorter separation bubble length may in part be due to a three-dimensional relieving effect.

In addition to the studies of Gurbacki and Jacobs, Blumenthal et al.[30] looked into differences in the average horn geometry between castings and the corresponding simulations. Recall that ice accretion tracings are often used to design 2-D smooth simulations. Most ice accretions have some variation in geometry along the airfoil span. Therefore, tracings taken at different locations along the span will differ. These tracings are used to design 2-D smooth simulations, so the geometry of a 2-D smooth simulation constructed from a tracing taken at one spanwise station will differ from one constructed from a tracing taken at a different spanwise station. Blumenthal et al.[30] quantified the differences in aerodynamic performance resulting from these variations (shown in Fig. 2.38) using a NACA 0012 airfoil model. A 2-D smooth simulation was constructed with interchangeable horn geometries. The aerodynamic performance of the NACA 0012 with three upper surface horns, representative of various cross sections of the horn along the airfoil span, was measured and compared with the casting on which the simulation was based. It was found that variations in horn height of 11% and 26% resulted in variations in $C_{l,max}$ of 7% and 13%, respectively (Fig. 2.39). Iced-airfoil C_d also changed markedly, with C_d,min of the shortest horn being 14% lower than C_d of the tallest horn. These results indicate that it is important that ice accretion tracings used to construct 2-D smooth simulations be taken at a spanwise station which is representative of the overall horn geometry.

Jackson[24] performed a similar study on the effects of tracing location on the aerodynamic

performance of 2-D smooth simulations on a NLF-0414 airfoil. An accretion was traced at three spanwise stations located 6 inches apart, and a 2-D smooth simulation was produced from each tracing. A fourth 2-D smooth simulation was constructed using a LEWICE predicted ice geometry. The cross sections of each of these 2-D smooth simulations are shown in Fig. 2.40. Variations in $C_{l,max}$ on the order of 18% were observed (Fig. 2.41), with the $C_{l,max}$ of the LEWICE simulation bracketed by the other simulations. C_d,min of the simulation based on the 30-inch station tracing was double that of the 42-inch station tracing, and C_d of the LEWICE simulation was in between these two simulations at positive angles of attack. These results agree with those of Blumenthal et al.[30] in suggesting that the selection of tracing location may have a substantial affect on aerodynamic performance and therefore must be chosen carefully to successfully simulate an ice accretion.

In addition to the effects of tracing location, another source of uncertainty regarding the geometry of ice accretion simulations comes from the inability to exactly reproduce ice accretion geometry, even for identical icing conditions. Thus, there is some variation from run to run in ice accretion geometry under nominally identical icing conditions. This variation has been documented in several earlier studies,[81–84] and may be on the order of the variation in ice geometry along the airfoil span. Examples of the repeatability of ice accreted in the Icing Research Tunnel at NASA Glenn are shown in Fig. 2.42 for horn and streamwise-ice shapes. For the horn-ice, upper-surface horn height and angle changed slightly from run to run, resulting in drag coefficients that varied by up to 20%. Based on the data taken by Blumenthal et al. and Jackson discussed above and shown in Fig. 2.38 - Fig. 2.41, these variations would likely have a notable effect on iced-airfoil aerodynamic performance.

In the current study, the non-repeatability of ice shapes was not examined in detail, as the goal was to develop a sub-scale simulation methodology for modeling the iced-airfoil performance of a given ice shape geometry rather than to determine the aerodynamic performance degradation associated with a given set of icing conditions. This second problem was investigated in an earlier study by Campbell et al.,[85–87] who related not just iced-airfoil performance but also aircraft performance (i.e., stall speed) to icing cloud conditions. Very small variations in icing conditions (e.g., LWC), on the order of the variations in the NASA Glenn Icing Research Tunnel due to icing cloud non-uniformity,[88] were shown to produce

measurable changes in iced-airfoil $C_{l,max}$ and $C_{d,min}$. This is an important consideration when viewing ice simulation data, as the differences in aerodynamic performance between a simulation and corresponding accretion are frequently on the order of differences which may result from different icing encounters in nominally identical (or very slightly different) icing conditions.

2.2.3 Iced-airfoil performance measurement uncertainty

Once an ice accretion simulation is constructed, it is usually instrumented with pressure taps so that lift and pitching moment may be measured. However, unlike a clean airfoil, which has a smooth, continuous surface, the ice accretion geometry is highly irregular. It is important to select pressure tap locations which will give representative measurements of the pressure around the simulation. Blumenthal[38] investigated the effect of pressure tap placement, and also the effects of different types of instrumentation. The two methods that were explored were the installation of pressure taps directly in a casting (Fig. 2.44a) and the use of a thin, two-dimensional profile of the simulation geometry, known as a pressure slice, in which to install the pressure taps (Fig. 2.43b). Blumenthal discussed that localized high points on the ice accretion generally correspond to regions of flow acceleration, so a pressure tap located at such a point would read a lower pressure than a tap placed nearby. Similarly, a pressure tap located immediately in front of an ice feather or roughness element may measure a higher pressure than a tap placed on top of the element. Of course, if the simulation is instrumented with a large number of pressure taps, these effects are less important since they tend to average out, but the complex geometry of most simulations restricts the number of pressure taps that may be practically installed. Blumenthal carefully selected tap locations for both tapped casting and pressure slice configurations of horn and streamwise-ice accretions such that the integrated effects would balance out. For the horn-ice simulations, both the tapped-casting and pressure-slice methods yielded similar integrated performance data. For the streamwise-ice simulations, ice feathers were found to have a notable effect on the C_p distribution on the upper surface of the simulation; Fig. 2.43 shows areas of localized higher pressure measured at taps which were located directly in front of feathers on the tapped casting or local maximums of the pressure slice geometry. These fluctuations did not have a

large effect on the downstream pressure distributions until just prior to stall. At high angles of attack, the differences in the C_p distributions corresponded to slightly lower values of C_l and C_m measured using the pressure-slice method compared with those measured using the tapped casting method.

While iced-airfoil C_l and C_m are often obtained using surface static pressure taps, iced-airfoil C_d is generally measured using a wake rake and standard momentum-deficit methods and is not as affected by pressure tap placement. However, it has been found that the spanwise position of the wake rake behind an ice simulation may have a large effect on the measured value of C_d, even on 2-D simulations. Busch et al.[6] reported variations in C_d of 32% at α = 0 deg. for a horn-ice casting, but found that the variation diminished to 11% at $\alpha = 4$ deg. (Fig. 2.44). For a 2-D simple-geometry simulation of the same horn-ice accretion, C_d varied by 20% at $\alpha = 0$ deg. and by 5% at $\alpha = 4$ deg. Blumenthal[38] measured variations of up to 16% for horn-ice and 25% for streamwise-ice castings at $\alpha = 0$ deg. The local increase in C_d in the case of castings appears to correlate loosely with increases in separation bubble size, but not directly with upper surface horn geometry. It is also interesting that variations of over 15% have been observed for clean airfoils at low Reynolds numbers by Guglielmo,[89] Althaus,[90] and Busch.[6] These results indicate that to obtain accurate measurements of C_d, wake surveys should be taken at multiple spanwise stations and averaged. Unfortunately, time and cost constraints frequently prohibit such measurements.

As with most other types of wind tunnel testing, one other issue that affects aerodynamic performance measurements relates to tunnel interference. According to Barlow, Rae, and Pope,[91] there are three corrections which must be applied to measurements obtained in a wind tunnel to extrapolate the 2-D data to free-flight conditions: solid blockage, wake blockage, and streamline curvature. Solid blockage refers to the reduction in test section area caused by the presence of the airfoil and ice simulation. Wake blockage refers to the reduction of flow velocity in the wake of the model. Both of these effects cause an increase in the effective freestream velocity near the airfoil model. Streamline curvature effects result from the presence of the tunnel walls, which prevent the streamlines from achieving the same paths as would be achieved in free flight. This causes an effective increase in airfoil camber which artificially increases the airfoil C_l and C_d. Corrections for each of these effects are

usually applied to aerodynamic performance measurements, but these corrections generally tend to be approximate and likely do not exactly yield the aerodynamic performance that would be measured in free flight.

2.3 Effects of Airfoil Geometry

Ice accretion almost always worsens airfoil aerodynamic performance, but some airfoils are more sensitive to ice contamination than others. Broeren and Bragg[92,93] and Broeren et al.[94]investigated the effects of intercycle ice, horn ice, and tall spanwise-ridge ice on NACA 23012, NACA 3415, and NLF-0414 airfoils (Fig. 2.45a). Intercycle ice refers to the ice on a wing or airfoil present immediately before a deicing cycle when the deicer is operating at steady state and tends to be smaller than horn ice or spanwise-ridge ice (discussed in Sections 2.1.5 and 2.1.7) because the ice has not had much time to accrete since the previous deicing cycle. The NACA 23012, NACA 3415, and NLF-0414 airfoils were selected in these studies because they have very different pressure distributions.

In Fig. 2.45b, the pressure distribution of each of these airfoils is shown at equivalent lift coefficients of approximately 0.6. The NACA 23012 has a very large suction peak on the upper surface near the leading edge followed by a strong adverse pressure gradient. At this lift coefficient, transition occurred near $x/c = 0.20$, and the adverse pressure gradient lessens downstream of this point but continues to the trailing edge of the airfoil. On the lower surface, the pressure gradient is favorable but gradually diminishes until $x/c = 0.40$ and remains nearly zero until $x/c \approx 0.95$. In contrast, the NLF-0414 airfoil has virtually no suction peak near the leading edge on the upper surface, but rather rapidly approaches a constant pressure which is maintained until just past $x/c = 0.70$. Beyond this location the C_p increases (becomes more positive) rapidly, creating a strong adverse pressure gradient and causing the boundary layer to separate just before reaching the trailing edge, near $x/c = 0.95$. On the lower surface, the pressure on the NLF-0414 decreases slightly more slowly from the leading edge downstream than on the NACA 23012 and the pressure gradient remains favorable until $x/c = 0.65$. The pressure then increases slightly until $x/c = 0.75$ after which the pressure rapidly increases. Note that the upper and lower surface pressures on the NLF-

0414 were very similar near $x/c = 0.75$ because the airfoil model had a flap (the NACA 3415 had a flap as well). The lower surface pressures on the flap were nearly constant until the airfoil trailing edge. The characteristics of the upper-surface pressure distribution of the NACA 3415 fit between those of the NACA 23012 and NLF-0414 airfoils. There was not a strong leading edge suction peak, but there was a mild adverse pressure gradient over much of the upper surface, beginning at $x/c = 0.16$ and extending to the trailing edge. Transition occurred near $x/c = 0.42$, farther aft than on the NACA 23012 but farther forward than on the NLF-0414.

Broeren et al.[94] used simple-geometry horn and ridge ice simulations of identical geometry and location on each of these airfoils to determine the relative effects on aerodynamic performance. The effects of these simulations on airfoil $C_{l,max}$ are summarized in Fig. 2.46. For each of these figures, simple-geometry simulations of a given height (indicated in the legend) were placed at various surface locations (indicated by the x-axis) on the airfoil. Negative values of s/c indicate that the horn was on the lower surface, while positive values indicate an upper-surface horn. For the NACA 23012m airfoil (Fig. 2.47a), all ice horns caused decreases in $C_{l,max}$ and a horn of a given height tended to decrease $C_{l,max}$ as it moved from the lower surface to the leading edge ($s/c = 0$) and aft along the upper surface. When located on the upper surface, C_{lmax} decreased with increasing horn height, as would be expected. On the lower surface, however, the largest horn caused the smallest degradation in $C_{l,max}$ (about 12%), and the medium-sized horn caused the largest degradation. As explained by the authors, this is because the lower-surface horn may have acted as a leading-edge flap and also extended the effective airfoil chord. This effect would have competed with the flow disturbance caused by the horn, creating the unpredictable trend observed in Fig. 2.47a.

The effects of the same horn-ice simulations on $C_{l,max}$ of the NLF-0414 and NACA 3415 airfoils are shown in Fig. 2.47b and 2.46c. As with the NACA 23012m, $C_{l,max}$ of the NLF-0414 tended to decrease as the horn moved from the lower surface to the leading edge and aft along the upper surface. Unlike the NACA 23012m, the tallest lower surface horn on the NLF-0414 increased $C_{l,max}$ by about 5%, again most likely due to a leading-edge flap effect. For leading-edge horn locations near $s/c = 0$, the NLF-0414 exhibited insensitivity to changes in horn height, while the NACA 23012m showed some sensitivity but much less than for horns

located at a different s/c. As may be expected from the airfoil pressure distributions, the effect of the horn-ice simulations on $C_{l,max}$ of the NACA 3415 was between that for the NACA 23012m and the NLF-0414. Like the NACA 23012m, no horn simulations increased airfoil $C_{l,max}$, but the degradation in $C_{l,max}$ due to a given horn simulation tended to be less for the NACA 3415 than for the NACA 23012m. Additionally, the sensitivity of the NACA 3415 to horn height in the leading edge region was greater than that of the NLF-0414 but less than that of the NACA 23012m. Despite these differences, the responses of these three airfoils to ice accretion did exhibit some similarities. For example, $C_{l,max}$ always decreased as the horn moved from lower s/c to higher s/c and they all showed similar sensitivity to horn height for aft upper surface horn locations, although the $C_{l,max}$ of the NACA 23012m for a given horn height at this location was much less than for the NLF-0414 and NACA 3415 airfoils.

Broeren et al.[94] also studied the effects of a $k/c = 0.0139$ quarter-round simple-geometry ridge simulation on $C_{l,max}$ of these airfoils (Fig. 2.47). In the figure, $C_{l,max}$ values are not shown for the NACA 23012m airfoil for chordwise locations between $x/c = 0.14$ and 0.30 because no clear $C_{l,max}$ value existed for these ridge locations. The NACA 23012m experienced the largest loss in maximum lift with the addition of the quarter-round for locations up to $x/c = 0.14$. The $C_{l,max}$ of both the NACA 23012m and the NACA 3415 showed a high degree of sensitivity to the location of the ridge upstream of this point. For more downstream ridge locations, the NACA 3415 became less sensitive to ridge location, though $C_{l,max}$ continued to decrease slightly as the ridge moved farther aft. The NACA 23012m, on the other hand, experienced a much smaller decrease in lift for a ridge located at $x/c = 0.30$ than at $x/ = 0.14$, and the degradation in $C_{l,max}$ appears to decrease even further as the ridge moves farther aft, though not a lot of data exist in this range. Trends in the NLF-0414 $C_{l,max}$ were similar to that of the NACA 3415 in that $C_{l,max}$ decreased as the ridge location moved from $x/c = 0.04$ to 0.30, but the NLF-0414 $C_{l,max}$ decreased less at a given ridge spanwise location than that of the NACA 3415 and it showed less sensitivity to ridge location.

Broeren et al.[92–94] further investigated the effects of airfoil geometry using simple-geometry simulations of intercycle ice and ice roughness. The effects of these simulations

on the $C_{l,max}$ of the three airfoils discussed above are shown in Fig. 2.48; the intercycle ice accretions are labeled with numbers, and the 80 and 150-grit sandpaper roughness corresponds to non-dimensional roughness heights of $k/c = 0.00046$ and 0.0023 above the paper substrate. $C_{l,max}$ of the iced NACA 23012 airfoil was most affected by all of the ice simulations, and with intercycle ice was even lower than the $C_{l,max}$ of the other two airfoils despite having a higher clean airfoil $C_{l,max}$. The NLF-0414 was the least affected by the simulated ice contamination, in most cases having the highest iced-airfoil $C_{l,max}$ despite having the lowest clean-airfoil $C_{l,max}$.

The above discussion illustrates that different airfoil geometries respond differently to different types of ice accretion, but many trends apply to all airfoils. It is also clear that the $C_{l,max}$ of the NACA 23012 is very sensitive to most forms of ice accretion, especially compared to the NLF-0414 and NACA 3415 airfoils. This sensitivity makes the NACA 23012 a good airfoil for use in studies on the simulation of iced-airfoil aerodynamics, as it tends to amplify the effects of geometric differences in various types of simulations. Recall that one of the objectives of the current study is to quantify differences between sub-scale ice accretion simulations and their corresponding castings. Since the high sensitivity of the NACA 23012 airfoil would provide an estimate of the "worst case" difference between a sub-scale simulation and a full-scale casting, it was selected for the current study as it is expected that these differences would be somewhat less for most other airfoil geometries.

Chapter 3

Experimental Methodology

As discussed in the Introduction, Broeren et al.[9] constructed full-scale, high-fidelity ice castings from molds of ice accretions, installed them on a 72-inch chord NACA 23012 airfoil model, and measured the resulting effects on aerodynamic performance in the ONERA F1 wind tunnel at high Reynolds number. This investigation of Broeren et al. provided a data set considered to give the "true" aerodynamic performance of a full-scale NACA 23012 airfoil with various types of ice accretion and can be used to validate sub-scale simulation techniques. In the present study, sub-scale simulations of each of the accretions studied by Broeren et al. were constructed and the aerodynamic performance degradation imparted by each simulation on a 18-inch chord NACA 23012 airfoil model was measured in the University of Illinois low-speed wind tunnel at low Reynolds number. This chapter provides a brief description of the wind tunnels used to measure airfoil aerodynamic performance with and without the simulated ice accretions and discusses in detail the airfoil models and data acquisition system used for aerodynamic testing at the University of Illinois. It also disusses the ice accretion acquisition process used by Broeren et al. to obtain full-scale ice castings and gives details regarding the design and construction of the sub-scale ice accretion simulations used in the current study. The final sections of the chapter analyze the uncertainty of the University of Illinois data acquisition system and the fluorescent oil-flow visualization procedure used in part to estimate mean separation bubble reattachment location. Much of this chapter was discussed previously by Busch[5] and will be presented here for completeness.

3.1 Aerodynamic Testing

3.1.1 Wind Tunnel

Full-scale aerodynamic testing was conducted by Broeren et al.[9] in the ONERA F1 wind tunnel (Fig. 3.1). The F1 tunnel is a subsonic, closed-return pressurized wind tunnel, capable of operating at pressures from 1 to 3.85 bars. The tunnel is powered by a 9.5 MW motor driving a 16 blade, adjustable pitch fan, and has a Mach number range of 0.05 - 0.36 and a Reynolds number range of up to 6.0 x 10^6/ft. The maximum Reynolds number tested was limited to Re = 16.0 x 10^6 based on airfoil chord due to concerns regarding the large forces on a very large airfoil model. The F1 test section is 11 M long, 4.5 M wide, and 3.5 M high. More details are given by Broeren et al.[9]

All sub-scale aerodynamic testing was conducted in a subsonic, low-turbulence, open-return wind tunnel at the University of Illinois at Urbana-Champaign (Fig. 3.2). The test section of the tunnel is 2.8 ft high x 4 ft wide x 8 ft long, and the contraction ratio between the inlet and the test section is 7.5:1. To account for wall boundary-layer growth, the test section is 0.5 inches wider at the downstream end than the upstream end. Flow is conditioned using a 4-inch thick honeycomb and four anti-turbulence screens in the wind tunnel inlet, giving the tunnel a freestream turbulence intensity of less than 0.1% at all operating speeds.[95] The tunnel is powered by a 125-hp AC motor driving a five-bladed fan, and is capable of reaching airspeeds up to 160 mph. This results in Re = 1.5 x 10^6/ft. For the testing discussed in this paper, Reynolds number was set to within 2% of the desired value. Data were collected for most configurations at Re = 1.8 x 10^6 and M = 0.18 as well as Re = 1.0 x 10^6 and M = 0.1. Selected simulations were also tested at Re = 0.50 x 10^6 and M = 0.05, but these data tended to be lower quality due to the low dynamic pressure at this condition.

3.1.2 Airfoil Models

The full-scale aerodynamic model used to obtain high Reynolds number aerodynamic performance data using ice castings was a 6-ft chord aluminum NACA 23012. The model was mounted vertically in the wind tunnel by securing a spar in the under-floor force balance (Fig. 3.3). The airfoil model had a removable leading edge to facilitate installation of ice

accretion castings. To fill the 11.5-ft span of the airfoil, ten 13.8-inch wide castings were placed end to end. The model had 72 pressure taps in a main chordwise row located at 43% span (above the test section floor) and 20 taps in a spanwise row at 70% chord on the upper surface. Lift and pitching moment were measured with both the surface static taps on the model and by the force balance in the tunnel floor. Drag was measured using a wake rake located at a fixed spanwise station (57%) one chord length behind the airfoil trailing edge. The rake had 100 probes with 20-mm spacing.

The sub-scale aerodynamic airfoil model used for this test was also a NACA 23012 (Fig. 3.4). The airfoil had an 18-inch chord and a 33.563-inch span with three removable leading edges: a baseline clean leading edge, a leading edge that was used for mounting App. C ice accretion simulations, and a leading edge that was used for mounting SLD ice accretion simulations. These leading edges attached to the main-airfoil body at 20% chord on the upper surface and 30% chord on the lower surface. The App. C removable leading edge follows the clean airfoil contour until 8% chord on the upper surface and 13% chord on the lower surface, at which point the ice simulations are bolted on. The SLD leading edge follows the contour of the clean airfoil on the lower surface until 23.6% chord. The main body of the airfoil has 77 pressure taps: 43 taps in a primary row located at 51.5% span (measured from the bottom of the model), 22 taps in a secondary row located at 41.7% span, and 12 taps in a spanwise row located at 70% chord.

The sub-scale airfoil model was installed vertically in the test section of the wind tunnel. The ceiling of the test section was removed, and an overhead crane was used to lower the model into position. The walls of the test section were plexiglas, and the suction surface of the NACA 23012 model could be easily seen from the wind tunnel control room. The model was held in place by clamping two spars between mounting brackets that were bolted to a force balance. Spacers were used to set the gap between the model and the floor of the test section to 0.02 inches. This insured that the model did not rub on the floor and corrupt the force-balance measurements. The ceiling was replaced, and a gap of approximately 1/8 inch was set between the test section ceiling and the model (with the wind off) using an adjustable ceiling stiffener mounted above the test section. With the tunnel running at $Re = 1.8 \text{ x } 10^6$, the gap between the ceiling and model became very small, and the exact gap distance was

adjusted with the tunnel running to be as small as possible while ensuring that the model did not rub on the tunnel ceiling. Gaps and cracks between the inside and outside of the tunnel were taped over using Scotch book tape or painter's tape to minimize leakage into the tunnel.

3.1.3 Data Acquisition

3.1.3.1 Force-Balance Measurements

Lift and pitching moment data were acquired using both a three-component force balance and by integrating the measured surface pressures around the airfoil model. The force balance (Fig. 3.5), built by Aerotech, used load cells to measure normal and axial forces on the airfoil model as well as pitching moment about the center of the balance in one of three available load ranges, shown in Table 3.1. The high range was used for all testing in the current study. The load cells had a full-scale output voltage of ± 20 mV, which was filtered at 1 Hz and amplified to a full-scale voltage of ± 5 V. The force balance was tared every few hours and after changes were made to the configuration of the airfoil model. For each force or moment measurement, 200 voltage samples were acquired at a rate of 100 Hz and averaged. The balance tare voltage was then subtracted, and the difference was multiplied by the corresponding balance range ratio, shown in Table 3.2. This final voltage (V_N, V_A, or V_M for normal-component voltage, axial-component voltage, or pitching-moment voltage, respectively) was plugged into the calibration matrix for the force balance (eq. 3.1) and the normal and axial forces, as well as pitching moment about the balance centerline, was determined. The force balance was also used to set the model angle of attack, controllable to within 0.1 deg.

$$\left\{ \begin{array}{c} F_N \\ F_A \\ M \end{array} \right\} =$$

$$\begin{bmatrix} 37.7 & 0.01359 & -0.2095 & 0.01094 & 0 & -0.000865 \\ -0.1607 & 8.3125 & -0.01638 & 0.007084 & 0 & 0.007660 \\ -0.01299 & -0.005521 & 1.247 & -0.002122 & 0 & 0.0001497 \end{bmatrix} \begin{Bmatrix} V_N \\ V_A \\ V_M \\ V_N^2 \\ V_A^2 \\ V_M^2 \end{Bmatrix} \tag{3.1}$$

Table 3.1 Load Ranges of Force Balance

	High Range	Medium Range	Low Range
Normal Force	±450 lbf	±225 lbf	±90 lbf
Axial Force	±90 lbf	±55 lbf	±18 lbf
Pitching Moment	±45 ft-lbf	±30 ft-lbf	±15 ft-lbf

Table 3.2 Range Ratios for Force-Balance

	High Range	Medium Range	Low Range
Normal Force	1	0.4944	0.2046
Axial Force	1	0.6278	0.2173
Pitching Moment	1	0.6755	0.3413

$$C_l = \frac{1}{q_\infty S}[F_N cos(\alpha) - F_A sin(\alpha)] \tag{3.2}$$

$$C_d = \frac{1}{q_\infty S}[F_N sin(\alpha) + F_A cos(\alpha)] \tag{3.3}$$

$$C_m = \frac{1}{q_\infty Sc}[M + F_N x_o + F_A y_o] \tag{3.4}$$

3.1.3.2 Pressure Measurement System

Static pressure measurements on the surface of the airfoil were made using static pressure taps in the body of the airfoil, and static and total pressure measurements in the wake of the airfoil were made using a traversable wake survey system. The pressures were measured by a Pressure Systems Inc. (PSI) System 8400. Electronically scanned pressure (ESP) modules

were used to sample pressures at 50 Hz for two seconds. Each ESP module had 32 ports, each of which was connected to a pressure tap on the model (or wake rake) using either vinyl or polyurethane tubing. Four modules were used to measure airfoil model surface static pressures: a five-psid module, 2 one-psid modules, and a 0.35-psid module. Additionally, the traversable wake rake used two 0.35-psid modules, one for static pressure measurements and one for total pressure measurements. Each ESP module had a calibration port and either one or two reference ports. A computer program was used to automatically calibrate all modules before each run. The computer program switched the modules between their run and calibration modes by exerting a 100-psi burst of nitrogen (from a nitrogen tank) for a specified time (usually 20 s) using ports on the module specifically for this purpose (the C1 and C2 ports). A vacuum pump was then used with a 5-psid Pressure Calibration Unit (PCU) to calibrate the 5 and 1-psid modules, and with a 1-psid PCU to calibrate the 0.35-psid modules. The ESP modules used to measure static pressures were referenced to the test section static pressure, while the ESP module used to measure total pressure (connected to the wake rake) was referenced to the atmosphere. Figure 3.6 shows a schematic of the pneumatic setup.

To compute the pressure distribution around the airfoil, the dynamic pressure q_∞ is needed. This can be obtained by measuring the difference between the test section and settling section static pressures and applying the Bernoulli equation (eq. 3.5) and conservation of mass for an incompressible fluid (eq. 3.6) along a streamline between these two stations.

$$\frac{1}{2}\rho U_{ts}^2 + P_{ts} = \frac{1}{2}\rho U_{ss}^2 + P_{ss} \tag{3.5}$$

$$A_{ss}U_{ss} = A_{ts}U_{ts} \tag{3.6}$$

Solving eq. 3.6 for U_{ss}, substituting the result into eq. 3.5, and rearranging gives

$$P_{ss} - P_{ts} = \frac{1}{2}\rho U_{ts}^2 \left[1 - \left(\frac{A_{ts}}{A_{ss}}\right)^2\right] \tag{3.7}$$

Also, the dynamic pressure in the test section is $q_\infty = \frac{1}{2}\rho U_{ts}^2$. Combining this with

eq. 3.7 gives an expression (eq. 3.8) for the dynamic pressure in terms of the static pressure difference between the test section and the settling section, which is easily obtained because this pressure difference is measured with a Setra model 239 pressure transducer. The pressure coefficient can then be calculated using its conventional definition, given in eq. 3.9. P_s is the measured static pressure on the airfoil surface and P_{ts} is the test section static pressure; the difference $P_s - P_{ts}$ is measured by the ESP modules connected to the airfoil because each of these modules is referenced to P_{ts}.

$$q_\infty = \frac{1}{2}\rho U_{ts}^2 = \frac{P_{ss} - P_{ts}}{1 - \left(\frac{A_{ts}}{A_{ss}}\right)^2} \tag{3.8}$$

$$C_p = \frac{P_s - P_\infty}{q_\infty} = \frac{P_s - P_{ts}}{P_{ss} - P_{ts}} \left[1 - \left(\frac{A_{ts}}{A_{ss}}\right)^2\right] \tag{3.9}$$

Once the C_p distribution around the airfoil is calculated, the lift and pitching moment coefficients can be determined as follows. The airfoil is divided into discrete panels, with each tap location being a divider between panels. The net force on each panel due to the pressure on that panel is assumed to act in the center of the panel. Also, the pressure used to determine this net force is the average of the pressures measured by the tap at the edge of the panel. The pressure is then divided into its normal and axial components and the net axial and normal forces due to the pressure over the panel is computed (eqs. 3.10 and 3.11). The incremental moment coefficient about the airfoil's quarter chord point is also determined using eq. 3.12.

$$\Delta C_n = \frac{C_{p_i} + C_{p_{i-1}}}{2} \left[\left(\frac{x}{c}\right)_{i-1} - \left(\frac{x}{c}\right)_i\right] \tag{3.10}$$

$$\Delta C_a = \frac{C_{p_i} + C_{p_{i-1}}}{2} \left[\left(\frac{y}{c}\right)_i - \left(\frac{y}{c}\right)_{i-1}\right] \tag{3.11}$$

$$\begin{aligned}\Delta C_m &= \frac{C_{p_i}\left[\left(\frac{x}{c}\right)_i - 0.25\right] + C_{p_{i-1}}\left[\left(\frac{x}{c}\right)_{i-1} - 0.25\right]}{2}\left[\left(\frac{x}{c}\right)_i - \left(\frac{x}{c}\right)_{i-1}\right] \\ &+ \frac{C_{p_i}\left(\frac{y}{c}\right)_i + C_{p_{i-1}}\left(\frac{y}{c}\right)_{i-1}}{2}\left[\left(\frac{y}{c}\right)_i - \left(\frac{x}{c}\right)_{i-1}\right] \end{aligned} \tag{3.12}$$

The normal and axial force coefficients are then easily obtained by summing the incremental forces over the N pressure taps (eqs. 3.13 and 3.14), and the lift coefficient can be determined with trigonometry (eq. 3.15). The pitching moment coefficient is computed by summing the incremental pitching moment coefficients as in eq. 3.16. Note that the lift and pitching moment coefficients computed using the surface pressure distribution are for the center section of the model, whereas the lift and pitching moment measured by the balance has been averaged over the entire 33.563-inch span of the model.

$$C_n = \sum_{i=2}^{N} \Delta C_{n_i} \tag{3.13}$$

$$C_a = \sum_{i=2}^{N} \Delta C_{a_i} \tag{3.14}$$

$$C_l = C_n cos(\alpha) - C_a sin(\alpha) \tag{3.15}$$

$$C_m = \sum_{i=2}^{N} \Delta C_{m_i} \tag{3.16}$$

3.1.3.3 Wake Survey System

Both total and static wake pressures were measured using a traversable wake rake, located 1.17 chord lengths downstream of the airfoil model (Fig. 3.7). The wake rake had 25 static and 25 total pressure taps placed on 6.5-inch probes every one inch for a span of 24 inches. It was controlled by a Lintech traverse which could move the wake rake so that it could take pressure measurements at much finer resolutions than would be possible if it were stationary. This traverse was capable of moving in both the spanwise and chordwise directions. A pressure

box was installed around the traverse mechanism to minimize leakage into the tunnel. The Lintech traverse could be manually operated or operated using a computer program. The computer program was used during data acquisition runs. For each angle of attack, the computer code started by moving the wake rake to the center of the wake, which it found by determining the region of the wake with minimum pressure. It then moved the wake rake outward until it detected a region of constant total pressure, which corresponded to the edge of the wake. After calculating the number of pressure measurements necessary to achieve the desired resolution, it moved back the other direction to complete taking pressure measurements in the wake. For most ice simulations, wake data were acquired at a single spanwise station located 4.13 inches above the primary row of pressure taps. For selected simulations, wake data were acquired at additional spanwise stations to determine the degree of spanwise non-uniformity present in the wake.

The momentum-deficit method discussed by Jones[96] was used to compute drag using the pressures measured by the wake rake. This method assumes the wake pressures are being measured in a plane 1, perpendicular to the freestream, which is sufficiently far behind the airfoil that the static pressure in the wake P_w is equal to the freestream static pressure P_∞. Using this plane, the drag per unit span can be written:

$$D' = \rho \int u_1(U_\infty - u_1)dy_1 \tag{3.17}$$

The wake rake is placed in another plane perpendicular to the freestream which is closer to the airfoil. Conservation of mass can then be applied to a streamtube between the two planes (eq. 3.18) and substituted into eq. 3.17 to yield eq. 3.19.

$$u_1 dy_1 = u_w dy \tag{3.18}$$

$$D' = \rho \int u_w(U_\infty - u_1)dy \tag{3.19}$$

The total pressures can be expressed as their static and dynamic components as follows:

$$P_\infty + \frac{1}{2}\rho U_\infty^2 = P_{o,\infty} \tag{3.20}$$

$$P_\infty + \frac{1}{2}\rho u_1^2 = P_{o,1} \tag{3.21}$$

$$P_w + \frac{1}{2}\rho u_w^2 = P_{o,w} \tag{3.22}$$

Solving these three equations for U_∞, u_1, and u_w, assuming the total pressure is constant between the wake rake plane and plane 1 so that $P_{o,1} = P_{o,w}$, and substituting into eq. 3.19, the following is obtained:

$$D' = 2\int \sqrt{P_{o,w} - P_w}\left(\sqrt{P_{o,\infty} - P_\infty} - \sqrt{P_{o,w} - P_\infty}\right) dy \tag{3.23}$$

Assuming $P_w = P_\infty$, eqs. 3.20 and 3.22 can be combined to obtain:

$$q_w = q_\infty - (P_{o,\infty} - P_{o,w}) \tag{3.24}$$

Lee[18] suggested that eq. 3.23 be rearranged by writing it in terms of dynamic pressures and substituting eq. 3.24 for q_w:

$$D' = 2\int \left[\sqrt{q_\infty - (P_{o,\infty} - P_{o,w})}\left(\sqrt{q_\infty} - \sqrt{q_\infty - (P_{o,\infty} - P_{o,w})}\right)\right] dy \tag{3.25}$$

This form is much more useful because the pressure difference $P_{o,\infty} - P_{o,w}$ can be obtained directly from measured pressures. The wake rake measures $P_{o,w} - P_{atm}$. Additionally, $P_{o,w} - P_{atm}$ at the edge of the wake is equal to $P_{o,\infty} - P_{atm}$. If these two pressure differences are subtracted, an expression for $P_{o,\infty} - P_{o,w}$ results (eq. 3.26). The drag can then be calculated directly from measured values by substituting this expression into eq. 3.25.

$$P_{o,\infty} - P_{o,w} = (P_{o,\infty} - P_{atm}) - (P_{o,w} - P_{atm}) \tag{3.26}$$

The value of the resulting integral was determined numerically using the trapezoidal rule, and the incremental drag can be expressed as eq. 3.27. If there are K probes located in the wake, and probe i is located at y_i, the incremental drag can be summed over the wake (starting at probe 0) to obtain the total drag, eq. 3.28, and the drag coefficient can then be easily computed (eq. 3.29).

$$\begin{aligned} \Delta D'_i &= \left[\sqrt{q_\infty - (P_{o,\infty} - P_{o,w_i})}\left(\sqrt{q_\infty} - \sqrt{q_\infty - (P_{o,\infty} - P_{o,w_i})}\right)\right. \\ &\quad \left. + \sqrt{q_\infty - (P_{o,\infty} - P_{o,w_{i-1}})}\left(\sqrt{q_\infty} - \sqrt{q_\infty - (P_{o,\infty} - P_{o,w_{i-1}})}\right)\right] \\ &\quad * (y_i - y_{i-1}) \end{aligned} \tag{3.27}$$

$$D' = \sum_{i=1}^{K} \Delta D'_i \tag{3.28}$$

$$C_d = \frac{D'}{q_\infty c} \tag{3.29}$$

3.1.4 Aerodynamic Test Procedure

The aerodynamic test procedure was mostly automated; a Pentium 4 computer was used to control most of the data acquisition equipment, as can be seen from the schematic of the experimental setup (Fig. 3.8). The power to the wind tunnel and the pressurized air supply (a nitrogen tank) for the PSI system was turned on, and at the beginning of each half day (in the beginning of the morning, afternoon, or evening) or after changing model configurations, the balance was tared. The balance tare was done automatically by a computer code. This code moved the balance through a range of angles-of-attack specified by the operator and recorded zero airspeed lift, drag, and pitching moment voltages for each angle. For each test run, the operator entered the desired model angle-of-attack and Reynolds number into the computer (which was computed using eq. 3.30). The computer code was then used to perform

a full calibration of the ESP modules, as described in section 3.1.3.2. After this was complete, the operator turned on a second switch to the tunnel and initiated the computer code used to run the tunnel. At this point, all subsequent steps were performed automatically by the computer until the test was complete. The code adjusted the model angle-of-attack to the beginning of the range specified by the operator and ramped the tunnel up to speed until it was within ± 2% of the desired Re. It then recorded force-balance and pressure data as described in section 3.1.3.

$$Re = \frac{\rho U_\infty c}{\mu} \tag{3.30}$$

3.1.5 Surface Oil-Flow Visualization Procedure

Surface oil-flow visualization is a technique in which the time-averaged flowfield on the surface of the airfoil can be examined. The airfoil model is first coated with a layer of lubricant, such as motor oil. The model is then sprayed with a mixture of mineral oil and fluorescent dye. When the wind tunnel is turned on, the shear forces exerted on the dye by the airflow cause it to flow along the surface of the airfoil. This oil movement forms streaks of fluorescent dye which are clearly visible in ultraviolet light. Dye subjected to higher shear stresses moves farther than dye subjected to lower shear stresses, forming regions of varying depth. By examining the length of the streaks and the depth of oil on the airfoil surface, regions of high and low shear stress can be located. Since turbulent flow exerts a higher shear stress at the wall than laminar flow, regions of laminar and turbulent flow can be distinguished. Furthermore, the point at which separation takes place can be seen because the shear stress at the separation point is zero. Therefore, the streaks of oil get shorter and shorter as the separation point is approached from upstream, and the point of separation is the point at which the oil streaks turn to oil specks (the shear stress at the wall is zero so the oil does not move). Additionally, regions of reverse flow are easily identifiable because the streak gets brighter as it moves upstream, suggesting that the flow was pushing the dye upstream in that particular location. The easy identification of these flowfield features make surface oil-flow visualization an ideal technique for investigating the time-averaged flowfield about an iced airfoil.

To prepare the airfoil for flow visualization, it was first thoroughly cleaned. The surface was freed of all dust and dirt so that a layer of smooth black contact paper could be applied. If loose dirt had been under the contact paper, it would have caused small bumps to form and would have interfered with the free flow of the fluorescent dye during a run. The black contact paper had a slight texture (i.e., it was not perfectly smooth), so another layer of very smooth, untextured, clear contact paper was placed over it. Once the contact paper had been applied, two strips of yellow electrical tape were labeled with the airfoil's x/c coordinates for use as scales. These strips were placed horizontally on the suction surface of the airfoil (on top of the contact paper), one 6 inches from the tunnel floor and the other 6 inches from the tunnel ceiling. A third strip was marked in inches and placed vertically along the trailing edge of the airfoil. A small piece of the same tape was marked with the angle of attack for which the current run was to be performed and placed in the lower right-hand corner of the box formed by the other three strips of tape. Next, a thin coat of synthetic motor oil was applied to the contact paper using a soft paper towel. The oil was applied using a circular motion. Once finished, excess oil was wiped off using gentle strokes in the downstream direction. This was to prevent the circular motion in which the oil was applied from interfering with the free flow of the fluorescent dye. After the oil was applied, black lights were placed around the model to illuminate the suction surface. These black lights provided the ultraviolet light needed to make the dye visible. An airbrush was then loaded with a mixture of about one ounce of mineral oil and five drops of Kent-Moore 28431-1 fluorescent dye. The airbrush was supplied with a pressure of 30-35 psi (using a nitrogen tank). The overhead lights were turned off so that the only source of light was the black lights, and the mixture of mineral oil and fluorescent dye was applied to the suction surface of the model. The test section was then closed, the model angle-of-attack was set, and the wind tunnel was ramped up to speed. The tunnel was turned off four minutes after it reached the desired operating speed, and black lights were again placed around the model in the tunnel. For the current study, the black lights were placed in the test section on either side of the model (see Fig. 3.9). This was found to provide adequate lighting to view the fluorescent dye without producing a large glare on the model. The oil on the model was briefly inspected to ensure that a reasonable amount of oil had been applied and nothing unusual happened during the run. Several photos

of the suction surface of the model were then taken using a Nikon model D100 digital SLR camera, using different exposure times and F-stops. The pictures were then briefly examined on a computer to ensure that they captured the important flowfield features, and the model was wiped clean using paper towels and a glass and surface cleaner. The process was then repeated for the next test case.

3.1.6 Wind Tunnel Corrections

The walls of the wind tunnel cause changes in the flowfield compared to that of natural flight through the atmosphere, so several corrections must be made. The most significant flowfield effects are solid blockage, wake blockage, and reduced streamline curvature. Barlow, Rae, and Pope[91] discussed some standard methods to correct for these effects, and these methods were used in this study. The methods discussed by Barlow, Rae, and Pope were taken from Allen and Vincenti[97] but modified to apply to the limiting case of $M = 0$ for low-speed flow. Note that M was not assumed equal to zero during the testing of Broeren et al.[9] on the full-scale ice castings at high Re, so the wind-tunnel corrections used for those tests were slightly different than those discussed here which were used during the sub-scale simulation tests.

Solid blockage occurs especially at high airfoil angles-of-attack, when the model acts to reduce the effective area of the test section. For conservation of mass to be satisfied, the air velocity must increase relative to its velocity if the model were not in the test section. This effect is even more evident for larger models, as they reduce the cross-sectional area of the test section more than smaller models. The amount the velocity increases due to this effect for an airfoil of thickness t and shape factor λ_2 (which can be found in Barlow, Rae, and Pope[91]) in a test section of width W can be estimated using eq. 3.31. This increase in velocity is known as the solid-blockage velocity increment ϵ_{sb}.

$$\epsilon_{sb} = \frac{\pi^2}{3}\frac{\lambda_2}{4}\frac{t^2}{W^2} \tag{3.31}$$

The shape factor for both the NACA 0012 and the NACA 23012 is approximately $\lambda_2 = 4$.

Another effect that must be corrected is wake blockage. The flow upstream of the airfoil

was at a uniform freestream velocity. Behind the airfoil, the flow was not uniform. In the airfoil wake, the flow velocity was less than the freestream velocity. For mass to be conserved, the flow velocity out of the wake had to be higher than the freestream velocity in the test section. This effect is known as wake blockage and can be estimated for an airfoil of chord c in a test section of height h using eq. 3.32 (where C_{d_u} denotes the uncorrected value of the drag coefficient). The wall-induced increase in velocity of the flow outside of the wake is known as the wake-blockage velocity increment ϵ_{wb}. The total increase in flow velocity ϵ was determined by adding the solid-blockage and wake-blockage velocity increments together (eq. 3.33).

$$\epsilon_{wb} = \frac{1}{2}\frac{c}{h}C_{d_u} \tag{3.32}$$

$$\epsilon = \epsilon_{sb} + \epsilon_{wb} \tag{3.33}$$

The walls also interfered with the natural curvature of the streamlines. This caused an increase in effective airfoil camber and artificially increased the measured lift and pitching moment. The effect of restricted streamline curvature is accounted for by eq. 3.34.

$$\sigma = \frac{\pi^2}{48}\frac{c}{h^2} \tag{3.34}$$

The correction factors described above are used in eqs. 3.35- 3.38 to correct the airfoil angle-of-attack as well as the lift, drag, and pitching moment coefficients. To correct the angle-of-attack, the uncorrected lift and pitching moment data were used. These corrections were applied to both the balance and pressure data.

$$\alpha_{cor} = \alpha_u + \frac{57.3\sigma}{2\pi}\left(C_{l_u} + 4C_{m_u}\right) \tag{3.35}$$

$$C_{l_{cor}} = C_{l_u}\left(1 - \sigma - 2\epsilon\right) \tag{3.36}$$

$$C_{d_{cor}} = C_{d_u}\left(1 - 3\epsilon_{sb} - 2\epsilon_{wb}\right) \tag{3.37}$$

$$C_{m_{cor}} = C_{m_u}\left(1 - 2\epsilon\right) + \frac{1}{4}\sigma C_{l_u} \tag{3.38}$$

3.2 Ice Accretion Simulation Acquisition

3.2.1 Icing Tunnel

Ice accretions for the 72-inch chord NACA 23012 airfoil model used by Broeren et al.[9] were generated in the NASA Glenn Icing Research Tunnel (IRT) on a 72-inch chord NACA 23012 icing model mounted vertically in the test section (Fig. 3.10). The IRT, which became operational in 1944, is a closed-return, atmospheric, refrigerated tunnel with a 6 ft. tall x 9 ft. wide test section (Fig. 3.11). It is powered by a 5000 hp fan and cooled by a 2100 BTU heat exchanger. The IRT is capable of velocities of up to 395 mph and temperatures down to -30 deg. F. It is equipped with 10 spray bars, each with 55 nozzles, that enable it to produce uniform icing clouds of up to 6 ft. x 5 ft. with droplet sizes between 14-50 microns and liquid water contents of 0.5-2.5 g/m^3. Ide and Oldenburg[98] provide more detailed information on the IRT.

3.2.2 Ice Accretion Acquisition

To generate an accretion, the appropriate icing conditions were set and the tunnel was given time to reach steady-state operation. The tunnel then ran for a specified amount of time, at which point the water spray stopped and the tunnel was turned off. Seven photographs of the accretion were then taken: a full-view and a close-up of the pressure surface, the suction surface, and the leading edge, and an overall picture of the total accretion. After the photographs were taken, an ice knife was used at specified locations near the model center span to melt through the ice to the airfoil surface to create a groove by which the ice shape could be traced. The ice knife was a 1/8-in. thick copper plate heated with a propane torch. Melted water was removed before it could refreeze using a shop vac. A cardboard template

which matched the contour of the clean airfoil surface was then inserted into the groove created by the ice knife (usually a table was placed under the template to provide support). The ice accretion was traced at three spanwise locations using this technique. The tracings were made by holding the pencil vertical, so as to capture ice features immediately above the cut as well as the features at the cut. When the tracings were complete, the maximum ice thickness was measured on the suction surface, the pressure suface, and the stagnation line. To generate ridge-ice accretions, an electric foil heater was added to the removable leading-edge of the icing model (Fig. 3.10). The input power to the heater was adjusted to provide an appropriate amount of heat such that water would flow over the heater and form a ridge just behind it.

3.2.3 Casting Construction

During the ice accretion testing, molds were made of selected ice accretions. For runs in which a mold was made, tracings were taken at only two spanwise locations: above and below the section of the accretion to be molded. Cutting the accretion with the ice knife at these locations also made it easier to pull out a removable section of the leading edge of the model (Fig. 3.10). The removable section was sufficiently short to ensure that the entire section to be molded was exposed to a uniform icing cloud. To make the mold, the removable section of the leading edge and its ice accretion were placed in a specially constructed duraply mold box. The mold material was poured into this mold box after it was taken to a cold room. The mold was allowed to cure overnight. The next day, IRT technicians allowed the ice to melt, disassembled the mold box, and removed the mold. At least two molds were obtained for each type of ice accretion: ice roughness, streamwise ice, horn ice, and spanwise-ridge ice. The mold procedure is described in additional detail by Reehorst and Richter.[99]

The molds were then taken back to the University of Illinois at Urbana-Champaign, where they were used to construct castings. To make a casting, the mold was placed in a second mold box which also contained a nylon plug that matched the contour of the removable leading edge of the aerodynamic model on which the casting would eventually be installed. The casting material, a polyurethane elastomer (RenCast 6430), was then poured into this mold box and allowed to cure for 24 hours. The result of this process was an approximately

14-inch span casting. Castings of seven ice accretions were constructed, representative of each type of accretion. The conditions under which the ice was accreted for each casting are listed in Appendix A.

To check the quality of the castings, a template of the clean airfoil leading edge was machined from aluminum and placed beside the master casting on the nylon plug. Initial attempts using the casting-pour method described above resulted in poor agreement between the aluminum template and cast ice shapes (in regions where comparisons of the clean airfoil surface could be made). The discrepancy was caused by uneven shrinkage of the casting material as it cured, which caused distortion of the ice shape. This shrinkage is present in the construction of all ice castings, but was especially prevalent here due to the large size and thick walls of the castings.

To mitigate this problem, a two-pour approach was developed in which a thin outer casting was bonded to a thicker inner casting. Fig. 3.12 illustrates this concept. In the figure, the geometry of the inner casting is white, and the outer casting is the gray portion bonded to the inner casting. Shrinkage was reduced in the outer casting by keeping the wall thin. Shrinkage in the inner casting was much less significant because the outer casting was poured after the inner casting cured (i.e., after it had already shrunk). To implement this approach, a new inner plug that matched the contour of the clean airfoil, but was offset inward by 1/4 inch, was fabricated from Duraply (MDO plywood). Using this plug, a new mold was made. Castings made from this new mold had the contour of the original nylon plug on the inside, and the contour of the clean airfoil, only offset inward by 1/4 inch, on the outside. Once these inner castings were cured, they were used as the plug along with the original ice accretion molds to make outer castings. These outer castings bonded to the inner castings on the inside and had the contour of the ice accretion on the outside. For the master castings, the outer casting was dyed so that mold material that broke off during the casting process could be easily identified and removed. The master casting of the EG1159 tall spanwise-ridge ice accretion is shown as an example in Fig. 3.12.

Because the original ice accretion molds must cure at freezing temperatures without producing any heat, mold durability is sacrificed. Usually these molds can only be used to produce one casting, since they are often destroyed upon removal from that casting. This first

casting is referred to as a "master" casting, and another more durable mold is made from the master casting. The new, more robust mold is made from a high-strength silcon RTV and usually survives the casting process, so it is used to make several "production" castings. The production castings were mounted on a removable leading edge that could be mounted to the aerodynamic model (Fig. 3.13a). For the testing of Broeren et al.,[9] ten 13.8-inch production castings were required for each accretion to fill the 11.5-ft aerodynamic model span (Fig. 3.13b). These castings were constructed using the same two-pour process described above to mitigate shrinkage effects. Once installed, the joints between the castings were smoothed by sanding and using a filler compound. Note that the EG1159 spanwise-ridge ice casting had a large degree of spanwise variation in ice geometry. To prevent large discontinuities in ice geometry when multiple castings were placed adjacent to each other on the aerodynamic model, a 6.9-inch portion of the master casting with relatively two-dimensional ice geometry was selected. The rest of the master casting was cut away, and two castings of this portion were poured. These castings were then bonded together to form a new EG1159 master casting with a more uniform ice geometry.

To ensure that the bond strength between the inner and outer castings would be sufficient, a tensile test was conducted on a sample of the cured casting material. The sample was constructed in two pours, identical to the fabrication method used for the actual casting construction, and machined to have a cross-sectional area of 0.25 in^2 (Fig. 3.14). The tensile strength of the specimen was measured to be over 3000 psi. The pressure difference between the inside and outside of the casting was estimated to be on the order of 10 psi, so this bond strength was sufficient.

3.2.4 Subscale Simulation Construction

As discussed in the Introduction, one objective of this research was to quantify the accuracy with which sub-scale 2-D smooth and simple-geometry simulations can model the aerodynamics of a full-scale ice accretion casting. To achieve this objective, 2-D smooth and simple-geometry simulations were constructed for each set of production castings.

To design these simulations, a sacrificial casting was made for each ice accretion (except the ice roughness accretions). The sacrificial casting was cut at the spanwise location at

which taps were drilled in the tapped casting for the test of Broeren et al.[9] Two tracings were made, one at each side of the cut. These tracings, which were slightly different because a small amount of casting material was removed by the saw blade, were averaged. For the 2-D smooth simulations, the tracings were scaled down by a factor of four and extruded using Pro-Engineer, a computer-aided design program. Pro-Engineer was also used to create 0.040-inch pilot holes for the taps in the ice shapes; these pilot holes would later be drilled out to 0.042-inch by hand. Once the CAD model of the 2-D smooth simulation was complete, the files were converted to .stl format and sent to Realize, Inc., where the shapes were fabricated from Somos 11120 using a stereolithography apparatus (SLA). Each 2-D smooth simulation consisted of three 11.187-inch long sections placed end to end to fill the span of the 33.563-inch aerodynamic model. One such 2-D smooth simulation is shown in Fig. 3.15. The center section was instrumented with pressure taps (Fig. 3.16). Instead of using rapid-prototyping methods, the simple-geometry simulations were constructed from off-the-shelf materials, typically balsa wood and strips of removable vinyl film with adhesive on both sides. Rectangular strips of balsa of the appropriate height and width were used to model the geometrically-scaled gross ice geometry for each type of accretion. For the streamwise ice accretions, book tape was stretched over the balsa to provide a simulation geometry that better matched the averaged ice tracing. To help locate the ice features on the airfoil surface, the 2-D smooth simulations (which had the same cross-section as the averaged ice tracing) were used as a template. The simple-geometry simulations did not have pressure taps, so all lift and pitching moment comparisons shown for these simulations are based on force-balance data. Frequently, the simple-geometry simulations were constructed in several phases, and the effects of the simulation on aerodynamic performance were measured in each phase. This approach helped to better identify the aerodynamic effects associated with a given geometric feature. The simulations of each accretion, and geometric details for each accretion, are discussed in more detail below.

Silicon carbide or aluminum oxide roughness elements were added to selected simulations to better model surface roughness present on the casting. Surface roughness can generally be characterized by chordwise location and extents, height, and concentration. The location and extents were determined by printing a full-scale template and aligning it with the casting.

This made it possible to determine the x/c and corresponding s/c of the roughness. Roughness height was measured at multiple spanwise stations (usually 10) on each casting using a pair of calipers. These measurements were averaged to determine an average roughness height. For regions of high roughness concentration, the height measured using this method was possibly smaller than the actual height, since the caliper was not always able to reach the smooth airfoil surface below the roughness.

Roughness concentration, as defined in this dissertation, is the ratio of the area of all individual roughness elements over the total airfoil surface area of the region. Casting roughness concentration was much more difficult to determine than roughness location and height, and could only be accurately measured on the sub-scale simulations where it was applied to a removable vinyl film. In these cases, the vinyl film could be removed from the ice simulation with the roughness intact and photographed against a white background. The roughness elements were dark and the vinyl film was clear, so there was strong contrast between the roughness elements and the background. The concentration could be determined by taking a digital picture (using a flash to mitigate shadow effects) of the roughness strip and counting the ratio of dark pixels to total pixels. This was accomplished using Adobe Photoshop 7.0, and the procedure is discussed in more detail by Jackson.[24] Since surface roughness on the castings were the same color as the airfoil surface, this procedure could not be used to determine casting roughness concentration. It will be shown in Chapter 4 that roughness concentration does not have a large effect on airfoil $C_{l,max}$ if the concentration is sufficiently high, and in most cases, the roughness concentration on the casting appeared to be above this threshold for at least a portion of the chordwise extents, suggesting that the exact concentration of roughness was unimportant provided the simulated roughness was of a sufficiently high concentration. In these cases, the vinyl film was saturated with roughness elements (this will be referred to as full concentration). For cases in which the casting roughness concentration appeared to be lower than this threshold, the concentration of roughness elements on the vinyl film was reduced to better match that present on the casting. All roughness in this dissertation was applied at the full concentration unless specified otherwise.

3.2.4.1 Ice Roughness Simulations

Two types of ice roughness were simulated in this study: glaze-ice roughness (designated EG1126) and rime-ice roughness (designated EG1134). Since there was no gross ice geometry other than surface roughness, only simple-geometry simulations were constructed of these two accretions, as the 2-D smooth simulation would essentially be just the clean airfoil. The simple-geometry simulations were constructed by placing grit strips consisting of removable vinyl film and roughness elements on the clean airfoil. On the airfoil upper surface, the glaze-ice roughness (on both the casting and sub-scale simulations) extended from x/c = 0.000, where it had a height $k/c = 0.0016$. The roughness height and concentration tended to diminish gradually until $x/c = 0.026$, where the roughness ended. Similarly, the glaze-ice roughness on the airfoil lower surface extended from $x/c = 0.004$, where it had a height k/c = 0.0011. Again, the height and concentration tended to diminish gradually until the roughness ended at $x/c = 0.041$. Photos of the glaze-ice roughness accretion are shown in Fig. 3.17. Because the glaze-ice roughness height covered such a large range, several different roughness heights were used to construct a geometrically-scaled simple-geometry simulation, chosen to match the k/c of the roughness on the casting at several chordwise stations. Roughness strips with heights k/c = 0.0013, 0.0006, 0.0009, and 0.0005 were placed at the appropriate locations on the airfoil upper surface to match the chordwise extent of the casting roughness. Roughness strips of height k/c = 0.0009, 0.0007, 0.0009, and 0.0003 were placed on the lower surface, again to match the roughness extents on the casting. For this simulation, the k/c = 0.0009 and 0.0003 roughness was applied at a reduced concentration to better match the surface roughness on the casting. This simulation is shown in Fig. 3.18. In addition to this geometrically-scaled simulation, which is the simulation constructed without *a priori* knowledge of the casting aerodynamics, several other simple-geometry simulations were also built to determine the effects of various roughness features on airfoil C_l and C_d (some of these were also designed to better match the casting aerodynamics). To determine the effects of roughness concentration, several simulations were built which had the same roughness height and chordwise location and extents but varied the concentration from 1% to 60%. Similarly, a trade study was conducted in which roughness height was varied from $k/c = 0.00007$ to

0.00184 with the other parameters held approximately constant. Finally, another trade study was conducted which examined the effects of roughness chordwise extent. These trade studies are discussed in Chapter 4.

The rime-ice roughness (Fig. 3.19) had a much longer chordwise extent than the glaze-ice roughness, from x/c = -.002 to 0.080 on the upper surface and from approximately x/c = 0.000 to 0.200 on the lower surface. The maximum height was about $k/c = 0.0003$ on each surface, occurring near the most upstream chordwise extent, with the roughness height and concentration diminishing to zero at the most rearward extent. The stagnation region on both the glaze and rime-ice accretions was relatively smooth and free of roughness. Two simple-geometry simulations were constructed of this accretion, with $k/c = 0.00007$ and 0.0016 roughness applied over the appropriate extents. Note that this roughness height was considerably smaller than the roughness present on the casting; this was because it was clear from testing of the glaze-ice roughness that geometric-scaling of the casting roughness would result in very conservative performance estimates.

3.2.4.2 Streamwise Ice Simulations

Two types of streamwise-ice accretion were simulated in this study, one with a surface-slope discontinuity near the leading edge of the airfoil (designated EG1125) and a second with a geometry that was more conformal to the airfoil leading edge (designated EG1162). Figures 3.20 and 3.21 show photos and tracings of each of these accretions. The first streamwise-ice accretion, EG1125, had a combination of roughness and feathers extending from x/c = -0.008 to 0.019 on the upper surface of the airfoil and from x/c = -0.006 to 0.029 on the lower surface. As with the ice roughness accretion discussed earlier, on both the upper and lower surfaces the roughness height and concentration gradually decreased from a maximum value at the most upstream extent to zero at the most downstream extent. The maximum roughness height of the EG1125 accretion was approximately $k/c = 0.0018$ on the upper surface and k/c = 0.0012 on the lower surface. The more conformal streamwise ice accretion, EG1162, had a combination of surface roughness and ice feathers extending from x/c = -0.008 to 0.065 on the upper surface and from x/c = -0.005 to 0.060 on the lower surface. The maximum roughness heights on this accretion were $k/c = 0.0014$ and $k/c = 0.0011$ on the upper and lower surfaces,

respectively. Extents corresponding to those on the appropriate casting were used when grit roughness was applied to the sub-scale simulations. In addition to 2-D smooth simulations, simple-geometry simulations of each of these accretions were constructed by stretching book tape over rectangular strips of balsa, and in some cases, grit roughness was applied on the simple-geometry simulations. The cross-sections of these simulations are compared with those of the 2-D smooth simulations in Fig. 3.22, and photographs of the EG1162 simple-geometry simulation are shown in Fig. 3.23.

3.2.4.3 Horn Ice Simulations

The horn-ice accretion (designated EG1164 and shown in Fig. 3.24) was modeled using sub-scale simple-geometry and 2-D smooth simulations. The upper horn had a height of $k/c = 0.020$ and was located at approximately $s/c = 0.009$. The angle of the upper horn with respect to the airfoil chord-line was $\theta = 27$ deg. The lower horn had a height of $k/c = 0.007$ and was located at s/c = -0.040. The 2-D smooth horn-ice simulation was rapid-protoyped using SLA, while the simple-geometry simulation used a 0.36 inch tall x 0.06 inch wide rectangular strip of balsa to represent the upper horn and a 0.12 x 0.06 inch strip of balsa to represent the lower horn. Figure 3.25 compares the cross-sections of the 2-D smooth and simple-geometry horn-ice simulations, and Fig. 3.26 shows photos of the simple-geometry horn-ice simulation.

3.2.4.4 Spanwise-ridge Ice Simulations

As discussed in Chapter 2, Broeren et al.[15] sub-classified spanwise ridges into two categories based on their key aerodynamic characteristics: tall ridges, which generate a long separation bubble; and short ridges, which generate a short separation bubble. Each type of ridge was simulated in this study. The tall ridge (designated EG1159) was located at $x/c = 0.05$ on the upper surface. This ridge had a height $k/c = 0.013$ and an angle of $\theta = 67$ deg (Fig. 3.27). with respect to the airfoil chord-line. On the lower surface, a smaller ridge formed downstream of the IPS. This ridge was more three-dimensional than the upper surface ridge and had a height at the tracing location of k/c = 0.0052. Cross-sections of the 2-D smooth and simple-geometry simulations constructed for this ridge are shown in Fig. 3.28, and photos of the simple-geometry simulation are shown in Fig. 3.29.

The short ridge (designated NGO671 and shown in Fig. 3.30) extended from $x/c = 0.13$ - 0.18 on the upper surface and had a height of $k/c = 0.0028$. The ridge was reasonably two-dimensional, but there was some variation in height along the span. From $x/c = 0.15$ - 0.20 on the lower surface, the airfoil was covered with large roughness elements. Mixed in with this roughness were large isolated chunks of ice ranging in height from $k/c = 0.008$ - 0.012 and averaging about $k/c = 0.009$, creating a highly three-dimensional geometry.

Since the lower surface ridge of the short-ridge shape was very three-dimensional, various methods of building 3-D simulations were explored. The highest geometric-fidelity option was to use a laser scanner to digitize the geometry of the casting and rapid-prototyping methods to produce a 3-D simulation. To determine the practicality of this approach, a sample of the upper surface ridge was sent to QC Inspection Services for scanning. The result of this process was a three-dimensional point cloud which could be loaded into Pro-Engineer, and with some manipulation, converted to a CAD model and exported as an .stl file that could be rapid-prototyped. The CAD model is compared with the casting sample in Fig. 3.32. Two samples were constructed at the Ford Lab at the University of Illinois using the Objet polyjet process – one sample was full-scale, and the other was 1/4-scale (this would be the size used on the aerodynamic model at the University of Illinois). The full-scale sample turned out well, capturing most of the geometric details present on the casting. However, the ridge and roughness was so small that most of this detail was lost when scaled down by a factor of 4. Note also that in Fig. 3.32b, some holes are visible in the CAD model. This is a common problem to have with laser scans, and it is possible to fill the holes (QC Inspection Services could do it for an extra fee). However, this was an exploratory excercise, so it was not done. Given the loss of detail in the sub-scale prototype, it was determined that it was not worth the added cost and complexity to create a scanned model of the ridge and that instead simple-geometry simulations would be used.

Both 2-D and 3-D simple-geometry simulations of the short ridge were constructed. In creating the simulations, one feature (e.g., surface roughness or a lower surface ridge) was added at a time until the simulation was complete so that the aerodynamic effects of each feature could be better identified. Two 2-D simulations (with and without roughness) were constructed: one which used only $k/c = 0.00092$ roughness to model the lower surface ridge,

and one which used a rectangular strip of balsa wood. The height of the balsa ($k/c = 0.0039$) was selected such that it represented the "average" height of the lower surface ridge, which was determined by averaging measurements of the height of the lower surface ice across the airfoil span. The upper ridge for these simulations, with and without $k/c = 0.00092$ roughness, are shown in Figs. 3.33a and 3.33b. To better model this spanwise variation on the lower surface, a three-dimensional lower surface ridge was also constructed (Fig. 3.33c). This ridge used a substrate of height $k/c = 0.0022$ on which cubes of balsa wood were mounted to simulate the chunks of ice present on the lower surface. Each cube measured $k/c = 0.0093$ tall x w/c = .0069 wide x $s/c = 0.0069$ thick, representative of the geometrically-scaled average chunk size on the casting. For the 3-D simulation, rivulets were modeled by applying Bondo at the relevant chordwise location and pushing a comb through it, leaving grooves (Figs. 3.33d and 3.33e). The simulated rivulets had a height slightly less than $k/c = 0.0017$ on the upper surface and less than $k/c = 0.0015$ on the lower surface were applied to the 3D simulations. Note that the exact height of the rivulets was difficult to determine because the caliper used to measure them was thicker than the spacing between each pair of rivulets. They had an average spanwise spacing of approximately 18 rivulets/inch and an average length of s/c = 0.028 on the upper surface (in the chordwise direction) and $s/c = 0.056$ on the lower surface.

3.3 Uncertainty Analysis

There are two kinds of experimental uncertainty: precision error and bias error. Precision error is random error that is introduced by the instrument making the measurement. An example of precision error is when an instrument produces a varying output when what it is measuring is unchanging. This type of error can be mitigated by making multiple samples and averaging them together. Bias error, on the other hand, is a systematic error introduced by the instrument favoring a particular outcome. The instrument may make consistently low or high measurments. An example of something that might introduce bias error is a poor calibration, such that the instrument consistentlly measures low values. The total error of an instrument is its bias error and precision error added together. This total error can be considered a fluctuating value made up of a steady component (bias error) and a fluctuating

component (random error).

The experimental uncertainties for this study were calculated using the second-power equation introduced by Kline and McClintock[100] and further discussed by Coleman and Steel.[101] The method used does not address precision uncertainties nor does it address uncertainties associated with wind tunnel corrections. Also, the precision uncertainties were very small compared to the bias uncertainties, so they were considered negligible.

Let a desired result R be a function of several measured values x_1, x_2, ...,x_n as in eq. 3.39. Then the experimental uncertainty associated with that result is given by eq. 3.40.

$$R = R\left(x_1, x_2, \ldots, x_n\right) \tag{3.39}$$

$$U_R = \sqrt{\left(\frac{\partial R}{\partial x_1} U_{x_1}\right)^2 + \left(\frac{\partial R}{\partial x_2} U_{x_2}\right)^2 + \cdots + \left(\frac{\partial R}{\partial x_n} U_{x_n}\right)^2} \tag{3.40}$$

This equation will be used to determine the uncertainties in the following sections. A summary of uncertainties can be found in section 3.3.4. Busch[5] and Blumenthal[38] used identical experimental setups in their research and performed the same uncertainty analysis in their theses.

3.3.1 Uncertainties of Variables Describing Flow Conditions

3.3.1.1 Dynamic Pressure

The freestream dynamic pressure in the test section was computed via eq. 3.8, which related q_∞ to the measured static pressure difference between the settling section and the test section and the contraction ratio between the inlet and test section. The contraction ratio was constant and its uncertainty considered negligible. Therefore, the only measurement that introduced uncertainty into the value of dynamic pressure was the pressure measurement. Hence, for the case of dynamic pressure, eq. 3.40 can be written as eq. 3.41. The uncertainty associated with this pressure difference is the uncertainty of the 1-psid ESP module, reported by the manufacturer to be 0.001 psi. Taking the partial derivative of eq. 3.8 with respect to $P_{ss} - P_{ts}$ and substituting the result as well as the uncertainty listed above into eqn 3.41

gives the uncertainty of the test section dynamic pressure.

$$U_{q_\infty} = \sqrt{\left(\frac{\partial q_\infty}{\partial(P_{ss} - P_{ts})} U_{P_{ss}-P_{ts}}\right)^2} \tag{3.41}$$

$$\frac{\partial q_\infty}{\partial(P_{ss} - P_{ts})} = \frac{1}{1 - \left(\frac{A_{ts}}{A_{ss}}\right)^2} \tag{3.42}$$

3.3.1.2 Atmospheric density

Atmospheric density ρ was determined using the ideal gas law $\rho_{atm} = \frac{P_{atm}}{RT_{amb}}$, where R is the gas constant of air, 1716 $\frac{ft-lbf}{slug-R}$. P_{atm} and T_{amb} were both measured quantities. The pressure transducer used to measure P_{atm} had an uncertainty of 0.008 psi and the thermocouple used to measure T_{amb} had an uncertainty of 1 deg. F; both of these uncertainties were reported by the manufacturer. Therefore, the uncertainty of the measurement of ρ_{atm} is

$$U_{\rho_{atm}} = \sqrt{\left(\frac{\partial \rho_{atm}}{\partial P_{atm}} U_{P_{atm}}\right)^2 + \left(\frac{\partial \rho_{atm}}{\partial T_{amb}} U_{T_{amb}}\right)^2} \tag{3.43}$$

where

$$\frac{\partial \rho_{atm}}{\partial P_{atm}} = \frac{1}{RT_{amb}} \tag{3.44}$$

$$\frac{\partial \rho_{atm}}{\partial T_{amb}} = -\frac{P_{atm}}{RT_{amb}^2} \tag{3.45}$$

3.3.1.3 Dynamic Viscosity

The dynamic viscosity μ is computed using the Sutherland Law:

$$\mu \approx \mu_o \left(\frac{T_{amb}}{T_o}\right)^{\frac{3}{2}} \frac{T_o + S_u}{T_{amb} + S_u} \tag{3.46}$$

Here, μ_o, T_o, and S_u are known constants with values of 3.58404 x 10^{-7} $\frac{slug}{ft-s}$, 491.6 R, and 199.8 R, respectively. Therefore, the uncertainty in μ can be computed:

$$U_\mu = \sqrt{\left(\frac{\partial \mu}{\partial T_{amb}} U_{T_{amb}}\right)^2} \tag{3.47}$$

$$\frac{\partial \mu}{\partial T_{amb}} = \frac{3}{2}\mu_o \sqrt{\frac{T_{amb}}{T_o}} \frac{T_o + Su}{T_o(T_{amb} + Su)} - \mu_o \left(\frac{T_{amb}}{T_o}\right)^{\frac{3}{2}} \frac{T_o + Su}{(T_{amb} + Su)^2} \tag{3.48}$$

3.3.1.4 Freestream Velocity

The uncertainty in the freestream velocity U_∞ can be found using the definition of dynamic pressure $q_\infty = \frac{1}{2}\rho_{atm} U_\infty^2$.

$$U_\infty = \sqrt{\frac{2q_\infty}{\rho_{atm}}} \tag{3.49}$$

The uncertainty associated with U_∞ is then

$$U_{U_\infty} = \sqrt{\left(\frac{\partial U_\infty}{\partial q_\infty} U_{q_\infty}\right)^2 + \left(\frac{\partial U_\infty}{\partial \rho_{atm}} U_{\rho_{atm}}\right)^2} \tag{3.50}$$

where

$$\frac{\partial U_\infty}{\partial q_\infty} = \frac{1}{\sqrt{2q_\infty \rho_{atm}}} \tag{3.51}$$

$$\frac{\partial U_\infty}{\partial \rho_{atm}} = -\frac{1}{\rho_{atm}} \sqrt{\frac{q_\infty}{2\rho_{atm}}} \tag{3.52}$$

3.3.1.5 Reynolds Number

The Reynolds Number was computed using the atmospheric density, freestream velocity in the test section, airfoil chord, and the dynamic viscosity of air. The uncertainty in Re can be determined using the uncertainties derived above. Writing eq. 3.40 in the applicable form, we find the uncertainty in Re is

$$U_{Re} = \sqrt{\left(\frac{\partial Re}{\partial \rho} U_\rho\right)^2 + \left(\frac{\partial Re}{\partial U_\infty} U_{U_\infty}\right)^2 + \left(\frac{\partial Re}{\partial c} U_c\right)^2 + \left(\frac{\partial Re}{\partial \mu} U_\mu\right)^2} \tag{3.53}$$

The corresponding partial derivatives are

$$\frac{\partial Re}{\partial \rho} = \frac{U_\infty c}{\mu} \tag{3.54}$$

$$\frac{\partial Re}{\partial U_\infty} = \frac{\rho c}{\mu} \tag{3.55}$$

$$\frac{\partial Re}{\partial c} = \frac{\rho U_\infty}{\mu} \tag{3.56}$$

$$\frac{\partial Re}{\partial \mu} = -\frac{\rho U_\infty c}{\mu^2} \tag{3.57}$$

The uncertainty in the measurement of the chord was estimated to be about 0.01 inches. The uncertainty in Re can then readily be found by substituting eqs. 3.54- 3.57 along with the uncertainties found earlier into eq. 3.53.

3.3.2 Force-Balance Uncertainties

Recall that the force balance measures the normal and axial forces as well as the pitching moment on the airfoil, and these forces and moments are then used to determine the aerodynamic coefficients C_l, C_d, and C_m according to eqs. 3.2 - 3.4. Eq. 3.40 can be written as follows for each coefficient:

$$U_{C_{l_{bal}}} = \left[\left(\frac{\partial C_{l_{bal}}}{\partial \alpha} U_\alpha \right)^2 + \left(\frac{\partial C_{l_{bal}}}{\partial F_N} U_{F_N} \right)^2 + \left(\frac{\partial C_{l_{bal}}}{\partial F_A} U_{F_A} \right)^2 + \left(\frac{\partial C_{l_{bal}}}{\partial q_\infty} U_{q_\infty} \right)^2 + \left(\frac{\partial C_{l_{bal}}}{\partial c} U_c \right)^2 + \left(\frac{\partial C_{l_{bal}}}{\partial b} U_b \right)^2 \right]^{\frac{1}{2}} \tag{3.58}$$

$$U_{C_{d_{bal}}} = \left[\left(\frac{\partial C_{d_{bal}}}{\partial \alpha} U_\alpha \right)^2 + \left(\frac{\partial C_{d_{bal}}}{\partial F_N} U_{F_N} \right)^2 + \left(\frac{\partial C_{d_{bal}}}{\partial F_A} U_{F_A} \right)^2 + \left(\frac{\partial C_{d_{bal}}}{\partial q_\infty} U_{q_\infty} \right)^2 + \left(\frac{\partial C_{d_{bal}}}{\partial c} U_c \right)^2 + \left(\frac{\partial C_{d_{bal}}}{\partial b} U_b \right)^2 \right]^{\frac{1}{2}} \tag{3.59}$$

$$U_{C_{m_{bal}}} = \Bigg[\left(\frac{\partial C_{m_{bal}}}{\partial M_{bal}} U_{M_{bal}} \right)^2 + \left(\frac{\partial C_{m_{bal}}}{\partial F_N} U_{F_N} \right)^2 + \left(\frac{\partial C_{m_{bal}}}{\partial F_A} U_{F_A} \right)^2 + \left(\frac{\partial C_{m_{bal}}}{\partial q_\infty} U_{q_\infty} \right)^2 + \left(\frac{\partial C_{m_{bal}}}{\partial c} U_c \right)^2 + \left(\frac{\partial C_{m_{bal}}}{\partial b} U_b \right)^2 \Bigg]^{\frac{1}{2}} \quad (3.60)$$

The uncertainties of the balance were 0.02% of full-scale for normal force, 0.03% for axial force, and 0.15% for pitching moment, according to the manufacturer. Additionally, the force balance could control the angle of attack to within 0.02 deg. The partial derivatives corresponding to the lift coefficient uncertainty are given in eqs. 3.61 - 3.66. Plugging these partial derivatives into eq. 3.58 gives the uncertainty of the lift coefficient computed from balance data. The uncertainties in drag and pitching moment were determined the same way using the partial derivatives corresponding to eqs. 3.59 and 3.60.

$$\frac{\partial C_{l_{bal}}}{\partial \alpha} = \frac{1}{q_\infty S} \left[-F_N sin(\alpha) - F_A cos(\alpha) \right] \quad (3.61)$$

$$\frac{\partial C_{l_{bal}}}{\partial F_N} = \frac{1}{q_\infty S} cos(\alpha) \quad (3.62)$$

$$\frac{\partial C_{l_{bal}}}{\partial F_A} = -\frac{1}{q_\infty S} sin(\alpha) \quad (3.63)$$

$$\frac{\partial C_{l_{bal}}}{\partial q_\infty} = -\frac{1}{q_\infty^2 S} \left[F_N cos(\alpha) - F_A sin(\alpha) \right] \quad (3.64)$$

$$\frac{\partial C_{l_{bal}}}{\partial c} = -\frac{1}{q_\infty b c^2} \left[F_N cos(\alpha) - F_A sin(\alpha) \right] \quad (3.65)$$

$$\frac{\partial C_{l_{bal}}}{\partial b} = -\frac{1}{q_\infty c b^2} \left[F_N cos(\alpha) - F_A sin(\alpha) \right] \quad (3.66)$$

3.3.3 Pressure System Uncertainties

3.3.3.1 Pressure Coefficient

To determine the uncertainty in the value of the pressure coefficient C_p (eq. 3.9), the uncertainties in the pressure differences $P_{ss} - P_{ts}$ and $P_s - P_{ts}$ must be known. As discussed above, $P_{ss} - P_{ts}$ is measured by the 1-psid ESP module and has an uncertainty of 0.001 psid. The difference $P_s - P_{ts}$ is measured directly by either a 0.35-psid, 1-psid, or 5-psid ESP module, and the uncertainties for each of these modules as reported by the manufacturer are shown in Table 3.3. The uncertainty in C_p can then readily be calculated using eqs. 3.67 - 3.69.

$$U_{C_p} = \sqrt{\left(\frac{\partial C_p}{\partial(P_s - P_{ts})} U_{P_s - P_{ts}}\right)^2 + \left(\frac{\partial C_p}{\partial(P_{ss} - P_{ts})} U_{P_{ss} - P_{ts}}\right)^2} \tag{3.67}$$

$$\frac{\partial C_p}{\partial(P_s - P_{ts})} = \frac{1}{P_{ss} - P_{ts}} \left[1 - \left(\frac{A_{ts}}{A_{ss}}\right)^2\right] \tag{3.68}$$

$$\frac{\partial C_p}{\partial(P_{ss} - P_{ts})} = -\frac{P_s - P_{ts}}{(P_{ss} - P_{ts})^2} \left[1 - \left(\frac{A_{ts}}{A_{ss}}\right)^2\right] \tag{3.69}$$

3.3.3.2 Lift Coefficient

By combining eqs. 3.10, 3.11, and 3.13 - 3.15, the lift coefficient can be expanded and arranged into the form of eq. 3.70.

$$\begin{aligned} C_l &= \frac{cos(\alpha)}{2} cos(\alpha) \left\{ (C_{p_2} + C_{p_1}) \left[\left(\frac{x}{c}\right)_1 - \left(\frac{x}{c}\right)_2 \right] + (C_{p_3} + C_{p_2}) \left[\left(\frac{x}{c}\right)_2 - \left(\frac{x}{c}\right)_3 \right] + \cdots \right. \\ &\quad \left. + (C_{p_N} + C_{p_{N-1}}) \left[\left(\frac{x}{c}\right)_{N-1} - \left(\frac{x}{c}\right)_N \right] \right\} - \frac{sin(\alpha)}{2} \left\{ (C_{p_2} + C_{p_1}) \left[\left(\frac{y}{c}\right)_2 - \left(\frac{y}{c}\right)_1 \right] \right. \\ &\quad \left. + (C_{p_3} + C_{p_2}) \left[\left(\frac{y}{c}\right)_3 - \left(\frac{y}{c}\right)_2 \right] + \cdots + (C_{p_N} + C_{p_{N-1}}) \left[\left(\frac{y}{c}\right)_N - \left(\frac{y}{c}\right)_{N-1} \right] \right\} \\ &= \sum_{i=2}^{N} \frac{cos(\alpha)}{2} \left\{ (C_{p_i} + C_{p_{i-1}}) \left[\left(\frac{x}{c}\right)_{i-1} - \left(\frac{x}{c}\right)_i \right] \right\} \\ &\quad - \frac{sin(\alpha)}{2} \left\{ (C_{p_i} + C_{p_{i-1}}) \left[\left(\frac{y}{c}\right)_i - \left(\frac{y}{c}\right)_{i-1} \right] \right\} \end{aligned} \tag{3.70}$$

The pressure coefficients C_p on the airfoil surface were obtained using the ESP modules,

Table 3.3 ESP Module Uncertainties as Estimated by the Manufacturer

Module	Module Uncertainty	Calibration Uncertainty	Total Uncertainty
5 psid	±0.0035 psid	±0.0010 psid	±0.0036 psid
1 psid	±0.0010 psid	±0.0010 psid	±0.0014 psid
0.35 psid	±0.00035 psid	±0.0002 psid	±0.0004 psid

as discussed earlier. On the NACA 23012 airfoil model, pressure taps located upstream of $x/c = 20\%$ on the upper surface and upstream of 23% on the lower surface were connected to a 5-psid ESP module. Secondary row taps located downstream of $x/c = 50\%$ as well as all spanwise taps were connected to a 0.35-psid ESP module. All remaining taps were connected to 1-psid modules. The lift coefficient uncertainty can then by written as shown in eq. 3.71 by writing eq. 3.40 in the appropriate form:

$$U_{C_l} = \sqrt{\left(\frac{\partial C_l}{\partial \alpha} U_\alpha\right)^2 + \sum_{i=2}^{N} \left(\frac{\partial C_l}{\partial C_{p_i}} U_{C_{p_i}}\right)^2} \tag{3.71}$$

The corresponding partial derivatives are given by the following set of equations:

$$\begin{aligned} \frac{\partial C_l}{\partial \alpha} &= \sum_{i=2}^{N} \frac{-sin(\alpha)}{2} \left\{ (C_{p_i} + C_{p_{i-1}}) \left[\left(\frac{x}{c}\right)_{i-1} - \left(\frac{x}{c}\right)_i \right] \right\} \\ &\quad - \frac{cos(\alpha)}{2} \left\{ (C_{p_i} + C_{p_{i-1}}) \left[\left(\frac{y}{c}\right)_i - \left(\frac{y}{c}\right)_{i-1} \right] \right\} \end{aligned} \tag{3.72}$$

$$\frac{\partial C_l}{\partial C_{p_i}} = \frac{cos(\alpha)}{2} \left[\left(\frac{x}{c}\right)_{i-1} - \left(\frac{x}{c}\right)_i \right] - \frac{sin(\alpha)}{2} \left[\left(\frac{y}{c}\right)_i - \left(\frac{y}{c}\right)_{i-1} \right] \tag{3.73}$$

3.3.3.3 Moment Coefficient

The same procedure was followed to determine the moment coefficient uncertainty. Combining eqs. 3.12 and 3.16 yields:

$$\begin{aligned} C_m &= \frac{1}{2} \sum_{i=2}^{N} \left\{ C_{p_i} \left[\left(\frac{x}{c}\right)_i - 0.25 \right] + C_{p_{i-1}} \left[\left(\frac{x}{c}\right)_{i-1} - 0.25 \right] \right\} \left[\left(\frac{x}{c}\right)_i - \left(\frac{x}{c}\right)_{i-1} \right] \\ &\quad + \left\{ C_{p_i} \left(\frac{y}{c}\right)_i + C_{p_{i-1}} \left(\frac{x}{c}\right)_{i-1} \right\} \left[\left(\frac{x}{c}\right)_i - \left(\frac{x}{c}\right)_{i-1} \right] \end{aligned} \tag{3.74}$$

Writing eq. 3.40 in the appropriate form yields eq. 3.75, and the necessary partial derivative is given by eq. 3.76.

$$U_{C_m} = \sqrt{\sum_{i=2}^{N} \left(\frac{\partial C_m}{\partial C_{p_i}} U_{C_{p_i}} \right)^2} \tag{3.75}$$

$$\frac{\partial C_m}{\partial C_{p_i}} = \frac{1}{2} \left\{ \left[\left(\frac{x}{c} \right)_i - 0.25 \right] \left[\left(\frac{x}{c} \right)_i - \left(\frac{x}{c} \right)_{i-1} \right] + \left(\frac{y}{c} \right)_i \left[\left(\frac{y}{c} \right)_i - \left(\frac{y}{c} \right)_{i-1} \right] \right\} \tag{3.76}$$

3.3.3.4 Drag Coefficient

Drag was calculated according to eqs. 3.27 - 3.29, which can be combined and expanded to form eq. 3.77:

$$\begin{aligned} C_d \;=\; & \frac{1}{q_\infty c} \sum_{i=1}^{K} (\sqrt{q_\infty^2 - q_\infty (P_{o,\infty} - P_{o,w_i})} + \sqrt{q_\infty^2 - q_\infty (P_{o,\infty} - P_{o,w_{i-1}})} - \\ & 2q_\infty + 2P_{o_\infty} - P_{o_{w_i}} - P_{o_{w_{i-1}}})(y_i - y_{i-1}) \end{aligned} \tag{3.77}$$

The pressures P_{o_∞}, $P_{o_{w_i}}$, and $P_{o_{w_{i-1}}}$ are measured referenced to P_{atm}, and the quantity $2P_{o_\infty} - P_{o_{w_i}} - P_{o_{w_{i-1}}}$ can be computed from directly measured values:

$$2P_{o_\infty} - P_{o_{w_i}} - P_{o_{w_{i-1}}} = 2(P_{o_\infty} - P_{atm}) - (P_{o_{w_i}} - P_{atm}) - (P_{o_{w_{i-1}}} - P_{atm}) \tag{3.78}$$

Then the uncertainty of the drag calculated using the wake pressures is eq. 3.79 with the corresponding partial derivatives given in eqs. 3.80 - 3.83. Also recall that the uncertainty of the 0.35-psid ESP modules used to measure the wake pressures was ± 0.00035 psi (Table 3.3).

$$U_{C_d} = \sqrt{\left(\frac{\partial C_d}{\partial q_\infty} U_{q_\infty} \right)^2 + \left(\frac{\partial C_d}{\partial c} U_c \right)^2 + \left(\frac{\partial C_d}{\partial P_{o_\infty}} U_{P_{o_\infty}} \right)^2 + \sum_{i=1}^{K} \left(\frac{\partial C_d}{\partial P_{o_{w_i}}} U_{P_{o_{w_i}}} \right)^2} \tag{3.79}$$

$$\frac{\partial C_d}{\partial q_\infty} = -\frac{1}{q_\infty^2 c}\sum_{i=1}^{K}(\sqrt{q_\infty^2 - q_\infty(P_{o,\infty} - P_{o,w_i})} + \sqrt{q_\infty^2 - q_\infty(P_{o,\infty} - P_{o,w_{i-1}})} - 2q_\infty + 2P_{o_\infty} - P_{o_{w_i}} - P_{o_{w_{i-1}}})(y_i - y_{i-1}) + \frac{1}{q_\infty c}\sum_{i=1}^{K}\left\{\frac{2q_\infty - (P_{o_\infty} - P_{o_{w_i}})}{2\sqrt{q_\infty^2 - q_\infty(P_{o_\infty} - P_{o_{w_i}})}} + \frac{2q_\infty - (P_{o_\infty} - P_{o_{w_{i-1}}})}{2\sqrt{q_\infty^2 - q_\infty(P_{o_\infty} - P_{o_{w_{i-1}}})}} - 2\right\}(y_i - y_{i-1}) \tag{3.80}$$

$$\frac{\partial C_d}{\partial c} = -\frac{1}{q_\infty c^2}\sum_{i=1}^{K}(\sqrt{q_\infty^2 - q_\infty(P_{o,\infty} - P_{o,w_i})} + \sqrt{q_\infty^2 - q_\infty(P_{o,\infty} - P_{o,w_{i-1}})} - 2q_\infty + 2P_{o_\infty} - P_{o_{w_i}} - P_{o_{w_{i-1}}})(y_i - y_{i-1}) \tag{3.81}$$

$$\frac{\partial C_d}{\partial P_{o_\infty}} = \frac{1}{q_\infty c}\sum_{i=1}^{K}(2 - \frac{q_\infty}{2\sqrt{q_\infty^2 - q_\infty(P_{o,\infty} - P_{o,w_i})}} - \frac{q_\infty}{2\sqrt{q_\infty^2 - q_\infty(P_{o,\infty} - P_{o,w_{i-1}})}})(y_i - y_{i-1}) \tag{3.82}$$

$$\frac{\partial C_d}{\partial P_{o_{w_i}}} = \frac{1}{q_\infty c}\left[\frac{q_\infty}{2\sqrt{q_\infty^2 - q_\infty(P_{o_\infty} - P_{o_{w_i}})}} - 1\right](y_i - y_{i-1}) \tag{3.83}$$

3.3.4 Sample Uncertainties

The tables that follow show the estimated uncertainties for the case of the clean NACA 23012 airfoil at $\alpha = 4$ deg. and $Re = 1.8$ x 10^6.

3.3.5 Surface Oil-Flow Visualization Uncertainties

Surface oil-flow visualization is a method by which the flowfield can be evaluated qualitatively. It is mainly used to help identify three-dimensional flow features that can be used in conjunction with the measured surface pressure distribution to increase understanding of what is happening at various points along the surface of the airfoil. The uncertainty in

Table 3.4 Sample uncertainties of variables describing flow conditions based on $Re = 1.8\text{x}10^6$

Parameter	Reference Value	Absolute Uncertainty	Relative Uncertainty (%)
c	18.000 in.	±0.01 in.	±0.0556
b	33.563 in.	±0.02 in.	±0.0596
q_∞	0.320 psi	±0.00102 psi	±0.319
T_{amb}	71.76 F	± 1.0 F	±1.39
P_{atm}	14.304 psi	± 0.008 psi	±0.0559
ρ_{atm}	$2.26\text{x}10^{-3}$ $\frac{slug}{ft^3}$	± $1.26\text{x}10^{-6}$ $\frac{slug}{ft^3}$	±0.0559
μ	$3.81\text{x}10^{-7}$ $\frac{slug}{ft-s}$	±$5.54\text{x}10^{-10}$ $\frac{slug}{ft-s}$	±0.145
U_∞	202.628 $\frac{ft}{s}$	±0.326 $\frac{ft}{s}$	±0.161
Re	1802410	±4160	±0.231

Table 3.5 Sample uncertainties of the force balance based on conditions of $\alpha = 4$ deg. and $Re = 1.8\text{x}10^6$

Parameter	Reference Value	Absolute Uncertainty	Relative Uncertainty (%)
α	4.163 deg.	±0.02 deg.	±0.480
C_l	0.548	± 0.00190	±0.347
C_d	0.01177	±0.00024	±2.08
C_m	-.00197	±0.00023	±12.1

Table 3.6 Sample uncertainties of the pressure measurements based on $\alpha = 4$ deg. and $Re = 1.8\text{x}10^6$ and using the pressure coefficient at $x/c = 21\%$.

Parameter	Reference Value	Abs. Uncertainty	Rel. Uncertainty (%)
C_p, 0.35-psid module	-.454	±0.00186	±0.409
C_p, 1-psid module	-0.962	±0.00448	±0.466
C_p, 5-psid module	-1.386	±0.01208	±0.871
C_l	0.5056	±0.000859	±0.155
C_d	0.00714	±0.000136	±1.912
C_m	-0.00155	±0.000269	±17.376

flow visualization stems from the unsteady nature of the flow field, which causes zones of reattachment to form instead of lines. The approximate reattachment line is in the center of the zone, at the point at which the flow appears to switch from forward flow to reverse flow. This line generally varies along the span, so assigning a single chordwise station to it can be misleading. Additionally, the readability of the scales is a source of uncertainty. The scales are labeled at every 5% chord, so the readability is another source of error on the order of $x/c = \pm 2\%$. It is estimated that these two sources of error combine to give the flow visualization method an uncertainty of $x/c = \pm 4\%$, but this figure varies depending on the extent of the spanwise variation of a particular ice shape.

Chapter 4

Results

The previous chapter discussed the flowfields of each type of ice accretion classified by Bragg et al.[4] and Broeren et al.:[15] ice roughness, streamwise ice, horn ice, and both tall and short spanwise-ridge ice. It also presented many of the challenges inherent to sub-scale ice accretion simulation. This chapter examines more closely each type of ice shape and integrates new and prior results regarding the effects of various geometric features of each on the iced-airfoil flowfield. Since each type of ice shape has different important flowfield characteristics, changes in geometry have different aerodynamic effects for each classification. In this chapter, for each ice shape type, the discussion of the effects of geometric changes on the iced-airfoil flowfield is followed by an analysis of the sub-scale simulation of each of the full-scale castings studied by Broeren et al.[9] at high Reynolds number. These simulations were designed using the methods presented in Chapters 2 and 3 to determine the accuracy with which this methodology could reproduce the aerodynamic performance of the casting on a sub-scale model at low Reynolds number. Prior to the discussion of iced-airfoil aerodynamics, the clean aerodynamic performance of the NACA 23012 measured in the University of Illinois low-speed wind tunnel is validated.

4.1 Clean NACA 23012 Aerodynamic Performance

The aerodynamic performance of the clean NACA 23012 measured in the University of Illinois at Urbana-Champaign (Illinois) wind tunnel is shown and compared with other published NACA 23012 data and XFoil[102] calculations in Fig. 4.1. According to the Illinois data, at Re = 1.8 x 10^6 the airfoil stalls at α = 14.4 deg., corresponding to a value of $C_{l,max}$ = 1.48. At higher angles of attack, the lift drops dramatically and pitching moment rapidly becomes

negative. This sharp dropoff in lift post-stall is indicative of leading-edge stall, caused by sudden separation of the boundary layer from the leading edge of the airfoil. This stall behavior is evident in the data of Broeren and Bragg[93] and Abbott and von Doenhoff[103] (also shown in Fig. 4.1) as well. The XFoil data show a much more gradual stall, but XFoil usually can not accurately predict $C_{l,max}$ and stall characteristics due to the associated large regions of separated flow. The value of $C_{l,max}$ indicated in the Illinois data agrees with the data of Broeren and Bragg from the Low-Turbulence Pressure Tunnel (LTPT), but this is below that indicated by the data of Abbott and von Doenhoff. This is likely a Reynolds number effect, as the data from Abbott and von Doenhoff was obtained at Re = 3.0 x 10^6 rather than 1.8 x 10^6. The pitching moment curve of the Illinois data increases more rapidly with angle of attack than for either the LTPT data or Abbott and von Doenhoff data, and reaches a maximum value of 0.018. XFoil predicts a similar maximum value of C_m, but the curve shows much more variation with angle of attack (both increasing and decreasing) at lower angles. The Abbott and von Doenhoff C_m data agree reasonably well below α = 4 deg., but begin to diverge above this angle. Broeren et al.[9] explained that Abbott and von Doenhoff reported some inaccuracies with their moment balance, which may explain the differences in measured C_m. Agreement in C_d between the LTPT data and the Illinois data is good, but both the Abbott and von Doenhoff and XFoil data show a lower value of C_d below $C_l = 0$; XFoil also predicts a lower value of C_d above $C_l = 1.1$. This may in part be due to the models used, as both the LTPT and Illinois airfoils models had removable leading edges to facilitate ice shape installation. This may have affected boundary-layer transition and increased airfoil C_d.

The effects of Reynolds number on the aerodynamic performance of the clean NACA 23012 airfoil are substantial. Figure 4.2 shows C_l, C_m, and C_d measured for two Reynolds numbers, Re = 12.0 x 10^6 and Re = 1.8 x 10^6, for approximately equal Mach numbers. Leading-edge stall is exhibited at both Reynolds numbers, but occurs at approximately 3.7 deg. lower angle of attack at the lower Reynolds number than at the higher Reynolds number. Also at the lower Reynolds number, the NACA 23012 has a shallower lift-curve slope and a $C_{l,max}$ 20% lower than at the higher Reynolds number. The dependence of pitching moment on angle of attack was greater for the lower Reynolds number case, and became nose-up at

a much lower angle of attack. Finally, the C_d curve at the lower Reynolds number increased more rapidly with increasing angle of attack than at Re = 12.0 x 10^6, was shifted upwards (resulting in a $C_{d,\alpha=0}$ = 0.0068), and demonstrated a more pronounced low-drag region from approximately 0 to 6 deg. than did the higher Reynolds number case. The high Reynolds number clean airfoil data were validated by comparison to other measurements of NACA 23012 airfoil performance by Broeren et al.,[9] and the observed Reynolds number trends are typical for conventional airfoils. As discussed in the Introduction (and shown later in this paper), many of these effects disappear or are mostly mitigated when an ice shape is present.

4.2 Ice Roughness

Ice roughness often results from the initial accumulation of ice on an airfoil before a larger geometry has had time to form. Because ice roughness has no large-scale ice geometry, it is usually represented by applying grit roughness to a clean airfoil model to construct a simple-geometry simulation. The roughness can be characterized predominantly by its height, concentration, and chordwise location and extent. The shape of the individual roughness elements may also be important, but was not investigated in this study. The effects of ice roughness on the airfoil flowfield come mainly through changes in the airfoil boundary layer, and each of these parameters can affect the magnitude of these changes. The aerodynamic effects of variations in these parameters are discussed by Bragg et al.[4] and are elaborated on further in this section.

4.2.1 Sub-scale Simulation of Ice Roughness with Full-scale Validation

Broeren et al.[9] measured the aerodynamic performance degradation of a NACA 23012 due to an ice roughness casting at full-scale and high Reynolds number. The details of the ice geometry are given in Section 3.2.4.1. For the current study, several sub-scale simulations were constructed based on this casting, and the effects of these simulations and the casting on C_l, C_m, and C_d of the NACA 23012 are shown in Fig. 4.3. The data for the full-scale casting were acquired at Re = 12.0 x 10^6 and M = 0.20, and the data for all other ice simulations shown in the figure were acquired at Re = 1.8 x 10^6 and M = 0.18. Clean airfoil data were

obtained at both freestream conditions. The addition of the full-scale casting caused the airfoil to achieve a $C_{l,max}$ of only 1.08 and to stall at approximately 11.8 deg. It also caused a more nose-up pitching moment at high angles of attack and increased C_d to 0.0096 at $\alpha =$ 0 deg.

In the present study, the full-scale ice roughness casting (designated EG1126) at $Re = 12.0$ x 10^6 was considered to give the "true" aerodynamics of the ice roughness accretion. For the sub-scale simulations at $Re = 1.8$ x 10^6, the ice shape was represented using several different simple-geometry simulations on an 18-inch chord NACA 23012 airfoil model, explained in detail in Section 3.2.4. The simple-geometry simulations were constructed by adding various roughness sizes to the NACA 23012 airfoil over the appropriate chordwise extent to attempt to duplicate the aerodynamic effects of the casting. The first simulation was a geometrically-scaled simulation and used several different roughness sizes on each the upper and lower surface chosen to match the k/c of the roughness on the casting at several chordwise stations. Roughness strips with heights $k/c = 0.0013$, 0.0006, 0.0009, and 0.0005, were placed on the airfoil upper surface to match the chordwise extent of the casting roughness. Roughness strips of height $k/c = 0.0009$, 0.0007, 0.0009, and 0.0003 were placed on the lower surface, again to match the roughness extents on the casting. This is the simulation that would have been constructed with no *a priori* knowledge of the casting aerodynamics and will be referred to as the geometrically-scaled simulation.

A comparison of the aerodynamic performance of the geometrically-scaled simulation and EG1126 casting is shown in Fig. 4.3. $C_{l,max}$ of the simulation is 4% lower and occurs about 1 degree earlier than for the casting, corresponding to an earlier break in C_m. This comparison is similar to that of Fig. 2.5, which compares the aerodynamic performance of an ice roughness casting to that of a simple-geometry simulation which uses grit roughness to represent the surface roughness on the casting. C_d of the EG1126 roughness simulation below $\alpha = 4$ deg. tended to be 20% - 30% higher than C_d of the casting at the same angle of attack. This simulation, unlike the simulation of Fig. 2.5, had roughness of the same k/c of the casting on the lower surface. Thus, at relatively low Reynolds number, the sub-scale simple-geometry roughness simulation tended to give a similar but slightly conservative estimate of the "true" iced-airfoil aerodynamic performance.

It may seem that a scaling method for ice roughness other than geometric scaling, such as boundary-layer scaling, may yield more accurate results. One such method, boundary-layer scaling, was considered. In boundary-layer scaling the ice simulation height relative to the local boundary-layer height just prior to $C_{l,max}$ (k/δ) is matched (instead of matching k/c, the ridge height non-dimensionalized by the airfoil chord). However, this would result in larger roughness heights than with geometric scaling, which, based on results to be presented shortly, would cause even larger aerodynamic performance penalties. A study by Whalen et al.[53] using both boundary-layer scaling and geometric scaling confirmed this for short-ridge ice simulations. At this time, it does not appear that boundary-layer scaling would produce more accurate simulations than geometric scaling, and more work is needed to better understand the discrepancies that result from geometrically-scaling ice roughness.

Several additional simple-geometry simulations of the ice roughness casting were also constructed to obtain better understanding and agreement with the casting aerodynamics and to explore the aerodynamic effects of minor changes in simulation geometry. Very good agreement with the casting $C_{l,max}$ was obtained with a simulation with a constant roughness height of $k/c = 0.0003$ over the appropriate extents; this simulation had a $C_{l,max}$ only 0.6% below that of the casting and modeled C_d more accurately at low angles of attack, but tended to have a lower C_d at angles of attack beyond $\alpha = 4$ deg (Fig. 4.3). A useful metric for comparing C_d at multiple angles of attack is the percent RMS difference in C_d over an appropriate angle of attack range, which will be referred to as $\Delta C_{d,RMS}$. The angle of attack range used in this study was that over which C_l varied linearly with α. The value $\Delta C_{d,RMS}$ is a percentage and is computed by determining the RMS of the percent difference between the casting C_d and simulation C_d at each angle of attack in the linear range (a total of N angles of attack):

$$\Delta C_{d,RMS} = \sqrt{\frac{\sum_{i=1}^{N} \left(\frac{C^i_{d,sim} - C^i_{d,casting})}{C^i_{d,casting}} 100\% \right)^2}{N}} \tag{4.1}$$

The value of $\Delta C_{d,RMS}$ for the $k/c = 0.0003$ roughness simulation was 16.0% over a range of angle of attack from α = -4 to 9 deg., compared with 20.8% for the geometrically-scaled

simulation.

An important factor to consider when comparing values of C_d is the method by which C_d is measured. It is common for C_d to vary along the span of an iced airfoil, as discussed in Chapter 2, but the full-scale casting C_d data presented in this paper were taken at only a single spanwise station. Most of the sub-scale data presented were also taken at a single spanwise station, although these data were all acquired in the same facility at identical spanwise stations. To give an estimate for the magnitude of the variation in C_d on the sub-scale model, measurements of C_d at five spanwise stations located two inches apart were taken for selected cases (Fig. 4.4). The maximum and minimum values of C_d measured during this spanwise sweep are indicated with error bars in Fig. 4.3, based on the geometrically-scaled roughness simulation. For this simulation, the variation in C_d was more prevalent at low angle of attack than high angle of attack, on the order of 17% deviation from the mean near $\alpha = 0$ deg. At $\alpha = 10$ deg., the variation was around 8%. Values of C_d obtained at various stations along the airfoil span are also shown in Fig. 4.4 for a simulation which modeled only the upper surface roughness of the EG1126 casting, and this simulation also had large variations in C_d. It is likely that C_d of the casting had similar spanwise variations, as other studies have reported spanwise fluctuations in C_d on the same order.[6,38] The level of agreement of C_d between the casting and simulations is therefore dependent on the spanwise station at which C_d is measured, and it is recommended that in future testing C_d be measured at several spanwise stations and averaged for comparison.

A third simulation was designed to represent only the initial portion of roughness on the casting. For this simulation, roughness strips of width 0.10 inches ($s/c = 0.0056$) were placed on the clean airfoil at a location corresponding to the most upstream extent of the roughness on the casting. The heights of this roughness matched the maximum height of roughness on the casting, $k/c = 0.0013$ and $k/c = 0.0009$ on the upper and lower surfaces, respectively. This resulted in $C_{l,max}$ nearly identical to the geometrically-scaled simulation, which matched k/c of the casting over the entire chord (Fig. 4.3). These results suggest that, for the NACA 23012 airfoil, $C_{l,max}$ is not extremely sensitive to small changes in roughness chordwise extents. The plot of Brumby (Fig. 2.3) indicates that $C_{l,max}$ is sensitive for larger changes in roughness extents (e.g., if the entire upper surface of the airfoil is roughened). The

EG1126 simulation with narrow strips of roughness modeled C_d of the casting at low angle of attack slightly more accurately than did the other simulations, but like the $k/c = 0.0003$ roughness simulation, had a lower C_d at angles of attack above $\alpha = 4$ deg. This further suggests that C_d is very sensitive to both roughness size and chordwise extent. The value of $\Delta C_{d,RMS}$ improved to 11.4% for the simulation which modeled only the first $s/c = 0.0056$ of the roughness on the casting.

The mismatch in aerodynamic performance between the casting and the simple-geometry simulation with matched k/c values prompted an investigation into the effect of roughness concentration. A trade study was conducted to determine what roughness concentration was best able to reproduce the $C_{l,max}$ and C_d of the casting for a given roughness height when applied over the same chordwise extents as the casting roughness. The roughness height chosen for this study was $k/c = 0.0018$, very similar to the maximum roughness height present on the casting. Figures 4.5a and 4.6 show the effect of increasing roughness concentration on aerodynamic performance of the NACA 23012 airfoil at $Re = 1.8$ x 10^6. As roughness concentration increases, $C_{l,max}$ decreases, up to a critical concentration of about 20% in this case (Fig. 4.5a). Beyond this critical concentration, $C_{l,max}$ is relatively insensitive to changes in roughness concentration. These results are consistent with those of earlier studies.[5,24] In Fig. 4.5a, the values of $C_{l,max}$ of the casting and clean NACA 23012 airfoil are indicated by dashed and dash-dot horizontal lines, respectively. For the roughness height investigated, the simple-geometry simulation with a $C_{l,max}$ most similar to that of the casting has a theoretical roughness concentration of 8%.

A comparison of C_d between the casting and each sub-scale simulation is given in Fig. 4.5b. In this figure, a value of $\Delta C_{d,RMS} = 0$ corresponds to perfect agreement between the casting and simulation, so smaller values of $\Delta C_{d,RMS}$ indicate better agreement with C_d of the casting. The horizontal dashed line shows $\Delta C_{d,RMS}$ for the clean NACA 23012 airfoil; this indicates how well the clean airfoil simulates C_d of the casting. For a roughness height of $k/c = 0.0018$, a concentration of 7% yielded the best agreement with the casting C_d while also having a similar $C_{l,max}$. Note that beyond the critical concentration of 20%, $\Delta C_{d,RMS}$ continues to change, suggesting that C_d does not remain as constant as $C_{l,max}$ for concentration variations in this range. In Fig. 4.5b, $\Delta C_{d,RMS}$ appears to approach a

value similar to the clean airfoil at higher roughness concentrations. This plot illustrates a shortcoming of using the parameter $\Delta C_{d,RMS}$ to quantify differences in drag; it can not show whether the drag of a simulation is above or below that of the casting. Fig. 4.6b shows the complete drag curves for several simulations using different roughness concentrations. C_d increases at most angles of attack as concentration increases. While the $\Delta C_{d,RMS}$ value of the clean airfoil is close to that of the simulation with 60% roughness (Fig. 4.5b), the clean airfoil has lower C_d and the 60% roughness simulation has higher C_d than the casting throughout the angle of attack range (Fig. 4.6b).

The effect of roughness concentration on $C_{l,max}$ of the NACA 23012 is shown again in Fig. 4.7, which compares the current data with those obtained by Jackson[24] on a NLF-0414, first pressented in Chapter 2. The NACA 23012 roughness had a height of $k/c = 0.00184$ and extended from $x/c = 0.000$ - 0.026 on the upper surface and from $x/c = 0.004$ - 0.041 on the lower surface. The larger roughness caused a much larger degradation in $C_{l,max}$ at a given concentration (this is consistent with results of the current study that will be presented below). This effect is exaggerated even further because the NACA 23012 airfoil geometry is much more sensitive to ice contamination and surface roughness than is the NLF-0414. Despite this much larger decrease in $C_{l,max}$, the trend of the current study is consistent with Jackson's data in that there is a critical roughness concentration beyond which further increases in concentration do not have a large effect on $C_{l,max}$.

The high degree of dependence of aerodynamic performance on roughness height motivated further investigation of this parameter. Several different simple-geometry simulations were built in addition to those described above by attaching roughness of various heights to the sub-scale airfoil over the same chordwise extents as the EG1126 casting ($x/c = 0.000$ - 0.026 on the upper surface, $x/c = 0.004$ - 0.041 on the lower surface). For each of these simulations, roughness was applied in maximum concentration, which ranged from nearly 100% for the smallest roughness heights to 50% for the largest roughness height. Figure 4.8a shows $C_{l,max}$ of each of these simulations compared to the clean NACA 23012 airfoil at $Re = 1.8 \times 10^6$ (the blue dashed line) and the full-scale casting at $Re = 12.0 \times 10^6$ (the horizontal black dash-dot line). To expand the range of roughness heights, two simulations (with $k/c = 0.00007$ and 0.00016) are also included in Fig. 4.8a which had the longer chordwise extents of

the roughness on the EG1134 rime-ice casting (x/c = -0.002 to 0.08 on the upper surface and x/c = 0.000 to 0.200 on the lower surface; this casting is discussed later in this section). The increased chordwise extent of the roughness likely had little effect on $C_{l,max}$, as explained earlier.

The maximum roughness height of k/c = 0.0016 and $C_{l,max}$ of the EG1126 casting (at 1.08) are indicated by the dash-dot lines in Fig. 4.8a. Not surprisingly, for the sub-scale simulations, $C_{l,max}$ decreases as roughness height increases. For small roughness heights, this change in $C_{l,max}$ is very rapid, but for roughness heights greater than k/c = 0.0003, the dependence of $C_{l,max}$ on k/c decreases. The roughness height for which the $C_{l,max}$ of the simulation is the same as that of the casting is about k/c = 0.0003, corresponding to the intersection of the line representing $C_{l,max}$ of the full-scale casting with the curve representing $C_{l,max}$ for various simulations. Figure 4.8b shows comparisons in C_d between the full-scale casting and each simulation of different roughness size. Adding roughness sizes below k/c = 0.0005 yielded the closest C_d to the casting, with $\Delta C_{d,RMS}$ values below 18% (reaching a minimum of about 11% for k/c = 0.00016 roughness). A roughness size of k/c = 0.0003 at maximum concentration had values of both $C_{l,max}$ and C_d in reasonably good agreement with the casting; this is one of the cases for which data are shown in Fig. 4.3.

From these plots, it is clear that multiple simple-geometry simulations using different combinations of roughness height and concentration may have the same $C_{l,max}$ as the casting. The effect of surface roughness is to remove momentum, increase skin friction, and alter the transition characteristics from what would occur on the clean airfoil.[4] It seems reasonable that a lower concentration of larger roughness elements could have a similar effect as a higher concentration of smaller roughness elements. The key to simulating ice roughness, therefore, appears to be selecting a combination of roughness height and concentration such that the simple-geometry simulation properly affects skin friction and boundary layer development over the angle of attack range of interest. Since both roughness height and concentration continuously vary with chordwise position on the ice accretion, it is not clear how to define this height/concentration combination. In other work, the concept of an "equivalent sand roughness" is often used.[104] This concept is discussed further at the end of this section, but unfortunately is not always practical for constructing ice simulations in part due to difficulties

in measuring ice geometries. It is difficult to accurately measure roughness concentration on an ice casting, but height can usually be measured. Therefore, in this study, emphasis is placed on roughness height, and a sufficiently large roughness concentration is used so that the simulation is in the range of Fig. 4.5a where $C_{l,max}$ is relatively insensitive to concentration. Using this approach, roughness concentration effects can be minimized.

In Fig. 4.9, the $C_{l,max}$ data for roughness of various heights discussed above along with other recent ice roughness simulation data for NACA 23012, NLF-0414, and 63_A213 airfoils has been added to the plot of Brumby, shown earlier in Fig. 2.3. Note that the trendlines of Brumby were based on a wide variety of roughness types on many airfoils at different Re and M, and the trends are only qualitative as there was a great deal of scatter in the data used to construct the trendlines. Lynch and Khodadoust[2] elaborate in more detail the shortcomings of the Brumby plot. In Fig. 2.3, roughness on the NACA 23012 airfoil tends to cause larger degradations in $C_{l,max}$ than the trendline would suggest. This is not surprising, as the large suction peak near the leading edge of the NACA 23012 airfoil is followed by a region of very strong adverse pressure gradient, which makes the NACA 23012 particularly sensitive to ice contamination. Roughness of the same height on the NLF-0414 and modified 63_A213 airfoils caused much smaller performance penalties, and the reduction in $C_{l,max}$ of the modified 63_A213 was very similar to reductions observed by Brumby. The NLF-0414 experienced smaller reductions in maximum lift and shows much less sensitivity than the NACA airfoils for which Brumby compiled data, likely because it has only a very mild adverse pressure gradient over much of the upper surface.

Broeren et al.[9] also measured the aerodynamic performance of a NACA 23012 with a second ice roughness casting. This second casting had a smaller maximum roughness height ($k/c = 0.0003$) and greater chordwise extent, and is characterized in more detail in Section 3.2.4.1. The effect of the casting on full-scale airfoil performance at high Reynolds number is shown in Fig. 4.10. The degradation in $C_{l,max}$ was not as severe as it was for the glaze-ice roughness, with the casting reaching a value of 1.28, and stall occurring at a slightly higher angle of attack of 12.9 deg. The C_d curve was shifted upwards by about the same amount as with the first roughness casting, with $C_{d,\alpha=0} = 0.0095$, but C_d is much lower at high angle of attack for the second ice roughness casting.

As was the case for the first ice roughness casting, multiple simple-geometry simulations were constructed of the second casting. The geometrically-scaled simulation of this casting used grit roughness of height $k/c = 0.00033$ applied from the airfoil leading edge to $x/c = 0.03$ on the upper surface and from the leading edge to $x/c = 0.04$ on the lower surface. Note that these extents were shorter than the extents of the casting, but based on the results discussed above, the difference in extents likely had little effect on $C_{l,max}$ and would have caused C_d to be slightly lower than it would be if the extents were greater (as they were for the casting). Comparisons between the geometrically-scaled simulation ($k/c = 0.00033$) and the casting (Fig. 4.10) show that the simulation resulted in a much larger degradation in $C_{l,max}$ than did the casting, with a value 15.7% too low. This difference in $C_{l,max}$ may have in part been due to a higher concentration of roughness on the simulation than on the casting. At the time of testing, it was thought that the roughness concentration on the casting was above the critical concentration, based on Fig. 4.7. Therefore, with the expectation that changes in roughness concentration would have only minimal impact on $C_{l,max}$, a high roughness concentration was used on the simulation to ensure uniformity of distribution and repeatability. Because the casting roughness was so small, it is possible that the roughness concentration was not above the critical concentration, resulting in a larger decrease in $C_{l,max}$ of the simulation. Over a narrow range of angle of attack, from $\alpha = 6$ to 10 deg., C_d of the geometrically-scaled $k/c = 0.00033$ roughness simulation agreed very well with the casting (Fig. 4.10). However, at all other angles of attack, C_d was too high, giving $\Delta C_{d,RMS} = 16.3\%$ from α = -4 to 10 deg. C_d at low angles of attack was also larger for the simulation than for the casting, but agreed well with the casting at higher angles of attack prior to stall. This trend in C_d is consistent with the simulations of both the full-scale and sub-scale ice roughness castings discussed earlier. Note that the $k/c = 0.00033$ roughness simulation had already been tested for the glaze-ice roughness case, and increasing the roughness extents to those on the EG1134 casting would have little effect on $C_{l,max}$ (as discussed earlier) and would cause C_d to increase slightly. C_d was already too high for this simulation, so changing the roughness extents would not have improved the simulation fidelity.

To determine the roughness height which best modeled the casting aerodynamics when applied at high concentration, other simulations were built using much smaller roughness

sizes. The most accurate simple-geometry simulation consisted of $k/c = 0.00007$ roughness. This simulation had a $C_{l,max}$ within 1% of the casting at a similar angle of attack, and the C_d curves were very similar up to $\alpha = 12$ deg., as shown in Fig. 4.10. The percent RMS difference in C_d between the casting and the $k/c = 0.00007$ roughness simulation was 7.2%, computed using eqn. 4.1 for α = -4 to 10 deg. The results for a simulation consisting of k/c = 0.00016 roughness are also shown in Fig. 4.10 to show the high sensitivity of $C_{l,max}$ and C_d to small changes in roughness height for roughness heights in this range.

The results for this second ice roughness shape indicate that geometric scaling of roughness height may not be the best scaling technique, especially when high roughness conetrations are used, as it tends to produce simulations which provide conservative performance estimates. On the other hand, Papadakis et al.[25] reported conflicting results when testing identical ice roughness simulations on full-scale and 1/4-scale horizontal tail models. The mean aerodynamic chord of the full-scale model was 49.25 inches and the testing was conducted at matched Re = 1.36 x 10^6 for each model. The roughness simulations consisted of sandpaper roughness of height k/c_{mac} = 0.00034 and 0.00036 applied to the full-scale and sub-scale models, respectively, at the same chordwise extents (from $x/c = 0.13$ on the lower surface to $x/c = 0.13$ on the upper surface). Papadakis et al. reported that the 1/4-scale model experienced a $C_{l,max}$ that was 0.08 higher than that of the full-scale model at a two degree higher angle of attack and reduced drag over much of the angle of attack range, suggesting that geometric scaling of roughness height tended to over-estimate iced-airfoil performance. However, in another test by Papadakis et al.,[105] geometrically-scaled roughness on a 1/4-scale tail model under-estimated iced-airfoil performance. These tests by Papadakis et al. used a 3-D tail geometry instead of a 2-D airfoil geometry, so comparisons should be made cautiously. Broeren et al.[94] investigated closely scaled $k/c = 0.00057$ and 0.00046 roughness on 36-inch and 18-inch chord 2-D airfoil models, respectively, and found that the resulting airfoil performance was very similar at nearly identical Re and M (Fig. 4.11). In Fig. 4.11, the abbreviation LSWT refers to the University of Illinois low-speed wind tunnel, where the 18-inch chord model was tested (which was also used in the current study), and LTPT refers to the NASA Langley Low-Turbulence Pressure Tunnel, where the 36-inch chord model was tested. For reference, a higher Re run conducted on the 36-inch chord airfoil model is also

shown. The values of $C_{l,max}$ of the two airfoils at the lower Re were nearly identical, but stall occurred one degree later for the larger model. Over much of the angle of attack range, C_d was also very simiar for the two airfoils, with the larger airfoil model having a slightly lower C_d from α = -2 to 4 deg. While these two roughness simulations cause very similar performance degradations, the degradation due to the smaller simulation is slightly larger even though the k/c of the roughness was smaller, results which are not out of line with the current study.

Another factor which is more likely responsible for some of the differences observed between the casting and the simple-geometry simulations is the type of roughness on each, as the casting roughness could not be exactly geometrically scaled. The roughness on the casting is of non-uniform height and density and would be best modeled by using roughness of non-uniform height and density on the simple-geometry simulation. This was not practical, so grit roughness of approximately constant height and density was used. For the EG1126 roughness accretion described above, roughness height and density were varied at discrete chordwise intervals to better approximate the roughness on the casting, but it still did not exactly replicate the casting roughness. Historically, to model wall surface roughness for engineering applications a parameter known as "equivalent sand roughness," introduced by Schlichting[104,106] and based on the data of Nikuradse[107] has been used. The equivalent sand roughness height (k_s) refers to the size of the uniformly distributed grit roughness (or sandpaper roughness) that causes the same increase in skin friction as the original roughness and is usually determined empirically. While it would be extremely useful if the parameter k_s was universal and could be applied to ice roughness accurately, Bons and Christensen[108] point out several deficiencies in the use of equivalent sand roughness to accurately reproduce the characteristics of what they refer to as "real" roughness, which tends to be randomly distributed and much more non-uniform than sand roughness. First, given details of the "real" roughness to be modeled (which are often difficult to obtain for ice roughness accretions because the airfoil underneath the roughness is not flat), it is difficult to determine an appropriate value of k_s, as many correlations have been published and the values of k_s vary dramatically from one correlation to the next.[109] Even if a representative value of k_s could be selected for ice roughness at a particular location on the airfoil, it would be difficult to

apply due to a large degree of spatial variation in the "real" roughness. Finally, equivalent sand roughness is defined based on having an equivalent skin friction coefficient and does not reliably and accurately predict boundary-layer transition and momentum loss,[108] which is important for properly representing the iced-airfoil aerodynamics. If improved accuracy over the results presented above is desired, it is recommended that further research be conducted to determine a type of "equivalent sand roughness" that is specifically tailored to predicting skin friction, momentum loss, and boundary-layer transition on an airfoil with ice roughness.

4.2.2 Ice Roughness Simulation Summary

A methodology for simulating ice roughness aerodynamics at low Reynolds number on a sub-scale model was developed and validated using full-scale castings tested in an earlier study by Broeren et al.[9] at high Reynolds number. Ice roughness increases skin friction, extracts momentum, and may cause the boundary layer to undergo bypass transition, resulting in premature trailing-edge stall. Several ice roughness simulations were constructed of two different ice castings and installed on an 18-inch chord NACA 23012 airfoil to improve the existing understanding of ice roughness and to determine the aerodynamic effects of various features of ice roughness such as height, concentration, and chordwise extent. Small variations in roughness height for small roughness sizes were found to have a very large effect on $C_{l,max}$, but $C_{l,max}$ was less sensitive to varations in height for larger roughness sizes. Airfoil C_d was also sensitive to roughness height. Variations in roughness concentration also had a large effect on $C_{l,max}$ and C_d, especially at low concentrations. Beyond a critical roughness concentration (which is dependent on roughness height), $C_{l,max}$ becomes much less sensitive to further increases, although C_d is still affected. Small changes in roughness chordwise extent do not have a large effect on $C_{l,max}$, but do affect C_d. Large changes in extent may affect both parameters. Because height, concentration, and extent all appeared to be important features to represent, a simple-geometry simulation with geometrically-scaled roughness of varying height and concentration was constructed to closely match the roughness on one of the full-scale castings. The ability of this simulation (as well as others) to reproduce the casting aerodynamics is summarized in Table 4.1. In the table, the first column lists the size of grit roughness used to build the simulation. The second column shows how accurately the

simulation reproduced $C_{l,max}$, both as a difference in C_l and a percent difference relative to $C_{l,max}$ of the casting. The third column shows how accurately each simulation reproduced the stall angle of attack. The last column shows the ability of each simulation to model C_d of the casting over the linear angle of attack range. This is shown both as $\Delta C_{d,RMS}$ as calculated in eq. 4.1 and as an absolute value, calculated as

$$\Delta C_{d,RMS} = \sqrt{\frac{\sum_{i=1}^{N} \left(C^i_{d,sim} - C^i_{d,casting}) \right)^2}{N}} \tag{4.2}$$

For the EG1126 glaze-ice roughness simulation, the geometrically-scaled simulation had a slightly lower $C_{l,max}$ than the casting and tended to over-predict C_d at low angles of attack (Table 4.1). At high angles of attack, it modeled C_d quite accurately. A second simulation, which used narrow strips of roughness on the upper and lower surfaces to model only the initial portion of roughness on the casting, had a very similar $C_{l,max}$ to the geometrically-scaled simulation, but better reproduced the casting C_d at low angles of attack. However, at high angles of attack, agreement in C_d worsened. The final simulation shown in Table 4.1 better reproduced the casting $C_{l,max}$ than either of the other simulations, but also used a roughness height much smaller than the maximum height measured on the casting (this simulation was constructed with *a priori* knowledge of the casting aerodynamics). It too better reproduced C_d of the casting at low angles of attack but had a lower C_d at high angles of attack.

The aerodynamic fidelity of each of the EG1134 rime-ice roughness simulations is shown in Table 4.2. For this accretion, the geometrically-scaled simulation greatly under-predicted $C_{l,max}$ and over-predicted C_d at low angles of attack, but agreement with the casting C_d at high positive angles of attack prior to stall was good. Two other simulations were constructed to better model $C_{l,max}$ and C_d at low angle of attack using k/c = 0.00016 and 0.00007 roughness. Both of these simulations better reproduced the casting $C_{l,max}$ and C_d. The k/c = 0.00007 roughness simulation almost exactly reproduced the aerodynamic performance, having $C_{l,max}$ within 1% of the casting and $\Delta C_{d,RMS}$ of only 7.2%.

The results shown in Tables 4.1 and 4.2 indicate that geometric-scaling of ice roughness tends to produce conservative estimates of iced-airfoil performance, especially for smaller iced-

Table 4.1 Summary of aerodynamic fidelity of EG1126 ice roughness simulations.

Simulation	**Simulation $C_{l,max}$ - Casting $C_{l,max}$**	**Simulation α_{stall} - Casting α_{stall} (deg)**	**Δ RMS C_d Simulation v. Casting (α = -4 to 9 deg.)**
Geometrically-scaled simple geometry -- k/c = 0.0018/0.0009 roughness on U.S., 0.0013/0.0009 roughness on L.S., casting extents	-0.042 (-3.9%)	-1.1	0.0022 (20.8%)
Simple geometry -- k/c = 0.0013 x 0.10" wide roughness on U.S., k/c = 0.0009 x 0.10" wide roughness on L.S.	-0.030 (-2.8%)	-1.1	0.0018 (11.3%)
Simple geometry -- k/c = 0.0003 roughness, casting extents	-0.006 (-0.6%)	-0.1	0.0024 (16.0%)

Table 4.2 Summary of aerodynamic fidelity of EG1134 ice roughness simulations.

Simulation	**Simulation $C_{l,max}$ - Casting $C_{l,max}$**	**Simulation α_{stall} - Casting α_{stall} (deg)**	**Δ RMS C_d Simulation v. Casting (α = -4 to 10 deg.)**
Geometrically-scaled simple geometry -- k/c = 0.0003 roughness, EG1126 extents	-0.20 (-15.7%)	-1.6	0.0016 (16.3%)
Simple geometry -- k/c = 0.00016 roughness, casting extents	-0.06 (-4.8%)	-0.6	0.0014 (12.8%)
Simple geometry -- k/c = 0.00007 roughness, casting extents	0.01 (0.6%)	-0.1	0.0008 (7.2%)

airfoil roughness heights. Other roughness simulations were able to more accurately model $C_{l,max}$ and C_d of the casting. Multiple combinations of roughness height and concentration were found to be able to provide accurate modeling of iced-airfoil aerodynamics. These results indicate that geometric scaling may not be the best scaling technique for ice roughness, and it is recommended that other scaling methods be explored. It is also noted in this section that little high fidelity ice roughness data exist from Re = 2.0 x 10^6 to Re = 4.6 x 10^6, and the variation in airfoil aerodynamic performance in this range is not well understood. Further research is suggested to determine the effects of Re in this range on ice roughness aerodynamics.

4.3 Streamwise Ice

A streamwise-ice shape differs from ice roughness in that there often exists a large leading-edge ice geometry. The geometry may introduce a strong adverse pressure-gradient, causing a short separation bubble to form. As defined by Tani,[13] short bubbles remove momentum from the boundary layer but do not have a global impact on the pressure distribution around the airfoil and do not grow significantly with increasing angle of attack. The degradation in performance due to streamwise-ice is also in part due to the presence of surface roughness on the airfoil, and the effects of this surface roughness are similar to those caused by ice roughness (described in the last section), coming mainly from the interaction between the roughness elements and the developing boundary layer and causing premature trailing-edge separation and increased C_d at low angle of attack.

4.3.1 Sub-scale Simulation of Streamwise Ice with Full-scale Validation

Broeren et al.[9] measured the aerodynamic performance of two different streamwise-ice castings on a NACA 23012 at high Reynolds number. Geometric details of each of these castings are provided in Section 3.2.4.2. The aerodynamic performance coefficients C_l, C_m, and C_d are shown in Fig. 4.12 for the first streamwise-ice accretion (designated EG1125). As with the ice roughness case described above, the full-scale casting and clean NACA 23012 data were taken in the ONERA F1 wind tunnel at a Re = 12.0 x 10^6 and M = 0.20 while the

sub-scale clean and simulation data were taken in the University of Illinois wind tunnel at Re = 1.8 x 10^6 and M = 0.18. Again, the full-scale casting is considered to give the true aerodynamic performance coefficients of the ice shape at flight Reynolds number. It causes the airfoil to stall at α = 11.9 deg., reducing $C_{l,max}$ to 1.12. Additionally, it changes the stall characteristics to a much more gradual, trailing-edge type stall. This effect is similar to that caused by the addition of ice roughness. C_d is increased by the addition of the casting, with $C_{d,min}$ = 0.0082 occurring at α = 1.6 deg. This is 47% higher than $C_{d,min}$ of the NACA 23012 airfoil at Re = 12.0 x 10^6, but only 24% higher than $C_{d,min}$ of the NACA 23012 airfoil at Re = 1.8 x 10^6. $C_{d,min}$ occurs at different angles of attack for each case.

In Fig. 4.12, four sub-scale simulations are compared with the full-scale casting. The 2-D smooth simulation is a rapid-prototyped constant cross-section representation of the ice shape, with no roughness added. The simple geometry simulation is a constant cross-section simulation built-up from balsa wood and book tape to capture the main geometric features of the ice shape. The 2-D smooth simulation with added roughness represents the simulation that would have been designed without *a priori* knowledge of the casting aerodynamics; the roughness had approximately the same non-dimensional height (k/c) as the roughness on the casting. The 2-D smooth simulation with faired feathers was the simulation with the most similar aerodynamic performance to the casting, and was designed with *a priori* knowledge of the casting aerodynamics (this simulation will be described further later in this section).

At Re = 1.8 x 10^6, the 2-D smooth simulations with and without roughness caused a larger penalty to both $C_{l,max}$ and C_d than the casting, but caused a similar stall behavior. For the 2-D smooth simulation without roughness, $C_{l,max}$ was 6% lower than the casting and occurred at a 0.6 deg lower angle of attack, while $C_{d,min}$ was higher than that of the casting by about 19%. Adding roughness of the same k/c as the casting caused $C_{l,max}$ to decrease a further 6% relative to the casting and $C_{d,min}$ to increase a further 26%. At high angles of attack, C_d of the two simulations converged, suggesting that roughness plays a smaller role in affecting C_d near stall than at low angles of attack.

In contrast to these two simulations, the simple geometry simulation had a $C_{l,max}$ that was 4.4% higher than the casting and stalled at a 0.4 deg. higher angle of attack than the casting. This simulation caused a slightly sharper drop in C_l post-stall than did the other

simulations discussed so far. Despite these minor discrepancies in C_l and stall behavior, C_d of the simple-geometry simulation agreed extremely well with C_d of the casting. The value of $\Delta C_{d,RMS}$ for the simple-geometry simulation was only 7.6%, compared with 23.7% for the 2-D smooth simulation from α = -4 to 9 deg. ($\Delta C_{d,RMS}$ was calculated using eqn. 4.1).

Previous studies have shown the aerodynamic performance of an airfoil with a streamwise ice accretion to be sensitive to roughness height and concentration,[7] as discussed in Chapter 2. Generally, increasing roughness height or concentration causes $C_{l,max}$ to decrease and C_d to increase. In view of these trends, the roughness size on the 2-D smooth simulation was altered in order to match the simulation aerodynamics to the full-scale casting. Since the aerodynamic penalty associated with the 2-D smooth simulation was too severe, it was recognized that the roughness inherently present on the 2-D smooth simulation had to be removed. It is evident in the tracing of the EG1125 streamwise-ice accretion that feathers were present on the accretion and were traced. These feathers are circled in Fig. 4.13. The 2-D smooth simulation was constructed by extruding this tracing. Therefore, these feathers, which are highly three dimensional in nature, were effectively treated as two-dimensional geometric features in the simulation process, resulting in small, artificial "ridges" along the span of the simulation near the leading edge of the airfoil. To reduce the influence of these ridges, a layer of tape was applied to the 2-D smooth simulation. This effectively faired the feathers (smoothing the simulation further) and eliminated the ridge caused by the tracing of the feathers. The effect of this fairing procedure was to increase $C_{l,max}$ to within 1.1% of the casting $C_{l,max}$ and to prolong stall to α = 11.6 deg., nearly the same angle beyond which the casting caused stall (Fig. 4.12). Additionally, C_d decreased to the level of the casting and simple-geometry simulation over a wide range of angle of attack, resulting in a $\Delta C_{d,RMS}$ = 8.1%. Although it is not shown in the plot, surface roughness of height k/c = 0.00007 was added to this simulation as well. This simulation $C_{l,max}$ matched that of the casting almost exactly, but C_d was slightly too high at low angles of attack, resulting in a higher value of $\Delta C_{d,RMS}$ of 16.9%.

Figure 4.14 shows the pressure distribution at α = 10 deg. around the NACA 23012 with the full-scale EG1125 casting and two sub-scale simulations. Again, the casting data were obtained at Re = 12.0 x 10^6 and M = 0.20 and the sub-scale simulation data were obtained

at Re = 1.8 x 10^6 and M = 0.18. The C_p distribution of the 2-D smooth simulation with faired feathers is very similar to the C_p distribution of the casting, which is consistent with the good agreement for C_l and C_d between the two. The 2-D smooth simulation with the roughness scaled to match k/c of the casting had a C_p distribution slightly different from that of the casting. From x/c = 0.02 - 0.10, C_p of this simulation had a lower magnitude than C_p of either the casting or the 2-D smooth simulation with faired feathers. Also, the airfoil trailing-edge pressure was lower for the 2-D smooth simulation with roughness, suggesting an earlier trailing-edge stall and in part explaining the higher C_d at this angle of attack.

Current sub-scale simulation techniques were again applied to determine the accuracy with which a second full-scale casting of a streamwise-ice shape, also tested by Broeren et al.[9] at Re = 12.0 x 10^6 and M = 0.20, could be modeled. This casting, designated EG1162, is described in detail in Section 3.2.4.2. The aerodynamic performance data for the full-scale casting and simulations for this second EG1162 streamwise-ice shape, which was more conformal to the airfoil leading edge, are shown in Fig. 4.15. While the EG1162 streamwise-ice casting had a similar effect on the value of $C_{l,max}$ as the EG1125 casting, decreasing it from 1.48 to 1.16, it had less of an effect on the stall type. Figure 4.15a shows that the airfoil still exhibited a leading-edge stall with a sharp dropoff in C_l beyond α = 11.9 deg. of similar magnitude to that observed on the clean airfoil beyond α = 14.4 deg. At low angles of attack, the EG1162 streamwise-ice casting caused a larger increase in C_d than did the EG1125 casting, but C_d of the NACA 23012 with the two castings converged with increasing angle of attack and was nearly identical above α = 10 deg.

Three simulations of this ice shape were built with no *a priori* knowledge of the casting aerodynamics: 2-D smooth, simple-geometry, and 2-D smooth + k/c = 0.0013 roughness simulations. The roughness added to the 2-D smooth simulation had similar height and extent to roughness present on the casting. Of these simulations, the 2-D smooth simulation had $C_{l,max}$ and α_{stall} most similar to the casting, differing by 3.0% and 0.6 deg., respectively. As with the EG1125 streamwise-ice shape, the simple-geometry simulation had $C_{l,max}$ slightly higher than the casting. The 2-D smooth + k/c = 0.0013 roughness simulation, which directly scaled k/c of the casting, had $C_{l,max}$ about 12% too low. The penalties to C_d were consistent with these trends in $C_{l,max}$. The 2-D smooth + k/c = 0.0013 roughness simulation had C_d

higher than the casting at all angles of attack. Both the simple-geometry and 2-D smooth simulations had C_d similar to the casting for angles of attack below α = 1 deg. and 3 deg., respectively, but tended to have lower C_d than the casting above these angles. The corresponding values of $\Delta C_{d,RMS}$ from α = -4 to 10 deg. were 16.2% and 11.1%. The 2-D smooth simulation likely imparted a slightly worse aerodynamic penalty than did the simple-geometry simulation because it had a small amount of two-dimensionalized surface roughness due to tracing of roughness elements present on the casting. These results are consistent with the ice roughness simulations and the other streamwise-ice 3 simulations in that geometric-scaling of surface roughness results in conservative performance estimates. From these studies, however, it appears that the full-scale casting aerodynamic performance can be bracketed by sub-scale 2-D smooth streamwise-ice simulations with and without roughness, provided that feathers are removed from the ice tracings used to create the 2-D smooth simulations.

A fourth simulation, 2-D smooth + $k/c = 0.00033$ roughness, was designed with *a priori* knowledge of the casting aerodynamics and resulted from a trade study which varied roughness height on the 2-D smooth simulation. $C_{l,max}$ of this simulation was approximately 3.0% greater than $C_{l,max}$ of the casting, with stall occurring at a 0.2 deg. higher angle. C_d agreed well with the casting, especially with consideration of the uncertainty inherent in measuring C_d at only one spanwise station. The $\Delta C_{d,RMS}$ for the 2-D smooth + $k/c = 0.00033$ roughness was 8.1%.

The C_p distributions for the 2-D smooth simulations with $k/c = 0.00033$ roughness and with $k/c = 0.0013$ roughness are compared to the C_p distribution of the EG1162 casting at α = 10 deg. in Fig. 4.16. Both sub-scale simulations had C_p distributions qualitatively similar to the casting, but had lower pressure (higher magnitude) suction peaks and slightly lower trailing-edge pressures. The differences in suction peak magnitude near $x/c = 0.0$ may also have in part been due to differences in pressure tap placement between the simulations and casting, as the gradients in this region are very high and Blumenthal[38] showed that pressure tap placement may have a small impact on the measured airfoil C_p distribution of streamwise-ice shapes (discussed in more detail in Chapter 2). Both simulations and the casting generated a short separation bubble, but the location and size of this latter bubble was slightly different on each. On the casting, the bubble formed at approximately x/c =

0.05. On the sub-scale simulation with geometrically-scaled $k/c = 0.0013$ roughness, the bubble formed at $x/c = 0.035$, and on the simulation with smaller $k/c = 0.0003$ roughness the bubble formed at $x/c = 0.07$. On this simulation, the bubble covered a larger chordwise extent than did the bubbles on the casting and the $k/c = 0.0013$ simulation, covering about 3% chord as opposed to 1%. The 2-D smooth simulation with $k/c = 0.0013$ roughness had a trailing-edge pressure that was higher than that of the 2-D smooth simulation with $k/c = 0.0003$ roughness, indicating poorer boundary-layer health and suggesting that the $k/c = 0.0013$ roughness simulation will cause the airfoil to stall at a lower angle of attack than the simulation with smaller roughness. This is consistent with the performance data shown in Fig. 4.15.

Figure 4.17 compares the performance degradation of the NACA 23012 due to the 2-D smooth and simple-geometry simulations (with roughness) of the EG1125 and EG1162 streamwise-ice shapes. The simple-geometry simulation of each shape had a very smooth surface, and the only difference between them was the gross leading-edge ice geometry (the cross-sections of each are shown in Fig. 3.22). Figure 4.17a shows that the values of $C_{l,max}$ were about 3% apart from each other for these 2-D simulations and the lift curve of the EG1125 simple-geometry simulation was less than that of the EG1162 simple-geometry simulation. Similarly, the two 2-D smooth simulations had surface roughness of similar size ($k/c = 0.0009$ for the EG1125 shape and $k/c = 0.0013$ for the EG1162 shape), so the only difference between the two simulations was the gross leading-edge ice geometry. $C_{l,max}$ of these two simulations was only 2% different. These results support the conclusions of Lee[18] and Kim and Bragg,[27] who found that small differences in gross leading-edge ice geometry on streamwise-ice shapes do not have a large effect on $C_{l,max}$ (especially when considering the initial degradation in $C_{l,max}$ from the clean airfoil). This suggests that the key to reproducing casting $C_{l,max}$ using sub-scale simulations is in properly modeling the surface roughness, as it is only necessary to approximately represent the gross leading-edge geometry. On the other hand, small variations in leading-edge geometry do appear to have a larger effect on airfoil C_d (Fig. 4.17b). The differences in C_d between the two simple-geometry simulations is on the same order as the difference between the simulation and the clean NACA 23012 at $Re = 1.8 \times 10^6$, and the same is true for the 2-D smooth simulations with roughness. Kim[17] also

reported significant variations in C_d with changing leading-edge gross ice geometry, and Lee[18] observed some variation as well but only at high lift coefficients. Taken together, these studies imply that to appropriately model C_d, both surface roughness and leading-edge geometry need to be represented accurately.

4.3.2 Streamwise Ice Simulation Summary

Streamwise ice affects the iced-airfoil flowfield through two main mechanisms: a short separation bubble generated by slope discontinuites in the ice geometry and surface roughness on the ice shape. To accurately model the aerodynamics of a full-scale ice shape, sub-scale simulations of streamwise ice should have a similar effect on the iced-airfoil flowfield over the angle of attack range of interest. Gross leading-edge ice geometry and surface roughness are the key features required to represent in order to model streamwise-ice aerodynamics. The detailed ice geometry at the leading edge does not have to be exactly reproduced, as long as the simulation geometry in this region generates a short separation bubble of similar size and location as on the original ice shape. Surface roughness should be modeled as well, since its effects on streamwise-ice flowfields are very similar to those for ice roughness flowfields. Increasing roughness height and concentration (to some critical concentration depending on roughness height) causes larger reductions in $C_{l,max}$ and increases in C_d. It was also shown that when constructing 2-D smooth simulations of streamwise ice, care should be taken not to extrude highly three-dimensional features such as ice feathers, as the character of the features will be altered and they may have a more severe aerodynamic effect when two dimensionalized.

Two sets of full-scale streamwise-ice castings tested by Broeren et al.[9] at high Reynolds number were simulated on a sub-scale airfoil model at low Re using 2-D smooth and simple-geometry simulations with and without roughness. A chart comparing the aerodynamic fidelity of each of the simulations is shown in Tables 4.3 and 4.4. These tables are similar to those shown for the ice roughness simulations and are explained in more detail in Section 4.2.2.

Both 2-D smooth simulations reproduced the casting $C_{l,max}$ to within 5%, as did the EG1125 simple-geometry simulation. The EG1162 simple-geometry simulation over-predicted

Table 4.3 Summary of aerodynamic fidelity of EG1125 streamwise-ice simulations.

Simulation	Simulation $C_{l,max}$ - Casting $C_{l,max}$	Simulation α_{stall} - Casting α_{stall} (deg)	Δ RMS C_d Simulation v. Casting (α = -4 to 9 deg.)
2-D smooth	-0.05 (-4.6%)	-0.6	0.0024 (23.7%)
Simple-geometry	0.05 (4.4%)	0.4	0.0008 (7.6%)
2-D smooth, faired feathers	0.01 (1.1%)	-0.3	0.0010 (8.1%)
2-D smooth + k/c = 0.0015 roughness on U.S. k/c = 0.0012/0.0009 roughness on L.S.	-0.12 (-10.6%)	-0.6	0.0047 (46.3%)

$C_{l,max}$ of the casting, but was within 8%. The stall angle of attack and C_d were also modeled fairly well by both the 2-D smooth and simple-geometry simulations. The addition of geometrically-scaled surface roughness to the 2-D smooth simulations ($k/c = 0.0015$ roughness on the upper surface and $k/c = 0.0012/0.0009$ roughness on the lower surface for the EG1125 simulation and $k/c = 0.0013$ roughness for the EG1162 simulation) tended to produce conservative estimates of C_l and C_d, similar to the trends observed for the ice roughness simulations. The geometrically-scaled roughness on the EG1125 2-D smooth simulation in particular had poor agreement with the casting aerodynamic performance, especially C_d. By fairing feathers that were traced and two-dimensionalized in this simulation, the $C_{l,max}$ of the 2-D smooth simulation (with faired feathers) increased to become 1% higher than the casting, and the comparison of C_d with the casting improved as well. For the other simulations, better agreement between sub-scale simulations and the corresponding full-scale castings was obtained by tailoring the surface roughness on the upper and lower surface to reproduce the casting C_d, but this would be difficult to do without *a priori* knowledge of the casting aerodynamics.

Table 4.4 Summary of aerodynamic fidelity of EG1162 streamwise-ice simulations.

Simulation	Simulation $C_{l,max}$ - Casting $C_{l,max}$	Simulation α_{stall} - Casting α_{stall} (deg)	Δ RMS C_d Simulation v. Casting (α = -4 to 10 deg.)
2-D smooth	0.03 (3.0%)	-0.6	0.0020 (11.1%)
Simple-geometry	0.09 (7.9%)	0.5	0.0029 (16.2%)
2-D smooth + k/c = 0.0013 roughness	-0.13 (-11.7%)	-1.6	0.0038 (25.8%)
2-D smooth + k/c = 0.00033 roughness	0.03 (3.0%)	0.2	0.0010 (8.1%)

4.4 Horn Ice

Previous research on horn-ice shapes has shown that the iced-airfoil flowfield is dominated by a long separation bubble generated by an adverse pressure gradient at the tip of the horn. The size of the separation bubble for given flow conditions is determined by the pressure gradient in which it occurs (a function of chordwise location and airfoil geometry) and gross horn geometry, which can be characterized by the horn height, angle with respect to the chord line, and sometimes horn tip radius. Surface roughness has been shown to have relatively smaller effects on iced-airfoil performance. This section covers the effects of changes in the gross horn geometry and which features need to be appropriately represented on sub-scale simulations. The horn-ice flowfield is discussed in more detail in Section 2.1.5 and by Bragg et al.,[4] and Jacobs,[36,37] and its unsteady characteristics are quantified by Gurbacki.[33,60]

4.4.1 Sub-scale Simulation of Horn Ice with Full-scale Validation

Broeren et al.[9] measured the aerodynamic performance degradation of a 72-inch chord NACA 23012 due to a horn-ice casting at Reynolds numbers from 4.6 x 10^6 - 16.0 x 10^6 and $M = 0.10$ - 0.28. This data set is considered to be representative of the true iced-airfoil aerodynamics. The casting caused a thin-airfoil type stall at $\alpha = 8.8$ deg., resulting in a $C_{l,max} = 0.86$ (Fig. 4.18). It also caused a considerable increase in pitching-moment curve slope, causing C_m to increase to almost 0.03 before airfoil stall, compared with C_m = -0.005 for the clean airfoil at

the same angle of attack and $C_m = 0.014$ just before clean airfoil stall. Airfoil drag increased substantially at all angles of attack due to the horn-ice casting, and iced-airfoil $C_{d,min}$ was nearly three times as large as that of the clean airfoil.

Simple-geometry and 2-D smooth simulations of the full-scale horn-ice castings investigated by Broeren et al.[9] were constructed at 1/4-scale and tested at Re = 1.8 x 10^6 and M = 0.18. Comparisons between this sub-scale data and the full-scale data at Re = 12.0 x 10^6 and M = 0.20 are shown in Fig. 4.18. Both the sub-scale simulations had similar effects, with the 2-D smooth simulation having a $C_{l,max}$ within 2% of the casting. The simple-geometry simulation had a 7% lower $C_{l,max}$. It is possible that this reduced $C_{l,max}$ of the simple-geometry simulation was at least in part due to poor simulation tolerances and positioning inaccuracies, since this simulation was constructed from balsa wood rather than rapid-prototyping techniques. The increased $C_{l,max}$ of the casting and 2-D smooth simulations may also have resulted from curvature of the horn, which was effectively changed the horn angle and was not captured with the simple-geometry simulation. The simple-geometry simulation was intended to provide an indicator of how accurate a low cost, easy-to-produce simulation could represent the true iced-airfoil aerodynamics. Note that the uncertainty in ice shape geometry due to the effects of tracing location and icing tunnel repeatability (Fig. 2.38 - Fig. 2.42) results in uncertainties in aerodynamic performance which may be on the order of the differences seen with the horn-ice simulations of Fig. 4.18. These results for $C_{l,max}$ compare reasonably well to the earlier study by Busch[5] comparing sub-scale 2-D smooth and simple-geometry simulations to a sub-scale horn-ice casting, suggesting, at least for horn-ice, that geometric scaling (maintaining a constant horn k/c) is appropriate and that Reynolds number does not need to be matched to obtain an accurate estimate of performance.

Consistent with these results for C_l, the 2-D smooth simulation had a C_d curve similar to that of the casting while the C_d of the simple-geometry simulation was generally higher than that of the casting and increased more rapidly with increasing angle of attack. The percent RMS difference in C_d for the 2-D smooth simulation from α = -4 to 8 deg. was 10.3%, while it was nearly 36% for the simple-geometry simulation. The differences observed in the comparison between the 2-D smooth simulation and the full-scale casting at high Re were similar to those reported in other studies which looked at the differences between 2-D

smooth simulations and corresponding castings of horn-ice on models of the same scale and at the same Re.[33,48] Therefore, it does not appear as if the difference in model scale or Reynolds number between the full-scale and sub-scale cases in the current study contributed a substantial amount of error beyond that introduced by the simplified horn geometry of the 2-D smooth simulation.

The pressure distributions around the horn-ice casting and each of the simulations at α = 8 deg. are shown in Fig. 4.19. The severe adverse pressure gradient at the tip of the horn causes a rapid acceleration of the flow around the tip followed by flow separation, resulting in a separation bubble downstream of the horn (indicated by the region of relatively constant pressure). The pressure distribution of the casting in Fig. 4.19 captured both of these effects. The pressure tap at the tip of the horn measured a highly localized region of low pressure at x/c = -0.018, with a C_p = -2.62. Downstream of this chordwise station is a region of approximately constant pressure extending to x/c = 0.050, with C_p = -2.35. Farther downstream of this point, pressure recovery begins. The relative qualitative sizes of the separation bubbles generated by each of the horn simulations can be estimated from the pressure distribution. The larger negative C_p in the separation bubble of the 2-D smooth simulation and the more upstream x/c location where pressure recovery begins indicates that the 2-D smooth simulation has a smaller separation bubble than does the casting. Along those lines, the lower magnitude of the constant C_p and larger chordwise extent of the constant-pressure region in the pressure distribution of the simple-geometry simulation indicates that it has a larger separation bubble than the casting. These trends are consistent with the results for $C_{l,max}$ and C_d, as ice simulation geometries which generate larger separation bubbles have been shown to cause larger aerodynamic penalties than those which generate smaller separation bubbles.[4] Note that the simple-geometry simulation did not have pressure taps installed, so there was no measured C_p corresponding to pressure on the horn for this simulation.

4.4.2 Horn Ice Simulation Summary

The horn-ice flowfield is dominated by a long separation bubble generated by the tip of the horn, and the size of this separation bubble as it grows with angle of attack should be

Table 4.5 Summary of aerodynamic fidelity of EG1164 horn-ice simulations.

Simulation	Simulation $C_{l,max}$ - Casting $C_{l,max}$	Simulation α_{stall} - Casting α_{stall} (deg)	Δ RMS C_d Simulation v. Casting (α = -4 to 8 deg.)
2-D smooth	-0.02 (-1.9%)	0.0	0.0022 (10.3%)
Simple geometry	-0.05 (-6.8%)	-1.1	0.0078 (35.7%)

appropriately represented. The important features to model on a horn-ice shape which affect separation bubble size are horn height, location, and angle with respect to the airfoil chord line. The detailed horn geometry is usually not important to represent. Parametric studies using simple-geometry horn-ice simulations have shown $C_{l,max}$ to decrease as horn height increases and as the horn moves farther aft along the upper surface of the airfoil.

Sub-scale simple-geometry and 2-D smooth simulations were constructed of a full-scale horn-ice casting tested by Broeren et al.[9] at high Reynolds number on a full-scale NACA 23012 airfoil model. The aerodynamic fidelity of each of these simulations is shown in Table 4.5 (the columns in this table are described in more detail in Section 4.2.2). The 2-D smooth simulation reproduced the aerodynamic performance of the casting very accurately, having $C_{l,max}$ within 2% of the casting and $\Delta C_{d,RMS} = 10.3\%$. The simple-geometry simulation caused too severe of an aerodynamic penalty, resulting in a much lower $C_{l,max}$ and higher C_d. This was likely due to positioning inaccuracies and tolerances of the simulation, since it was constructed from off-the-shelf materials rather than being rapid-prototyped. These results show that as long as the horn height, location, and angle are accurately represented, no surface roughness is necessary to model horn-ice aerodynamics.

4.5 Spanwise Ridge Ice

As discussed in the Introduction, with spanwise-ridge ice the airfoil leading edge generally remains clean and free of ice (due to the use of a thermal ice protection system), so the boundary layer has time to establish before reaching the ridge. Spanwise ridges frequently generate separation bubbles. Broeren et al.[15] have classified two types of spanwise-ridges:

short ridges, which generate short separation bubbles, and tall ridges, which generate long separation bubbles. The two types of ridges require different techniques to properly simulate, since geometric features that are important on short ridges are not necessarily important on tall ridges, and vice versa. This section discusses important geometric features on each type of ridge and current methods for simulating spanwise-ridge ice.

4.6 Tall Ridges

Tall ridges are usually much greater than the local boundary-layer height at pre-stall angles of attack and generate long separation bubbles, similar to horn-ice shapes, but since ridges are usually located much farther aft on the airfoil surface, the boundary-layer has time to develop before reaching the ridge. Therefore, the flowfield around a spanwise-ridge is similar to that around a flow obstacle, whereas for horn ice the flowfield is similar to that of a backward-facing step. As with horn ice, the flowfield is dominated by the separation bubble and larger bubble sizes tend to correspond with larger performance degradations. Recall that the long separation bubble increases in size with increasing angle of attack and has a global effect on the flowfield. The effect of a tall ridge on the pressure distribution of a NACA 23012 airfoil is shown in Fig. 4.20. In the figure, a tall ridge is located at $x/c = 0.05$ on the upper surface of the airfoil (the lower surface ridge is located at $x/c = 0.10$). The ridge prevents the formation of the suction peak which normally forms near the leading edge on the clean airfoil. With the ridge, the C_p in this region remains positive. There is a rapid increase in pressure as the flow decelerates immediately in front of the ridge followed by a sharp decrease in pressure at $x/c = 0.05$ as the flow accelerates over the top of the ridge. Downstream of this extreme decrease in pressure is a region of constant pressure, indicative of a separation bubble. Near $x/c = 0.20$, pressure recovery begins, but the iced C_p distribution never matches that of the clean airfoil, as the trailing-edge pressure is lower in the iced case. Thus, the tall ridge has a global effect on the airfoil pressure distribution, altering it from leading-edge to trailing edge. Broeren et al.[15] discuss in additional detail the flowfields of tall ridge ice accretions.

4.6.1 Sub-scale Simulation of Tall Ridge Ice with Full-scale Validation

Broeren et al.[9] obtained aerodynamic performance data for a casting of a tall spanwise ridge, described in more detail in Section 3.2.4.4, on a 72-inch chord NACA 23012 at Re = 12.0 x 10^6 and M = 0.20. C_l, C_m, and C_d for the EG1159 spanwise-ridge casting are shown in Fig. 4.21. The ridge casting caused a more severe penalty in aerodynamic performance than did any of the other simulations, causing stall to occur at a much lower α = 5.1 deg. This stall was much more gradual than the stall for the clean NACA 23012, indicative of a thin-airfoil stall rather than a leading-edge stall. This is consistent with the classification of spanwise-ridge ice by Bragg et al.[4] This early stall resulted in a $C_{l,max}$ of only 0.48. Additionally, $C_{d,min}$ increased to about 0.0226 and occurred near α = -4 deg., much lower than the angle of attack at which $C_{d,min}$ occurred for the clean airfoil. These values correspond to a 74% decrease in $C_{l,max}$ and a 311% increase in $C_{d,min}$ compared to the clean NACA 23012 airfoil at the same Reynolds number of 12.0 x 10^6.

Sub-scale 2-D smooth and simple-geometry simulations of the casting were constructed and the aerodynamic performance of an 18-inch chord NACA 23012 with the simulations installed was measured at Re = 1.8 x 10^6 and M = 0.18. The considerations discussed above were taken into account during the design of these simulations. Since surface roughness was shown to have a measurable effect on C_l and C_d, it was added to the ridges of the 2-D smooth simulation with the same extents and roughness height as the casting (k/c = 0.0009 on the upper surface, k/c = 0.0018 on the lower surface). The 2-D smooth simulation with no roughness had $C_{l,max}$ higher than the casting by about 10.6% and stalled at a 1.0 deg. higher angle of attack. The agreement in C_d of this simulation with the casting was good, with a value of $\Delta C_{d,RMS}$ = 12.4%.

To model the surface roughness present on the casting, roughness with height k/c = 0.0009 and k/c = 0.0018 was added to the upper and lower surface of the 2-D smooth simulation, respectively, to match the k/c and extents of the roughness on the spanwise-ridge casting. This caused a slight reduction in $C_{l,max}$, giving a value within 1.0% of the casting. This simulation had a stall that was even more gradual than the stall of the casting, with C_l leveling off but not decreasing over the range of angle of attack at which C_l was measured.

The addition of roughness caused an increase in C_d at positive angles of attack. This worsened the comparison with the casting from $\alpha = 0$ to 2 deg., but improved agreement above $\alpha = 2$ deg. Over the range α = -4 to 4 deg., $\Delta C_{d,RMS}$ decreased to 14.6%.

The aerodynamic performance of a simple-geometry simulation of the ridge is also shown in Fig. 4.21. $C_{l,max}$ of this simulation was about 3.3% higher than that of the casting and slightly below $C_{l,max}$ of the 2-D smooth simulation. Like the 2-D smooth simulation, the simple-geometry simulation had C_d slightly too high at low angle of attack and slightly too low at very high angle of attack. The disagreement in C_d at low angles of attack was likely caused by significant three-dimensionality of the lower surface ridge, which was difficult to represent appropriately with 2-D simulations. To gauge the variation in C_d along the span of the airfoil, C_d measurements were taken at 5 different spanwise stations two inches apart behind the simple-geometry simulation (a nominally two-dimensional simulation). The short error bars shown in Fig. 4.21 (associated with the simple-geometry simulation) are representative of the minimum and maximum C_d values obtained in this spanwise sweep. These spanwise C_d data are shown in detail in Fig. 4.22. At $\alpha = 0$ deg., C_d deviated from the average by less than 7%, and this deviation diminished to less than 4% at $\alpha = 4$ deg. The error bars in Fig. 4.21, which are difficult to discern due to their small size, reflect this deviation. It is clear from Fig. 4.22 that at no spanwise station did the simulation drag equal the casting drag, suggesting that this simulation indeed did over-predict the reported casting C_d at 4 deg. and under-predict it at 0 deg., as indicated by the error bars in Fig. 4.21. However, it is likely that similar variations were present on the 2-D smooth simulations and on the casting during the testing of Broeren et al.[9] With this consideration, C_d of the 2-D smooth simulation with added roughness may have been very similar to C_d of the casting over the angle of attack range of interest. It is interesting to note that the height of the ridge on the lower surface was much less than the ridge on the upper surface and it is likely that this ridge behaved as a short ridge, discussed in the next section.

The trends in spanwise C_d for the simple-geometry tall-ridge simulation are similar to those observed for 2-D horn-ice simulations[5] in previous studies (discussed in Chapter 2) in that the spanwise variation in C_d decreased as α increased and the variation is of similar magnitude to that of the 2-D horn-ice simulations at each angle of attack. However, the

magnitude of the variation in C_d was much less for both angles for the spanwise-ridge ice simulation than for the ice roughness simulations discussed earlier (Fig. 4.4). To determine if this was due to the presence of grit roughness on the simulation, $k/c = 0.00092$ roughness was added behind the upper surface ridge at the appropriate chordwise extents ($x/c = 0.05$ to 0.135). This roughness height approximately matched the height of rivulets present on the casting. The spanwise variation in C_d is also shown for this simulation in Fig. 4.22, and the roughness is not seen to have any appreciable effect on the magnitude of the deviation from the average.

The pressure distribution around the spanwise-ridge ice casting is shown in Fig. 4.23. The ridge eliminates the suction peak on the leading edge region of the airfoil. At $x/c = 0.05$, the location of the upper surface ridge, the pressure decreases suddenly. Similar to the horn-ice shape, the pressure tap located at the tip of the ridge captures the rapid acceleration of flow over the ridge tip, resulting in a small spike in the C_p distribution at $x/c = 0.05$. As with the horn-ice shape, the severe adverse pressure gradient at the tip of the ridge causes flow separation downstream of the ridge, resulting in a separation bubble. This is indicated by the region of constant pressure extending downstream of $x/c = 0.05$ to $x/c = 0.20$ (for the casting). The C_p distribution also shows a reduced pressure recovery relative to the clean airfoil case, resulting in decreased trailing-edge pressure on the iced airfoil.

Qualitatively, the C_p distributions of the sub-scale spanwise-ridge ice simulations look very similar to the C_p distribution of the full-scale casting (Fig. 4.23). Like the casting, the sub-scale simulations eliminate the leading-edge suction peak, generate separation bubbles, and reduce pressure recovery. However, the separation bubbles downstream of the ridge appear to be slightly smaller for the sub-scale simulations than for the casting. The constant pressure region extends only to about $x/c = 0.15$ for the 2-D smooth simulation and $x/c = 0.18$ for the simple-geometry simulation and 2-D smooth simulation with roughness. Also indicative of smaller separation bubbles on the sub-scale simulations is the higher magnitude (lower pressure) of the constant pressure plateau, which ranges from about C_p -1.30 to -1.44 for the sub-scale simulations compared with C_p -1.18 for the casting. The C_p distributions for the casting and 2-D smooth simulations with and without roughness look similar on the lower surface also. The C_p distribution of the simple-geometry simulation does not appear

to capture the separation bubble behind the lower surface ridge as well as the 2-D smooth simulations because it had no pressure taps in that location.

To further compare the flowfields of the casting and sub-scale simulations, surface oil-flow visualization images were acquired. Figure 4.24a is an oil-flow visualization image of the full-scale casting taken at $\alpha = 3$ deg. at $Re = 12.0$ x 10^6 and $M = 0.20$. Flow is from left to right, and the spanwise-ridge casting is visible on the far left of the image. The estimated mean separation bubble reattachment location has been highlighted, and is positioned at approximately $x/c = 0.44$. Downstream of this line, the flow moves toward the airfoil trailing edge. Upstream of this line is a region of recirculation inside the separation bubble generated by the ridge. Flow on the airfoil surface in this region is in the upstream direction, toward the airfoil leading edge. Figure 4.24b is an oil-flow visualization image of the spanwise-ridge ice 2-D smooth simulation at $\alpha = 3$ deg. In this figure, the pressure tap row (used to obtain the C_p distribution) is located at the z = 0-inch spanwise station. Like the C_p distribution, the flowfield around the 2-D smooth simulation is qualitatively similar to that of the casting. Again, the estimated separation bubble mean reattachment location has been highlighted, with recirculating flow upstream of this region and flow toward the airfoil trailing edge downstream of this region. For this simulation, reattachment is estimated to have occurred at $x/c = 0.33$. This smaller separation bubble on the 2-D smooth simulation is consistent with the C_p distribution of Fig. 4.23. Note that there is slightly more spanwise non-uniformity in the flowfield of the 2-D smooth simulation than in the flowfield of the casting, but overall both flowfields appear to be reasonably two-dimensional at this angle of attack.

4.6.2 Tall-Ridge Ice Simulation Summary

As with horn ice, the long separation bubble generated by a tall ridge dominates the flowfield, and the detailed geometry of a tall ridge is not as important to represent as its height and surface location, which both have an impact on the size of the separation bubble. As such, airfoil aerodynamic performance may be extremely sensitive to each of these parameters. For a given surface location, the aerodynamic performance degradation tends to increase with increasing ridge height. For a given ridge height, the largest degradation in airfoil $C_{l,max}$

tends to occur when the ridge is immediately upstream of the location of maximum adverse pressure gradient at angles of attack just prior to stall. The largest increase in airfoil C_d occurs when the ridge is located near $C_{p,min}$, where the local air velocity is maximum. Because the boundary layer has time to establish before reaching the ridge, surface roughness was found to sometimes have an affect on both $C_{l,max}$ and C_d, depending on its location, height, and extents.

Sub-scale 2-D smooth and simple-geometry tall-ridge ice simulations with and without grit roughness were designed based on a tall spanwise-ridge ice casting tested by Broeren et al.[9] at Re = 12.0 x 10^6 and M = 0.20 on a 72-inch chord NACA 23012 airfoil. The aerodynamic fidelity of each of these simulations is summarized in Table 4.6 (the columns in this table are described in more detail in Section 4.2.2). The 2-D smooth simulation over-predicted $C_{l,max}$ by over 10% but modeled C_d reasonably well. The simple-geometry simulation had $C_{l,max}$ similar to that of the casting but did not model C_d as well as the 2-D smooth simulation. Both simulations stalled about 1 deg. later than the casting. Since earlier research has shown roughness to sometimes have an effect on $C_{l,max}$ and C_d of airfoils with spanwise-ridge ice accretion, the roughness on the casting was geometrically-scaled and added to the 2-D smooth simulation. Table 4.6 shows that this resulted in improved agreement with $C_{l,max}$ and C_d of the casting compared to the 2-D smooth simulation without roughness. In the table, α_{stall} appears to be over-predicted by this simulation, but examination of Fig. 4.21 shows an extremely gradual stall in which C_l continued to increase slightly; stall began at the same angle as for the casting. Because the effects of surface roughness appear to vary from shape to shape for tall ridges, it should be included on sub-scale simulations.

4.7 Short-Ridge Ice

As the name implies, short ridges tend to have smaller heights than tall ridges, but the real distinction between the two types of ridges is determined by the effect of the ridge on the airfoil pressure distribution. Broeren et al.[15] describe short ridges as generating short, stable separation bubbles which do not grow with angle of attack and have only a local effect on the airfoil pressure distribution. This is illustrated in Fig. 4.20, which compares the effects

Table 4.6 Summary of aerodynamic fidelity of EG1159 tall ridge-ice simulations.

Simulation	Simulation $C_{l,max}$ - Casting $C_{l,max}$	Simulation α_{stall} - Casting α_{stall} (deg)	Δ RMS C_d Simulation v. Casting (α = -4 to 4 deg.)
2-D smooth	0.05 (10.6%)	1.1	0.0041 (12.4%)
Simple-geometry	0.02 (3.4%)	1.0	0.0065 (23.8%)
2-D smooth + k/c = 0.0009 roughness on U.S., k/c = 0.0018 roughness on L.S.	-0.01 (-1.0%)	1.0	0.0044 (14.6%)

of short and tall ridges on the airfoil pressure distribution. The short upper surface ridge for which the pressure distribution is shown is located at $x/c = 0.13$, and a lower surface ridge is present at $x/c = 0.15$. With the short ridge, the airfoil achieves a suction peak near the airfoil leading edge of similar magnitude to that achieved when clean. The pressure distribution departs from the clean case near $x/c = 0.10$, just upstream of the ridge. Here, the flow rapidly decelerates before encountering the ridge, and then accelerates over the top of the ridge, similar to the case of the tall ridge. A short separation bubble is present behind the short ridge (indicated by the region of constant pressure) extending from $x/c = 0.15$ - 0.16, and pressure recovery begins just after $x/c = 0.16$. This is much sooner than in the case of the tall ridge. Also notice that the C_p distribution of the short ridge closely agrees with the clean airfoil C_p distribution downstream of $x/c = 0.20$, and the trailing-edge pressure is essentially the same in both the clean and iced cases. The short ridge significantly altered the airfoil pressure distribution only from $x/c = 0.10$ to $x/c = 0.20$; it had only a local effect on the flowfield. Broeren et al.[15] note that the ridge height k/c can not be used alone to determine if a ridge is a short ridge or a tall ridge. Other factors, such as ridge shape and surface location, as well as airfoil geometry, affect the type of separation bubble generated and must also be considered.

4.7.1 Sub-scale Simulation of Short Ridge Ice with Full-scale Validation

Broeren et al.[15] recently acquired aerodynamic performance data for a 72-inch chord NACA 23012 airfoil with a short ridge ice casting at Re = 12.0 x 10^6 and M = 0.20 and quantified the accuracy of sub-scale simulation techniques for this type of accretion. Compared to the clean NACA 23012 at Re = 12.0 x 10^6, the short ridge-ice casting caused $C_{l,max}$ to decrease by 17% to 1.51 and α_{stall} to occur 3.1 deg. earlier (Fig. 4.25). The short ridge also caused airfoil C_d to more than double at all angles of attack shown in Fig. 4.25.

As discussed in Section 3.2.4.4, the upper surface ridge on the casting was reasonably two-dimensional but the lower surface ridge was highly three-dimensional. Therefore, two sets of simple-geometry simulations were constructed for this casting. One set used purely 2-D geometries with and without roughness, and the other used a 3-D geometry to model the lower surface ridge. Since the upper-surface ridge happened to have a cross-sectional geometry that was close to rectangular, a 2-D simple-geometry simulation with the same height and chordwise extent was reasoned to be a representative geometry. The lower surface 2-D simple-geometry ridge simulation was also rectangular. Its height was selected by calculating the weighted average of the frontal area of the "chunks" of ice on the lower surface (discussed in more detail in Section 3.2.4.4). The 3-D lower surface ridge simple-geometry simulation modeled these ice "chunks" more accurately, capturing their location, height, width, and depth using balsa wood cubes applied to a substrate. Previous research on small ridges has not provided consistent data on the effect of surface roughness, so the simple-geometry simulation was tested both with and without surface roughness. To model surface roughness, standard grit roughness was applied to the 2-D simulations and simulated rivulets to the 3-D simulations. Both were applied with similar chordwise extents and k/c as was measured on the casting.

The aerodynamic performance of the 2-D sub-scale simulations on an 18-inch chord NACA 23012 airfoil at Re = 1.8 x 10^6 and M = 0.18 is shown in Fig. 4.25. In the figure, three simulations are compared with the NG0671 full-scale short ridge-ice casting: a 2-D simple-geometry simulation of the upper and lower surface ridges, the same simulation with surface roughness added to both the upper and lower surface ridges, and the same simulation with

surface roughness added to the lower surface ridge only, which was created with *a priori* knowledge of the casting aerodynamics. The data of Fig. 4.25a show that the simple-geometry simulation without roughness had $C_{l,max} = 1.52$, very similar to the casting $C_{l,max}$ value of 1.51 but with a more abrupt stall. Adding roughness only to the lower surface ridge did not affect $C_{l,max}$. In fact, removing the lower surface ridge simulation entirely also had no effect on $C_{l,max}$, consistent with previous discussions and with previous research on other types of accretion which has shown that lower surface ice accretion tends to have the most impact at low angle of attack and minimal impact at high angle of attack[5,27] (these studies are discussed in more detail in Chapter 2). The addition of grit surface roughness caused $C_{l,max}$ to drop markedly to 1.29. The roughness caused a slightly more gentle stall, but it was still more abrupt than that caused by the casting.

The 2-D simple-geometry simulation (without roughness) tended to have lower values of C_d than the casting at most angles of attack, except near the angle of attack at which $C_{l,max}$ occurred (Fig. 4.25b). There was a sharp decrease in C_d over the range α = -3 to 0 deg., similar to that which was measured for the clean NACA 23012 airfoil at $Re = 1.8 \times 10^6$. This decrease in C_d over this α range was not present for either the casting or the clean NACA 23012 at $Re = 12.0 \times 10^6$. The addition of $k/c = 0.00092$ roughness to the upper and lower surface ridges on the subscale simulation caused C_d to increase at all angles of attack, and caused especially large increases in C_d at high angles of attack. This is consistent with the C_l curves, in which the addition of roughness caused decreased values of C_l at high angle of attack and stall to occur earlier than without roughness. The increased C_d at low angle of attack (from $\alpha \approx$ -8 to 6 deg.) caused by roughness on the lower surface ridge improved agreement with C_d of the casting in this range. However, agreement with casting C_d at high angles of attack worsened. Overall agreement with C_d of the casting from α = -4 to 11 deg. was slightly worse, with $\Delta C_{d,RMS}$ increasing from 15.1% without roughness to 17.4% when roughness was added. Since C_d for the simulation with roughness agreed well with the casting at low angles of attack and C_d for the simulation without roughness agreed well at high angles of atack, a third simulation was constructed in which roughness was applied to the lower surface only. As shown in Fig. 4.25b, this resulted in good agreement with the casting C_d at very low and very high angles of attack, but C_d of the simulation was still less

than C_d of the casting over a large part of the α range shown. The value of $\Delta C_{d,RMS}$ for this simulation was 12.0%.

It was expected that the 3-D simple-geometry simulation of the lower surface ridge would improve agreement in C_d with the casting. Compared to the 2-D simulation, C_d was much higher, but so much so that it was also higher than C_d of the casting from below $\alpha = 5$ deg (Fig. 4.26). At higher angles of attack, C_d of the 3-D simulation without rivulets agreed reasonably well with the casting. When simulated rivulets were added, C_d increased at higher angles of attack, resulting in a simulation C_d higher than the casting C_d at all angles of attack. It is interesting that the lower surface rivulets didn't seem to have as large an effect as the upper surface rivulets, as the value of C_d at low α was very similar between the two simulations with and without rivulets, but at high angle of attack C_d was higher for the simulation with the rivulets. It is possible that the large simulated ice "chunks" on the lower surface had a dominating effect compared to the rivulets. From α = -4 to 11 deg., $\Delta C_{d,RMS}$ was 13.7% and 11.8% for the 3-D simulations with and without the rivulets, respectively, indicating only a slight improvement over the 2-D simulations in the overall modeling of C_d.

As would be expected from previous discussions, there was virtually no difference in $C_{l,max}$ between the 2-D and 3-D simple-geometry simulations, since the upper surface ridge remained unchanged. When rivulets were added, $C_{l,max}$ decreased from 1.52 to 1.41. This compares with a $C_{l,max} = 1.29$ for the simulation in which surface grit roughness was added to the upper surface ridge. Thus, the rivulets did not have as adverse an impact on $C_{l,max}$ as the grit roughness, despite having a greater height ($k/c = 0.00092$ for the grit roughness and $k/c = 0.0017$ for the rivulets). This is consistent with the trends in C_d discussed earlier. From these results, roughness does not appear to improve the comparison of $C_{l,max}$ between the casting and simulations, which is in agreement with the results found earlier by Busch.[5]

The effect of the casting and selected sub-scale simulations on the C_p distribution of the NACA 23012 is shown in Fig. 4.27. Note that the simple-geometry simulations did not have pressure taps installed, so no pressure data are shown at the location of the ridge ($x/c = 0.13$ to 0.18) for these simulations. As discussed earlier, short ridges have predominantly local effects on the airfoil C_p distribution. The main effect of the ridge is to cause a local increase in pressure just upstream of the front of the ridge ($x/c = 0.13$) due to flow deceleration. The

ridge then causes a sharp decrease in pressure as the flow accelerates over the top, as can be seen in the C_p distribution of the casting (which did have pressure taps installed) at $x/c = 0.13$. A short separation bubble usually forms downstream of the ridge, and is most evident in the C_p distribution of the 2-D simple-geometry simulation with grit roughness. Farther downstream, pressure is recovered and the C_p distribution closely resembles that of the clean airfoil. At very high angles of attack near stall, such as that shown in Fig. 4.27, the short ridge may cause a slight loss in pressure recovery, resulting in a slightly lower trailing-edge pressure. This is indicative of poorer trailing-edge boundary-layer health than for the clean airfoil and generally suggests that the iced airfoil will stall at a lower angle of attack.

The simulation which caused the most severe penalties to the integrated performance of the airfoil was that with grit roughness on both the upper and lower surface ridges. It can be seen in Fig. 4.27 that this simulation caused the leading-edge suction peak to have a reduced magnitude (higher pressure) than did the other simulations or the casting, and the reduced suction on the upper surface of the airfoil for this simulation persisted to the location of the ridge ($x/c = 0.13$). The separation bubble downstream of the ridge was larger for this simulation than the others and resulted in delayed pressure recovery. Farther downstream, the trailing-edge pressure was lower than any other simulation, consistent with the lower $C_{l,max}$ and α_{stall} of the 2-D simple-geometry simulation with grit roughness. The 2-D simple-geometry simulation with no roughness had $C_{l,max}$ and C_d most similar to that of the casting, and as would be expected, its C_p distribution was most similar as well. The leading-edge suction peak was nearly identical, as was the pressure immediately upstream of the upper surface ridge. The trailing-edge pressure was slightly lower than for the casting, which is surprising because the 2-D simple-geometry simulation had slightly higher $C_{l,max}$ and α_{stall} than the casting. This may be due to the large Reynolds number difference between the two cases.

Broeren et al.[15] showed that Reynolds number effects on short spanwise ridges are small over the range Re = 4.6 x 10^6 - 15.9 x 10^6, but noted that Reynolds number effects are important on this type of shape over a range of 1.0 x 10^6 - 1.8 x 10^6. Also, the sensitivity of the short ridge-ice simulations to geometric details such as surface roughness suggests that Reynolds number effects may not be negligible. Unfortunately, no data exist for identical

short spanwise-ridge ice shape geometries at Reynolds numbers from 1.8 x 10^6 - 4.6 x 10^6, so it is not known how much of the performance difference observed between the sub-scale simulation and full-scale casting aerodynamic performance is due to differing geometry or Reynolds number effects.

4.7.2 Short Spanwise-ridge Ice Simulation Summary

As with tall ridges, iced-airfoil aerodynamic performance is very sensitive to the location and height of short ridges. The short ridge generates a short separation bubble, which affects downstream boundary-layer development, and it is important for a short-ridge simulation to accurately reproduce the height and location of this bubble. For a given ridge location, $C_{l,max}$ tends to decrease and C_d increase with increasing ridge height. However, this trend is not universal, as some short ridges have been observed to increase $C_{l,max}$ beyond that of the clean airfoil. $C_{l,max}$ may actually increase with increasing ridge height for very small short ridges before beginning to decrease again. For locations from $x/c = 0.05$ to 0.25 on the NACA 23012 airfoil tested, $C_{l,max}$ tends to increase and C_d decrease as the ridge moves farther aft. Another difference from tall ridges is that the detailed geometry of the short ridge has a large effect on $C_{l,max}$ and C_d and should be modeled appropriately when constructing ice simulations. Surface roughness had a significant effect on iced-airfoil performance, but did not improve simulation fidelity in this study.

The aerodynamic fidelity of various two and three-dimensional simple-geometry simulations of a short-ridge casting tested at high Reynolds number on a full-scale NACA 23012 airfoil is summarized in Table 4.7. These simulations are described further in Section 3.2.4.4, and each of the columns in the table are described in more detail in Section 4.2.2. Of these simulations, the two and three-dimensional simple-geometry simulations without roughness modeled $C_{l,max}$ most accurately. Simulations with both upper and lower surface roughness tended to over-predict C_d and under-predict $C_{l,max}$. These results suggest that surface roughness does not improve simulation fidelity. As was the case with the ice roughness and streamwise-ice accretions, the simulations with surface roughness provide conservative estimates of (and provide a lower bound to) iced-airfoil performance. Little data regarding the Re effects of short-ridge ice in the range of Re = 1.8 x 10^6 to 4.6 x 10^6 exist, and it is

Table 4.7 Summary of aerodynamic fidelity of NGO671 short ridge-ice simulations.

Simulation	**Simulation $C_{l,max}$ - Casting $C_{l,max}$**	**Simulation α_{stall} - Casting α_{stall} (deg)**	**Δ RMS C_d Simulation v. Casting (α = -4 to 12 deg.)**
2-D simple geometry	0.00 (0.0%)	0.4	0.0027 (15.1%)
2-D simple-geometry + k/c = 0.0009 roughness	-0.22 (-14.7%)	-1.6	0.0042 (17.4%)
2-D simple geometry + k/c = 0.0009 roughness on L.S. only	0.01 (0.7%)	0.4	0.0023 (12.0%)
3-D simple geometry	0.01 (0.7%)	0.4	0.0020 (11.8%)
3-D simple geometry + rivulets	-0.10 (-6.7%)	-0.6	0.0026 (13.7%)

recommended that further testing be conducted in this range to determine if Re effects are in part responsible for the conservative performance estimates of the sub-scale short-ridge simulations with geometrically-scaled surface roughness.

Chapter 5

Summary, Conclusions, and Recommendations

5.1 Summary

In this dissertation, a sub-scale ice simulation methodology was developed based on an understanding of iced-airfoil flowfields and validated using full-scale iced-airfoil aerodynamic performance data. Four different types of iced-airfoil flowfields were investigated, using the classifications of Bragg et al.:[4] ice roughness, streamwise ice, horn ice, and spanwise-ridge ice. Broeren et al.[15] further sub-divided the spanwise ridge ice classification into two sub-categories, short-ridge ice and tall-ridge ice, and each of these were investigated as well. Multiple sub-scale simulations representative of each type of ice shape were constructed and installed on an 18-inch chord NACA 23012 airfoil model. These simulations were of varying fidelity and were constructed using an approach which enabled the aerodynamic effects of individual geometric features to be determined. The aerodynamic performance degradation of the NACA 23012 due to each of the simulations was measured and compared with performance data obtained by Broeren et al.[9] on a 72-inch chord (full-scale) NACA 23012 airfoil model using high-fidelity ice castings at near-flight Reynolds numbers. These full-scale data are considered to give the "true" iced-airfoil aerodynamic performance and were used to quantify the accuracy with which the sub-scale simulations could reproduce C_l, C_m, and C_d so that the sub-scale simulation techniques developed in this study could be validated.

Two types of ice simulation were investigated in detail: 2-D smooth and simple-geometry simulations. A 2-D smooth simulation is a constant cross-section extrusion of a 2-D tracing of an ice accretion cross-section, and a simple-geometry simulation uses simple-geometric shapes to emulate the general shape of the ice accretion, but does not capture the more intricate details of the geometry. Simple-geometry simulations in particular were used to isolate the

effects of individual geometric features, as it was easy to construct them by adding one feature at a time. For most of the simulations in this study, grit roughness was added to the ice simulations to determine its effect on the flowfield, as previous research has shown it to be signficant for some types of flowfields but not all. Roughness height measurements were obtained from a corresponding ice casting, and the roughness height was geometrically scaled to maintain a constant k/c on the sub-scale airfoil model. On many simulations, additional sizes of grit roughness were applied in addition to the geometrically-scaled roughness to gauge the aerodynamic effects of roughness height.

The ability of each geometrically-scaled simulation at low Reynolds number to reproduce the full-scale iced-airfoil aerodynamics at high Reynolds number (using the ice casting data from Broeren et al.[9]) depended on the ice shape type. Geometrically-scaled ice shape simulations with larger gross geometries, such as horn ice and spanwise-ridge ice, tended to more accurately reproduce the iced-airfoil aerodynamics than simulations with smaller ice geometries, such as streamwise ice and ice roughness. For these simulations with smaller ice geometries, geometrically scaling roughness generally resulted in conservative estimates of aerodynamic performance, but the use of smaller roughness heights applied at higher concentrations usually improved the ability of the simulation to model iced-airfoil performance.

5.2 Conclusions

Ice accretions usually have such complex geometries that they can not be exactly reproduced and scaled, so it is important to have an understanding of the key features of the ice shape which must be reproduced to properly model the iced-airfoil aerodynamics. A methodology was developed in which these features were identified and the accuracy of simulations which represented these features was quantified. The steps of this methodology are:

- Given an ice accretion, classify it as ice roughness, streamwise ice, horn ice, or tall or short spanwise-ridge ice
- For the appropriate classification, document and measure the geometric features which have been identified as having a significant effect on the iced-airfoil flowfield

- Depending on the ice shape type, construct simple-geometry or 2-D smooth simulations which geometrically-scale the gross-ice geometry

- For shapes in which roughness is important, add geometrically-scaled grit roughness of the appropriate concentration. This was shown to generally yield conservative performance estimates; to bracket the true iced-airfoil performance, it is recommended that the simulation be tested with and without the grit roughness

- Consult the results of this study to estimate the accuracy with which the simulation can be expected to reproduce the true iced-airfoil performance

Each type of iced-airfoil flowfield is affected by different geometric features as follows:

- **Ice Roughness** - Roughness elements on the airfoil leading edge often cause regions of localized separation, increasing skin friction and removing momentum from the flow, and may cause the boundary layer to undergo bypass transition, resulting in a less energetic transition process and causing premature trailing-edge stall, reduced $C_{l,max}$, and increased C_d. Therefore, it is important for an ice roughness simulation to reproduce these effects at each angle of attack in the α range of interest. Geometric features which affect the iced-airfoil performance are roughness height, concentration, location, and chordwise extent. Roughness height affects both airfoil $C_{l,max}$ and C_d. As roughness height increases (for constant roughness concentration, location, and chordwise extent), $C_{l,max}$ decreases and C_d increases. $C_{l,max}$ is most sensitive to changes in roughness height for very small heights and becomes less sensitive at larger heights. Roughness concentration also affects airfoil $C_{l,max}$ and C_d. As roughness concentration increases, $C_{l,max}$ increases up to a critical concentration (which is dependent on roughness height), beyond which $C_{l,max}$ becomes much less sensitive to changes in concentration. C_d increases as roughness concentration increases, even beyond the critical concentration at which $C_{l,max}$ becomes insensitive. Roughness extent affects mainly C_d, but large changes may affect $C_{l,max}$. Decreases in chordwise extent of only a few percent chord caused reductions in iced-airfoil C_d. Multiple combinations of roughness height and concentration may provide accurate modeling of iced-airfoil aerodynamics.

- **Streamwise Ice** - A short separtion bubble forms due to discontinuties in the ice geometry or at the interface between the ice and airfoil. This separation bubble removes momentum from the reattached boundary layer, reducing boundary-layer health. Therefore, it is important for a sub-scale simulation to generate a short separation bubble of similar size at a similar location, which requires a modification of the airfoil leading-edge geometry. To model $C_{l,max}$, this modification does not have to exactly match that of the orginal ice shape as long as an appropriate separation bubble is generated. Further compounding the effect of the short separation bubble is the presence of roughness on the ice, which acts in a manner similar to that described for ice roughness. Accordingly, it is important to represent the height, concentration, location, and extent of surface roughness on streamwise ice. Streamwise ice may also be more three-dimensional than other types of ice shapes due to the presence of ice feathers and nodules. If using a 2-D smooth simulation to model the iced-airfoil aerodynamics, these features should not be included in the tracing used to make the simulation as they would be extruded into two-dimensional ridge-like features, causing a different effect on the flowfield than did the feathers on the original ice shape.

- **Horn ice** - The horn-ice flowfield is dominated by a long separation bubble generated from the tip of the horn. The aerodynamics of a horn-ice shape can be accurately modeled by reproducing the size of this separation bubble and the point at which separation occurs. Features shown to affect the size of the separation bubble and affect airfoil $C_{l,max}$ and C_d are horn height, location, angle, and sometimes tip radius. With all other parameters equal, for horns located on the upper surface of the airfoil, increasing horn height usually causes reductions in $C_{l,max}$ and increases in C_d due to increased separation bubble size. Horns located farther aft and with greater angles up to 90 deg. also tend to cause larger aerodynamic penalties than those located closer to the leading edge and with lower angles. Surface roughness does not usually have a large effect on separation bubble size and is not necessary to include in a horn-ice simulation.

- **Tall spanwise-ridge ice** - Tall spanwise-ridge ice is similar to horn ice in that the flowfield is dominated by a long separation bubble, but different in that the boundary

layer has time to establish before reaching the ice shape. As with horn-ice, it is important to properly represent the long separation bubble generated by the ridge. However, because the boundary layer has formed on the airfoil surface prior to reaching the ridge, surface roughness located upstream of and on the ridge is important to represent as well. Roughness downstream of the ridge, located in the separation bubble, does not have a signficant effect on airfoil performance. Ridge features affecting airfoil $C_{l,max}$ and C_d are height, location, and surface roughness upstream of the separation point. Increasing ridge height causes a larger separation bubble and reduced airfoil $C_{l,max}$ and increased C_d. Ridges between the locations of maximum local air velocity and maximum adverse pressure gradient of the clean airfoil cause the largest reductions in $C_{l,max}$, and ridges located near the clean airfoil maximum local air velocity cause the largest increases in C_d. The addition of surface roughness caused a decrease in $C_{l,max}$ and an increase in C_d at most angles of attack.

- **Short spanwise-ridge ice** - Short spanwise-ridge ice shapes generate short separation bubbles, rather than the long bubbles generated by tall spanwise-ridge ice, and have only a local effect on the airfoil C_p distribution. It is important for a sub-scale simulation to appropriately represent this separation bubble, and ridge height, location, and geometry have all been shown to be important. Airfoil $C_{l,max}$ decreases and C_d increases with increasing ridge height for a given location or for more forward locations and a given height. The geometry of the ridge also affects airfoil aerodynamics, as differently-shaped simulations of identical height and location may yield different performance penalties. As with tall ridges, the boundary layer has time to develop before reaching the short ridge, and surface roughness was shown to have a signficant effect on both $C_{l,max}$ and C_d. In this study, the addition of surface roughness caused conservative estimates of aerodynamic performance and worsened simulation accuracy. This may in part have been due to Reynolds number effects, as no data exist regarding the effects of Re from 2.0 to 4.6 x 10^6 (Re effects above 4.6 x 10^6 have been shown to be small).

A summary of the aerodynamic fidelity of the geometrically-scaled simulations for the clean airfoil and each ice casting tested is given in Table 5.1. This table summarizes the

simulations that were based solely on the geometry of the casting and required no *a priori* knowledge of the casting aerodynamics. In the table, the first column lists the type of flowfield being simulated. The first flowfield listed is the clean NACA 23012 airfoil flowfield (with no ice shape); this is provided for reference, and all other entries in the column are iced-airfoil flowfields. The second column describes the simulation used to represent the flowfield in the first column. The third column shows how accurately the simulation reproduced $C_{l,max}$ of the full-scale NACA 23012 with the corresponding ice casting (at high Re), both as an absolute difference in $C_{l,max}$ and a percent difference relative to $C_{l,max}$ of the casting. The fourth column shows how accurately each simulation reproduced the stall angle of attack. The last column shows the ability of each simulation to model C_d of the full-scale ice casting, shown both as $\Delta C_{d,RMS}$ as calculated in eq. 4.1 and as an absolute value as calculated in eq. 4.2. These values are representative of the RMS of the percent difference between the casting C_d and simulation C_d at each angle of attack in the linear range. Values of zero in this column correspond to perfect agreement between the simulation and casting.

The first entry in the table is for the clean NACA 23012 and is provided to show the effect of Reynolds number on the clean airfoil performance. The 18-inch chord NACA 23012 airfoil model is considered to be the sub-scale simulation of the 72-inch chord NACA 23012 airfoil and has $C_{l,max}$ nearly 24% below that of the full-scale model and stalls at a 3.7 deg. lower angle of attack. Over the range of angle of attack from -7 to 14 deg., the RMS difference in C_d between the sub-scale and full-scale NACA 23012 is 35.7%. These large differences are expected due to known Re effects.

When examining the comparisons for the iced cases, it is important to note that the differences in $C_{l,max}$ and α_{stall} between most simulations of a given ice shape are small compared to the original degradation in aerodynamic performance from the clean airfoil. Uncertainties in ice geometry should also be considered when using sub-scale methods, as previous studies[24, 30, 81, 87] discussed in Section 2.2.2 have shown that variations in $C_{l,max}$ as large as 13-18% and even larger variations in C_d may result from using tracings taken at different spanwise stations, icing tunnel repeatability issues, or very small variations in icing cloud conditions. These latter two issues are associated with the ice accretion process rather than the aerodynamic simulation of a given ice shape, and the corresponding uncertainties are

Table 5.1 Summary of aerodynamic fidelity of geometrically-scaled two-dimensional ice casting simulations. These simulations were designed with no *a priori* knowledge of the casting aerodynamics. The alphanumeric designation of each corresponding ice casting is provided after each flowfield type and described in detail in Section 3.2.4.

Type of Flowfield on 72-in. chord NACA 23012, Re = 12.0 x 10^6, M = 0.20	**Geometrically Scaled Simulation on 18-in. chord NACA 23012, Re = 1.8 x 10^6, M = 0.18**	**Simulation $C_{l,max}$ - Casting $C_{l,max}$**	**Simulation α_{stall} - Casting α_{stall} (deg)**	**Δ RMS C_d Simulation v. Casting (Linear α Range)**
Clean Airfoil, No Ice	Clean Airfoil, No Ice	-0.352 (-23.7%)	-3.7	0.0030 (35.7%)
Glaze Ice Roughness, EG1126	Simple geometry + k/c = 0.0013/0.0005 roughness on U.S., k/c = 0.0009/0.0003 roughness on L.S.	-0.042 (-3.9%)	-1.1	0.0022 (20.8%)
Rime Ice Roughness, EG1134	Simple-geometry + k/c = 0.0003 roughness (EG1126 extents)	-0.200 (-15.7%)	-1.6	0.0016 (16.3%)
Streamwise Ice, EG1125	2-D smooth + k/c = 0.0015 roughness on U.S., k/c = 0.0012/0.0009 roughness on L.S.	-0.120 (-10.6%)	-0.6	0.0047 (46.3%)
Streamwise Ice, EG1162	2-D smooth + k/c = 0.0013 roughness	-0.135 (-11.7%)	-1.6	0.0038 (25.8%)
Horn Ice, EG1164	2-D smooth	-0.016 (-1.9%)	0.0	0.0022 (10.3%)
Tall Spanwise-ridge Ice, EG1159	2-D smooth + k/c = 0.0009 roughness on U.S., k/c = 0.0018 roughness on L.S.	-0.005 (-1.0%)	1.0	0.0044 (14.6%)
Short Spanwise-ridge Ice, NGO671	3-D Simple-geometry + rivulets	-0.10 (-6.7%)	-0.6	0.0026 (13.7%)

not reflected in Table 5.1 as this study examined only the uncertainties associated with the sub-scale simulation of a known ice geometry. Also note that additional mncertainties may exist in aerodynamic measurement procedures due to issues such as pressure tap placement and C_d measurement procedures.

For all flowfield types, geometric scaling resulted in conservative estimates of $C_{l,max}$. For horn and tall spanwise-ridge ice, the geometrically-scaled simulations had $C_{l,max}$ within 2% of the castings. For ice roughness and streamwise-ice, the geometrically-scaled simulations generally had significantly lower $C_{l,max}$ than the castings, as much as 15.7% in the case of the

geometrically-scaled EG1134 rime-ice roughness simulation. Each of the geometrically-scaled simulations had α_{stall} within 2 deg. of the corresponding casting. As with the modeling of $C_{l,max}$, C_d of the horn and spanwise-ridge ice simulations tended to have better agreement with the corresponding castings than did the ice roughness and streamwise-ice simulations, which tended to over-predict C_d.

The poorer agreement of the ice roughness and streamwise ice simulations is likely due to inadequate simulation of the surface roughness on the casting, which is more important for smaller ice shapes. On larger shapes, degradation in $C_{l,max}$ is due mainly to the formation of a separation bubble on the upper surface of the airfoil; surface roughness generally plays a minor role. The problems in accurately modeling surface roughness on the simulations stem from the difficulty in making accurate measurements of roughness height and concentration on the casting, and both roughness height and concentration were shown to be important on these types of ice shapes. Roughness height measurements need to be based on the clean airfoil surface below the ice or the roughness height above the gross ice shape (whichever is applicable), which often is not accessible in regions of high roughness concentration. The inability to get to the clean airfoil or gross ice shape surface introduces a large degree of uncertainty in casting roughness height measurements. Roughness concentration is difficult to measure because the boundary between a roughness element and the ice substrate below is often not clear. Further complications arise because both the height and concentration of roughness on the casting vary continuously with chordwise position, and it is difficult to precisely control the application of grit roughness to exactly match the variation in roughness properties.

With regard to the EG1125 streamwise-ice 2-D smooth simulation, feathers were traced and inappropriately extruded along the span of the airfoil. These feathers created small, artificial ridge-like features which likely generated either more or larger short separation bubbles than did the casting, resulting in unrepresentatively large penalties to $C_{l,max}$ and C_d. Smoothing and fairing these features improved the aerodynamic fidelity of the simulation. This is shown in Table 5.2, which provides a summary of the simple-geometry and 2-D smooth simulations which had aerodynamic performance most similar to the corresponding castings. These simulations were built after the geometrically-scaled simulations had already been

Table 5.2 Summary of aerodynamic fidelity of most accurate ice casting simulations. These simulations required *a priori* knowledge of the casting aerodynamics. The alphanumeric designation of each corresponding ice casting is provided after each flowfield type and described in detail in Section 3.2.4. For the horn and tall-ridge ice shapes, the geometrically-scaled simulations were the most accurate simulations.

Type of Flowfield on 72-in. chord NACA 23012, Re = 12.0 x 10^6, M = 0.20	**Most Accurate Simulation on 18-in. chord NACA 23012, Re = 1.8 x 10^6, M = 0.18**	**Simulation $C_{l,max}$ - Casting $C_{l,max}$**	**Simulation α_{stall} - Casting α_{stall} (deg)**	**Δ RMS C_d Simulation v. Casting (Linear α Range)**
Glaze Ice Roughness, EG1126	Simple-geometry + s/c = 0.0055 strips of k/c = 0.0013 roughness on U.S., k/c = 0.0009 roughness on L.S.	-0.03 (-2.8%)	-1.1	0.0018 (11.3%)
Rime Ice Roughness, EG1134	Simple-geometry + k/c = 0.00007 roughness	0.008 (0.6%)	0.0	0.0008 (7.2%)
Streamwise Ice, EG1125	2-D smooth, faired feathers	-0.009 (-0.8%)	-0.3	0.0010 (8.1%)
Streamwise Ice, EG1162	2-D smooth + k/c = 0.0003 roughness	0.034 (3.0%)	0.2	0.0010 (8.1%)
Horn Ice, EG1164	2-D smooth	-0.016 (-1.9%)	0.0	0.0022 (10.3%)
Tall Spanwise-ridge Ice, EG1159	2-D smooth + k/c = 0.0009 roughness on U.S., k/c = 0.0018 roughness on L.S.	-0.01 (-1.0%)	1.0	0.0044 (14.6%)
Short Spanwise-ridge ice, NGO671	Simple geometry + k/c = 0.0009 roughness on L.S. only	0.01 (0.7%)	0.4	0.0023 (12.0%)

tested and were designed to provide improved agreement with the casting. The table shows that, by fairing the feathers on the EG1125 2-D smooth streamwise-ice simulation, agreement in $C_{l,max}$ improved to within 1% and $\Delta C_{d,RMS}$ decreased to 8.1%. Additionally, fairing the feathers delayed airfoil stall by 1.3 deg. relative to the 2-D smooth simulation, producing very good agreement with the casting.

Table 5.2 also provides a summary of the other sub-scale simulations built with *a priori* knowledge of the casting aerodynamics which had aerodynamic performance most similar to the corresponding castings for each type of flowfield. For the ice roughness and streamwise-ice simulations, roughness sizes with smaller k/c than that measured on the castings were used because geometrically-scaled surface roughness caused aerodynamic penalties which were too

large. As would be expected, these simulations showed much better agreement in both $C_{l,max}$ and C_d for all iced-airfoil flowfields. $C_{l,max}$ was modeled to within 3% and $\Delta C_{d,RMS}$ was less than 15% for all flowfield types. The aerodynamic fidelity of the ice roughness and streamwise ice simulations in particular improved, as surface roughness has a large impact on the flowfield for these shapes. Very little improvement in simulation fidelity was obtained by modifying the amount of surface roughness on the tall spanwise-ridge ice simulation, and no attempts were made to model the surface roughness on the horn-ice simulation because earlier studies have shown roughness to have little effect on $C_{l,max}$ and C_d for this type of flowfield.

5.3 Recommendations

This study has developed and validated a sub-scale ice simulation methodology based on the current understanding of iced-airfoil aerodynamics. Through the course of the investigation, several issues arose that would be beneficial to address in later studies. Specific recommendations for future research are:

- Obtain iced-airfoil C_d measurements at multiple spanwise stations when using sub-scale simulations or ice castings. In the current study, most comparisons were based on C_d values obtained at a single spanwise station for both the casting and sub-scale simulations. The comparison of C_d between a casting and simulation may be dependent on this spanwise station. Variations in C_d on the order of 8 - 17% for glaze ice roughness and 3 - 10% for spanwise-ridge ice were found on the sub-scale simulations, and it is likely that similar (and perhaps larger) variations were present for the full-scale castings as well. Large variations in casting C_d may be expected due to spanwise variation in the ice shape geometry, but the variations in C_d along the airfoil span for nominally 2-D simulation geometries needs to be explored further. It is recommended that further research be conducted to understand this variation and that until fully understood, C_d be measured at multiple spanwise stations and averaged to obtain a representative value over the airfoil span.

- Conduct additional research regarding the Reynolds number effects on iced-airfoils from Re = 1.8 to 4.6 x 10^6, especially for streamwise ice and short-ridge ice, as little data currently exist for Reynolds numbers in this range. For both of these flowfield types, geometrically-scaled surface roughness caused conservative performance estimates, and it is possible that Reynolds number effects are in part responsible for these discrepancies.

- Develop a better understanding of the effects of surface roughness on the iced-airfoil flowfield. In this study, it was shown that roughness height, concentration, location, and chordwise extent are important parameters to represent on a sub-scale simulation, but geometrically-scaled simulations which closely reproduced these features tended to produce conservative estimates of aerodynamic performance. Agreement between simulation and casting performance was improved through the use of different sizes and concentrations of surface roughness, but no boundary-layer measurements were obtained so it is not clear if this improved agreement was coincidental or resulted from better modeling of the effects of roughness on the iced-airfoil flowfield. It is recommended that additional flowfield measurements be obtained to better understand the effects of variations in roughness size and concentration on the boundary layer. This understanding may suggest whether or not an equivalent sand roughness parameter specifically tailored for use on iced airfoils is appropriate, and if so, could be used to develop such a parameter. It may also provide new insights regarding better scaling methods for ice roughness that could be used to produce more accurate sub-scale simulations.

Figures

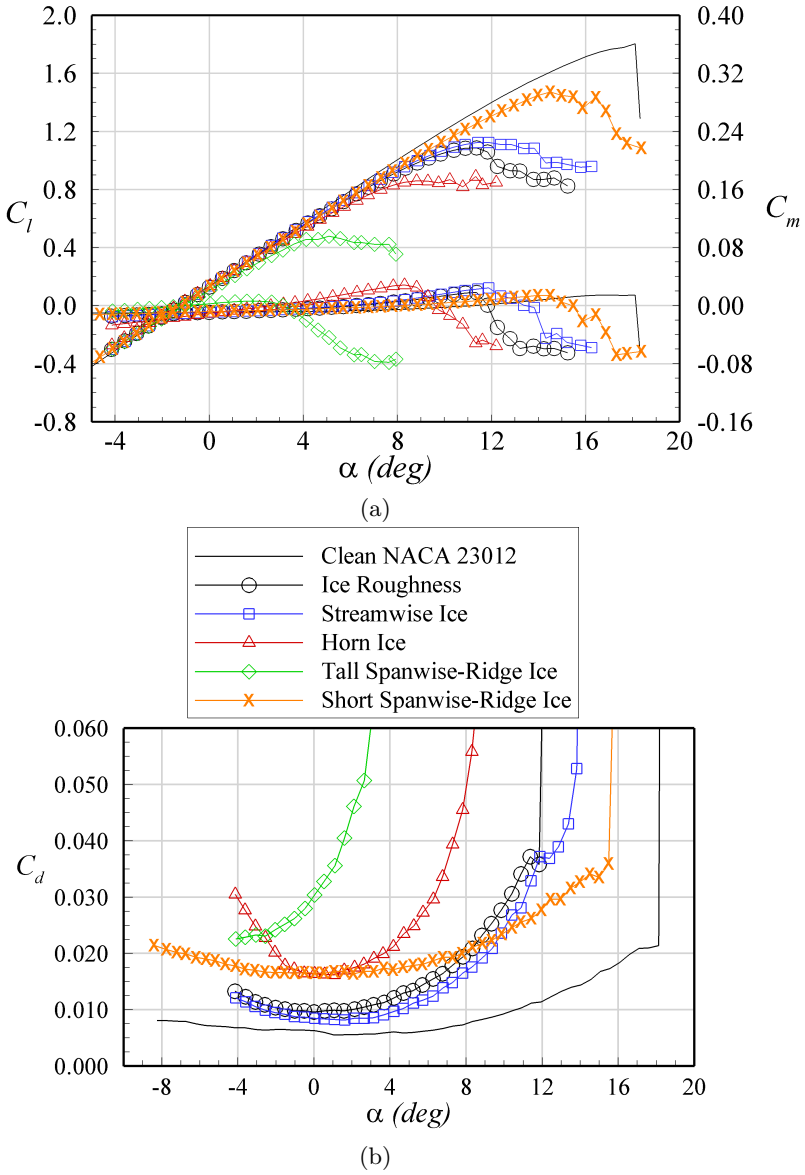

Fig. 1.1 Comparison of (a) C_l, C_m, and (b) C_d measured by Broeren et al.[9,15] using full-scale ice castings of each type of accretion on a 72-inch chord NACA 23012 airfoil model at Re = 12.0 x 10^6 and M = 0.18.

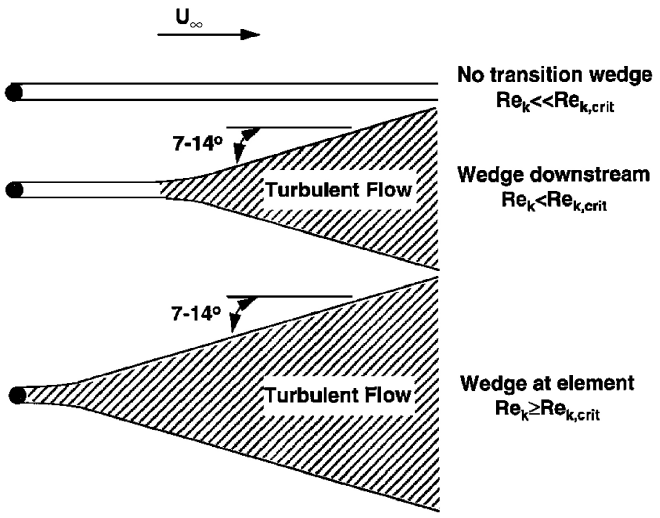

Fig. 2.1 Transition wedges generated behind an isolated roughness element for various values of Re_k.[4]

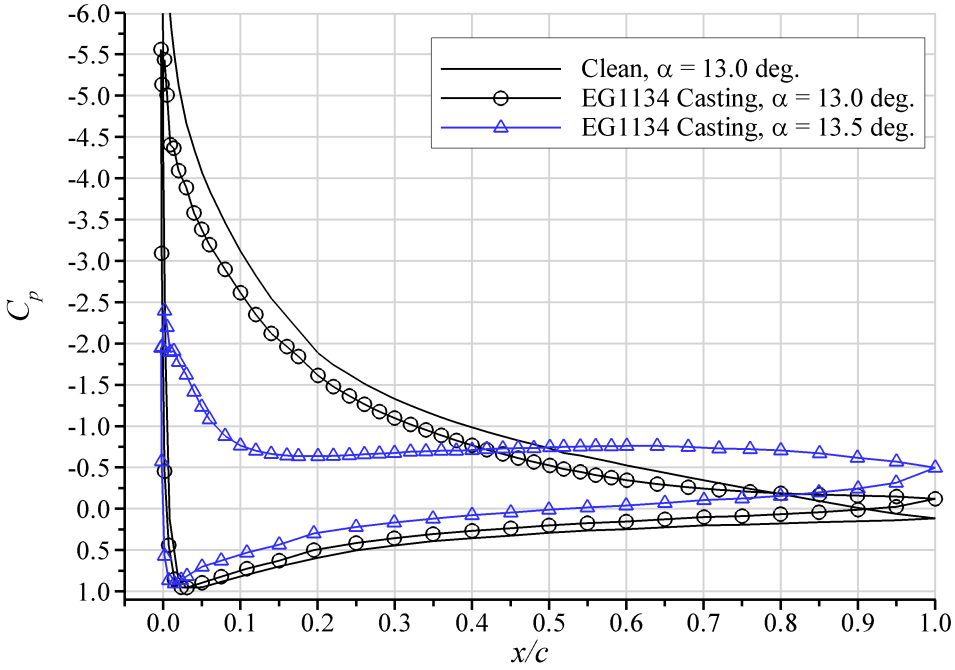

Fig. 2.2 Surface pressure distribution of a NACA 23012 airfoil with a rime-ice roughness casting at Re = 12.0 x 10^6 and M = 0.20. Data were obtained from Broeren.[29]

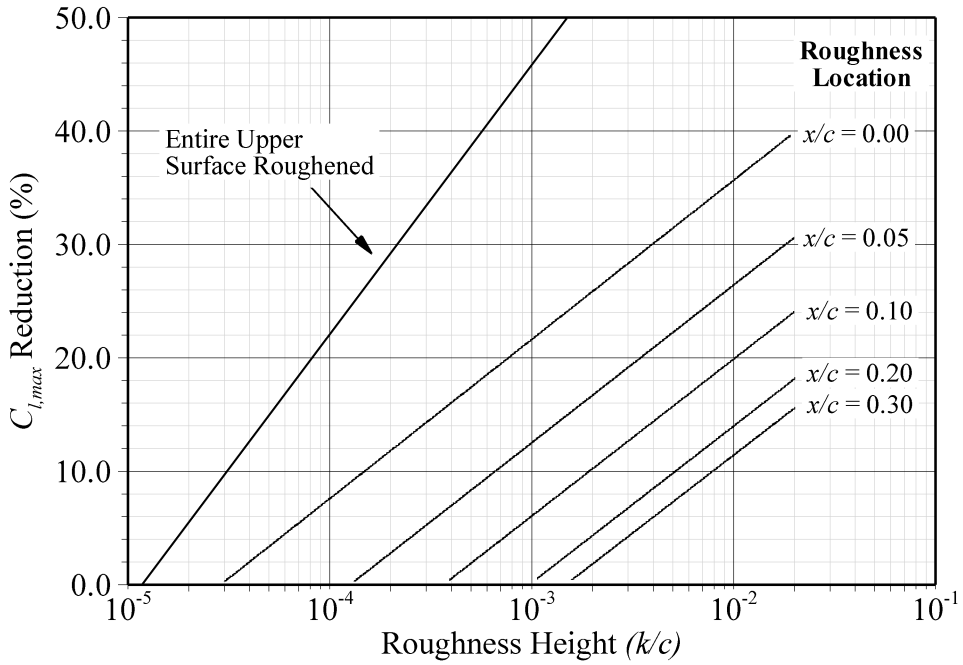

Fig. 2.3 Effect of roughness height and location on magnitude of $C_{l,max}$ degradation, adapted from Brumby.[23]

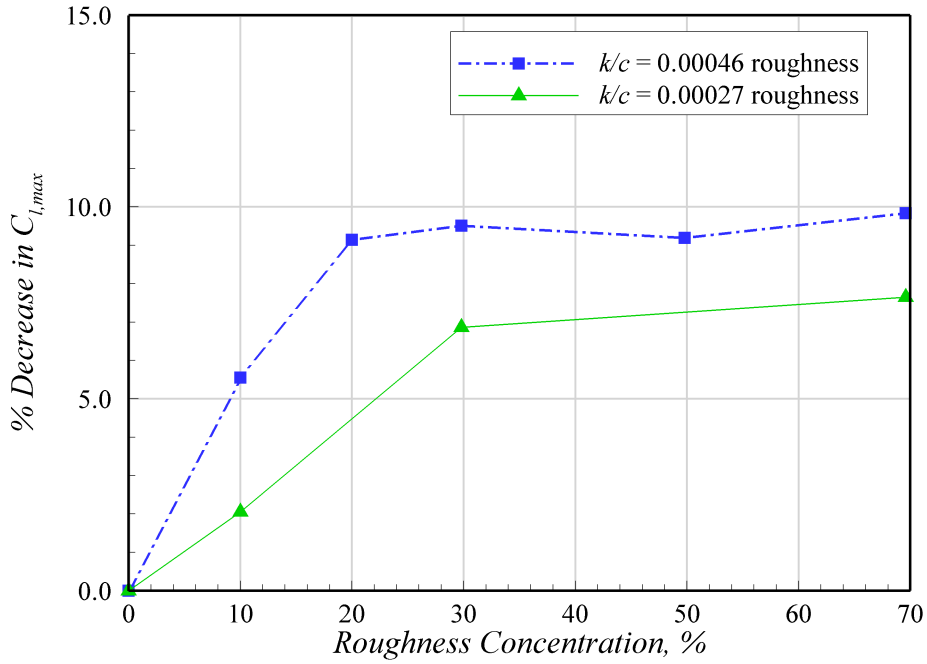

Fig. 2.4 Effect of roughness concentration as a percent reduction in $C_{l,max}$ between an iced and clean NLF-0414 airfoil. Data from Jackson.[24]

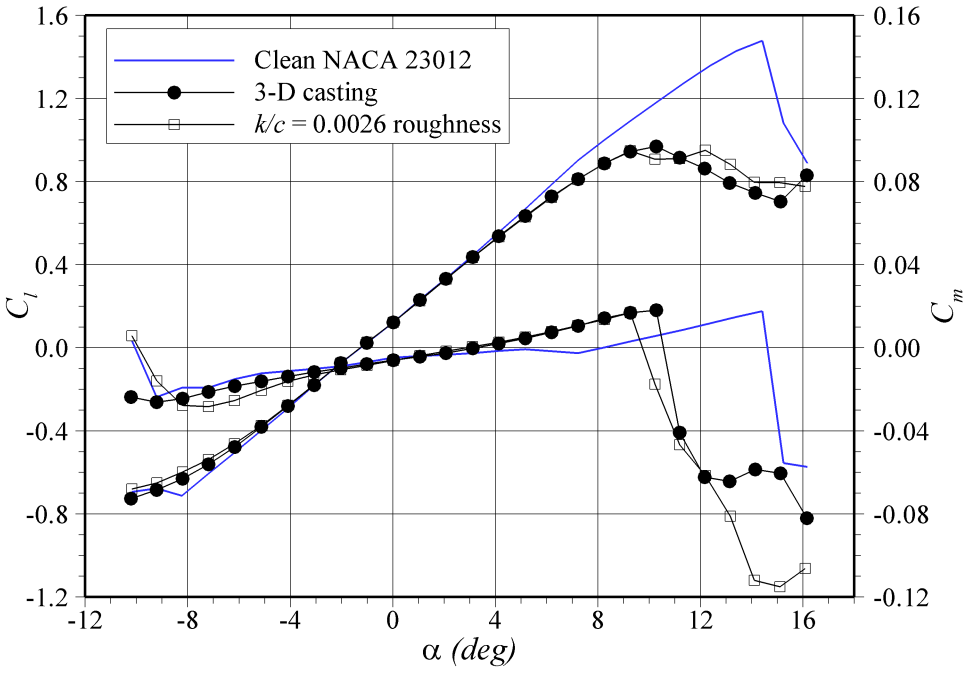

(a)

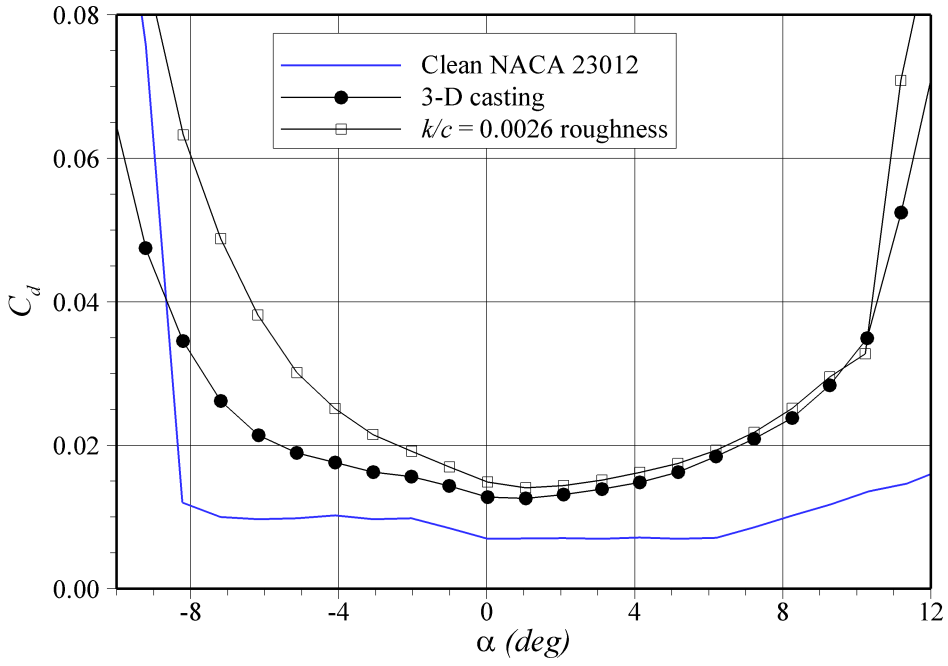

(b)

Fig. 2.5 Comparison between ice roughness casting and simulated ice roughness on an 18-inch NACA 23012 airfoil.[5] $Re = 1.8 \text{ x } 10^6$, $M = 0.18$

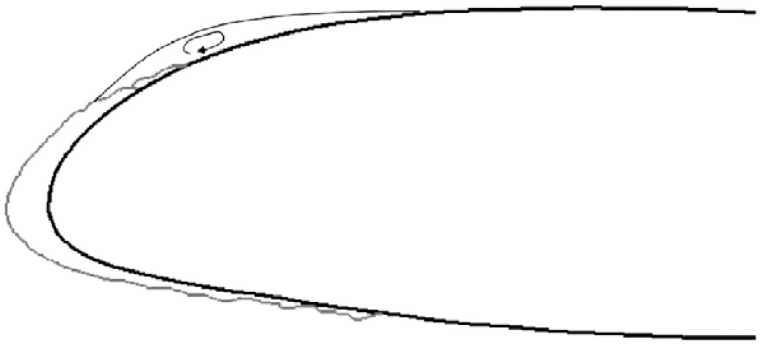

Fig. 2.6 Illustration of a laminar short bubble which may form at the junction between a streamwise-ice accretion and the airfoil.[4]

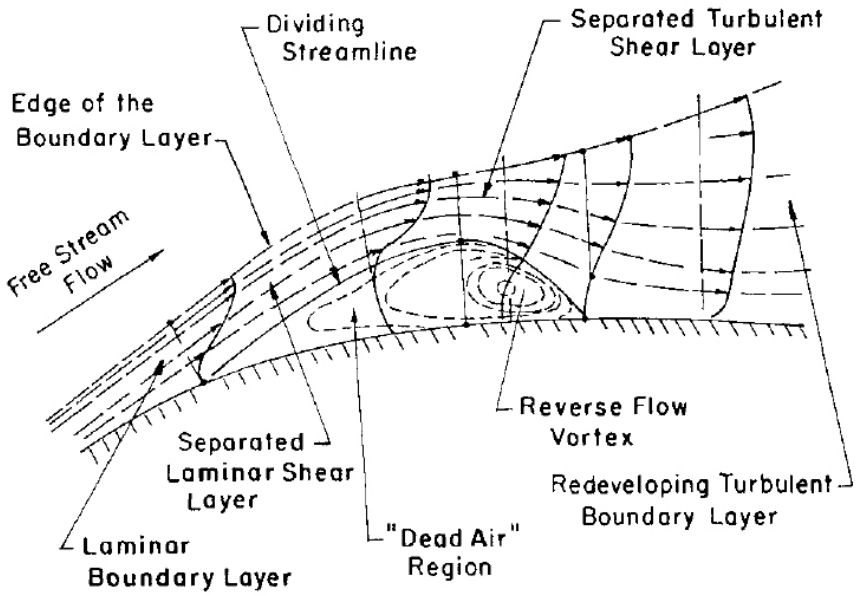

Fig. 2.7 Schematic of a laminar separation bubble.[110]

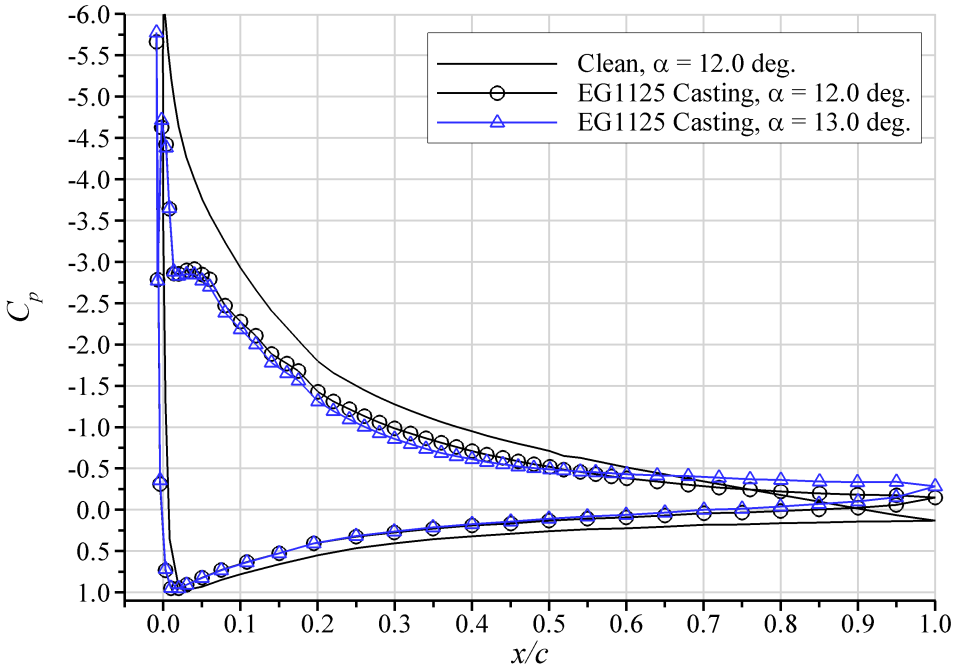

Fig. 2.8 Surface pressure distribution of a NACA 23012 airfoil with a streamwise-ice casting at Re = 12.0 x 10^6 and M = 0.20. Data from Broeren.[29]

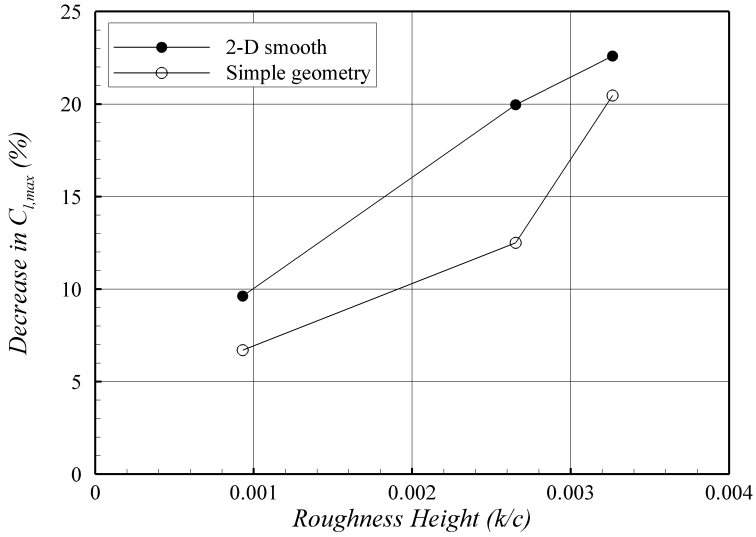

(a)

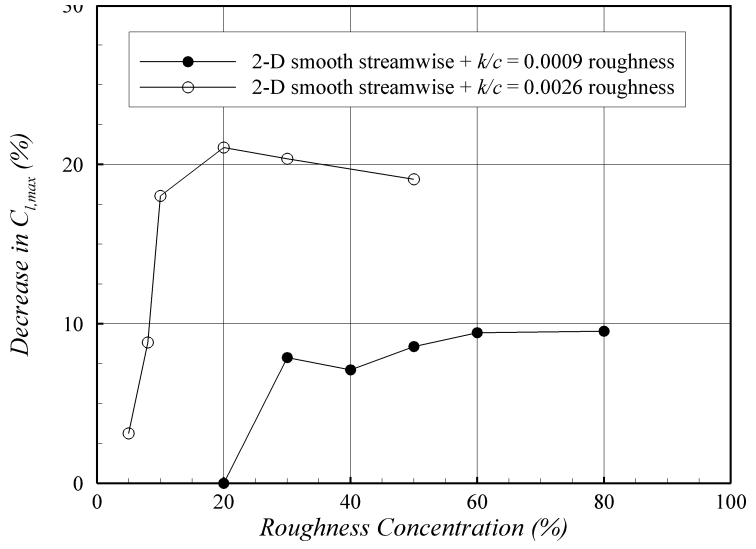

(b)

Fig. 2.9 (a) Effect of surface roughness height on $C_{l,max}$ of a NACA 23012 airfoil with 2-D smooth and simple-geometry streamwise-ice simulations, and (b) effect of roughness concentration on $C_{l,max}$ of a 2-D smooth streamwise-ice simulation. (adapted from Busch[5]) The percent degradation in $C_{l,max}$ for these simulations is shown relative to $C_{l,max}$ of the appropriate simulation with no grit roughness. The roughness was applied from x/c = -0.004 to 0.01 on the upper surface and from x/c = 0.02 to 0.13 on the lower surface at a concentration of 50% for the k/c = 0.0033 and 0.0026 grit roughness and 80% for the k/c = 0.0009 roughness. Data were obtained at Re = 1.8 x 10^6 and M = 0.18.

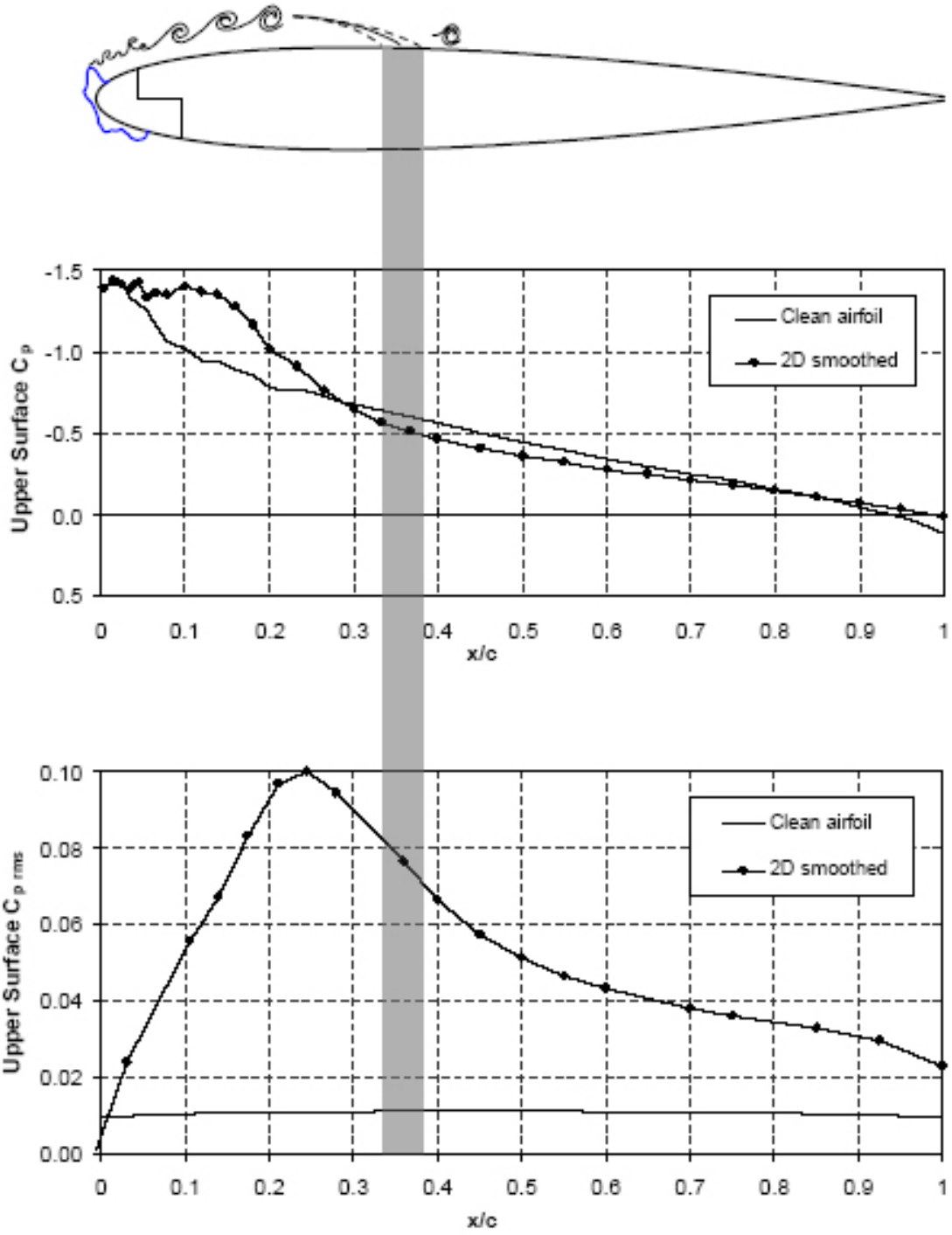

Fig. 2.10 Schematic of flowfield behind a 2-D smooth horn-ice simulation and corresponding mean and RMS C_p distribution on upper surface of NACA 0012 airfoil.[33] Data obtained at $\alpha = 4$ deg., $Re = 1.8$ x 10^6, and $M = 0.18$.

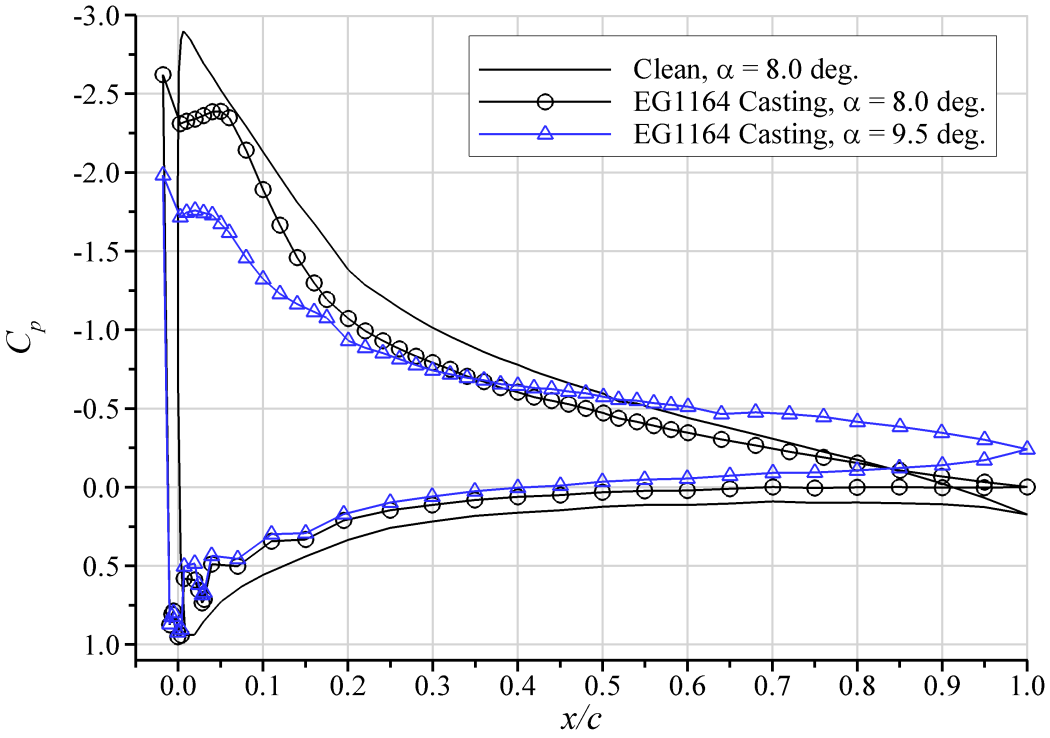

Fig. 2.11 Surface pressure distribution of a NACA 23012 airfoil with a horn-ice casting at Re = 12.0 x 10^6 and M = 0.20. Data from Broeren.[29]

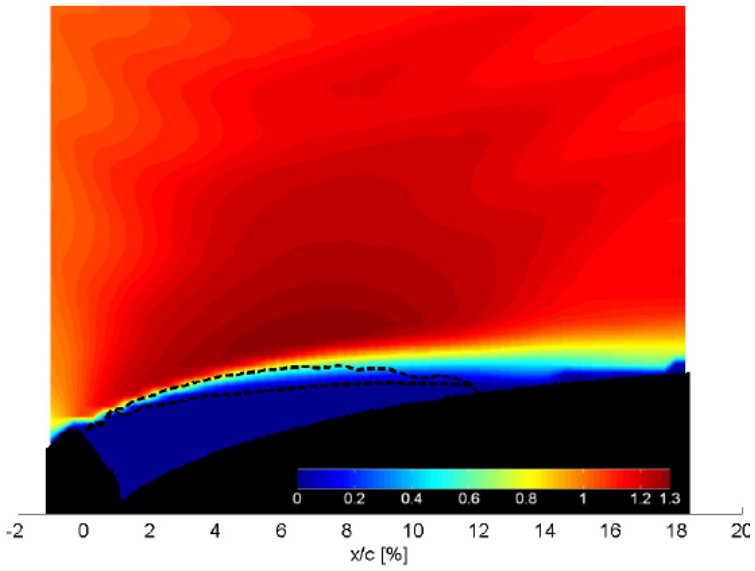

Fig. 2.12 Mean streamwise velocity non-dimensionalized by freestream velocity around a 2D-smooth horn-ice simulation on a NACA 0012 airfoil at α = 0 deg., Re = 0.9 x 10^6, and M = 0.20.[36] The mean separation and stagnation streamlines are indicated by the upper and lower dashed lines, respectively.

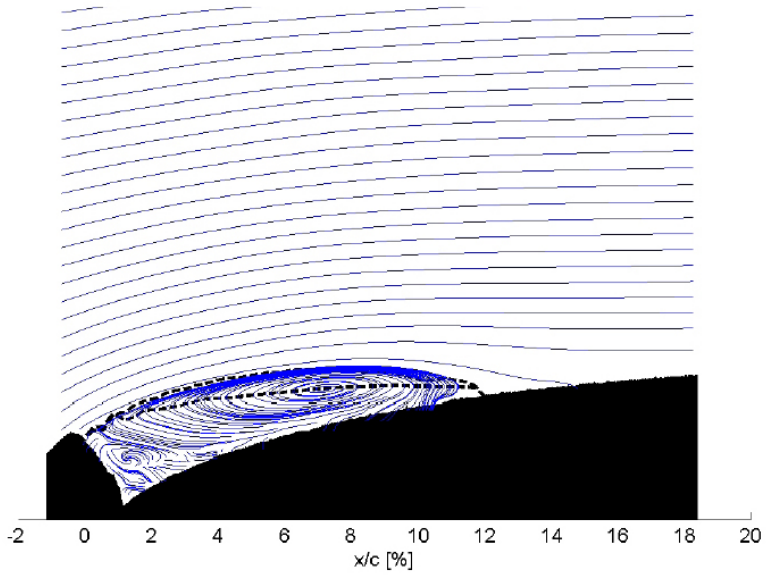

Fig. 2.13 Mean streamlines around a 2D-smooth horn-ice simulation on a NACA 0012 airfoil at $\alpha = 0$ deg., $Re = 0.9$ x 10^6, and $M = 0.20$.[36] The mean separation and stagnation streamlines are indicated by the upper and lower dashed lines, respectively.

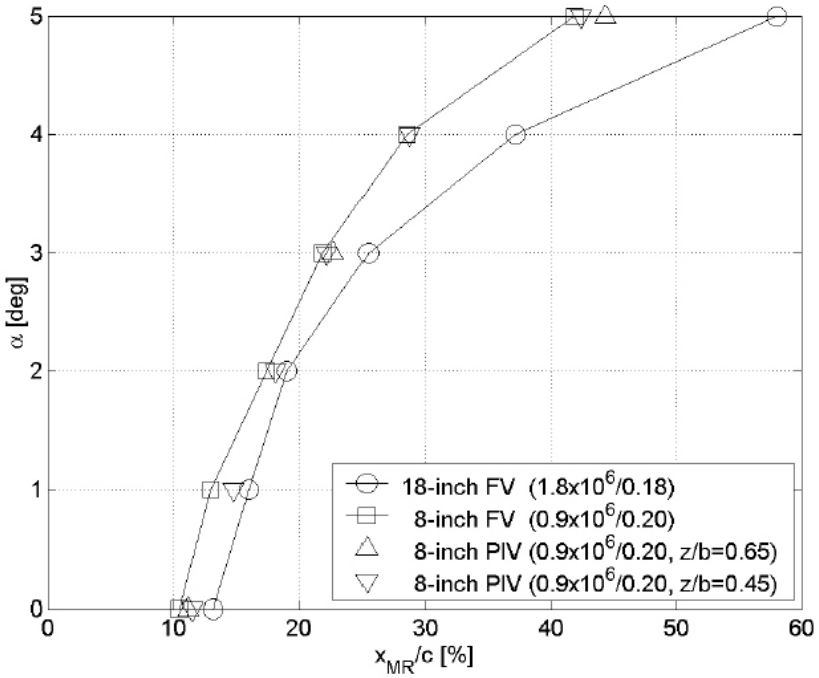

Fig. 2.14 Comparison of mean separation bubble reattachment location at various angles of attack downstream of a 2D-smooth horn-ice simulation on a NACA 0012 airfoil.[36] The 18-inch chord airfoil data were obtained by Gurbacki[33] using surface oil-flow visualization and the 8-inch chord airfoil data were obtained by Jacobs[37] using both surface oil-flow visualization and PIV at two spanwise stations.

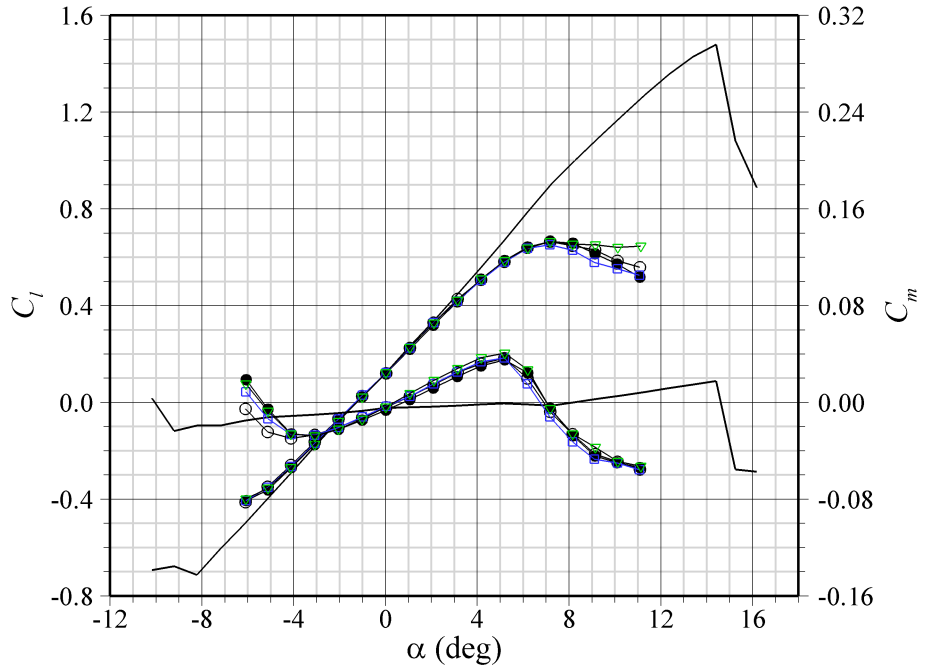

(a)

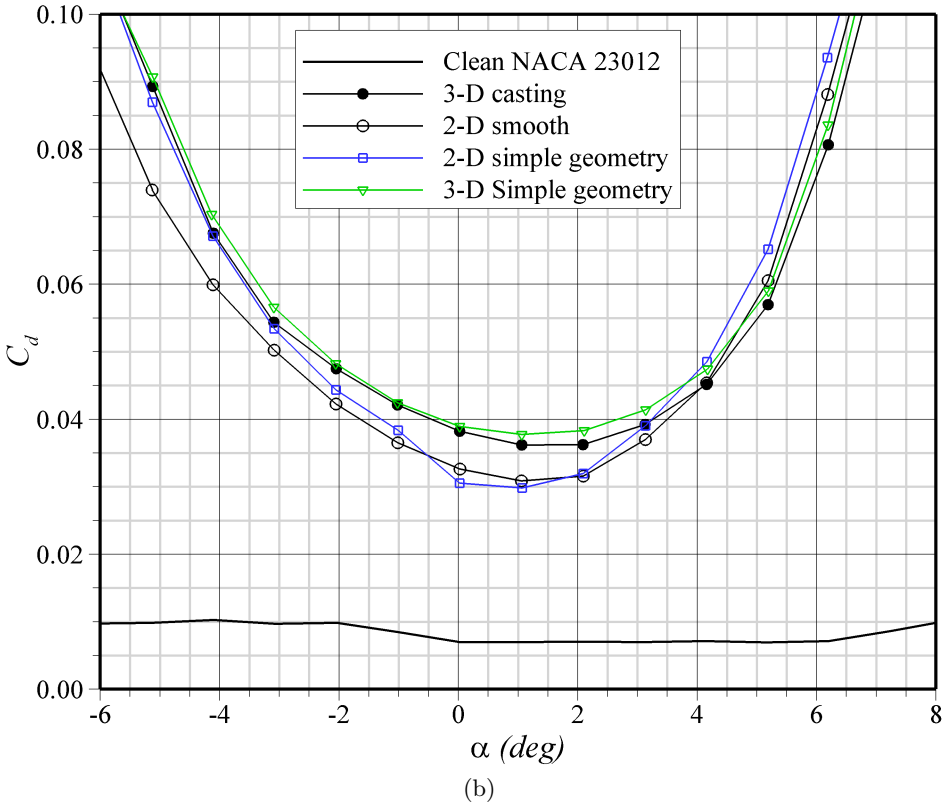

(b)

Fig. 2.15 Effects of 2-D smooth, 2-D simple geometry, and 3-D simple geometry simulations with a horn-ice casting on (a) C_l, C_m, and (b) C_d of a NACA 23012 airfoil at $Re = 1.8$ x 10^6 and $M = 0.18$, adapted from Busch.[5]

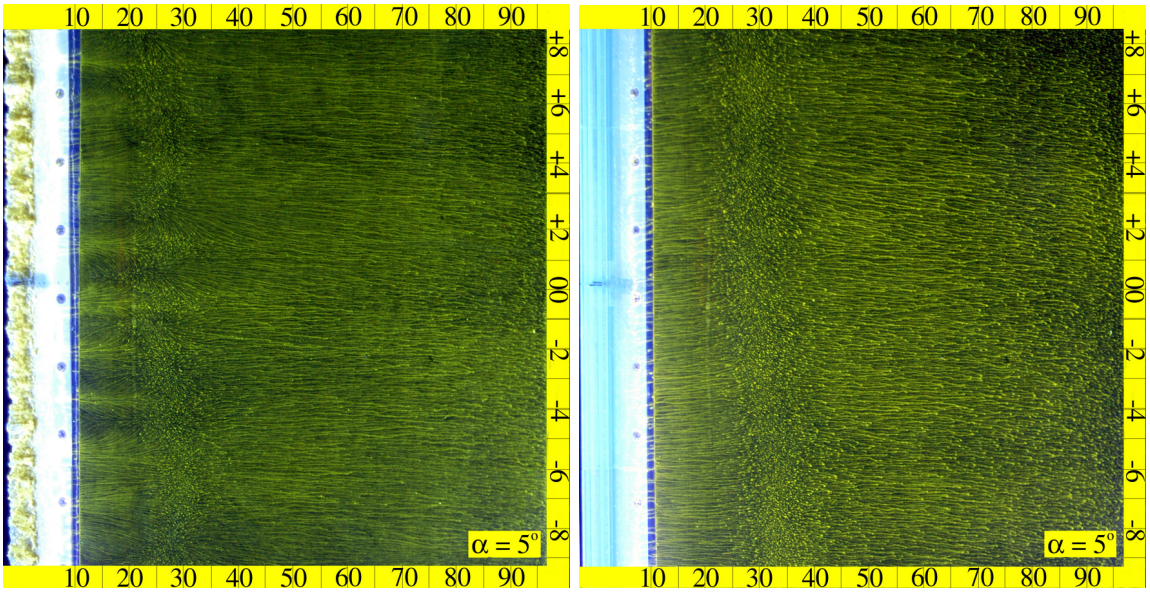

Fig. 2.16 Comparison of the surface flowfield behind a (a) horn-ice accretion casting and a (b) 2-D smooth horn-ice simulation. The mean separation bubble reattachment line has been highlighted. Re = 1.8 x 10^6 and M = 0.18.[6]

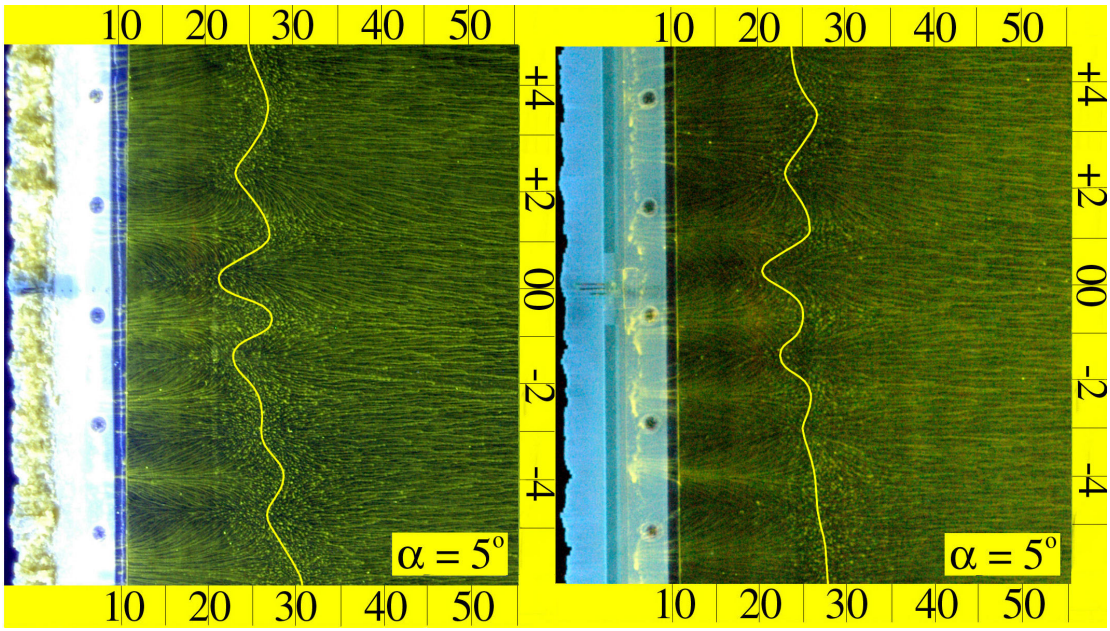

Fig. 2.17 Comparison of the surface flowfield behind an ice accretion casting (left) and a simple-geometry simulation with spanwise variation (right). This image is of the center third of the airfoil model only. The mean separation bubble reattachment line has been highlighted. Re = 1.8 x 10^6 and M = 0.18.[6]

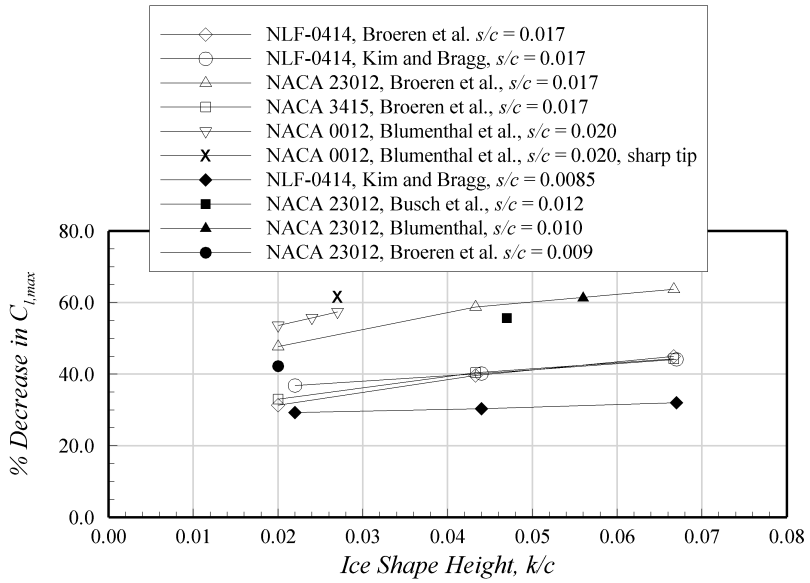

Fig. 2.18 Effect of horn height on iced-airfoil C_l,max for various airfoils. Data from Broeren et al.,[94] Kim and Bragg,[27] Blumenthal et al.,[30] Busch et al.,[1] Blumenthal,[38] and Broeren et al.[9]

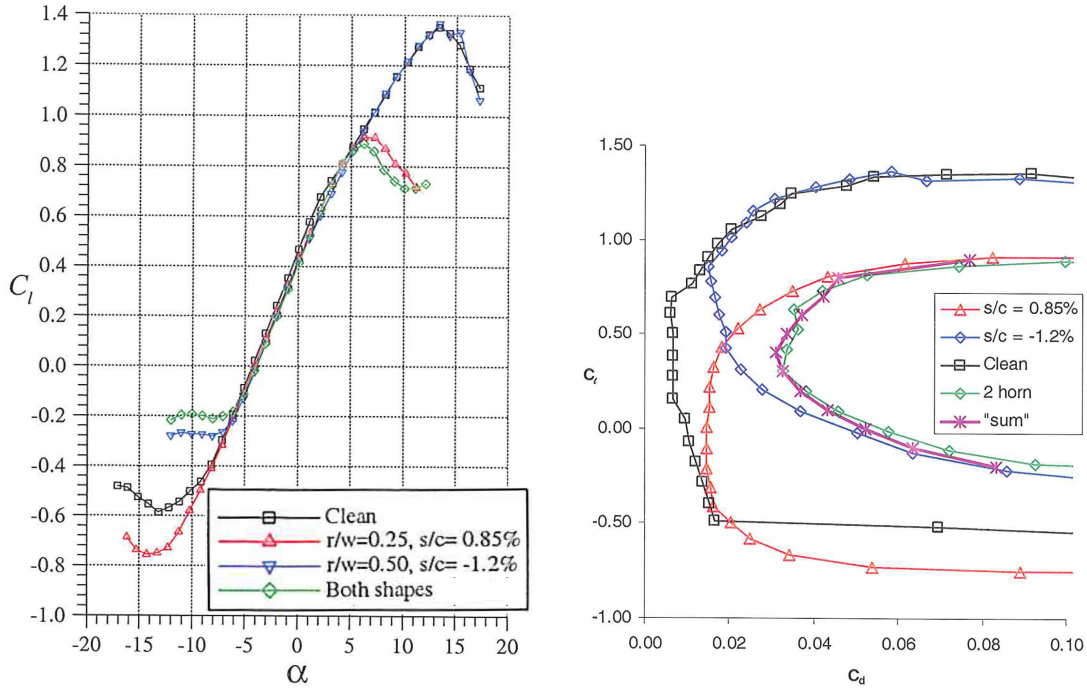

(a) (b)

Fig. 2.19 Effect of $k/c = 0.044$ upper and lower surface horns on NLF-0414 airfoil C_l and C_d at $Re = 1.8$ x 10^6 and $M = 0.18$.[27]

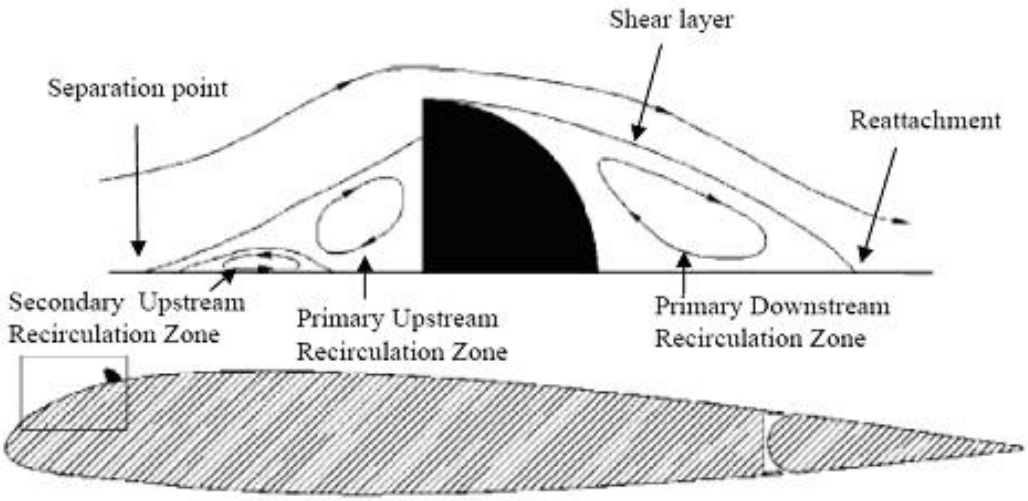

Fig. 2.20 Schematic of flowfield about a simple-geometry simulation of a ridge-ice accretion, adapted from Lee et al.[111]

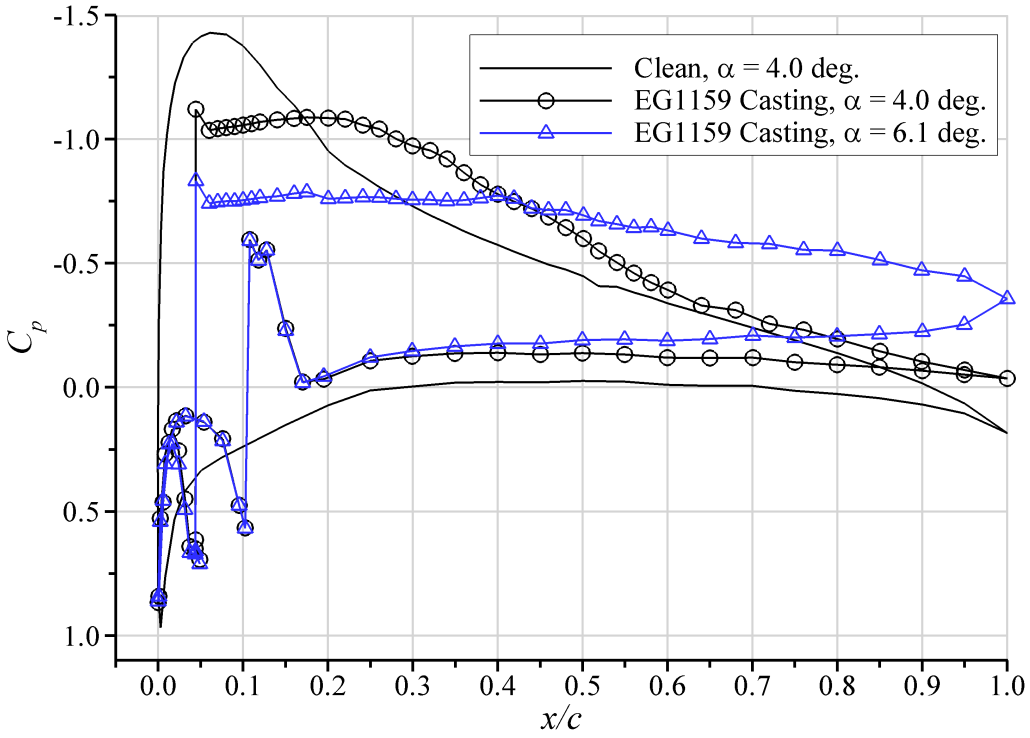

Fig. 2.21 Surface pressure distribution of a NACA 23012 airfoil with a tall spanwise-ridge ice casting at Re = 12.0 x 10^6 and M = 0.20. Data from Broeren.[29]

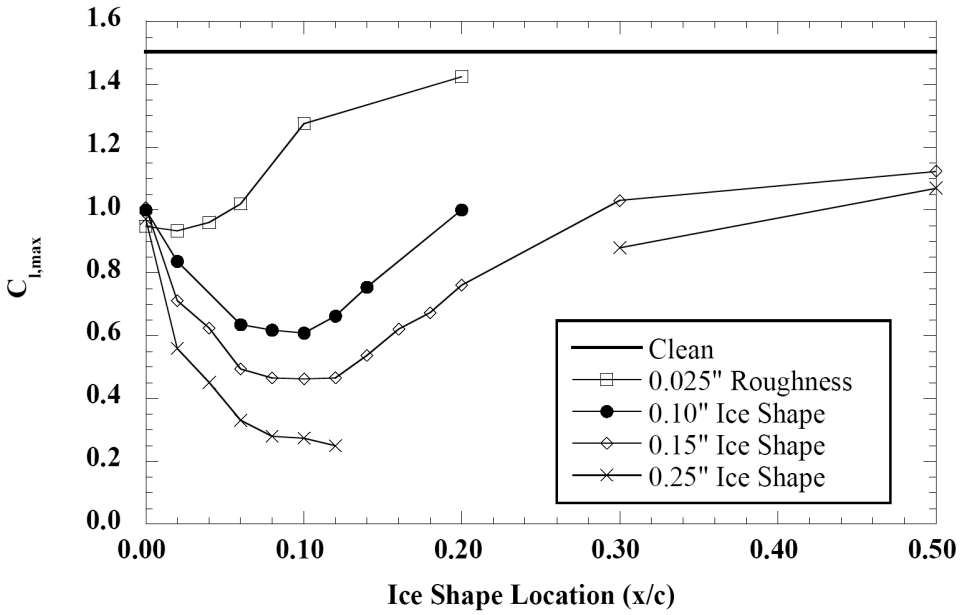

Fig. 2.22 Effect of simple-geometry ridge height and location on $C_{l,max}$ of a NACA 23012m airfoil.[18]

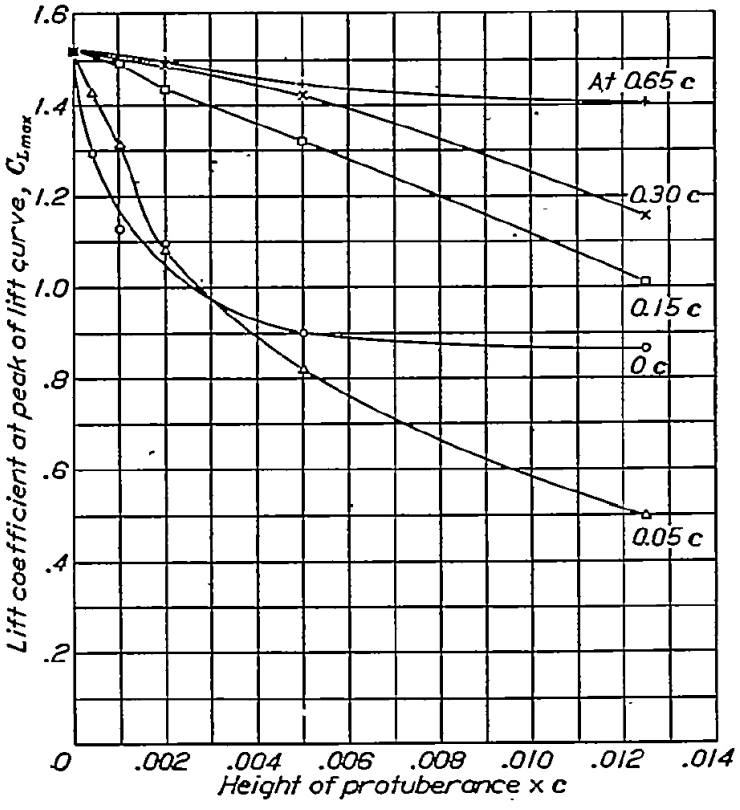

Fig. 2.23 Effect of spoiler height and location on $C_{l,max}$ of a NACA 0012 airfoil.[51]

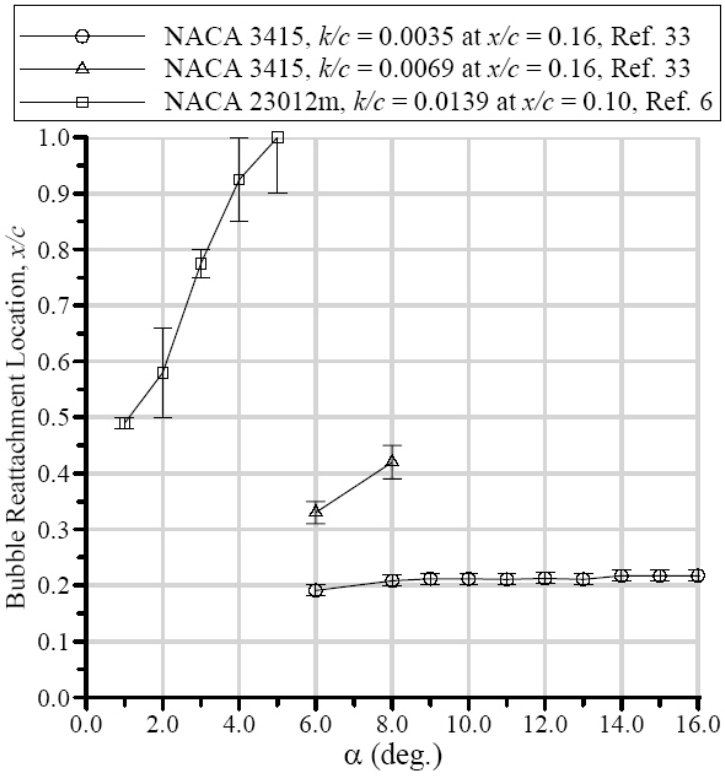

Fig. 2.24 Mean separation bubble reattachment location for two tall ridge-ice simulations (NACA 3415, $k/c = 0.0069$ and NACA 23012m, $k/c = 0.0139$) and a short ridge-ice simulation (NACA 3415, $k/c = 0.0035$).[15] Data taken by Lee and Bragg[50] and Whalen[53] at $Re = 1.8$ x 10^6 and $M = 0.18$.

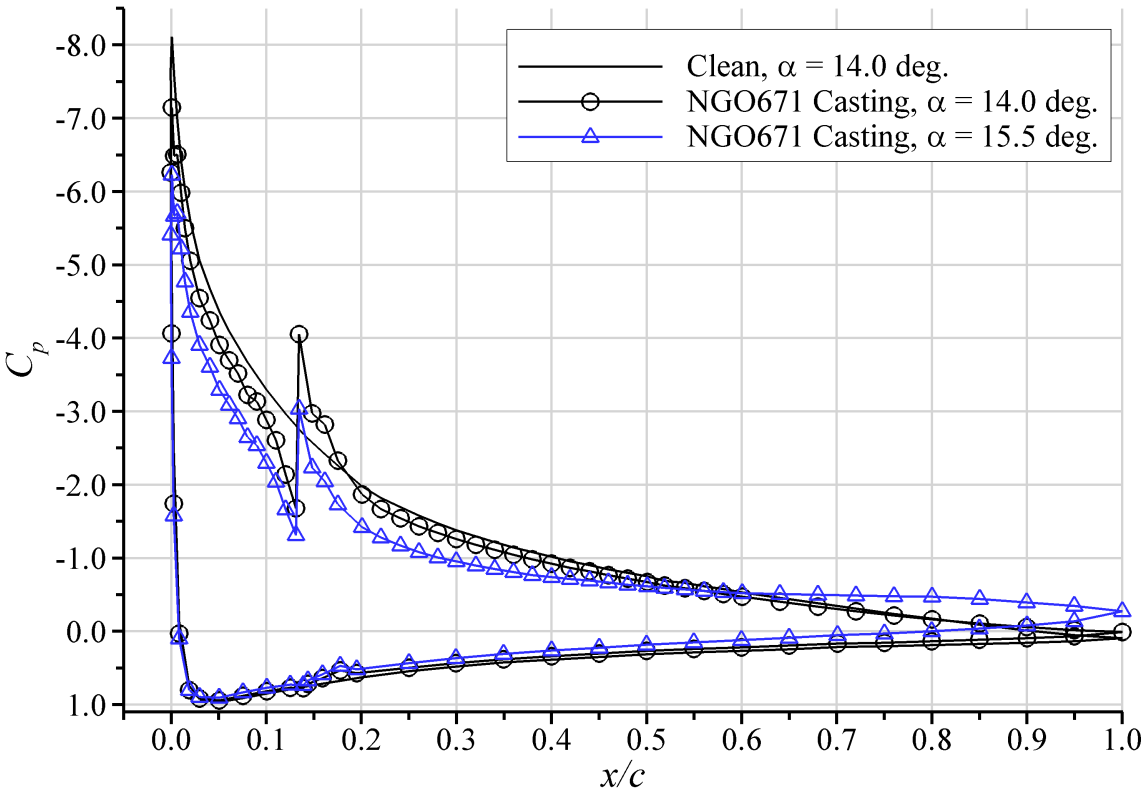

Fig. 2.25 Surface pressure distribution of a NACA 23012 airfoil with a short spanwise-ridge ice casting at Re = 12.0 x 10^6 and M = 0.20.

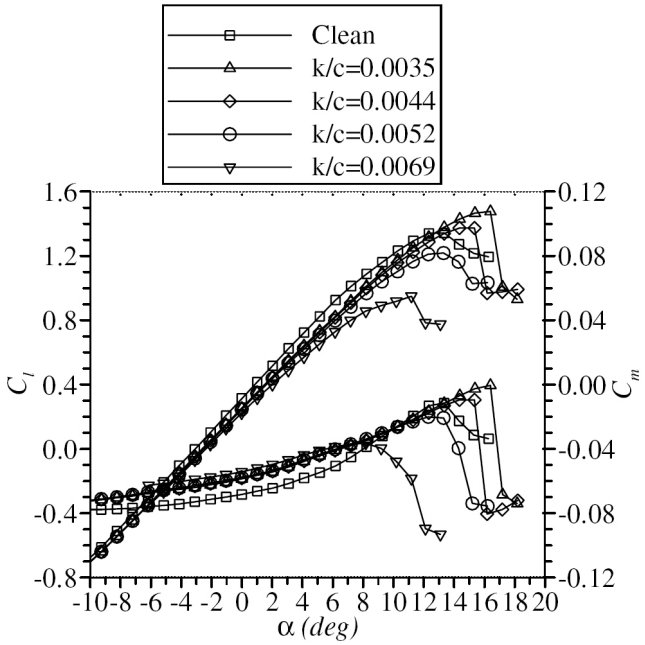

Fig. 2.26 Effect of short-ridge height on the aerodynamic performance of the NACA 3415 airfoil.[49] In each case, the ridge was located at x/c = 0.16. The data were obtained at Re = 1.8 x 10^6 and M = 0.18.

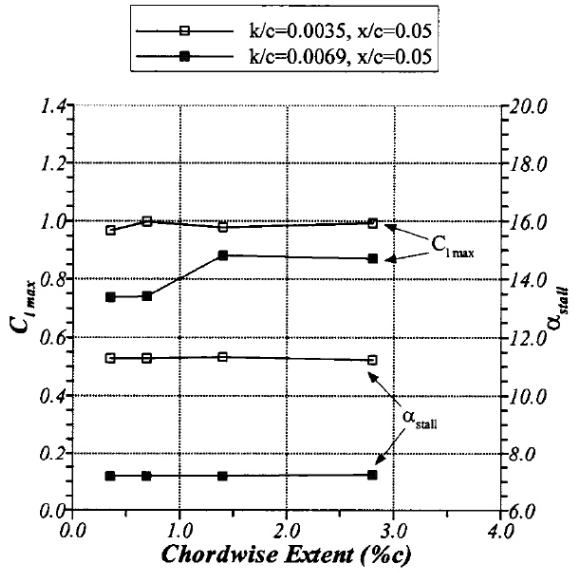

Fig. 2.27 Effect of short-ridge chordwise extents on the $C_{l,max}$ of the NACA 23012 airfoil.[53] In each case, the ridge was located at $x/c = 0.10$. The data were obtained at $Re = 1.8$ x 10^6 and $M = 0.18$.

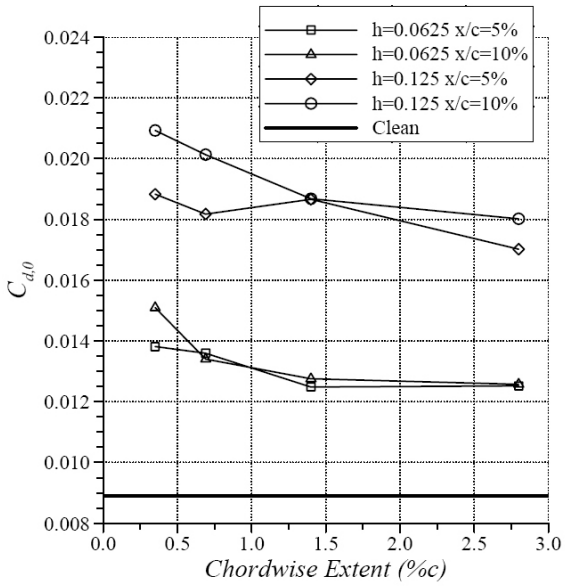

Fig. 2.28 Effect of short-ridge chordwise extents on the zero angle of attack C_d of the NACA 23012 airfoil.[54] The non-dimensional ridge heights were $k/c = 0.0035$ and 0.0069 for the 0.0625-inch and 0.125-inch ridges, respectively. The data were obtained at $Re = 1.8$ x 10^6 and $M = 0.18$.

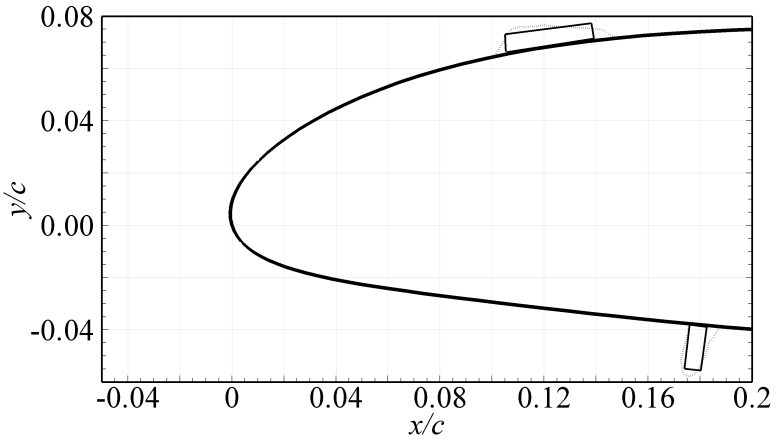

(a)

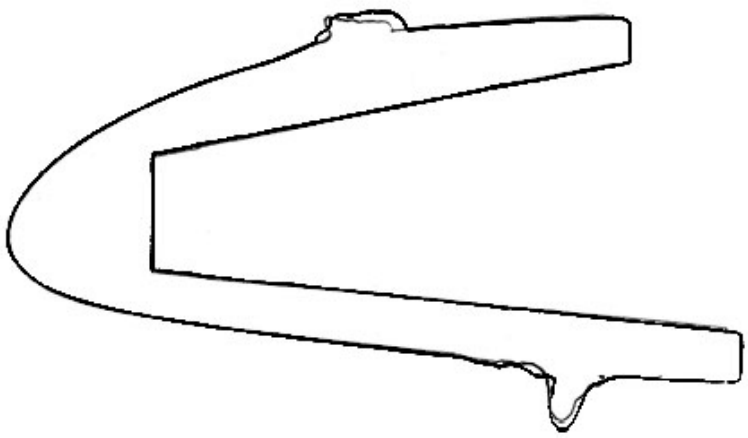

(b)

Fig. 2.29 Comparison of (a) 2-D smooth and simple-geometry simulations of a short spanwise-ridge ice accretion[7] and (b) tracings of the same ridge-ice accretion at two additional spanwise stations.[5]

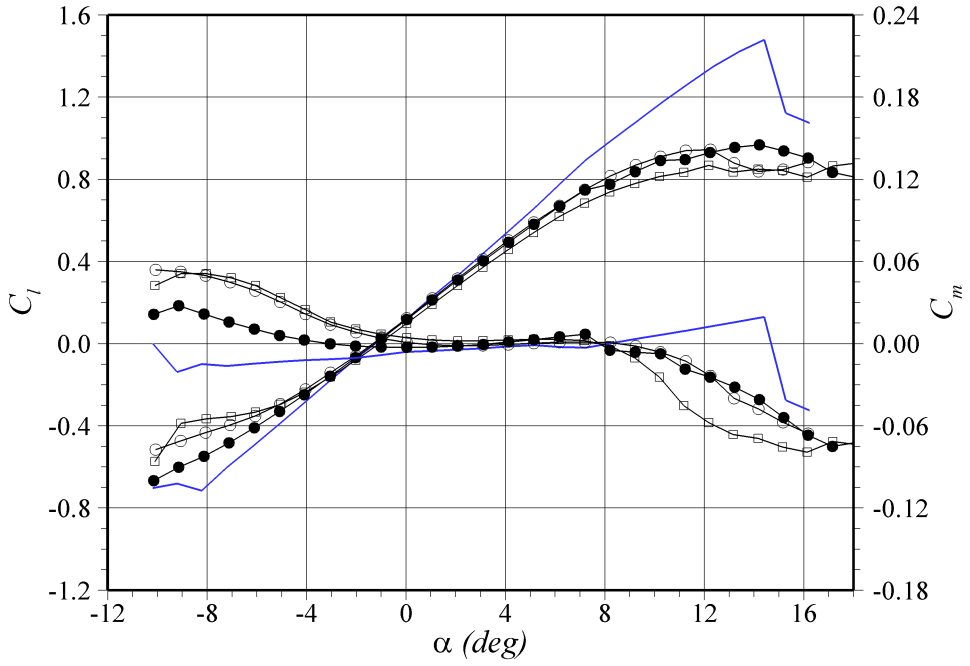

(a)

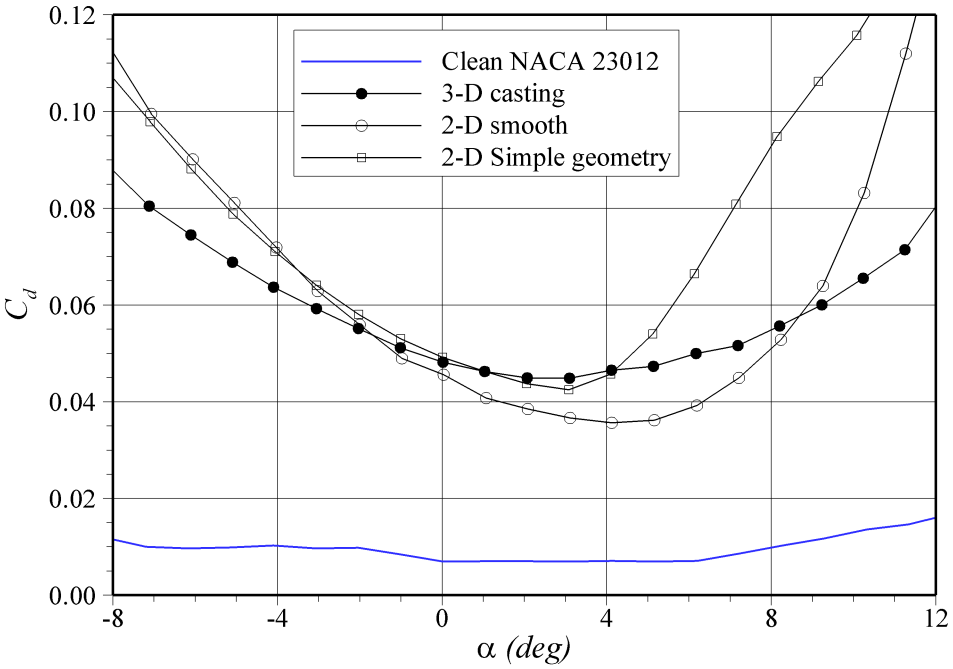

(b)

Fig. 2.30 Comparison of aerodynamic performance among a short ridge casting and 2-D smooth and simple-geometry simulations.[7]

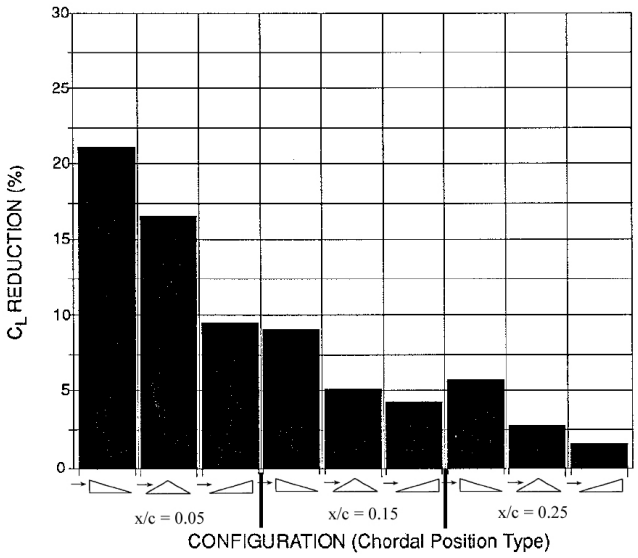

(a)

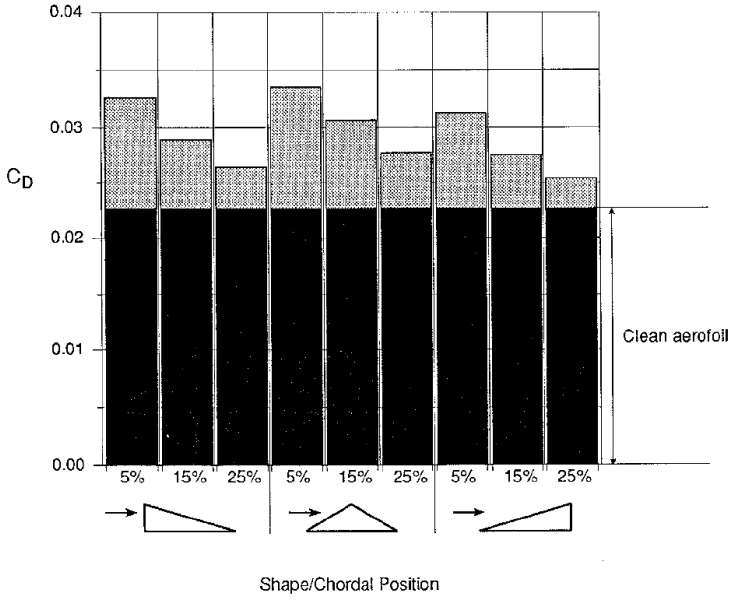

(b)

Fig. 2.31 Degradation in (a) $C_{l,max}$ and (b) C_d at $\alpha = 0$ deg. of NACA 0012 airfoil due to $k/c = 0.035$ simple-geometry short-ridge simulations of various shapes located at different chordwise positions. Adapted from Calay et al.[55]

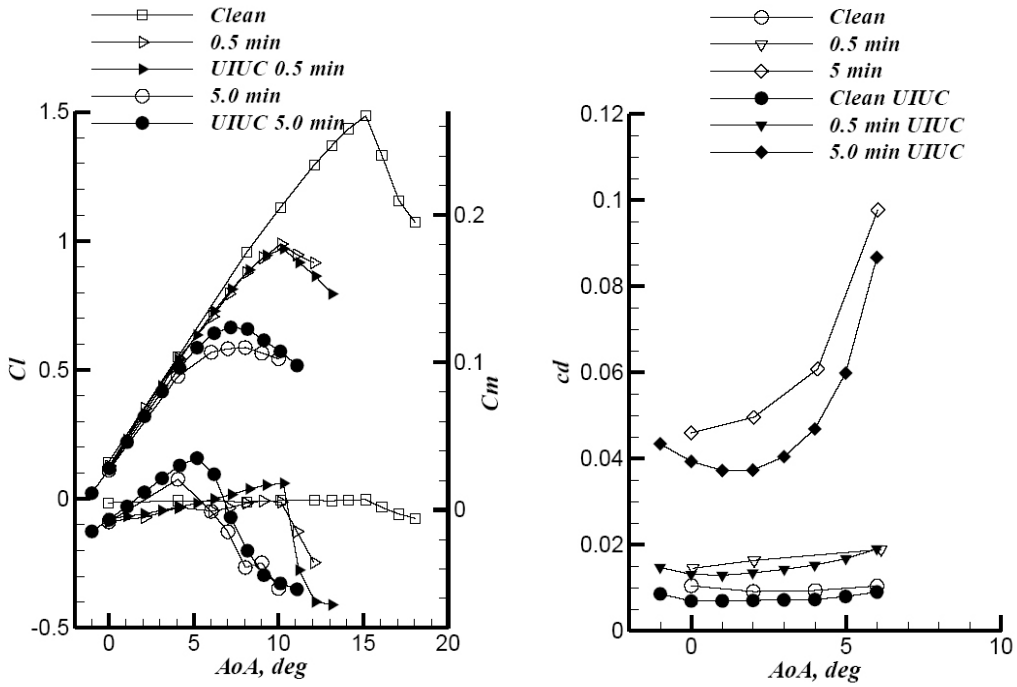

(a) (b)

Fig. 2.32 Comparison of (a) C_l, C_m, and (b) C_d iced-airfoil data taken in the NASA Glenn Icing Research Tunnel with ice casting data obtained in the University of Illinois at Urbana-Champaign (UIUC) low-speed aerodynamic wind tunnel for 0.5-min ice roughness and 5.0-min horn-ice accretions.[66] The IRT data were obtained at Re = 2.6 x 10^6 and M = 0.235, and the LSWT data were obtained at Re 1.8 x 10^6 and M = 0.18.

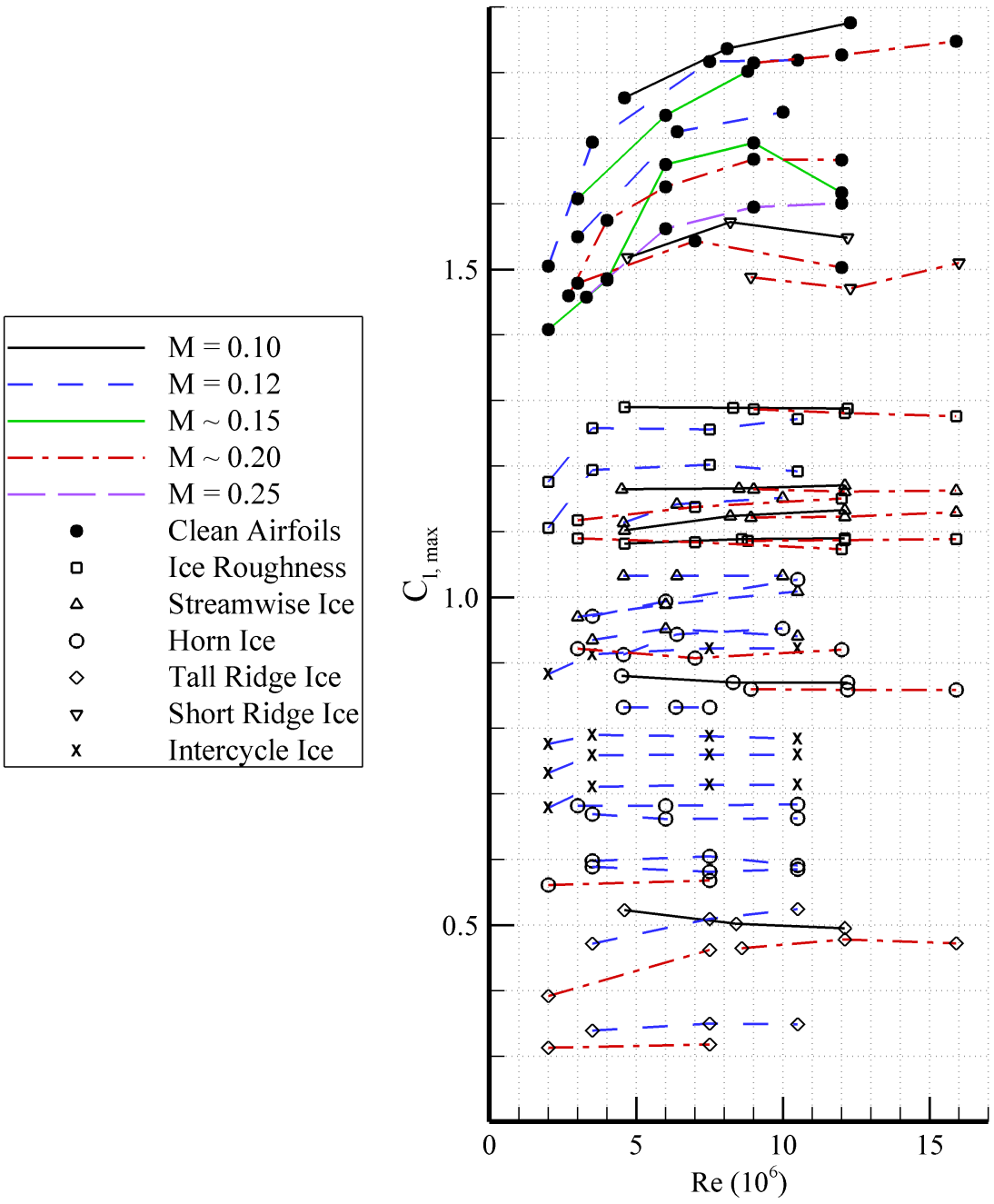

Fig. 2.33 Effect of Reynolds number at constant Mach number on $C_{l,max}$ for different types of ice accretion. Data from Broeren et al.,,[9,15,58,94] Broeren and Bragg,,[92] Addy et al.,[48] Addy and Chung,[19] and Morgan et al.[112]

.

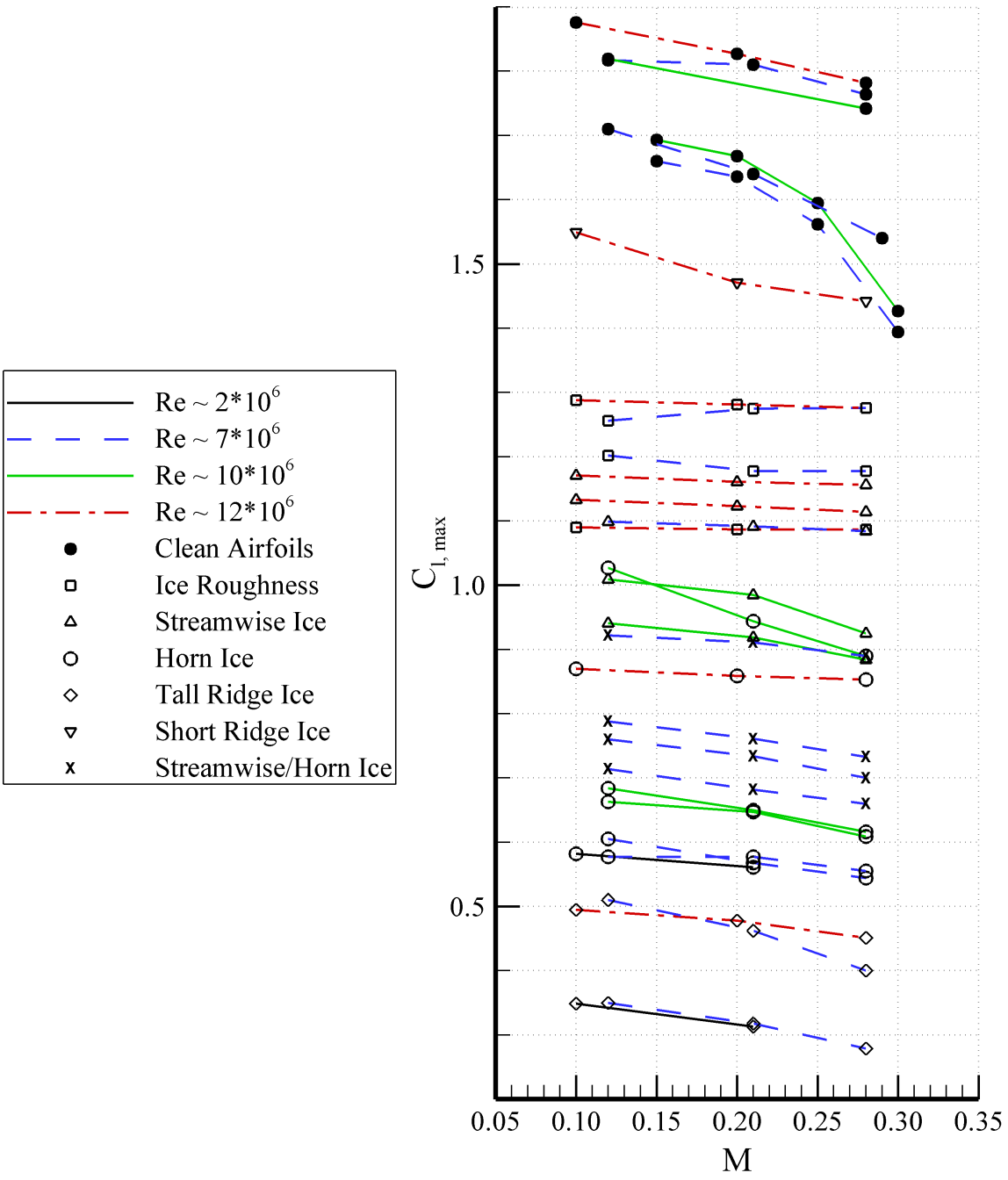

Fig. 2.34 Effect of Mach number at constant Reynolds number on $C_{l,max}$ for different types of ice accretion. Data from Broeren et al.,,[9,15,58,94] Broeren and Bragg,,[92] Addy et al.,[48] and Addy and Chung.[19]

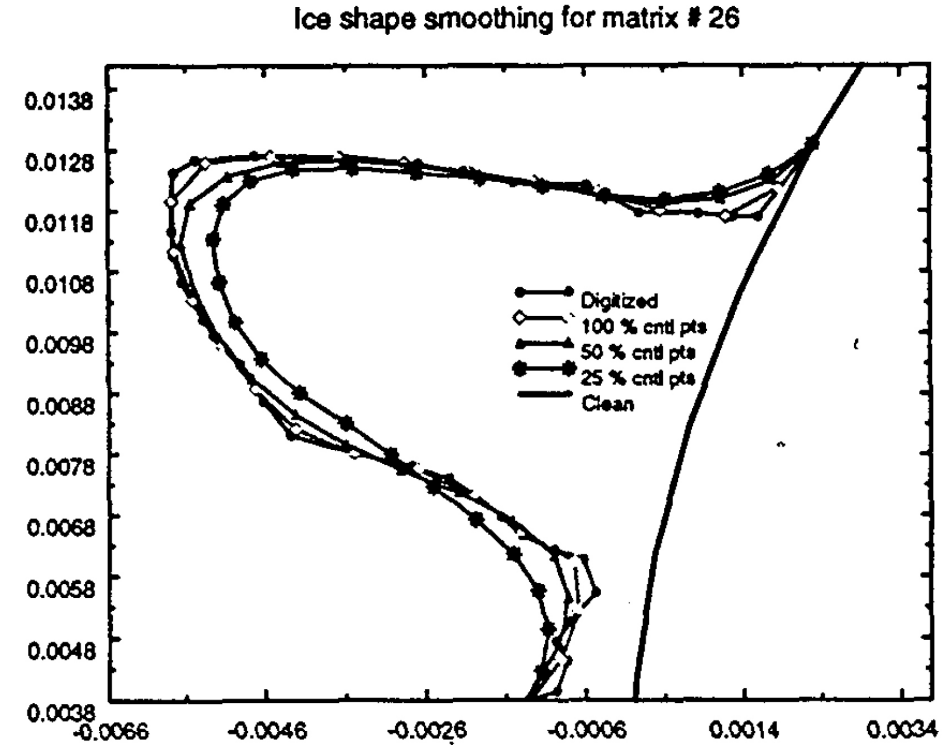

(a)

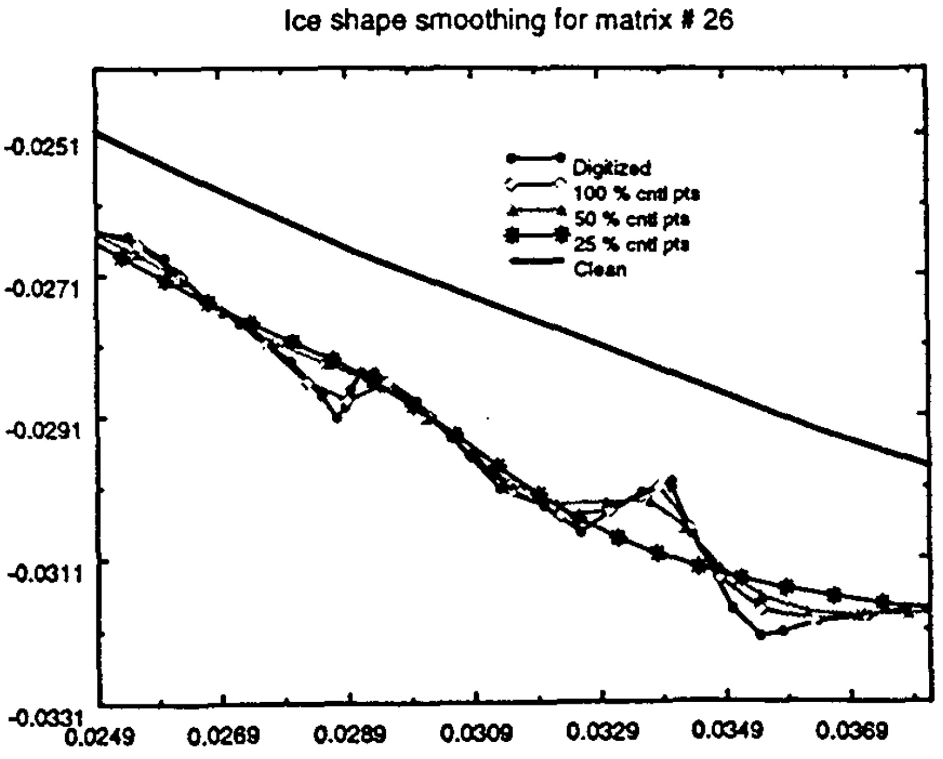

(b)

Fig. 2.35 Examples of different levels of smoothing applied to the upper and lower surface of a digitized tracing of a horn-ice accretion.[79]

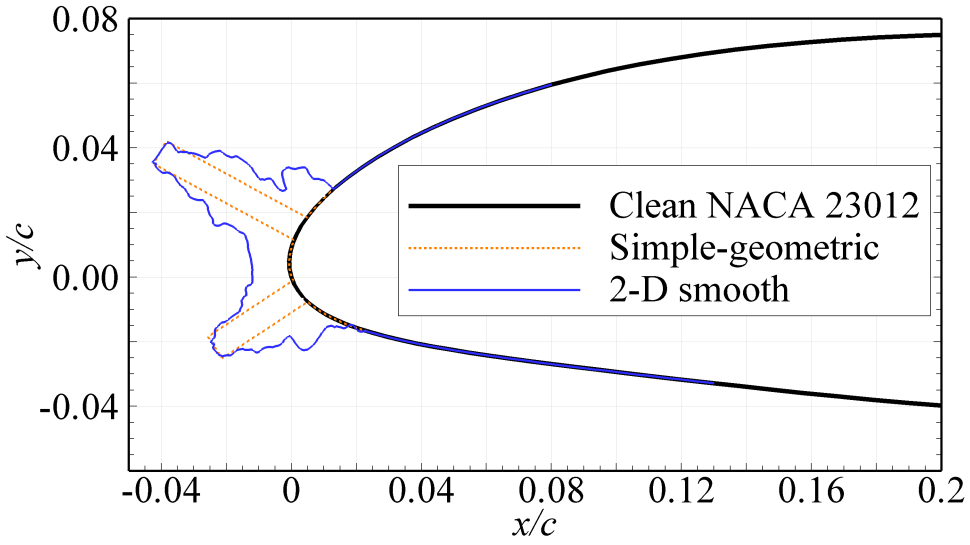

Fig. 2.36 Comparison of simple-geometry and 2-D smooth horn-ice simulations.[6] The 2D-smooth simulation cross section was formed from a tracing of a horn-ice accretion.

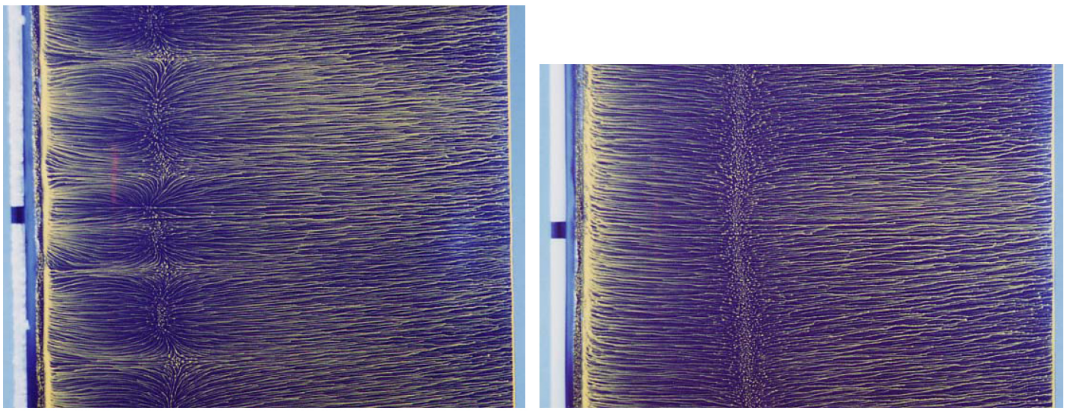

(a) (b)

Fig. 2.37 Fluorescent oil-flow visualization images of a horn-ice (a) casting and (b) 2-D smooth simulation on a NACA 0012 airfoil at $\alpha = 4$ deg. and $Re = 1.8$ x 10^6.[33]

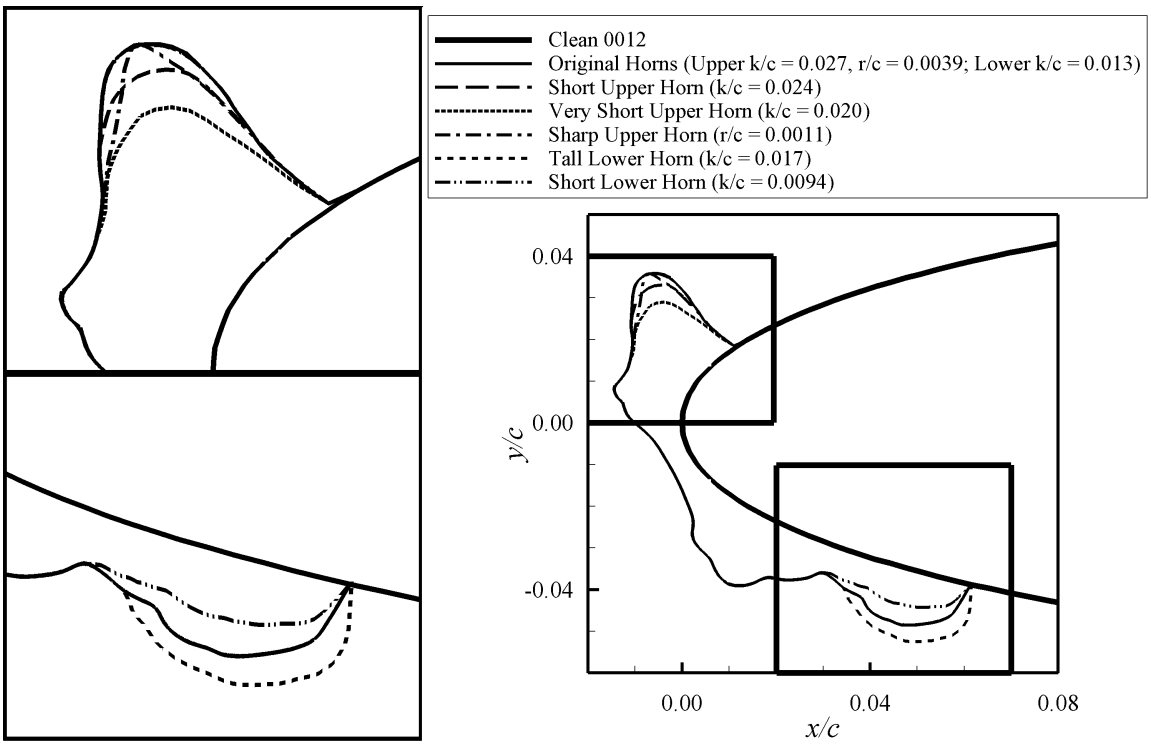

Fig. 2.38 Example of the variation in ice geometry that may result from taking tracings at different spanwise stations on a NACA 0012 airfoil.[30]

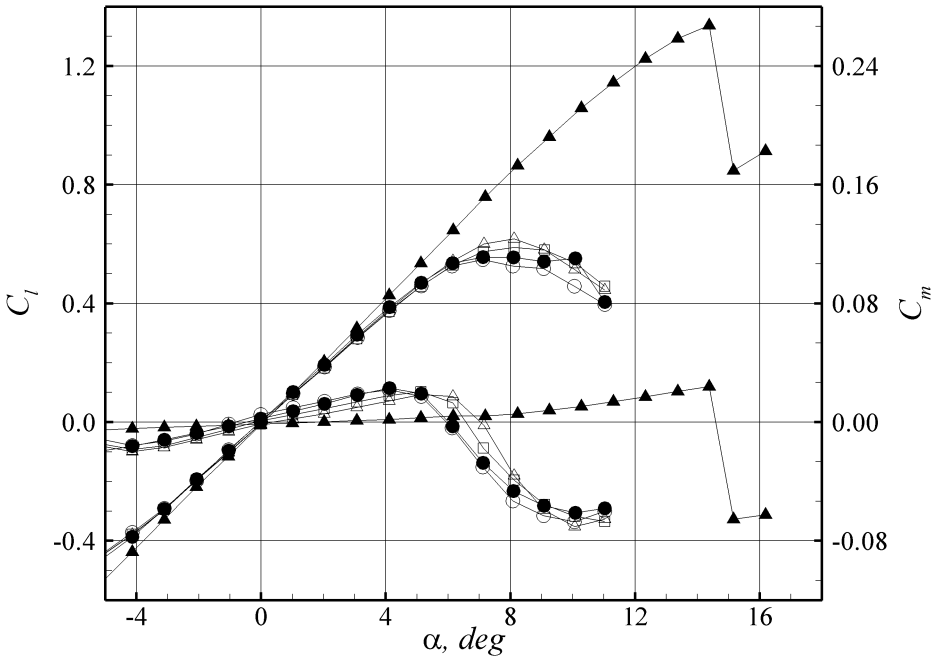

(a)

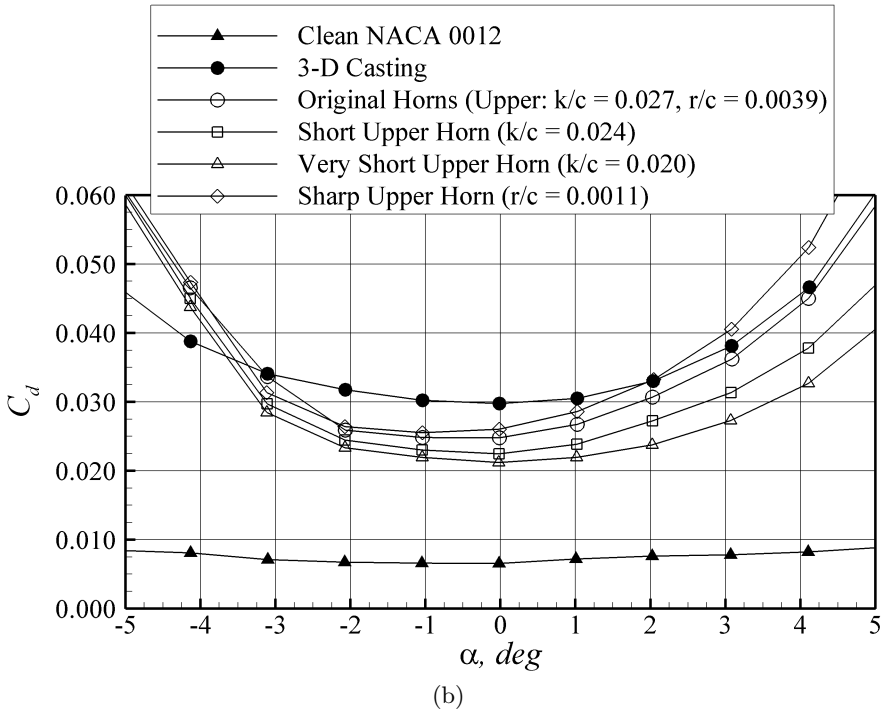

(b)

Fig. 2.39 Effects of minor variations in upper-surface horn geometry that result from different tracing locations on C_l, C_m, and C_d of a NACA 0012 airfoil.[30] Data obtained at Re = 1.8 x 10^6 and M = 0.18.

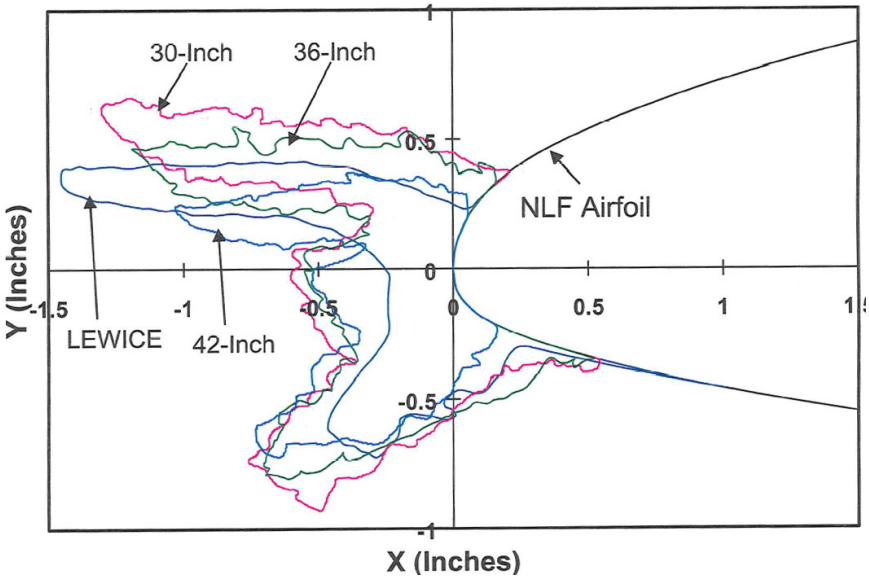

Fig. 2.40 Cross-sections of four 2-D smooth simulations investigated by Jackson on a NLF-0414 airfoil.[24] Three of the simulations were based on tracings of an ice accretion, and the fourth was based on LEWICE.

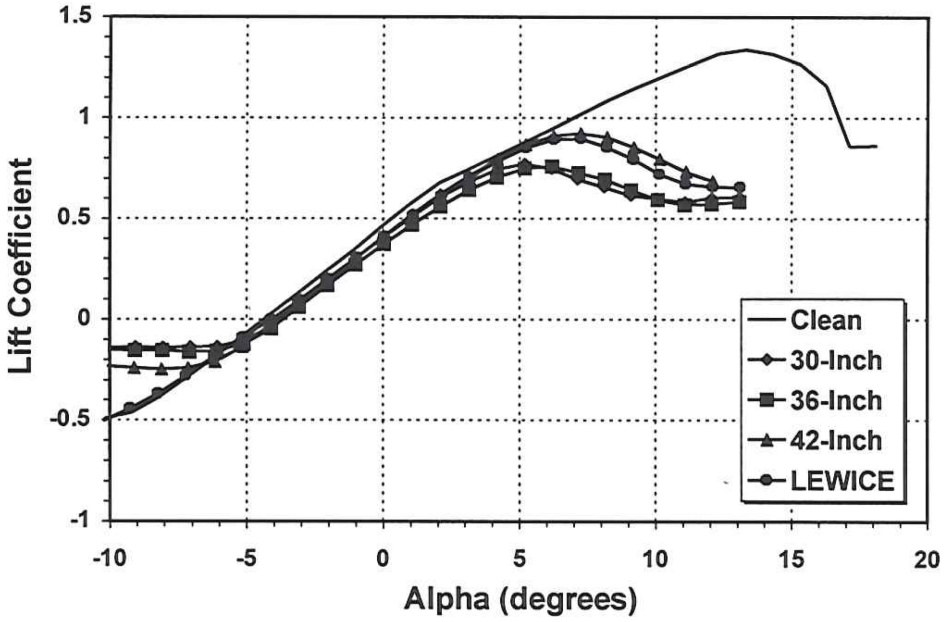

(a)

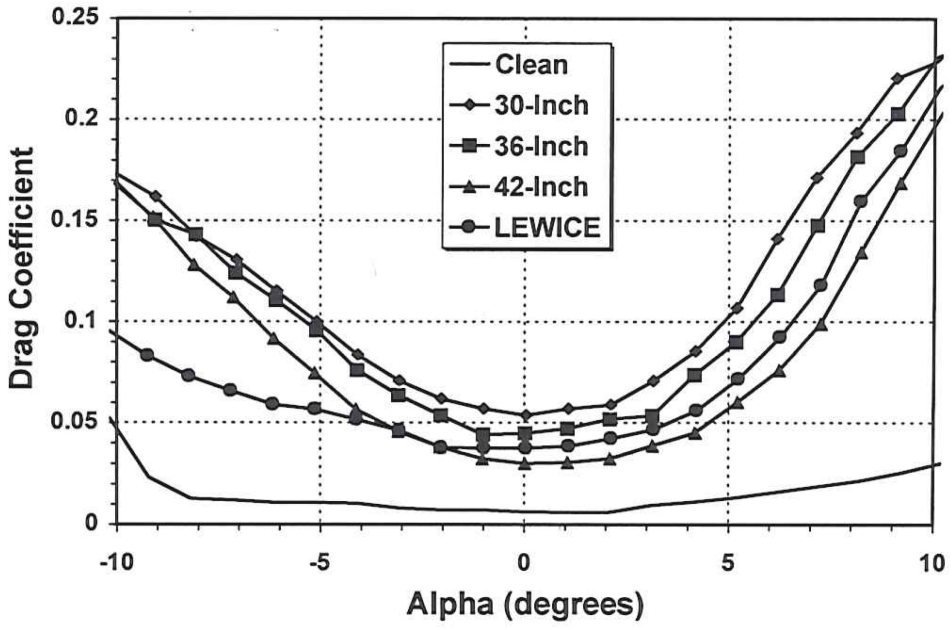

(b)

Fig. 2.41 Comparison of aerodynamic performance of NLF-0414 airfoil with the four 2-D smooth simulations investigated by Jackson.[24] $Re = 1.8 \text{ x } 10^6$, $M = 0.18$.

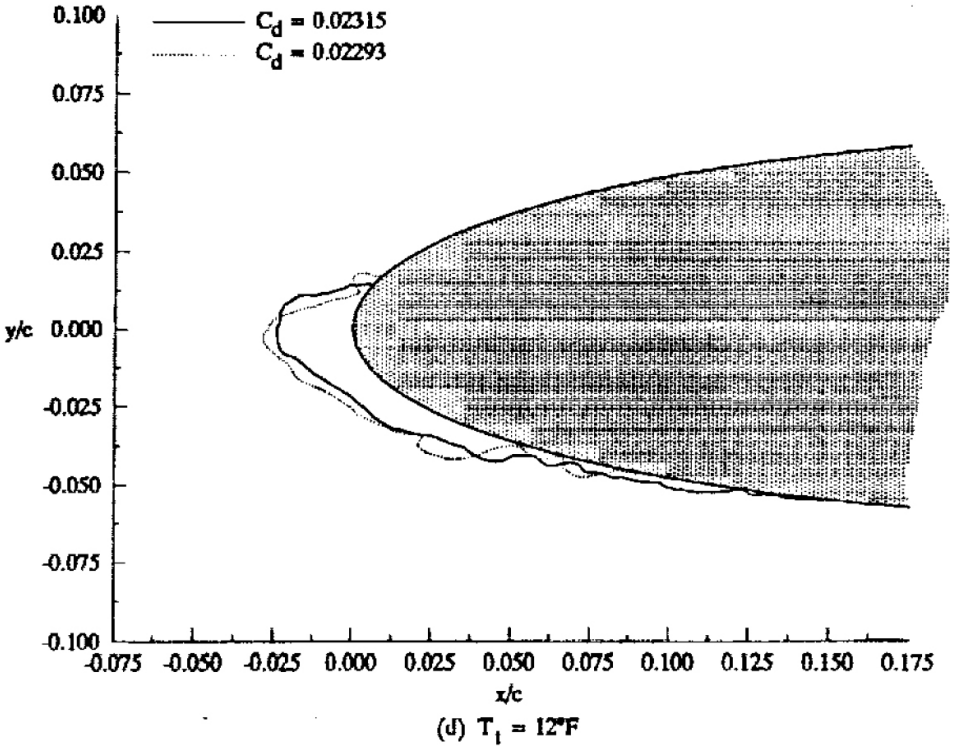

(a)

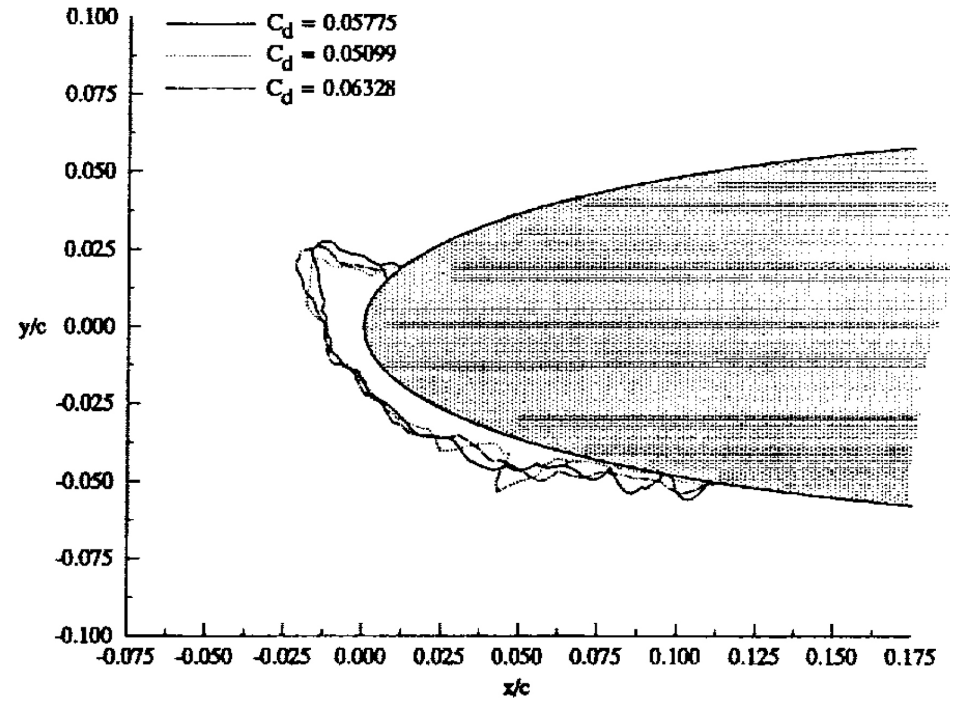

(b)

Fig. 2.42 Representative ice accretion repeatability in the NASA Glenn Icing Research Tunnel for (a) streamwise ice and (b) horn ice.[81]

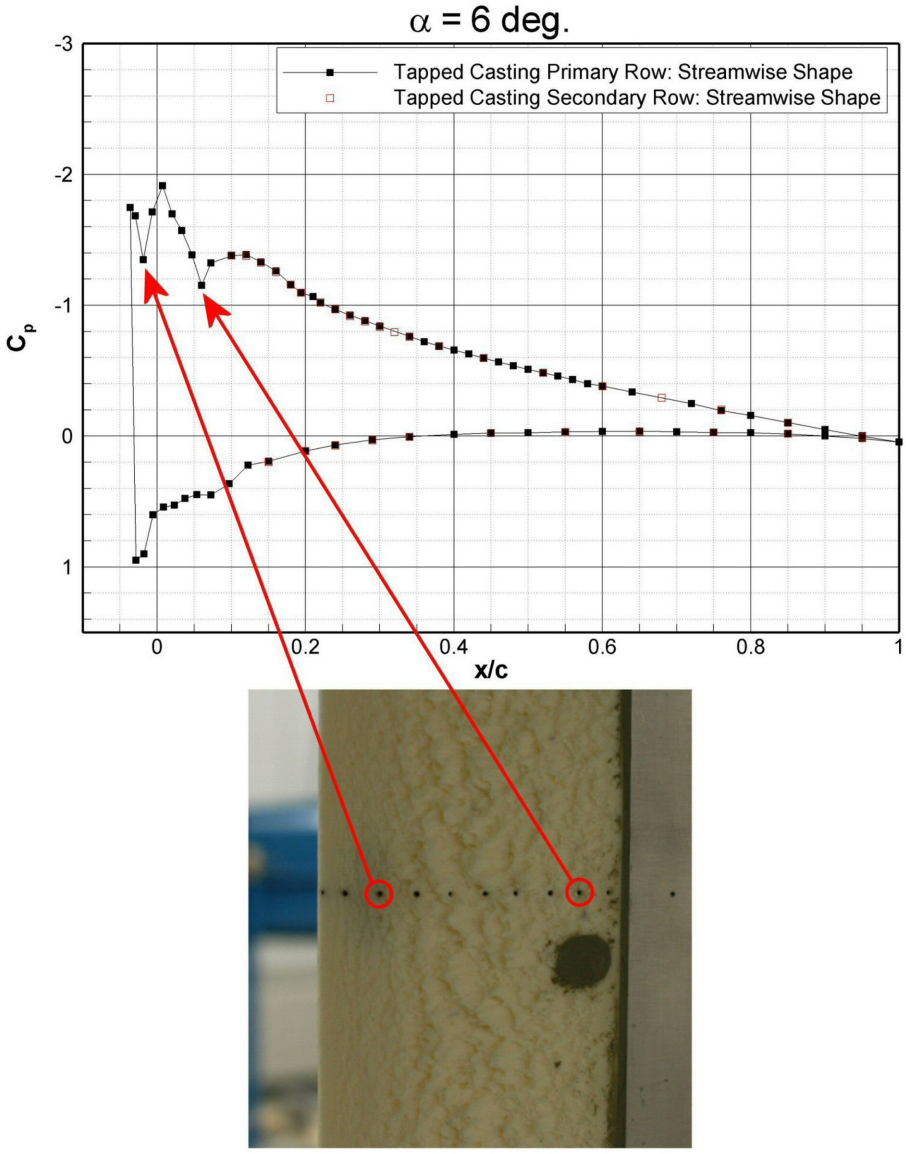

(a)

Fig. 2.43 (continued on next page)

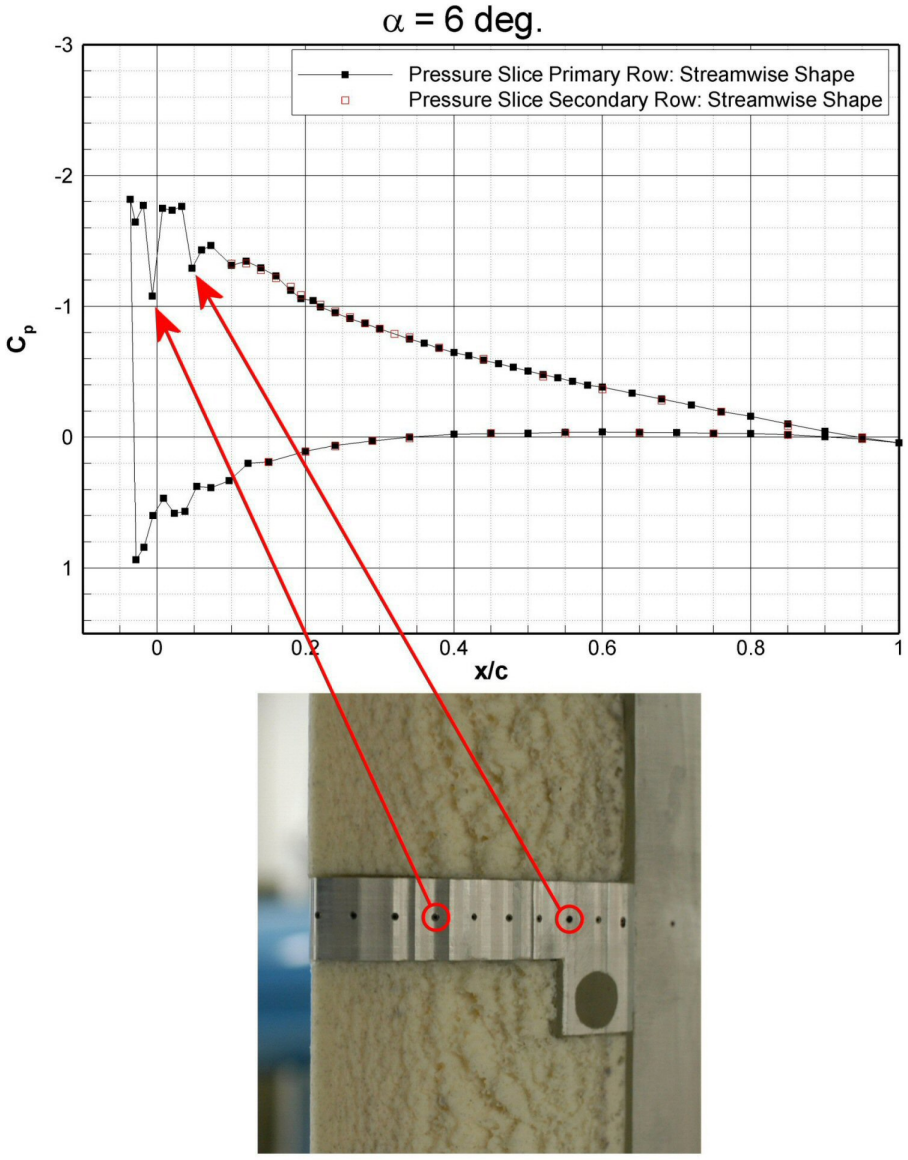

(b)

Fig. 2.43 Measured surface pressure distributions for a NACA 23012 airfoil with castings of streamwise ice instrumented with (a) pressure taps drilled directly into the surface and (b) a 2-D pressure slice.[30]

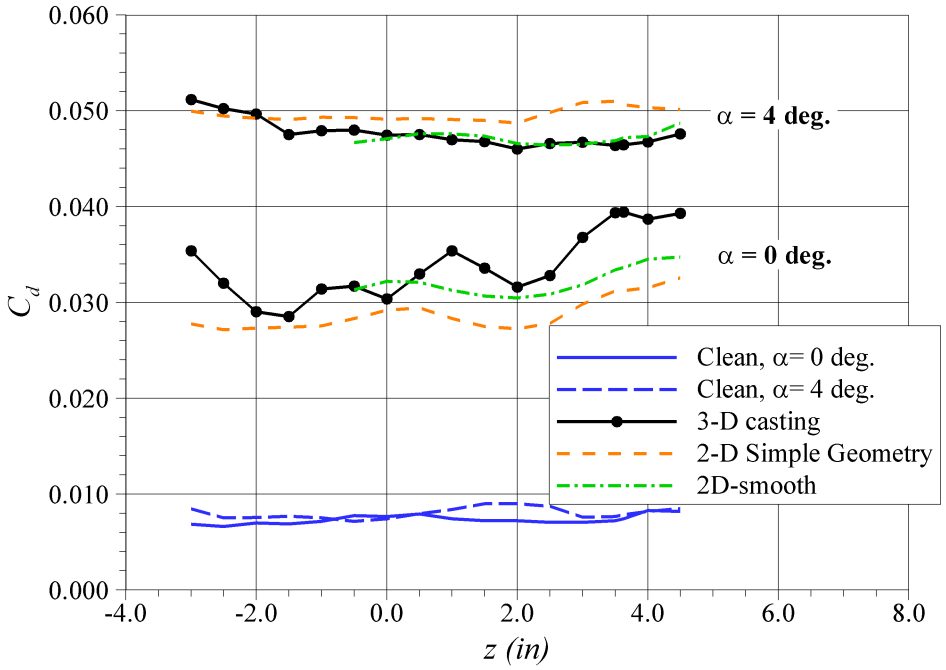

Fig. 2.44 Variation in C_d measured at different spanwise stations behind a NACA 23012 airfoil with a horn-ice casting and 2-D simulations.[6] Re = 1.8 x 10^6, M = 0.18

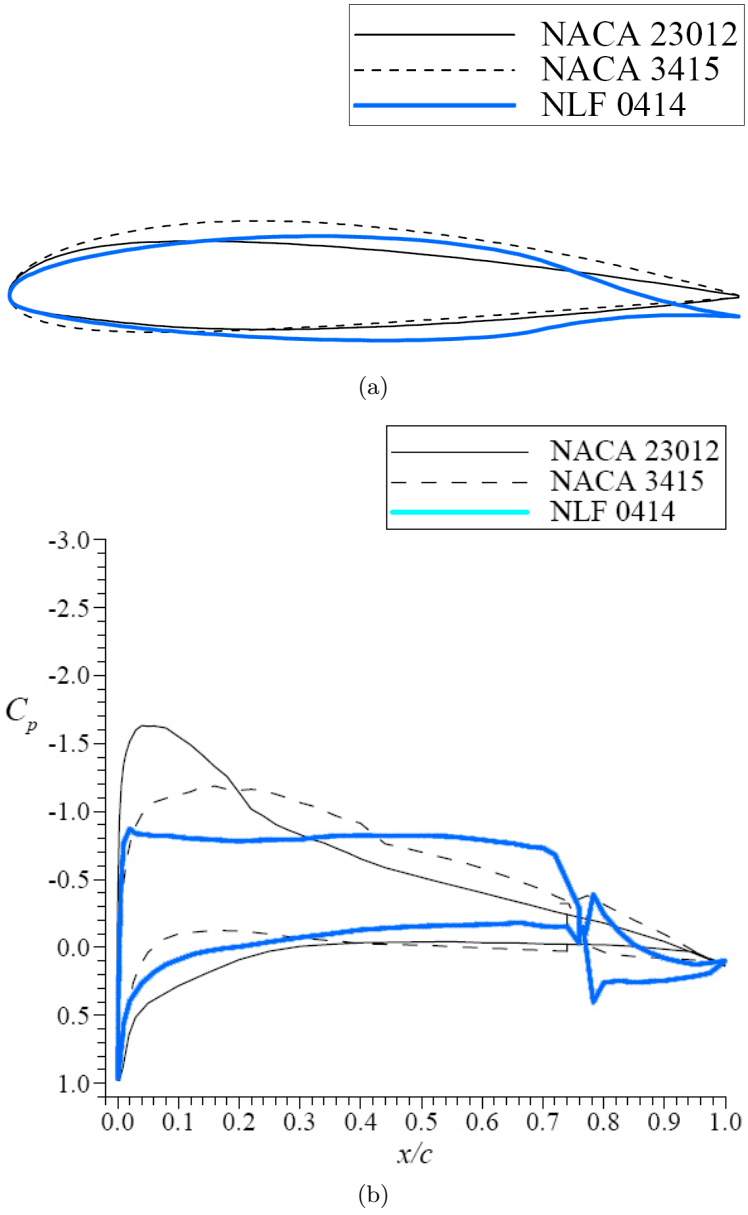

Fig. 2.45 (a) Geometry of clean NACA 23012, NACA 3415, and NLF-0414 airfoils and (b) comparison of clean airfoil pressure distributions of each airfoil at $C_l \approx 0.6$.[92] Data obtained at $Re = 1.8$ x 10^6 and $M = 0.18$.

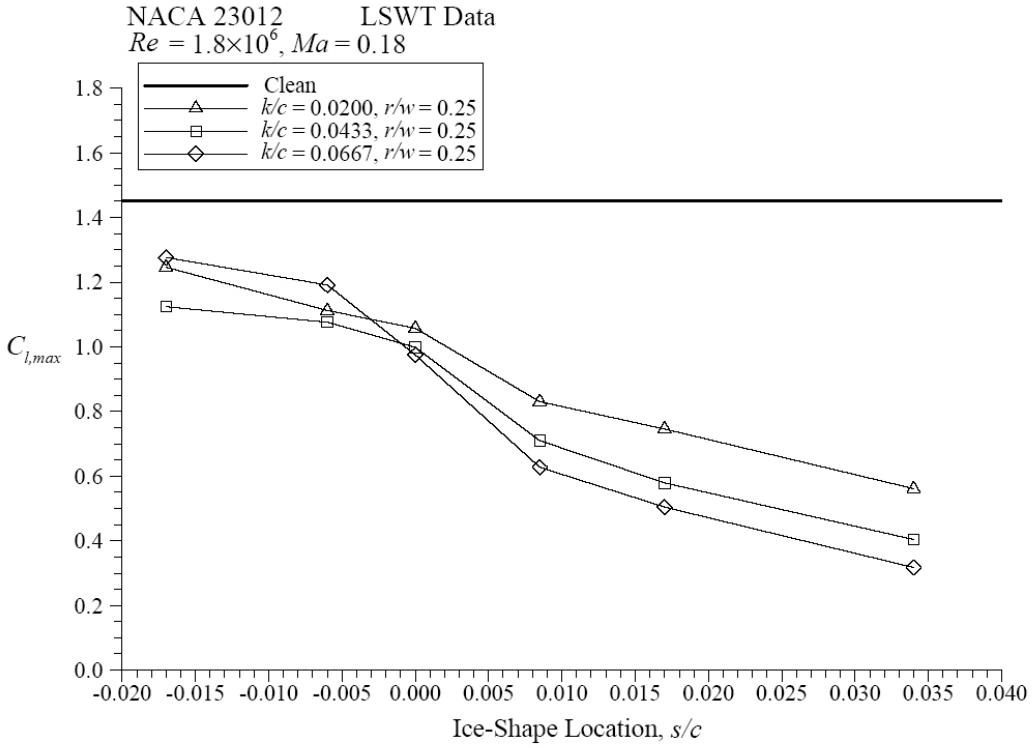

(a)

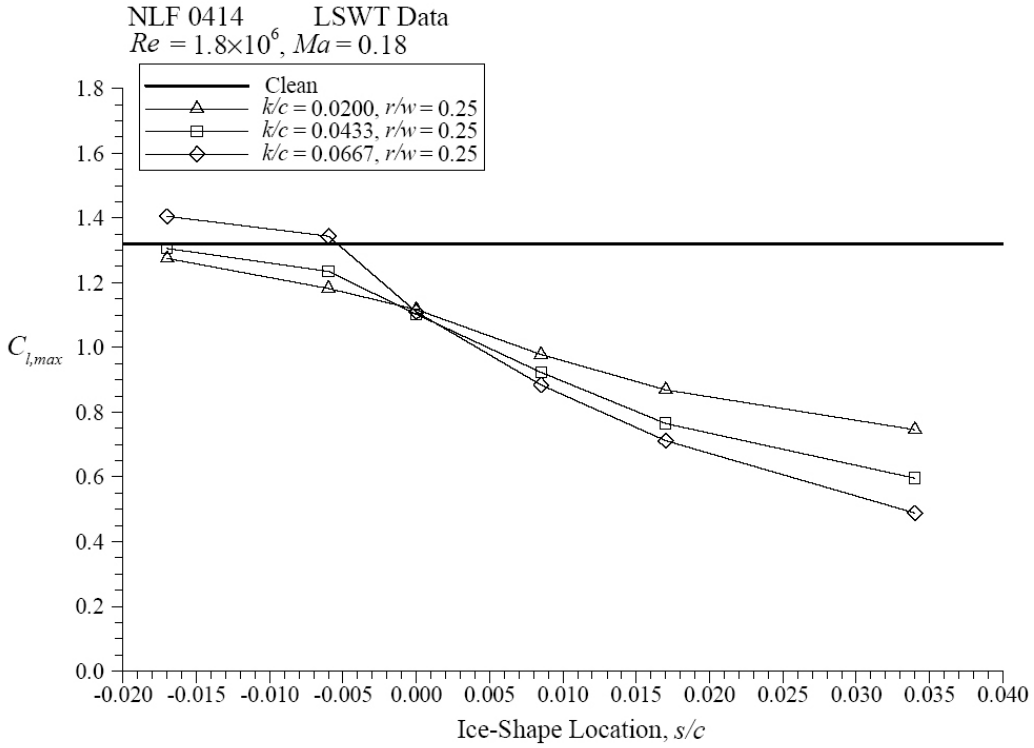

(b)

Fig. 2.46 (continued on next page)

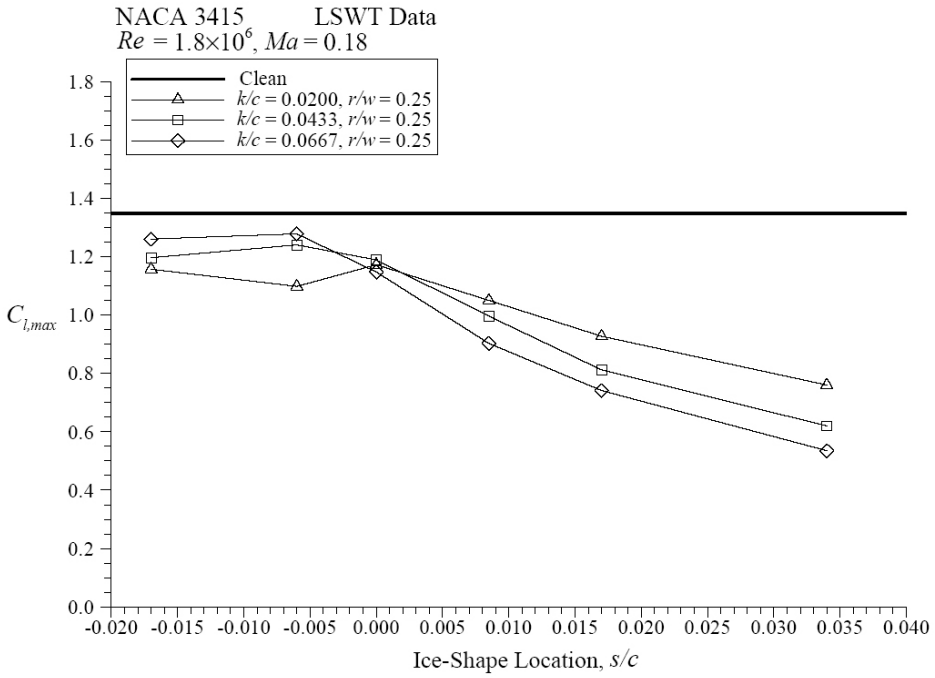

(c)

Fig. 2.46 Effect of simple-geometry horn-ice simulations on $C_{l,max}$ of the (a) NACA 23012, (b) NLF-0414, and (c) NACA 3415 airfoils.[94]

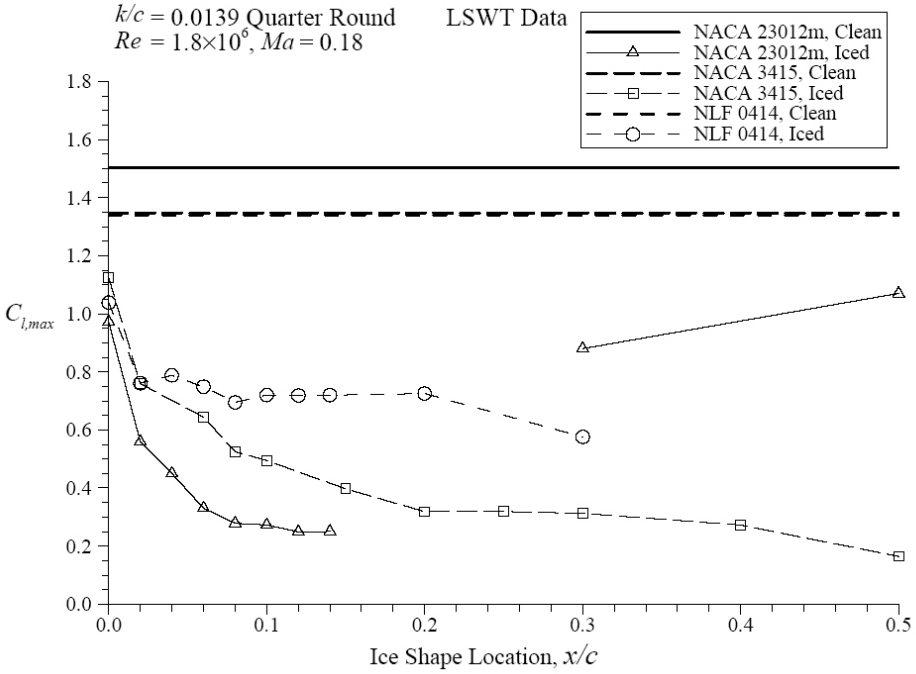

Fig. 2.47 Effect of a $k/c = 0.0139$ simple-geometry ridge simulation on the $C_{l,max}$ of NACA 23012m, NLF-0414, and NACA 3415 airfoils for various ridge locations.[94]

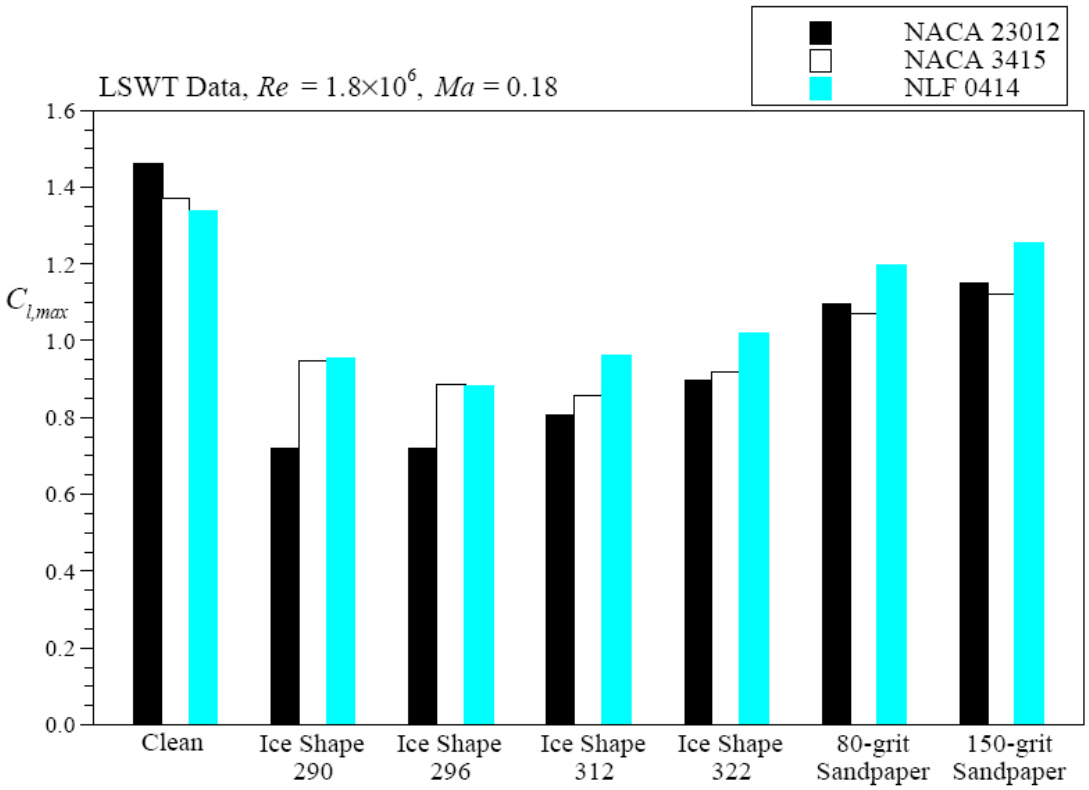

Fig. 2.48 Effect of simple-geometry intercycle ice and ice roughness simulations on the $C_{l,max}$ of NACA 23012m, NLF-0414, and NACA 3415 airfoils.[94]

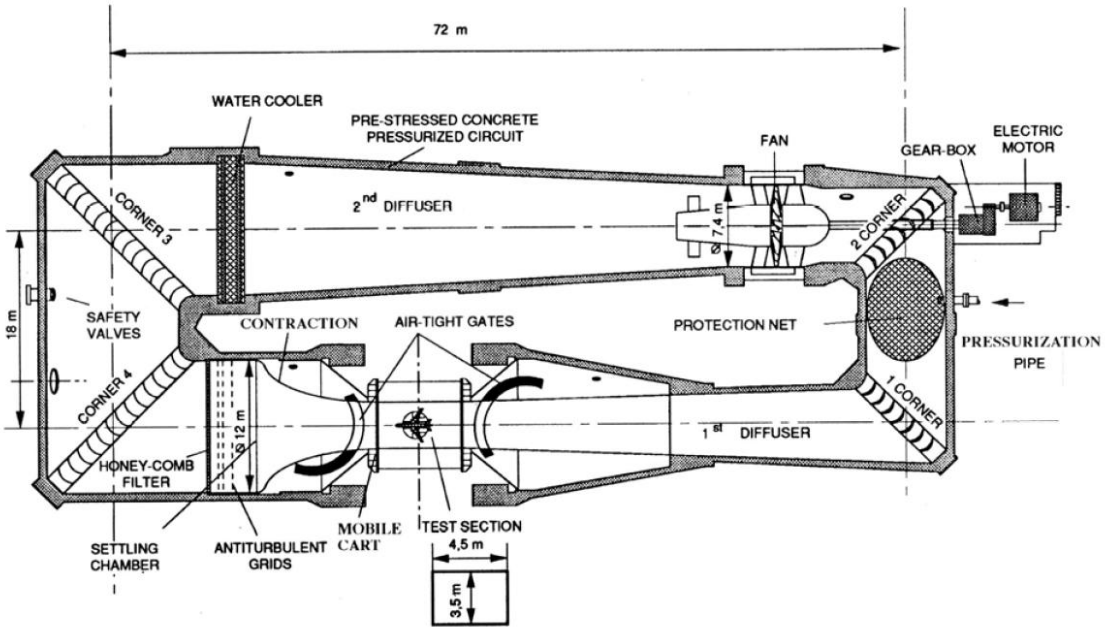

Fig. 3.1 Schematic of the ONERA F1 wind tunnel.[15]

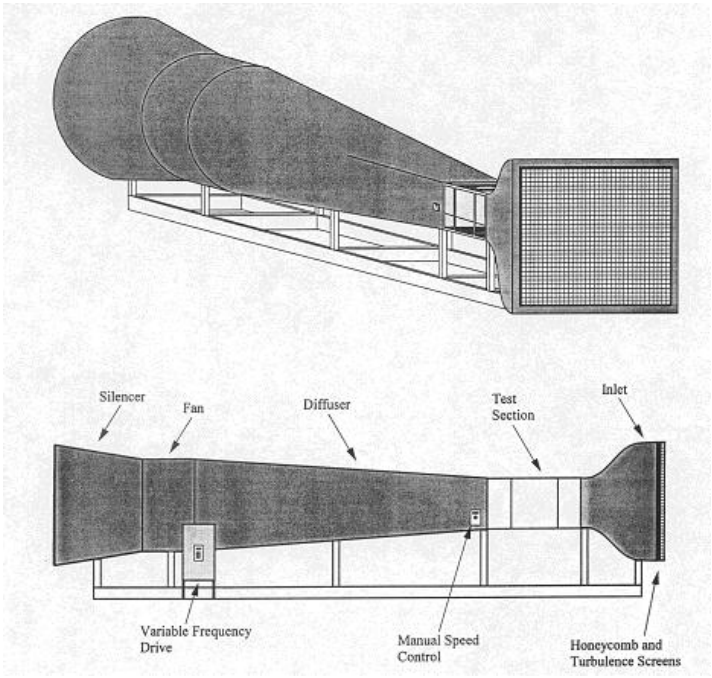

Fig. 3.2 UIUC 3 x 4 ft subsonic wind tunnel.[33]

Fig. 3.3 6-ft chord NACA 23012 model installed in ONERA F1 wind tunnel.[10]

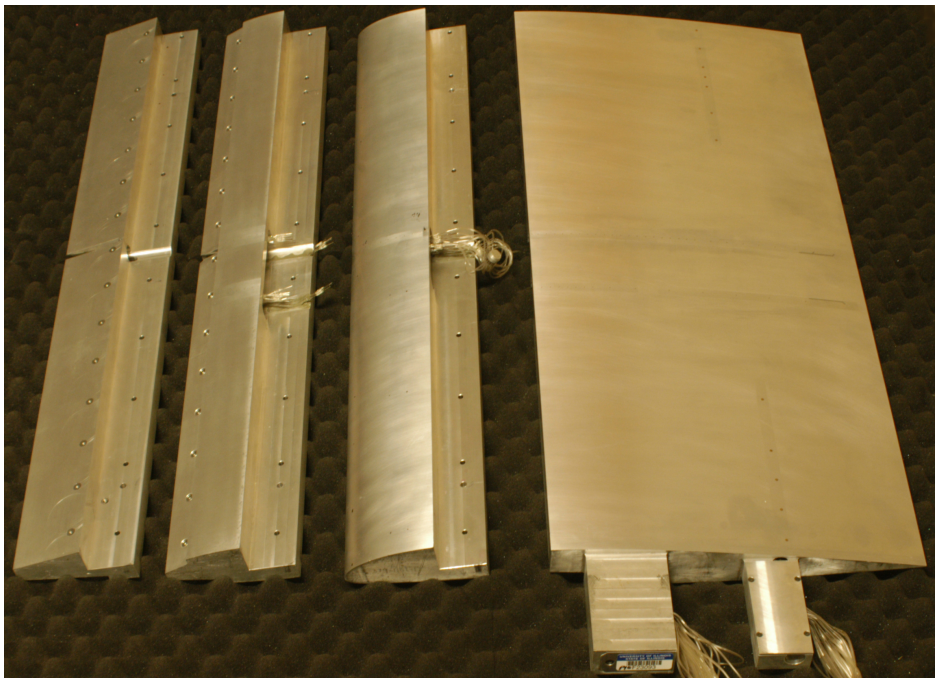

Fig. 3.4 18-inch chord NACA 23012 model with removable leading edges. From left to right: SLD leading edge, App. C leading edge, clean leading edge, main airfoil body.

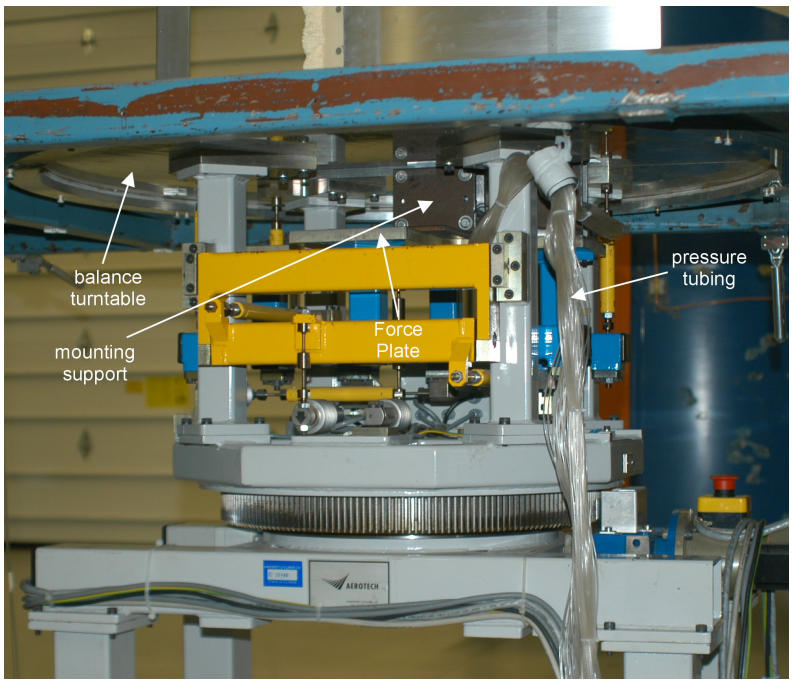

Fig. 3.5 Three-component force balance used to measure airfoil lift and pitching moment.[38]

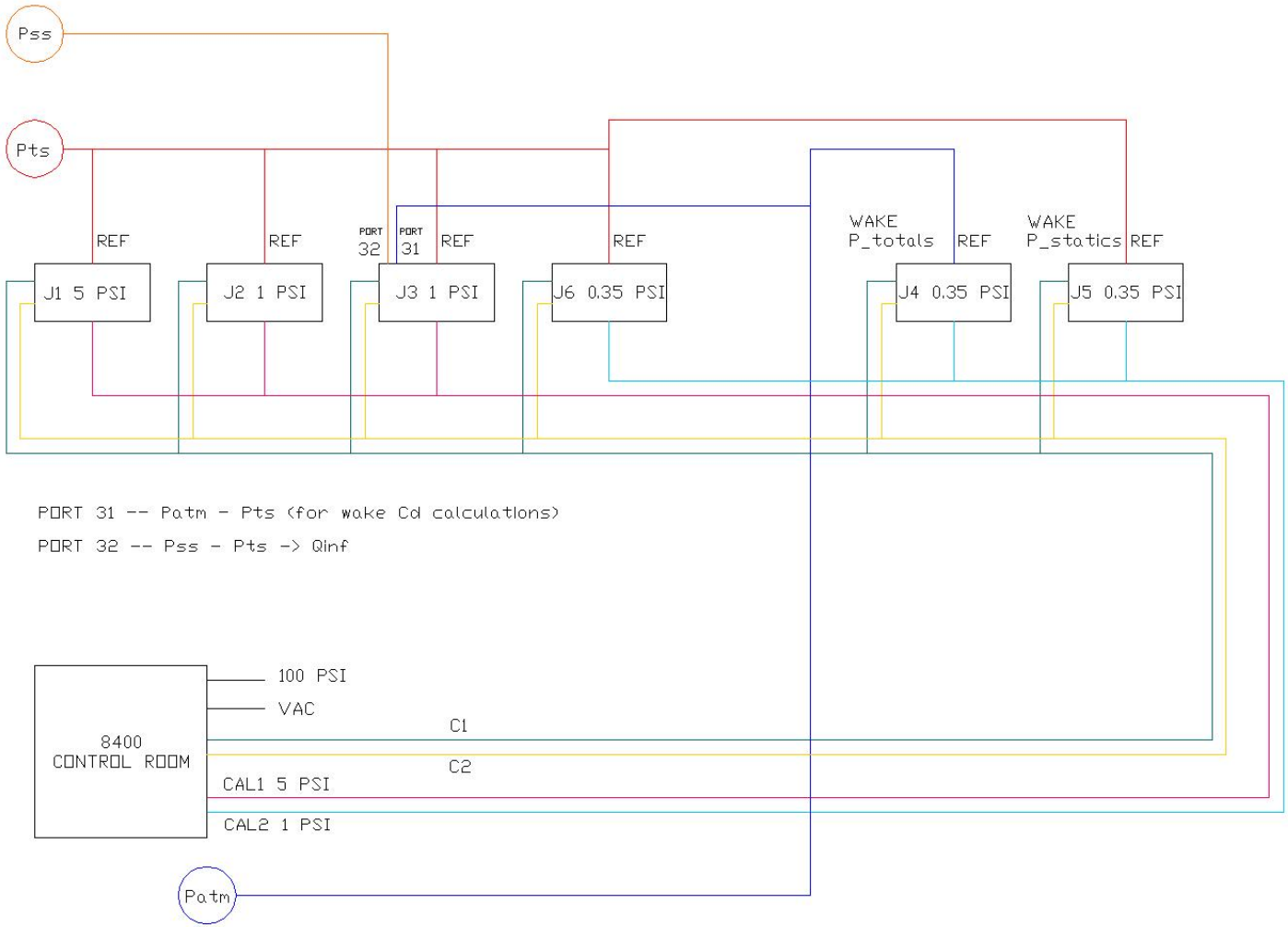

Fig. 3.6 Schematic of the pneumatic system used to obtain pressure measurements.

Fig. 3.7 Traversable wake rake installed behind NACA 23012 model.

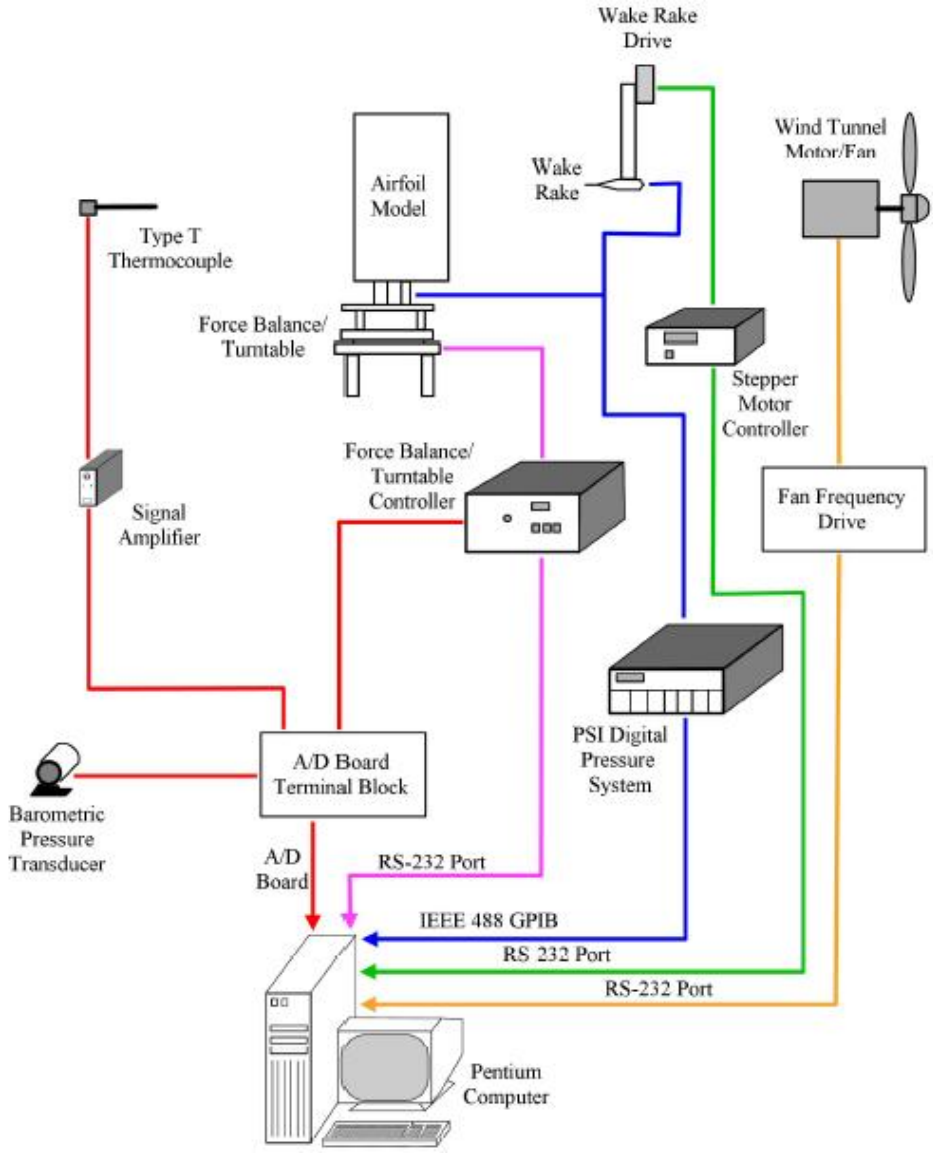

Fig. 3.8 Experimental setup of data acquisition equipment.[38]

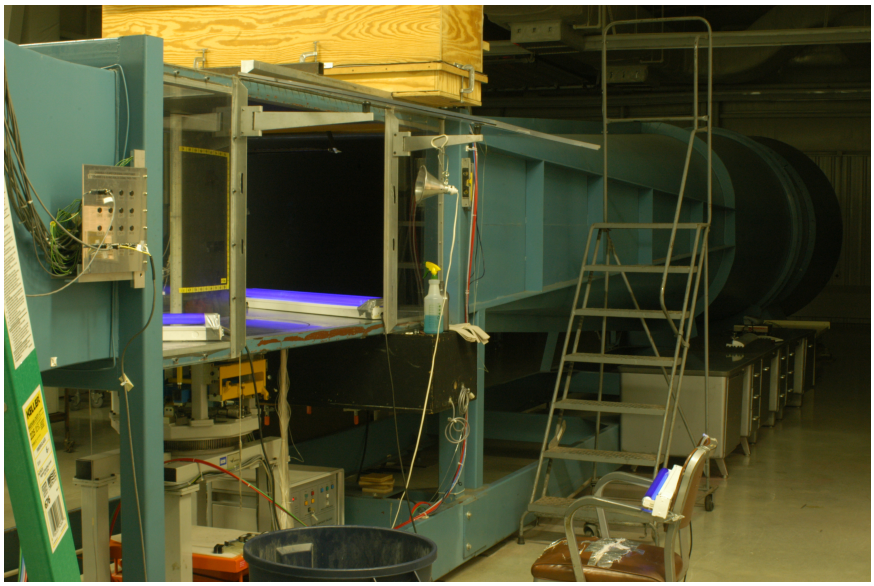

Fig. 3.9 Fluorescent oil-flow visualization setup.

Fig. 3.10 72-inch chord NACA 23012 icing model installed in test section of the NASA Glenn Icing Research Tunnel, shown with the leading-edge heater used to generate a tall spanwise-ridge ice shape.[3]

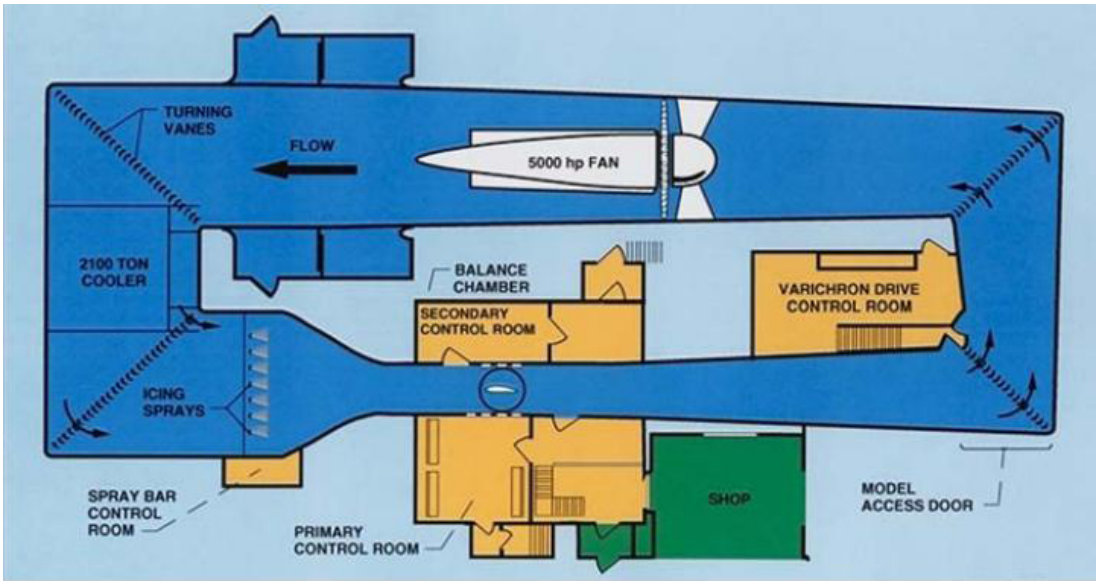

Fig. 3.11 Schematic of the NASA Glenn Icing Research Tunnel.[113]

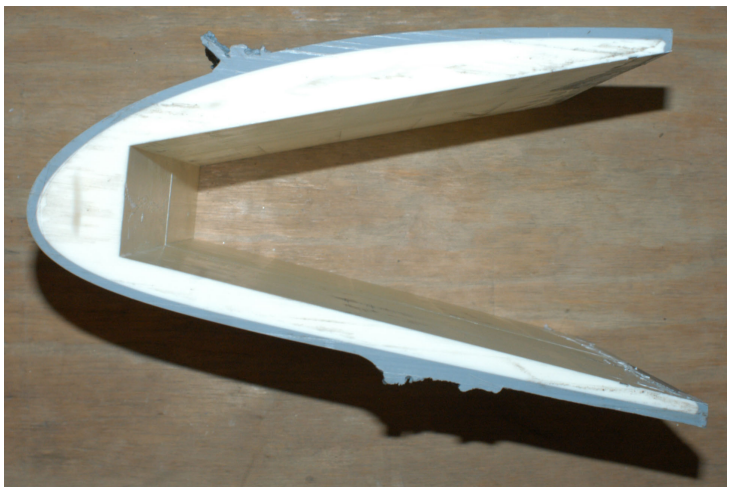

Fig. 3.12 Two-pour approach for creating ice castings: the first pour is the inner portion of the casting (white) and the second pour is the outer portion of the casting (gray)

(a)

(b)

Fig. 3.13 (a) EG1159 tall spanwise-ridge ice castings mounted on removable leading edge of aerodynamic model[10] and (b) EG1164 horn-ice castings installed on aerodynamic model in ONERA F1 wind tunnel.[9]

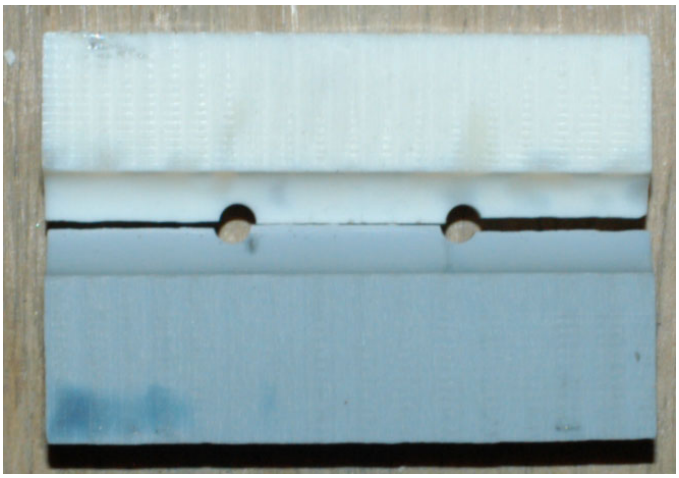

(a)

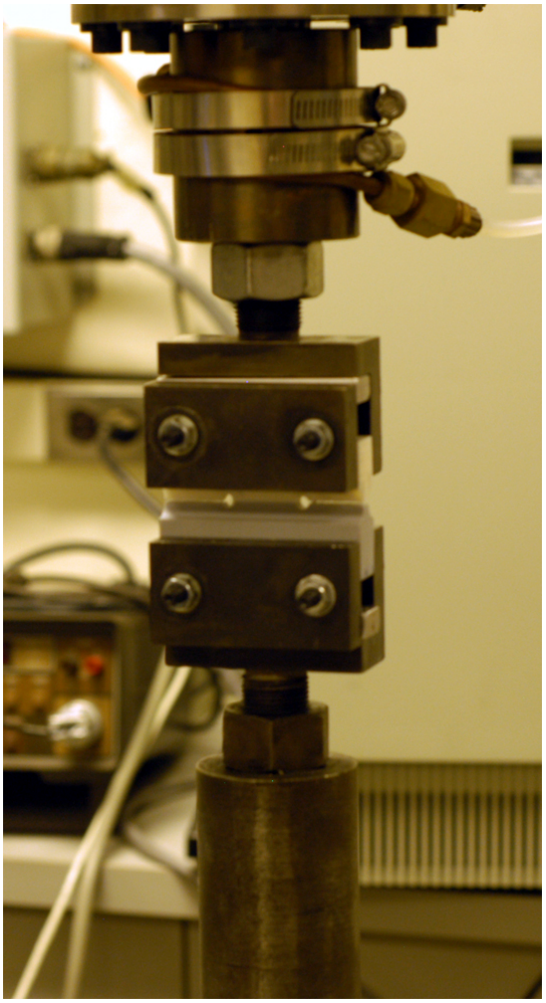

(b)

Fig. 3.14 (a) Sample of two sections of casting material bonded to each other and (b) sample installed in tensile test machine.[9]

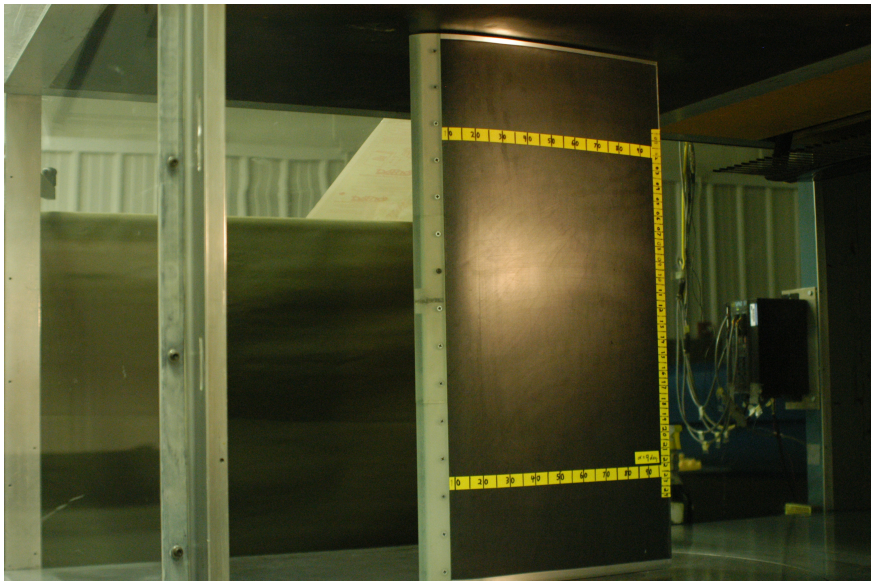

Fig. 3.15 2-D smooth streamwise-ice simulation installed on the NACA 23012 airfoil model.

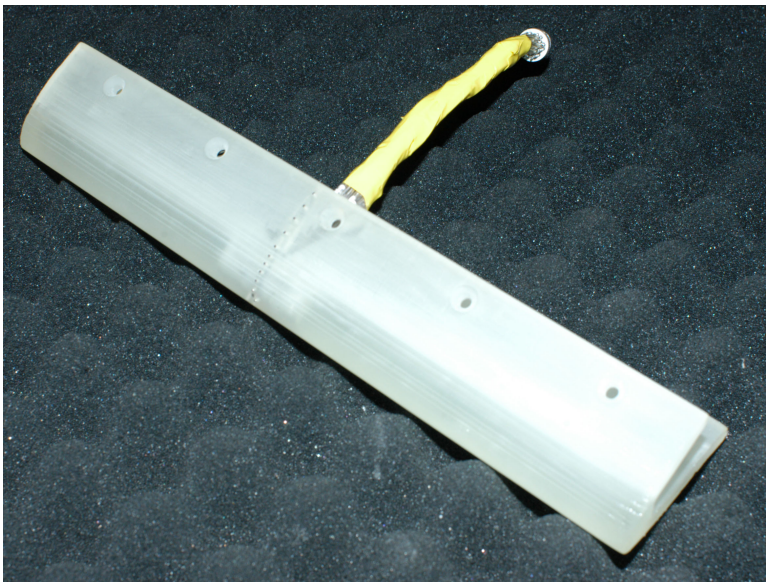

Fig. 3.16 Portion of the EG1125 2-D smooth streamwise-ice simulation.

(a)

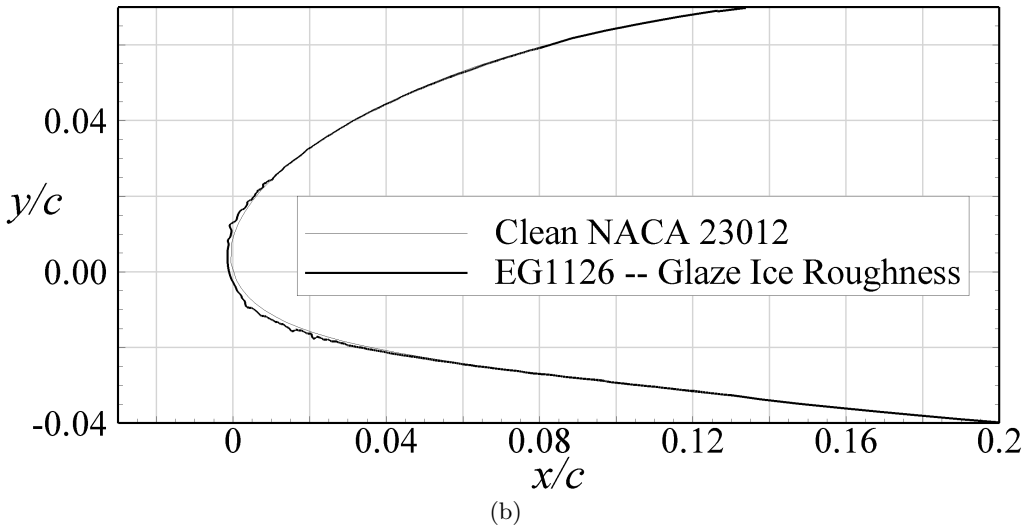

(b)

Fig. 3.17 Photos and tracing of EG1126 ice roughness accretion.

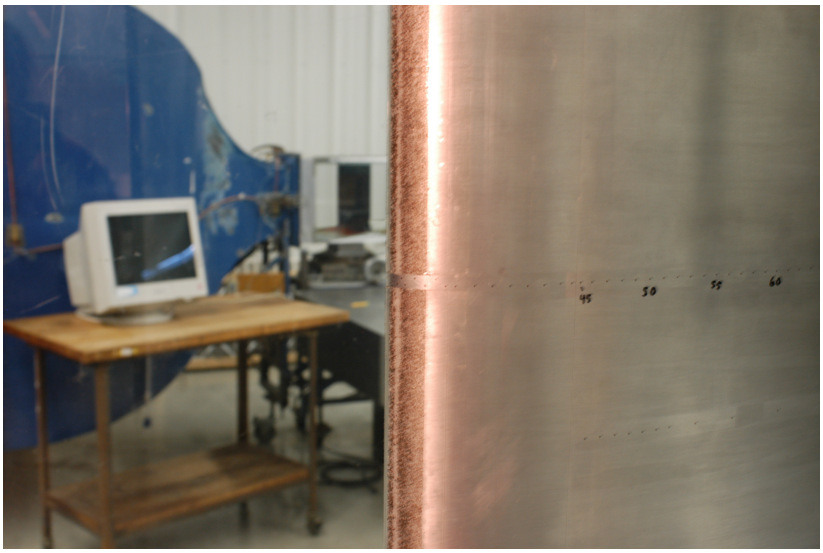

(a)

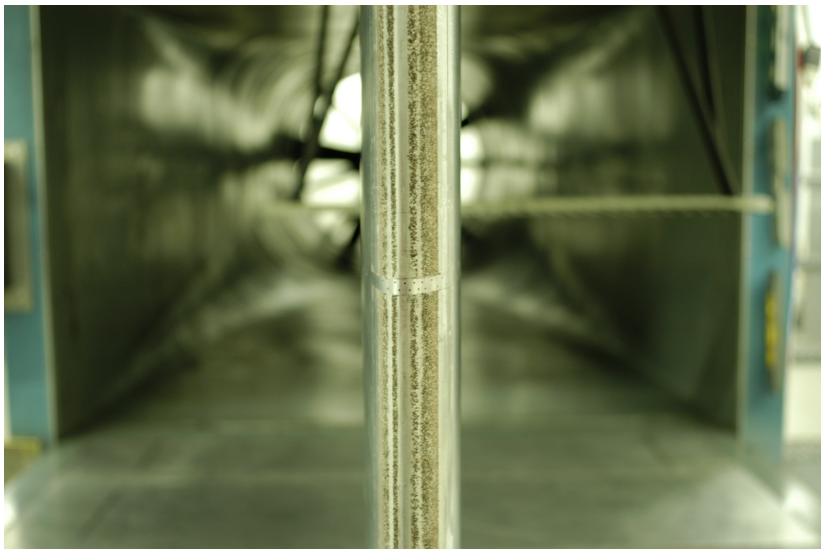

(b)

Fig. 3.18 Geometrically-scaled EG1126 simulation using several different roughness heights: (a) airfoil upper surface and (b) airfoil leading edge.

(a)

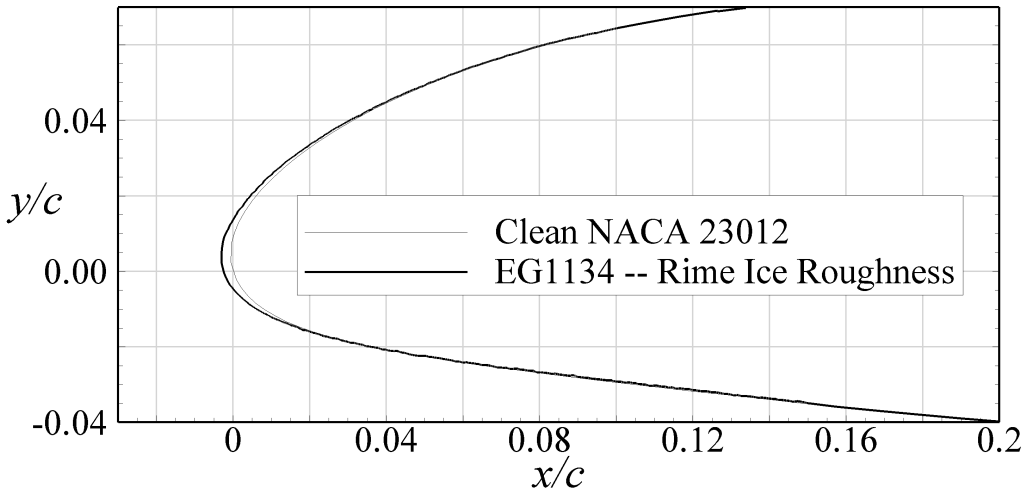

(b)

Fig. 3.19 Photos and tracing of EG1134 ice roughness accretion.

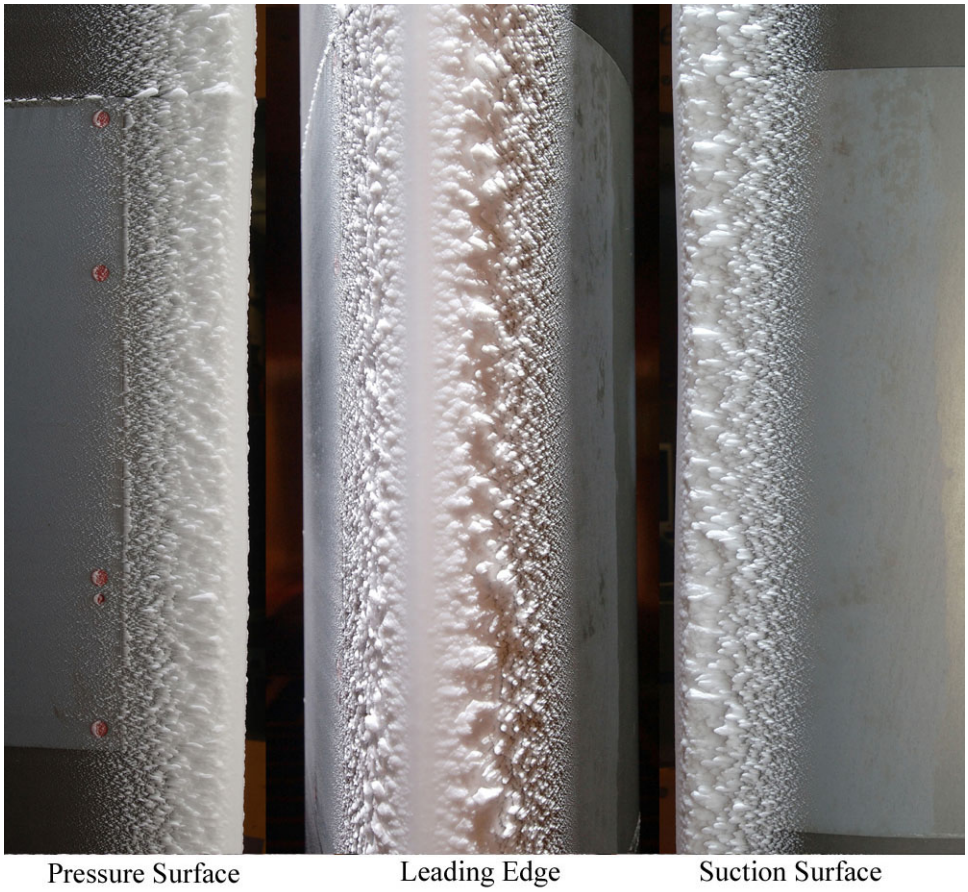

(a)

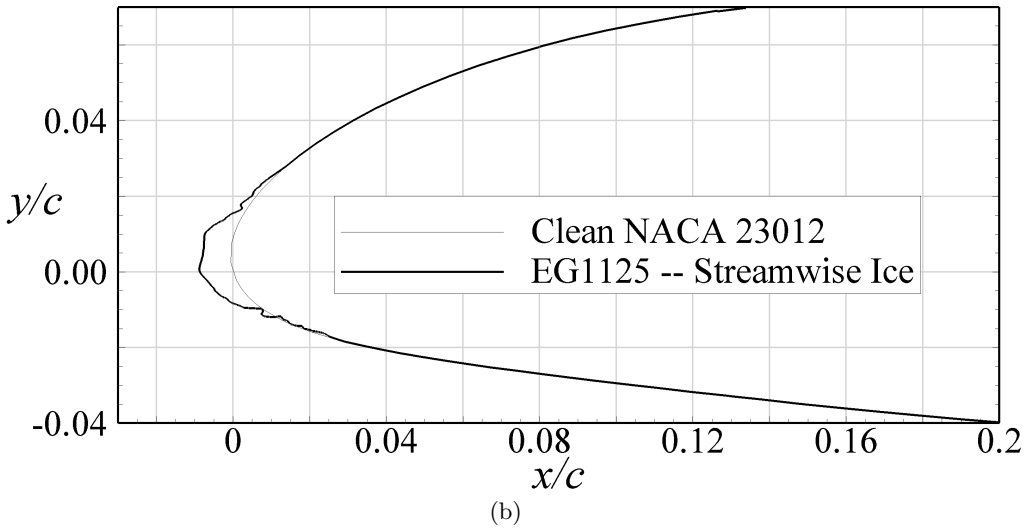

(b)

Fig. 3.20 Photos and tracing of EG1125 streamwise-ice accretion.

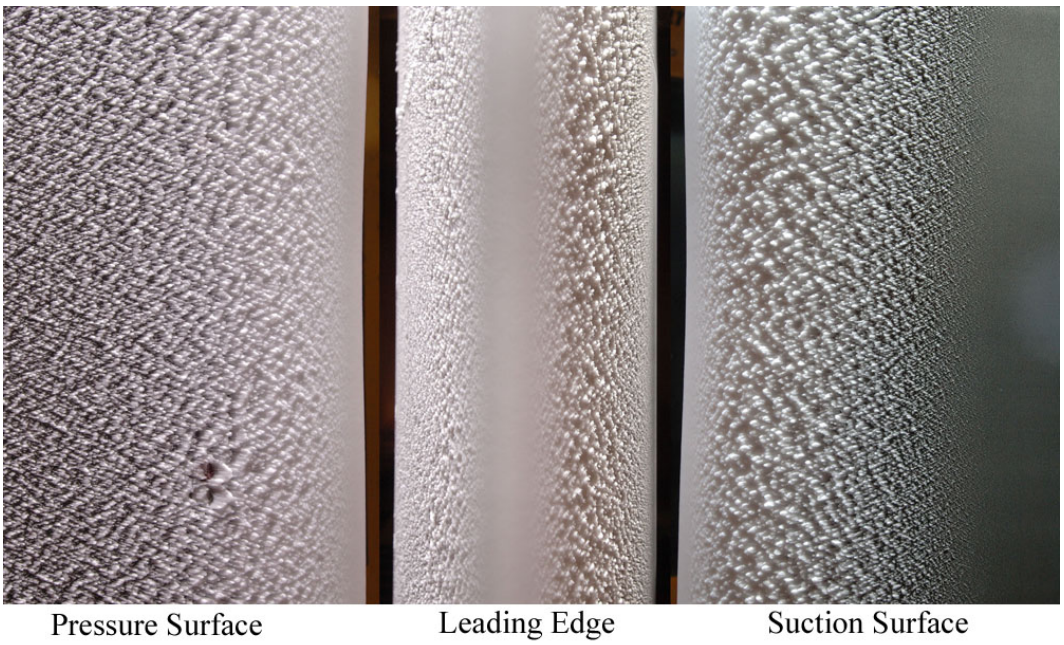

(a)

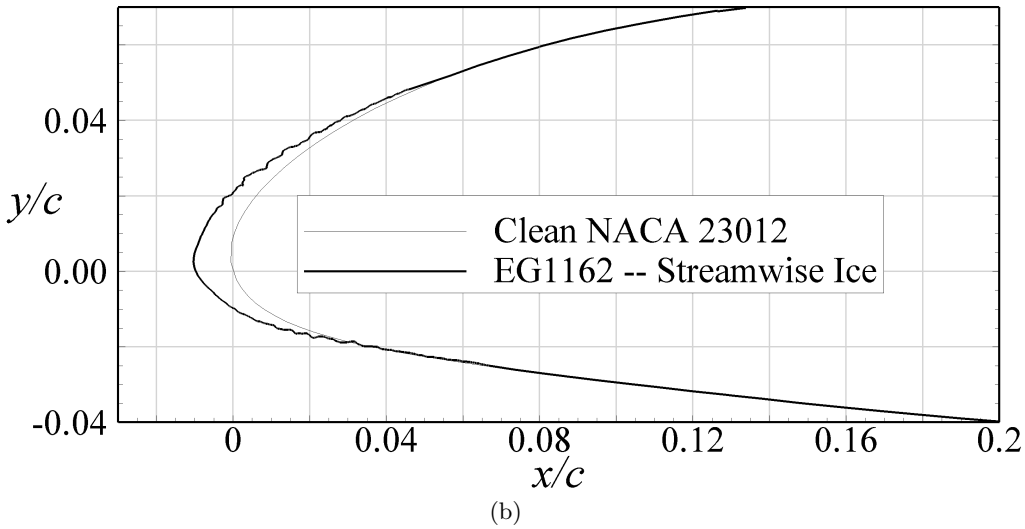

(b)

Fig. 3.21 Photos and tracing of EG1162 streamwise-ice accretion.

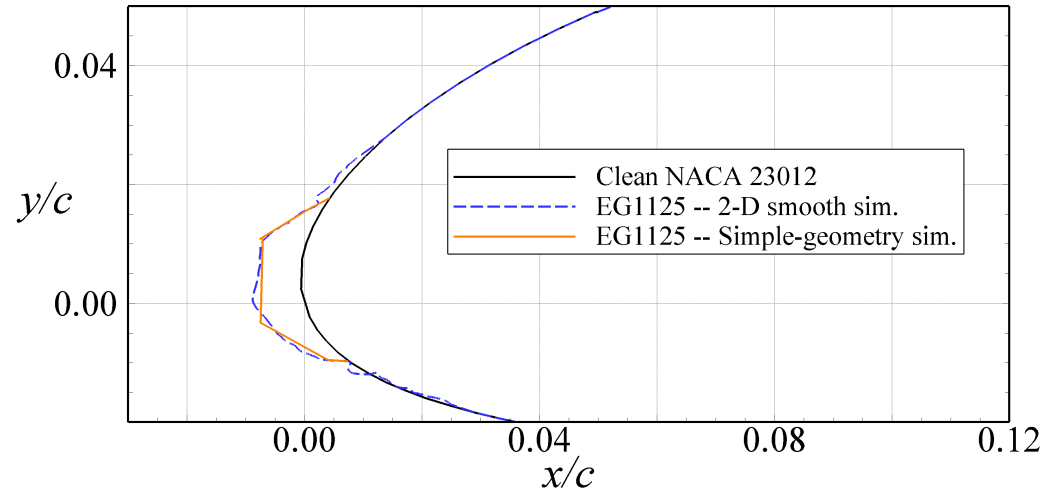

(a)

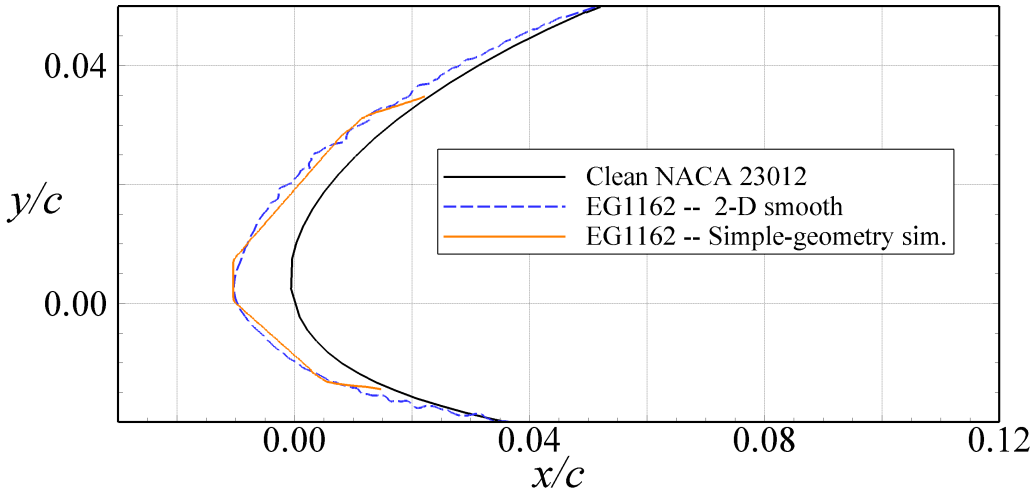

(b)

Fig. 3.22 Cross-sections of 2-D smooth and simple-geometry simulations of (a) EG1125 streamwise ice and (b) EG1162 streamwise ice.

(a)

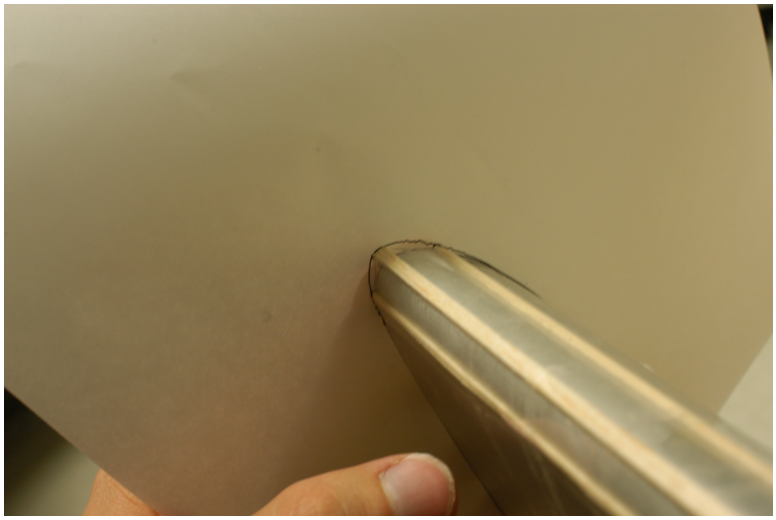

(b)

Fig. 3.23 EG1162 simple-geometry simulation: (a) end view of book tape stretched over balsa strips and (b) comparison of simple-geometry cross-section with ice tracing.

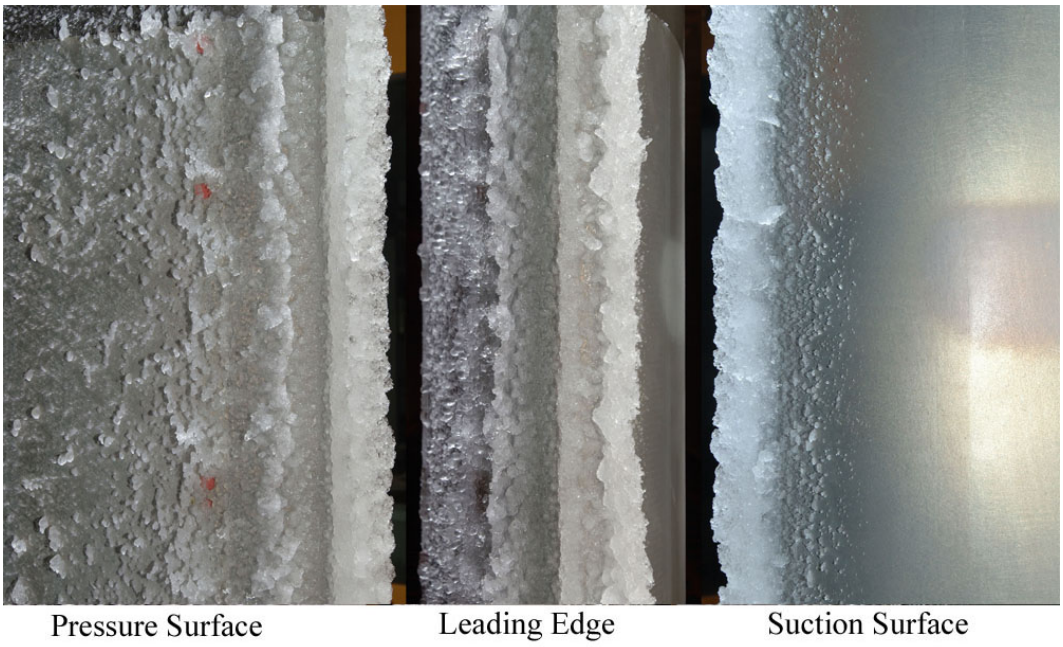

(a)

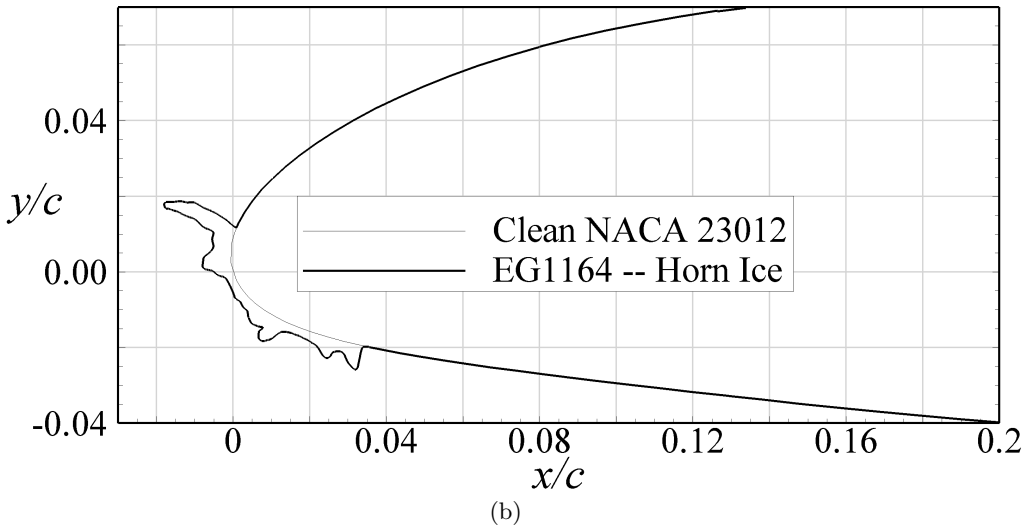

(b)

Fig. 3.24 Photos and tracing of EG1164 horn-ice accretion.

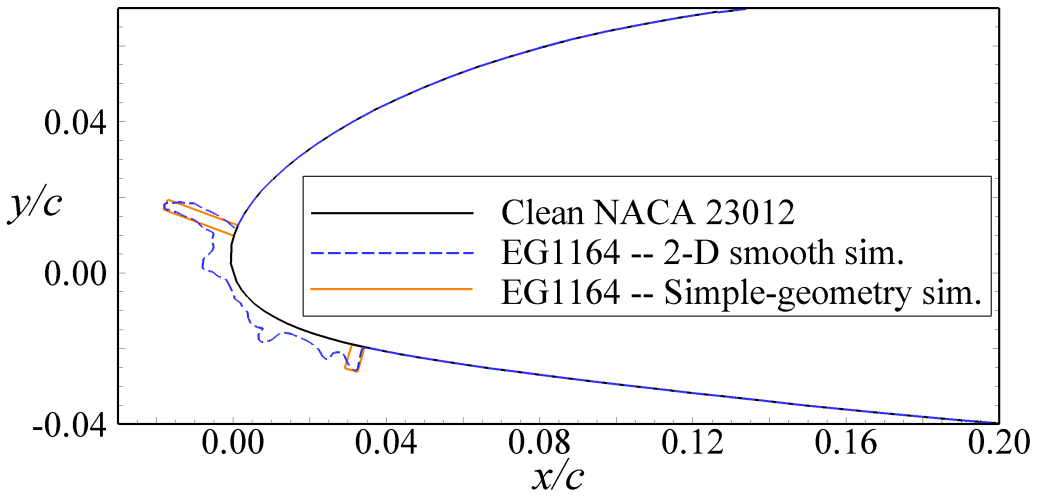

Fig. 3.25 Cross-sections of 2-D smooth and simple-geometry simulations of EG1164 horn ice.

(a) (b)

Fig. 3.26 EG1164 simple-geometry simulation: airfoil (a) lower surface and (b) leading edge.

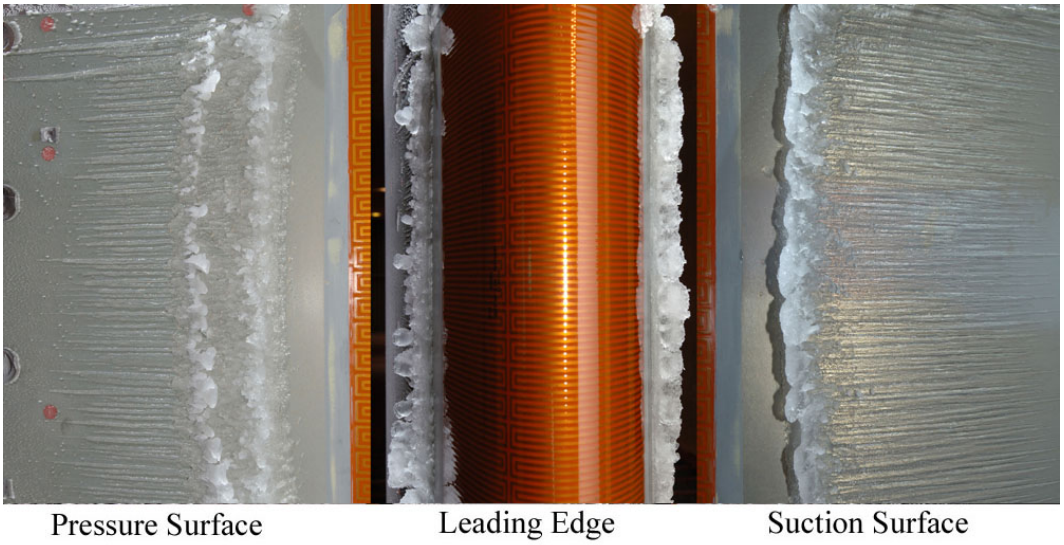

(a)

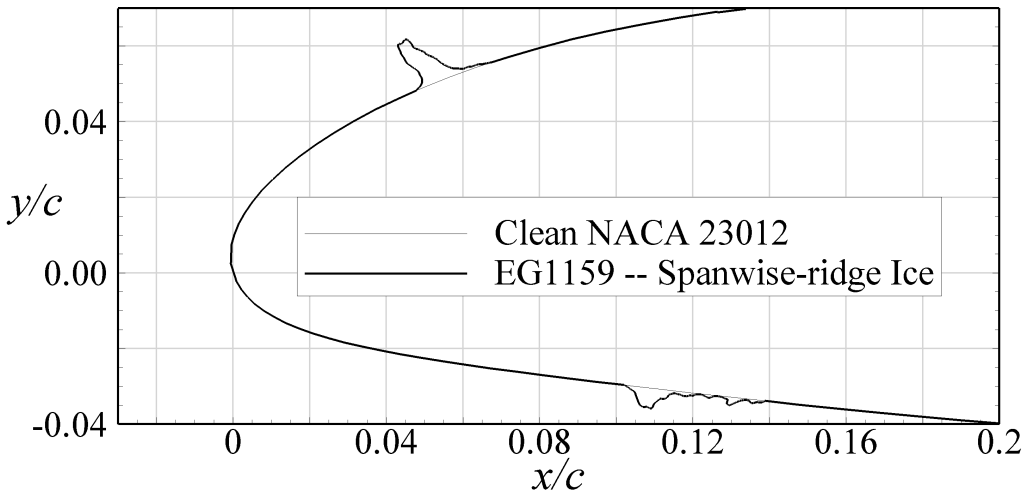

(b)

Fig. 3.27 Photos and tracing of EG1159 tall spanwise-ridge ice accretion.

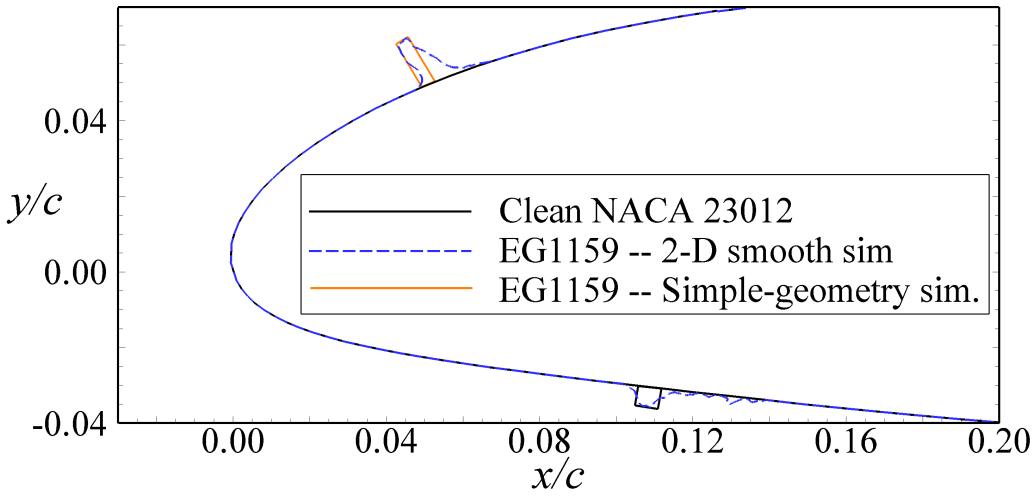

Fig. 3.28 Cross-sections of 2-D smooth and simple-geometry simulations of EG1159 tall spanwise-ridge ice.

(a) (b)

Fig. 3.29 Tall spanwise ridge ice simple-geometry simulation: airfoil (a) upper surface and (b) leading edge.

(a)

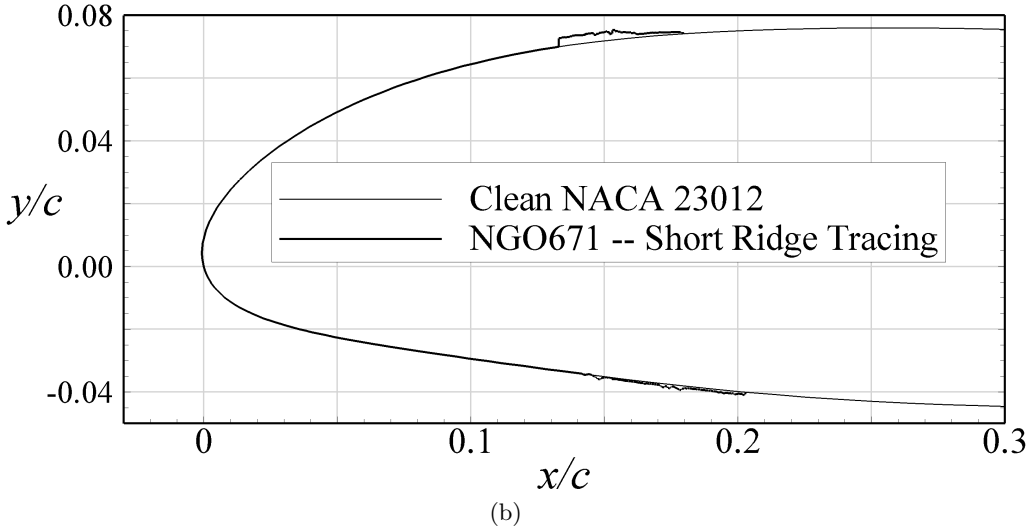

(b)

Fig. 3.30 Photos and tracing of NGO671 short spanwise-ridge ice accretion.

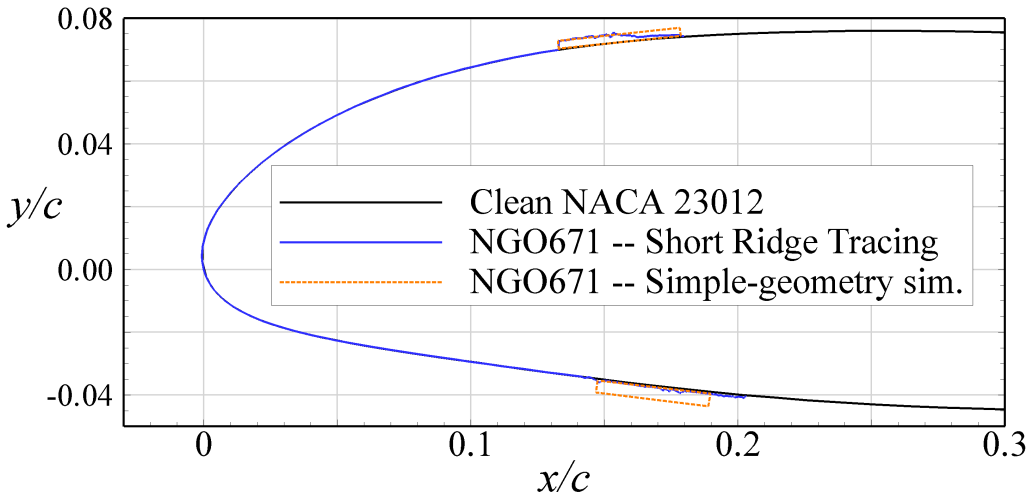

Fig. 3.31 Cross-sections of 2-D smooth and simple-geometry simulations of NGO671 short spanwise-ridge ice.

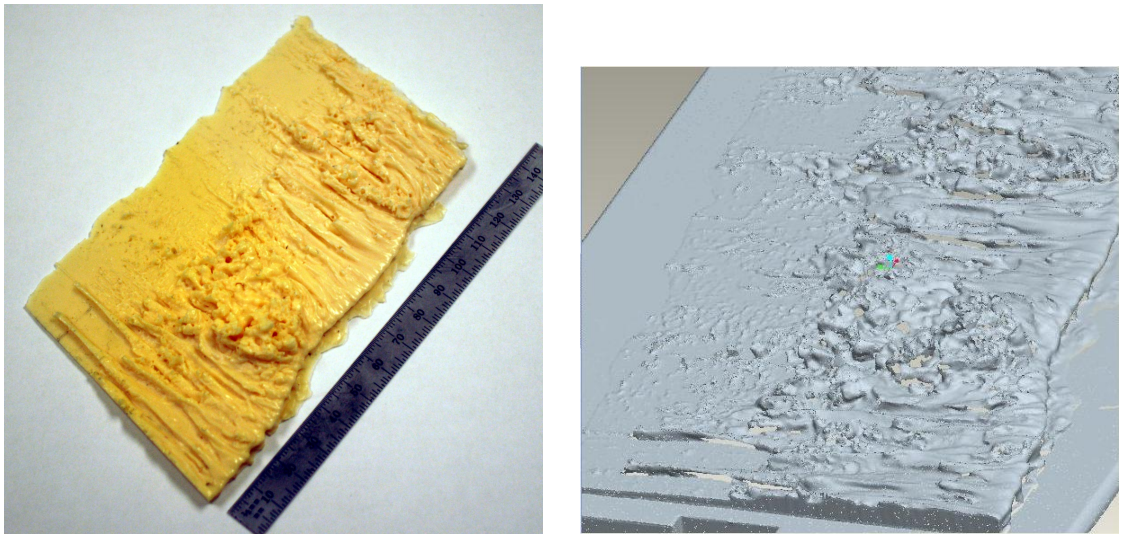

(a) (b)

Fig. 3.32 Comparison of short ridge (a) casting sample and (b) point cloud generated by a laser scan.

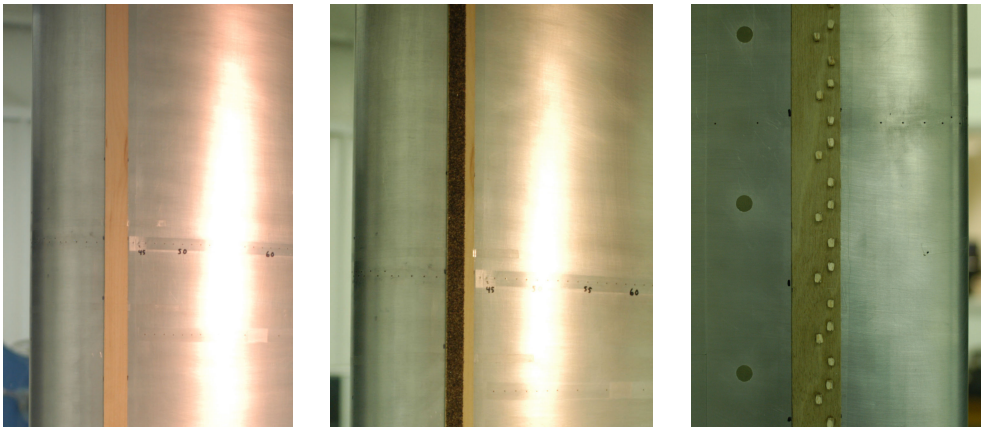

(a) (b) (c)

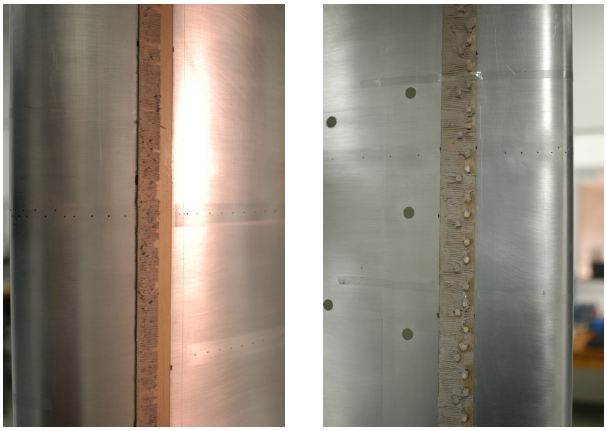

(d) (e)

Fig. 3.33 Some variations of the simple-geometry simulations of the short ridge: (a) 2-D simple-geometry upper surface ridge, (b) 2-D simple-geometry upper surface ridge with surface roughness, (c) 3-D simple-geometry lower surface ridge, (d) 2-D simple-geometry upper surface ridge with simulated rivulets, and (e) 3-D simple-geometry lower surface ridge with simulated rivulets.

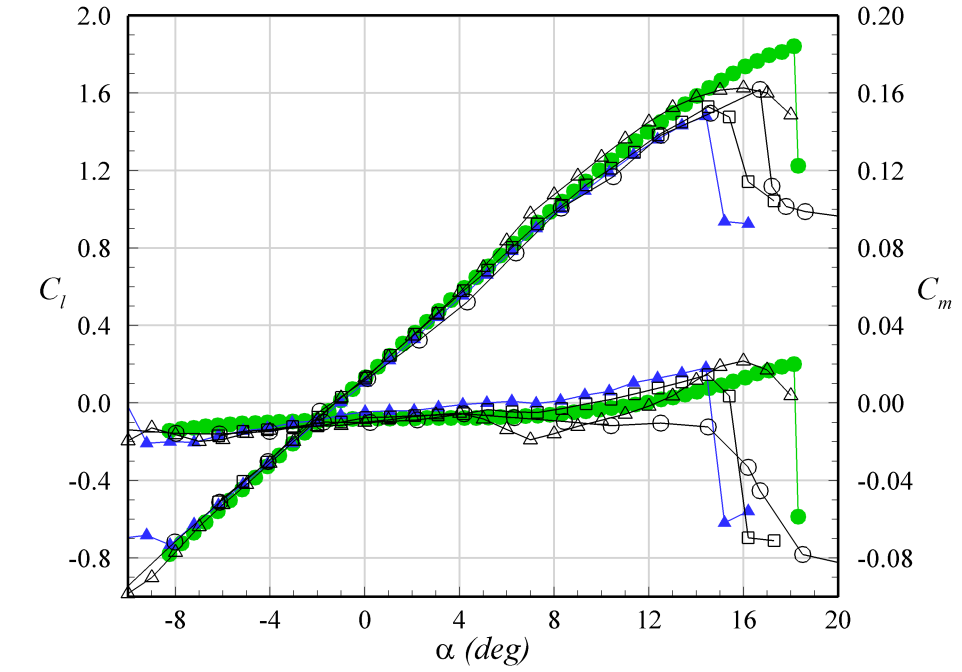

(a)

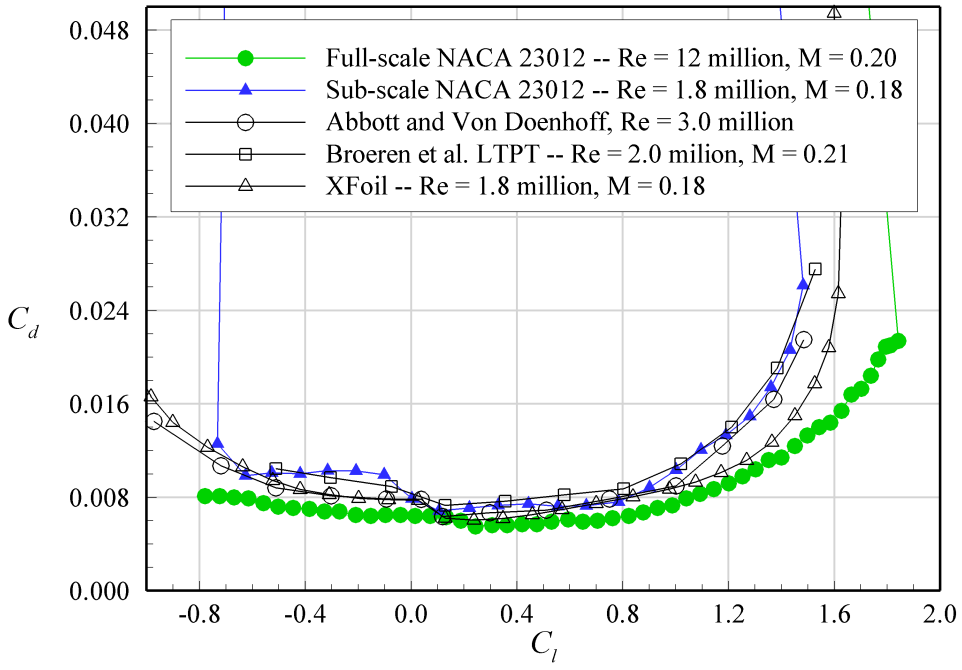

(b)

Fig. 4.1 Validation of clean NACA 23012 aerodynamic performance data using data from Broeren et al.,[93] Abbott and Von Doenhoff,[103] and XFoil.[102]

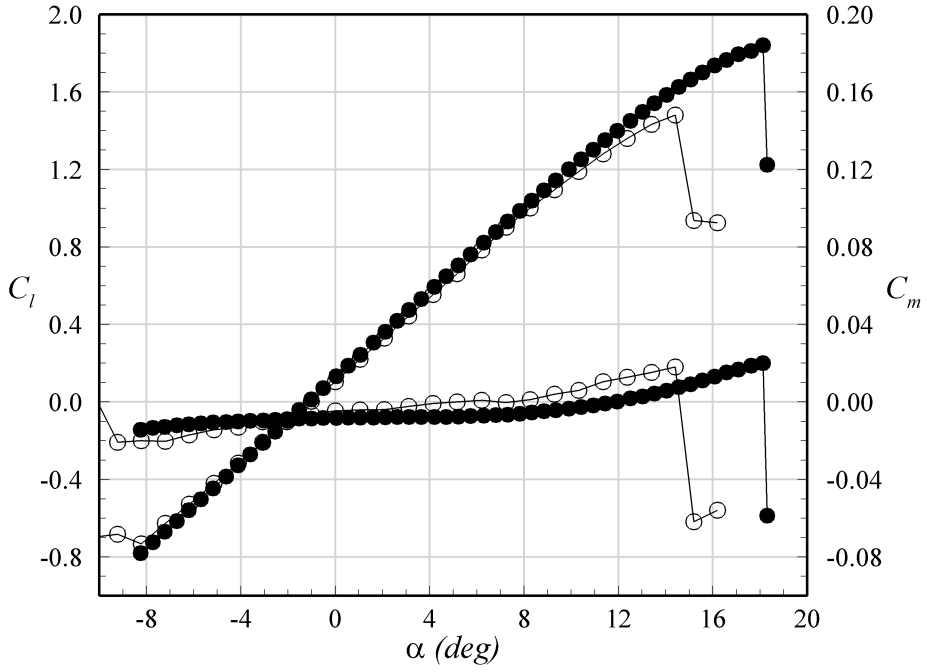

(a)

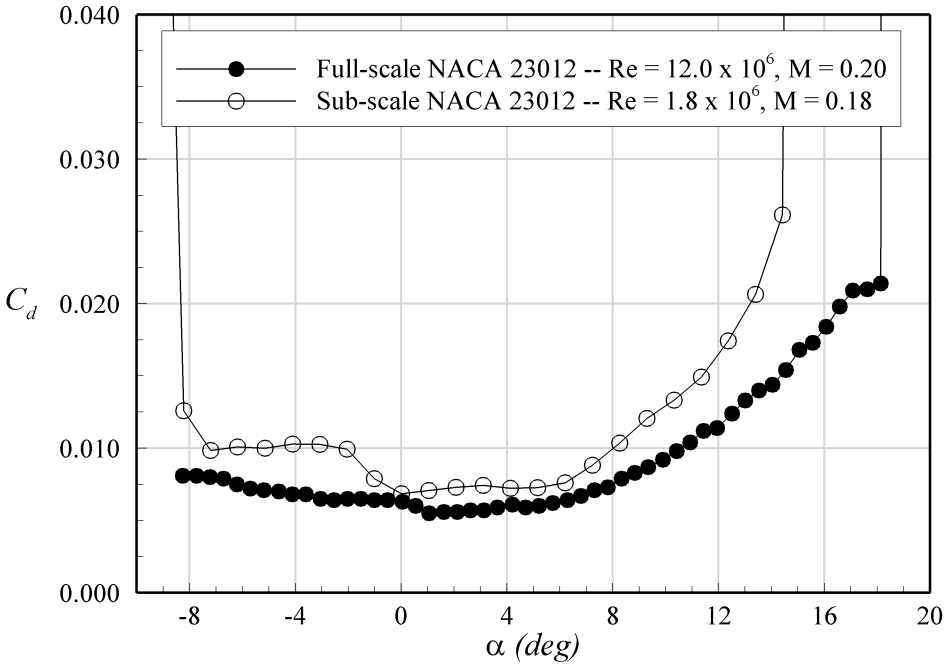

(b)

Fig. 4.2 Comparison of clean NACA 23012 performance at two different Reynolds numbers.

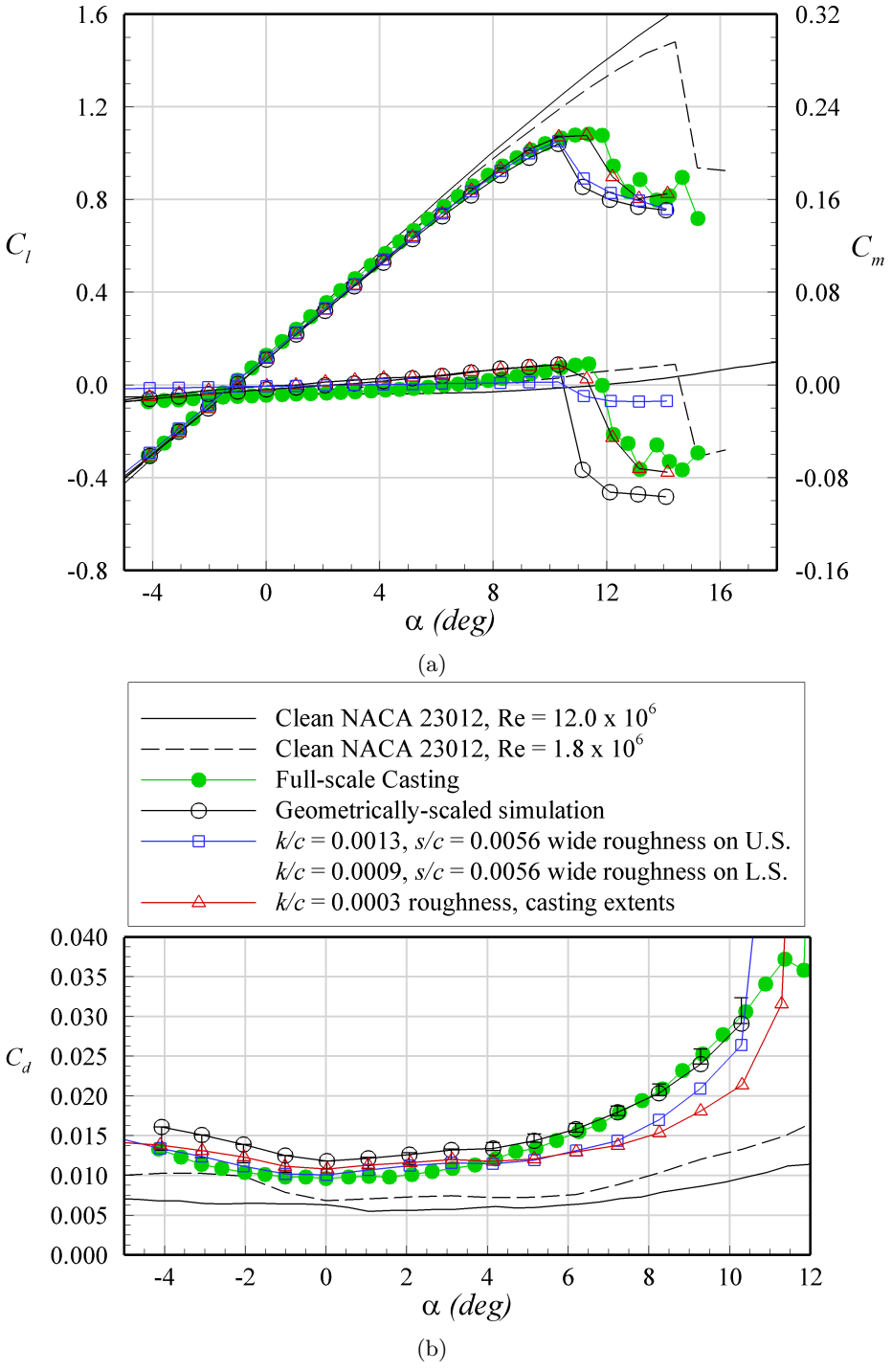

Fig. 4.3 Comparison of C_l, C_m, and C_d of EG1126 glaze ice roughness simulations. The casting data were acquired at Re = 12.0 x 10^6 and M = 0.20, all other ice simulation data were acquired at Re = 1.8 x 10^6 and M = 0.18.

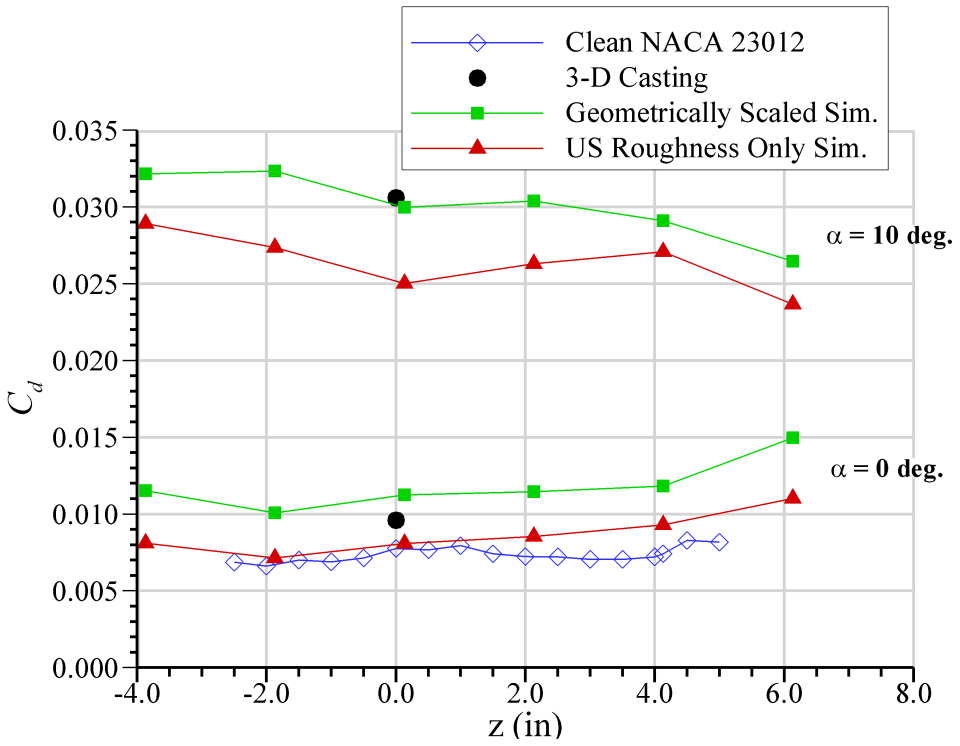

Fig. 4.4 Comparison of sub-scale simulation C_d at multiple spanwise stations for EG1126 ice roughness simulations at Re = 1.8 x 10^6 and M = 0.18. Casting C_d data were obtained at a single spanwise station only at Re = 12.0 x 10^6 and M = 0.20.

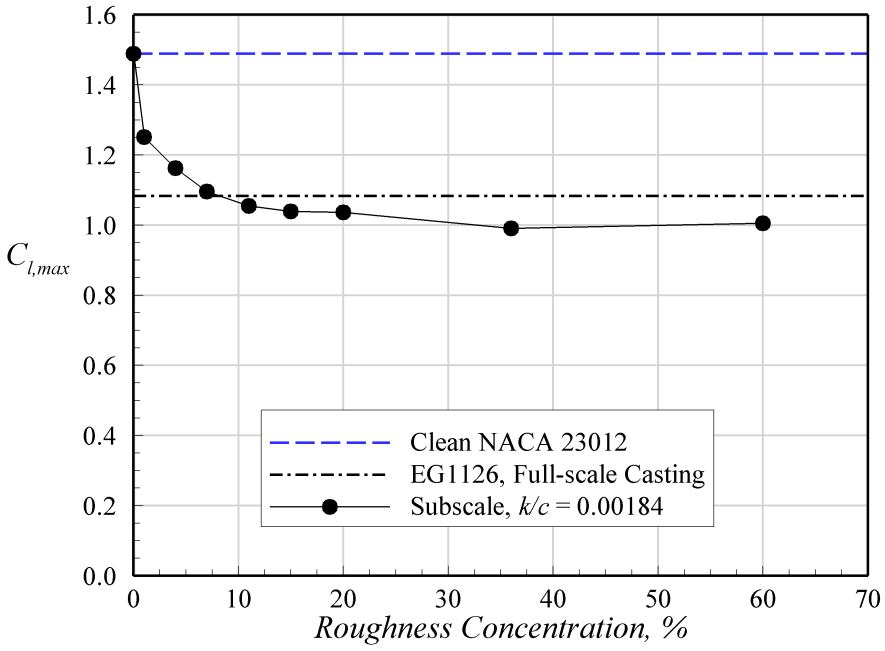

(a)

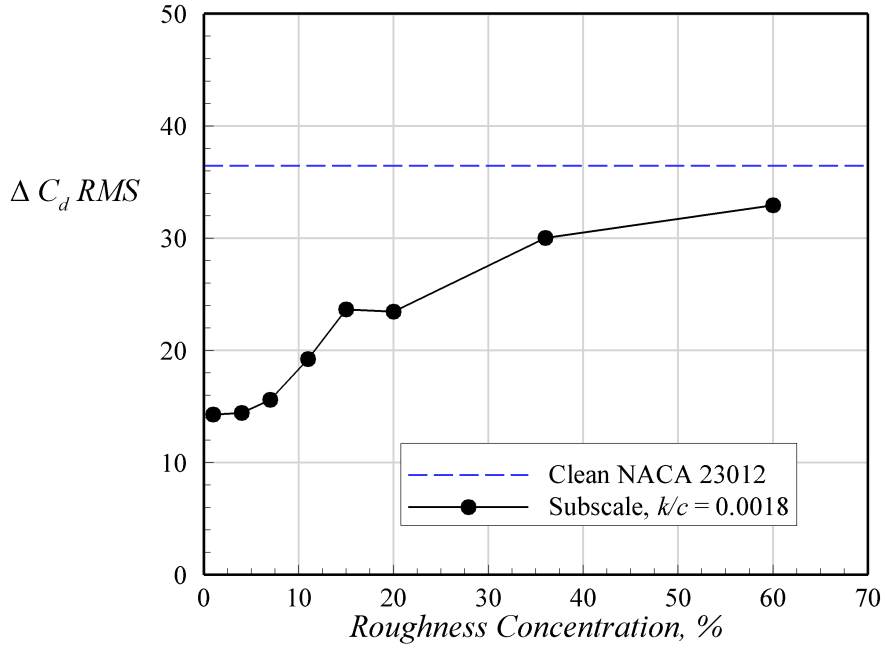

(b)

Fig. 4.5 Effect of simulated roughness concentration on comparisons of (a) $C_{l,max}$ and (b) C_d with the full-scale casting on the NACA 23012 airfoil. The roughness chordwise extents are those of the EG1126 casting: $x/c = 0.000$ to 0.026 on the upper surface and $x/c = 0.004$ to 0.041 on the lower surface.[11] Simulation data obtained at Re = 1.8 x 10^6 and $M = 0.18$, casting data obtained at Re = 12.0 x 10^6 and $M = 0.18$.

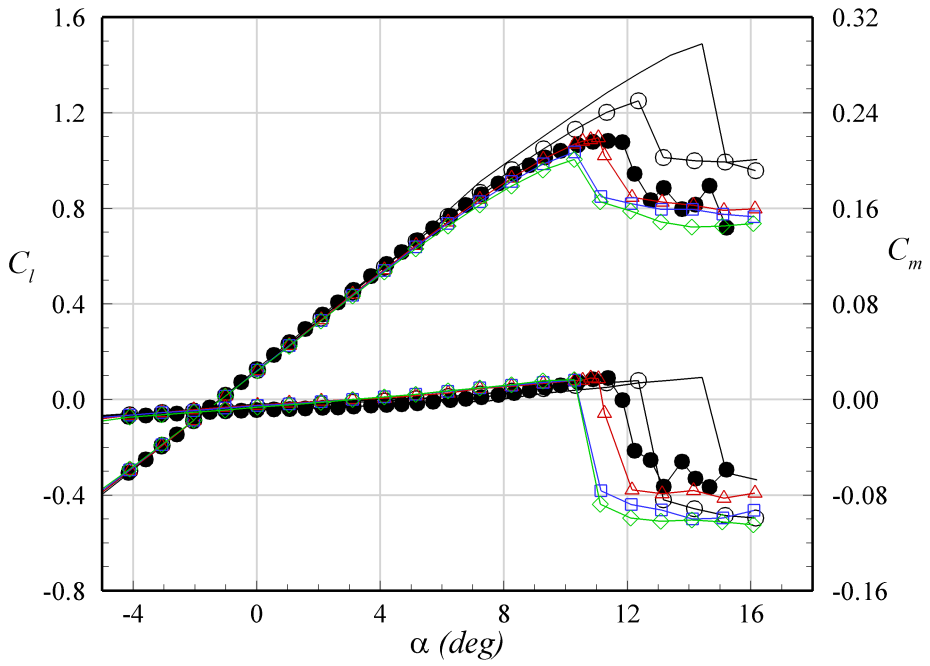

(a)

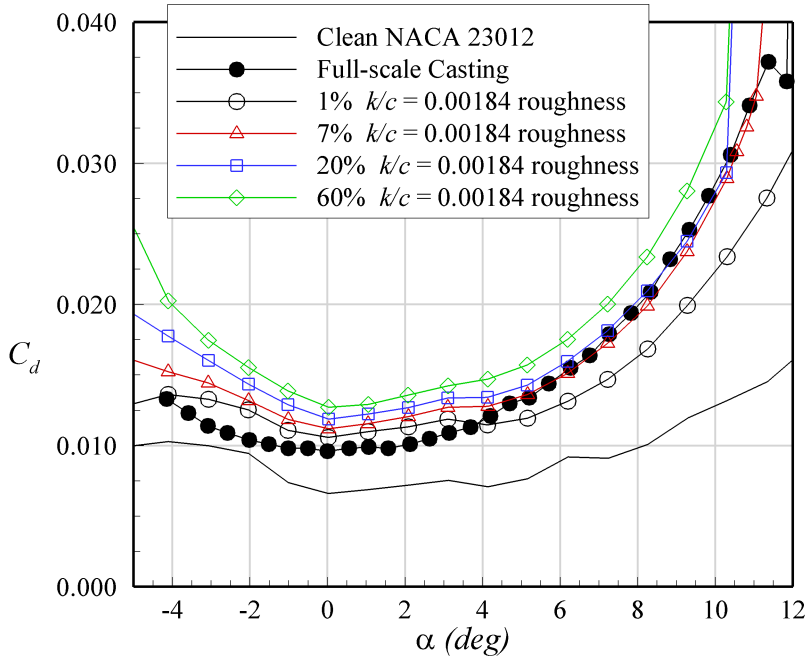

(b)

Fig. 4.6 Effect of roughness concentration on the aerodynamic performance of the NACA 23012 airfoil. Data obtained at Re = 1.8 x 10^6 and M = 0.18.

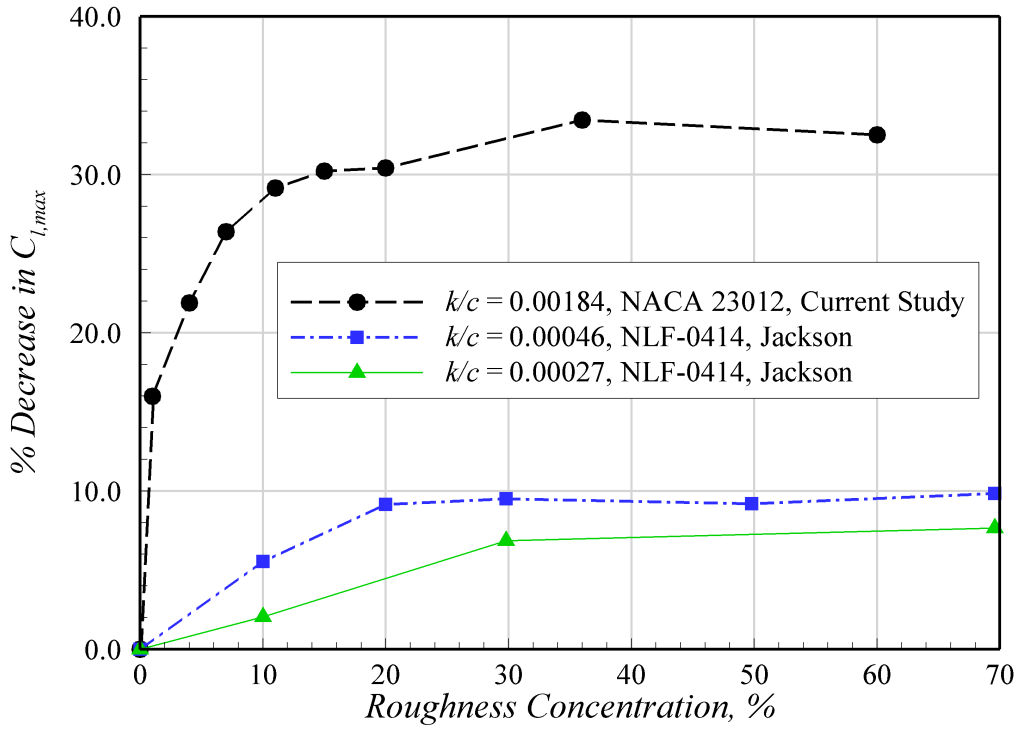

Fig. 4.7 Effect of roughness concentration as a percent reduction in $C_{l,max}$ between iced and clean NACA 23012 and NLF-0414 airfoils. Data from the current study and Jackson[24] at Re = 1.8 x 10^6 and M = 0.18.

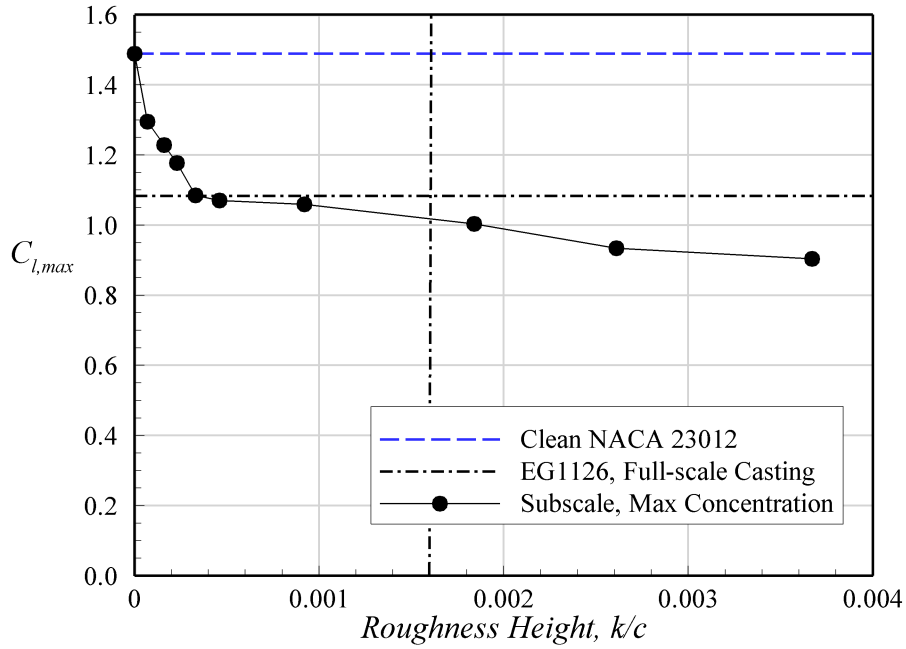

(a)

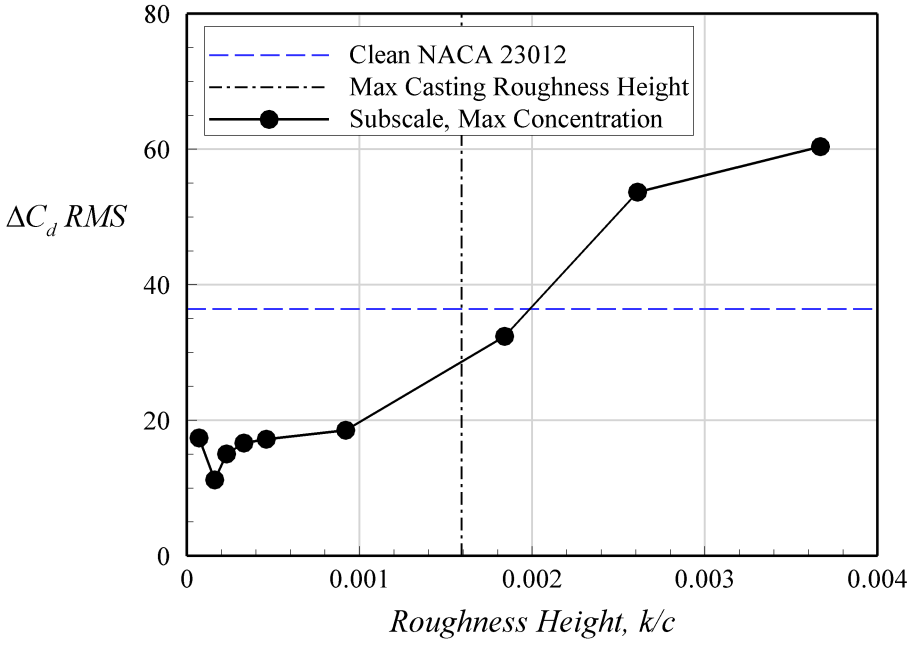

(b)

Fig. 4.8 Effect of simulated roughness height on comparisons of (a) $C_{l,max}$ and (b) C_d with the full-scale EG1126 casting on the NACA 23012 airfoil. The roughness chordwise extents are those of the EG1126 casting, with the exception of the two smallest heights, which have the extents of the EG1134 casting. Simulation data obtained at Re = 1.8 x 10^6 and M = 0.18.

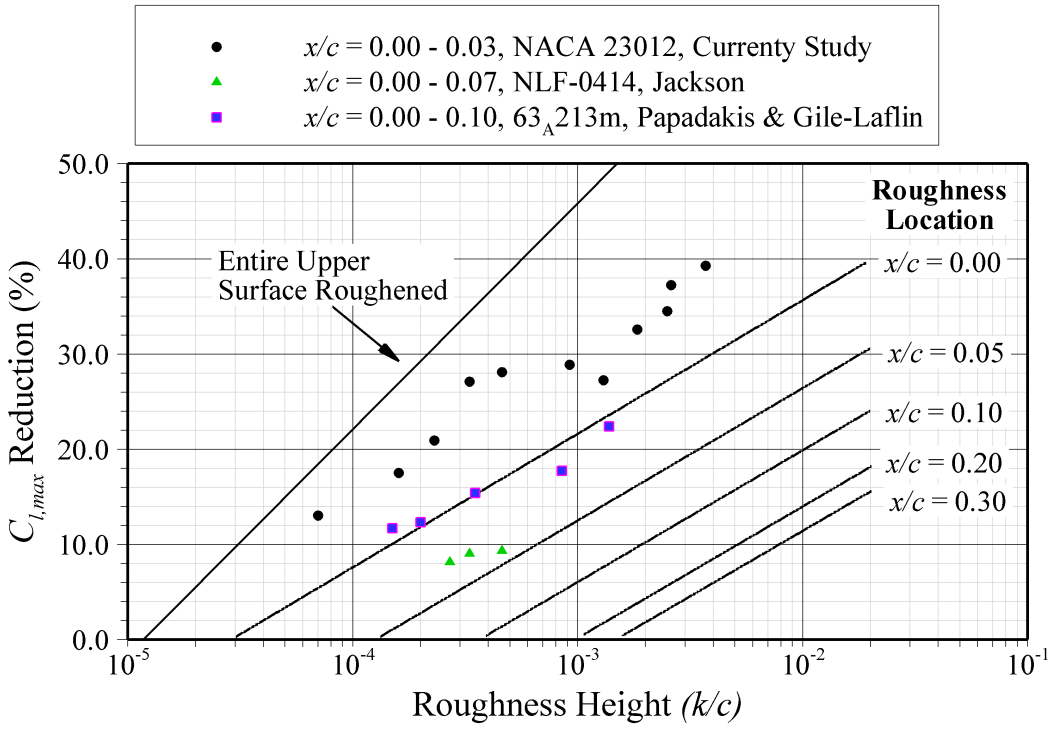

Fig. 4.9 Effect of ice roughness height and location on magnitude of $C_{l,max}$ degradation. The data were obtained from the current study, Jackson,[24] and Papadakis and Gile-Laflin[71] and plotted on Brumby's chart,[23] orginally shown in Fig. 2.3.

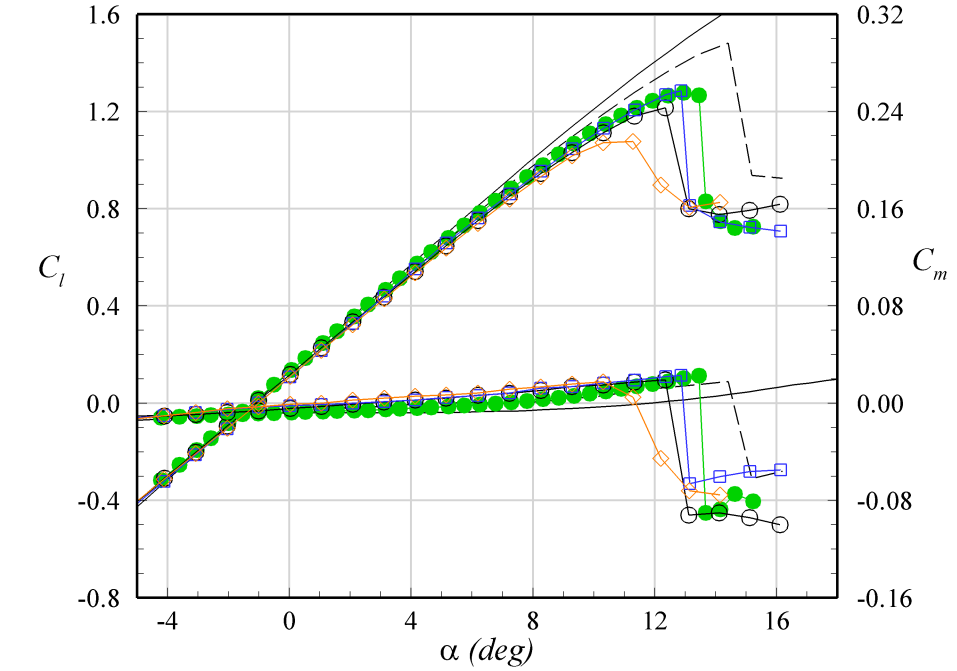

(a)

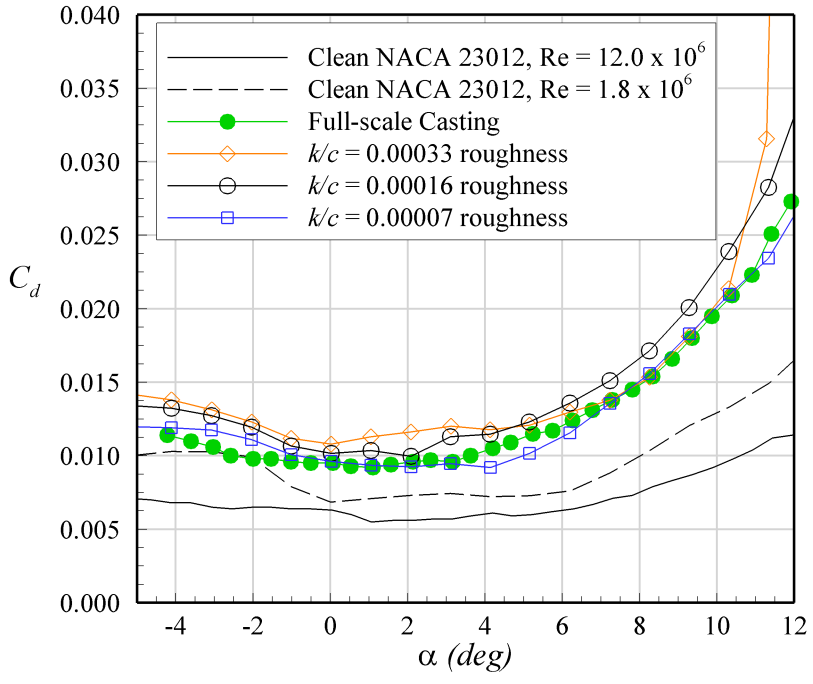

(b)

Fig. 4.10 Comparison of C_l, C_m, and C_d of EG1134 rime ice roughness simulations. The casting data were acquired at Re = 12.0 x 10^6 and M = 0.20, all other ice simulation data were acquired at Re = 1.8 x 10^6 and M = 0.18.

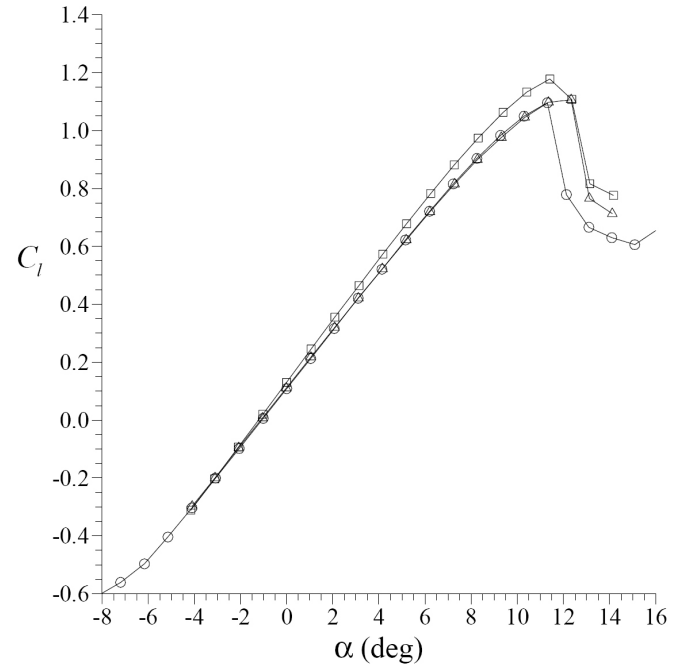

(a)

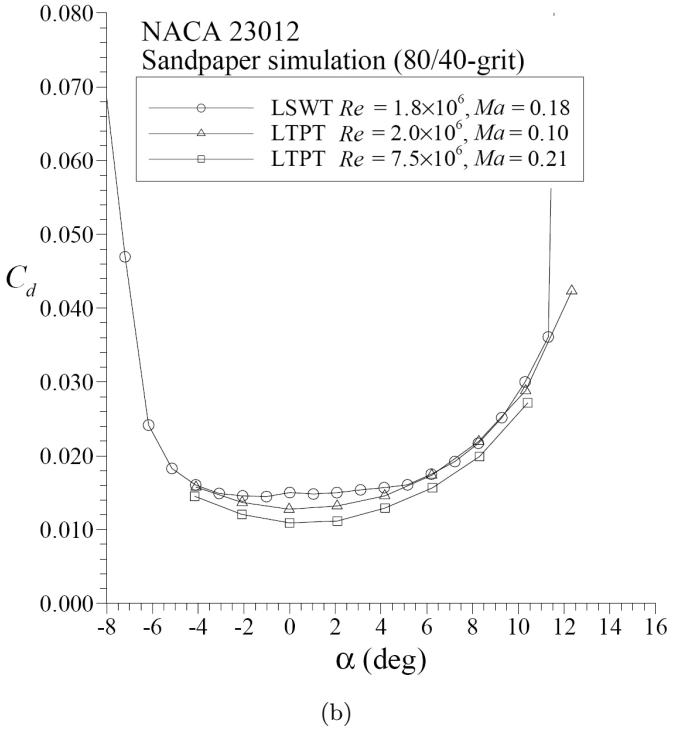

(b)

Fig. 4.11 Comparison of NACA 23012 airfoil performance with sandpaper roughness simple-geometry ice simulations geometrically-scaled to have similar values of k/c on 36-inch chord and 18-inch chord models.[94]

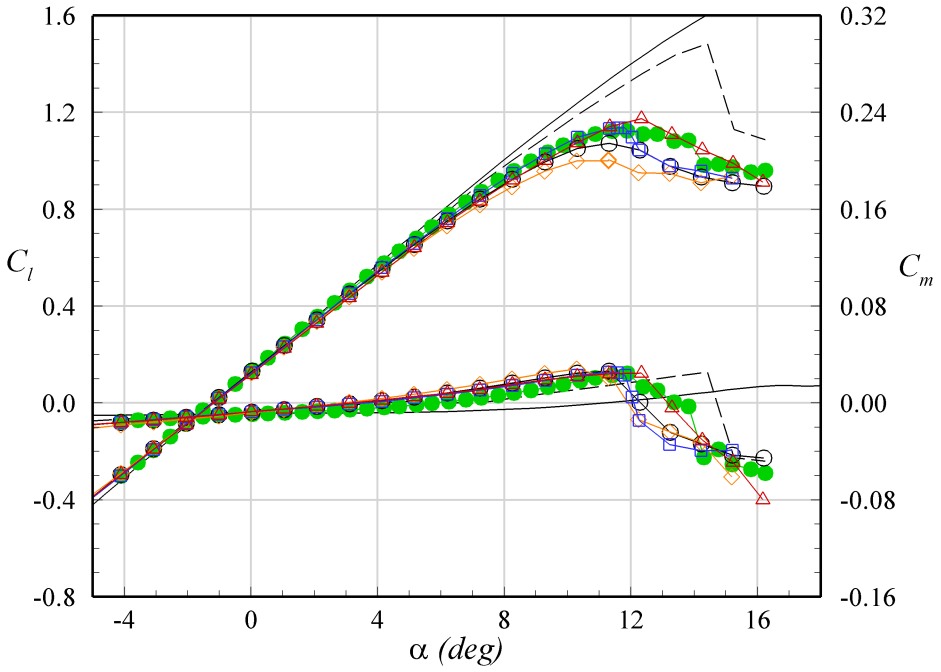

(a)

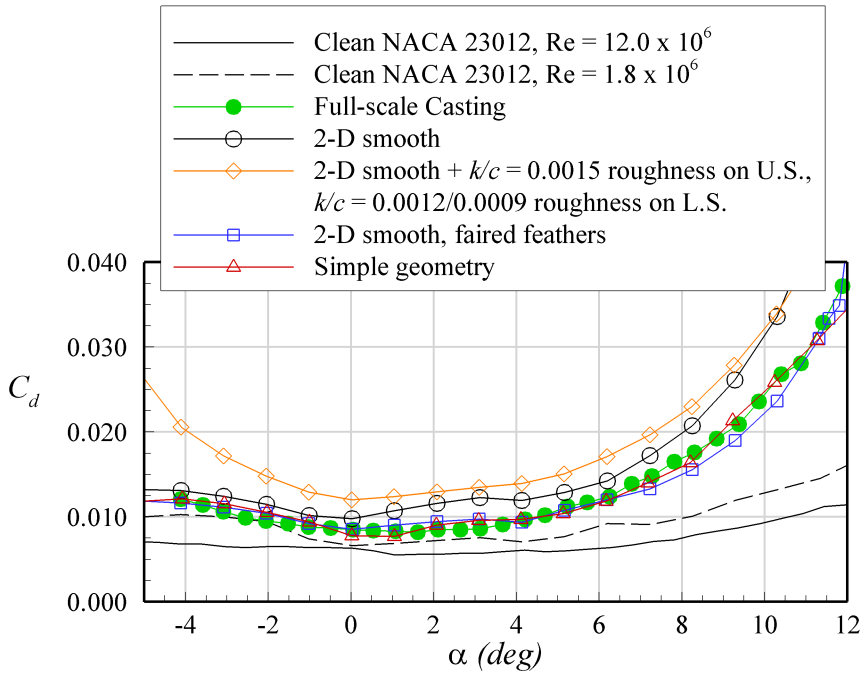

(b)

Fig. 4.12 Comparison of C_l, C_m, and C_d of EG1125 streamwise-ice simulations. The casting data were acquired at Re = 12.0 x 10^6 and M = 0.20, all other ice simulation data were acquired at Re = 1.8 x 10^6 and M = 0.18.

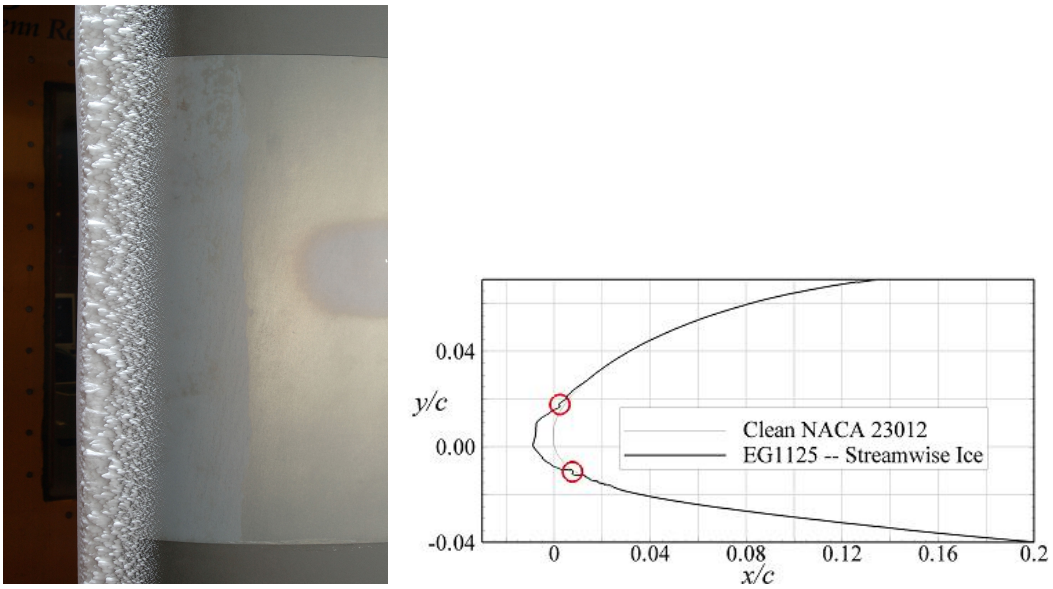

(a) (b)

Fig. 4.13 Photograph of ice feathers on a streamwise-ice accretion located near the leading-edge on the upper surface of a NACA 23012 airfoil and (b) a tracing of the same streamwise-ice accretion with traced feathers circled.[11]

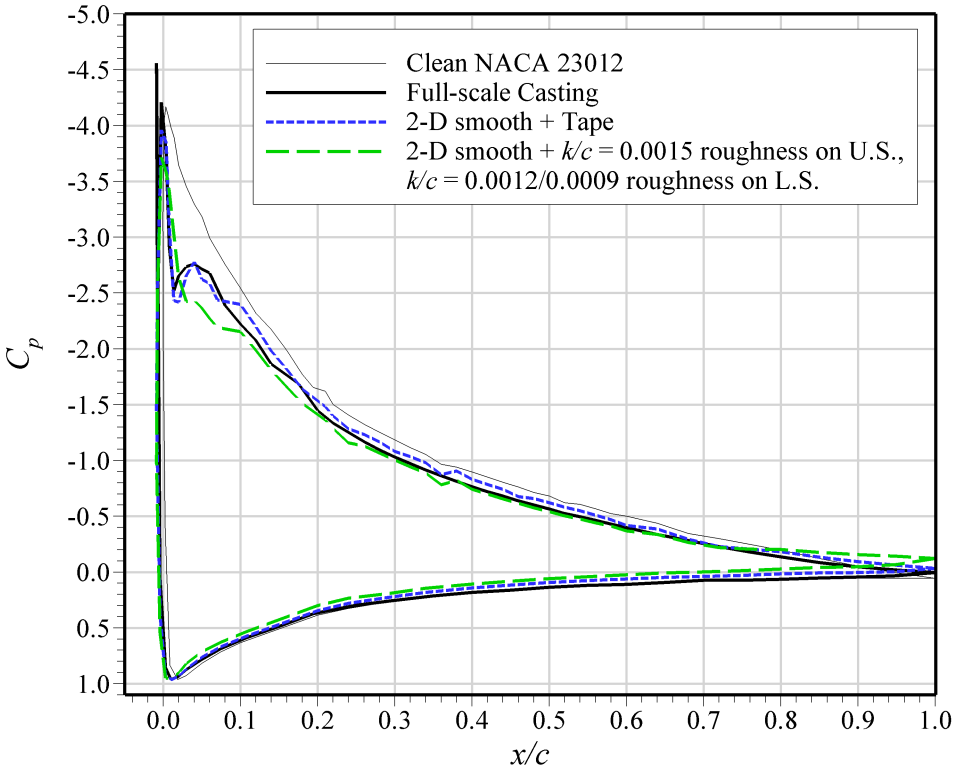

Fig. 4.14 Pressure distribution around EG1125 streamwise-ice simulations at $\alpha = 10$ deg.

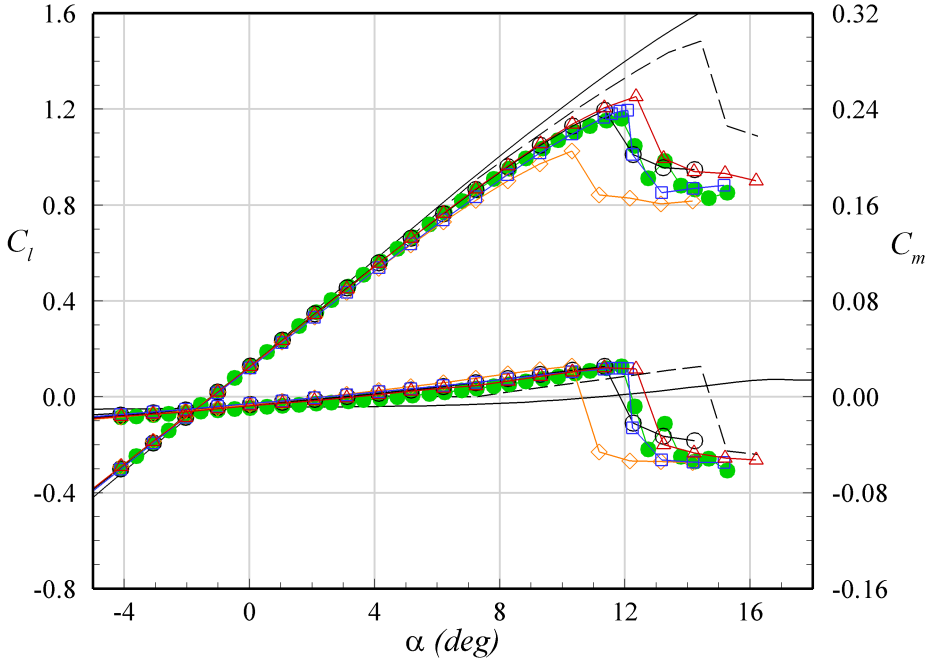

(a)

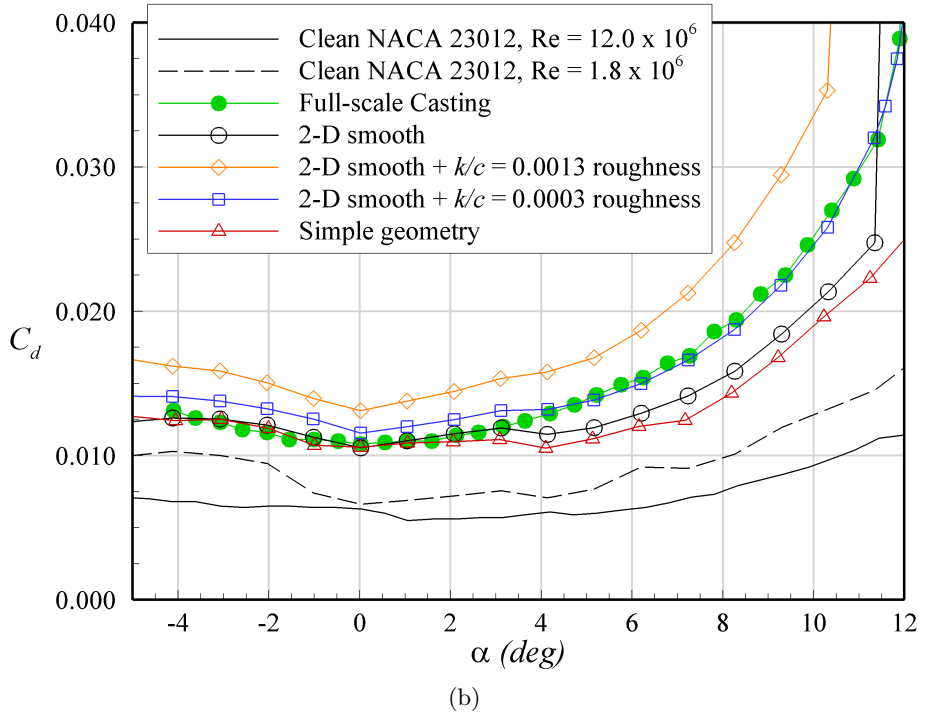

(b)

Fig. 4.15 Comparison of C_l, C_m, and C_d of various 2-D smooth streamwise-ice simulations with the EG1162 streamwise-ice casting. The casting data were acquired at $Re = 12.0 \text{ x } 10^6$ and $M = 0.20$, and the simulation data were acquired at $Re = 1.8 \text{ x } 10^6$ and $M = 0.18$.[11]

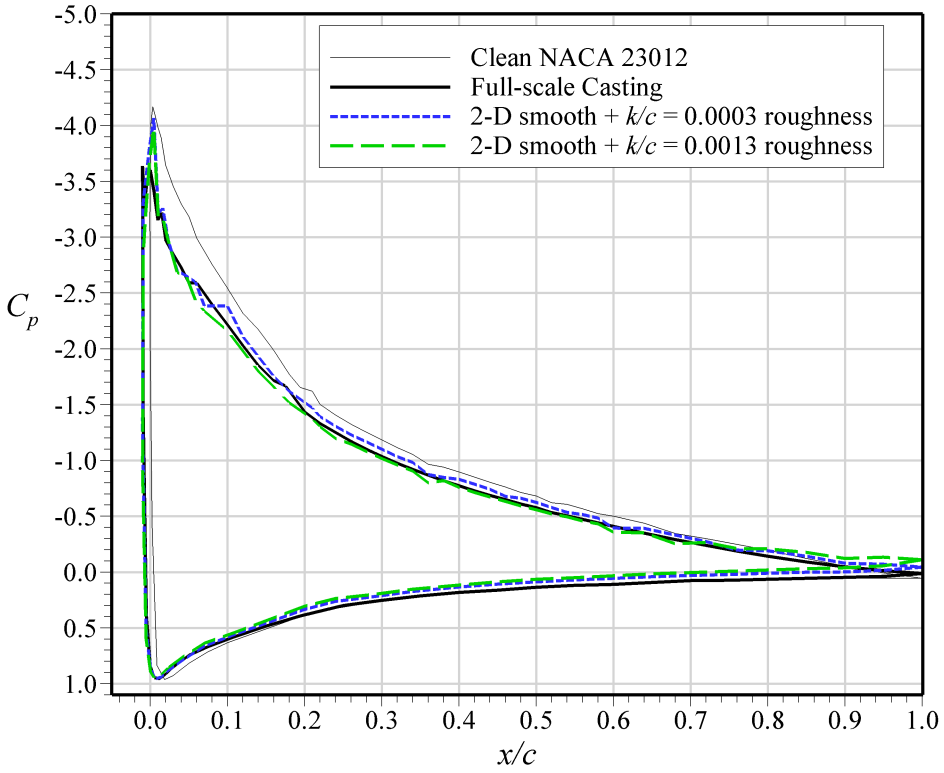

Fig. 4.16 Pressure distribution around EG1162 streamwise-ice simulations at $\alpha = 10$ deg.

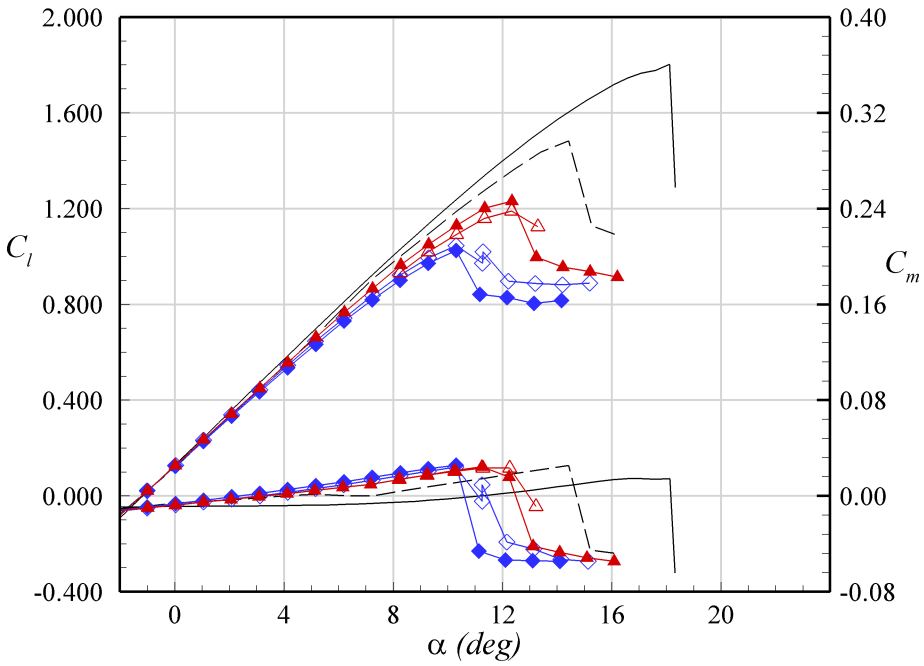

(a)

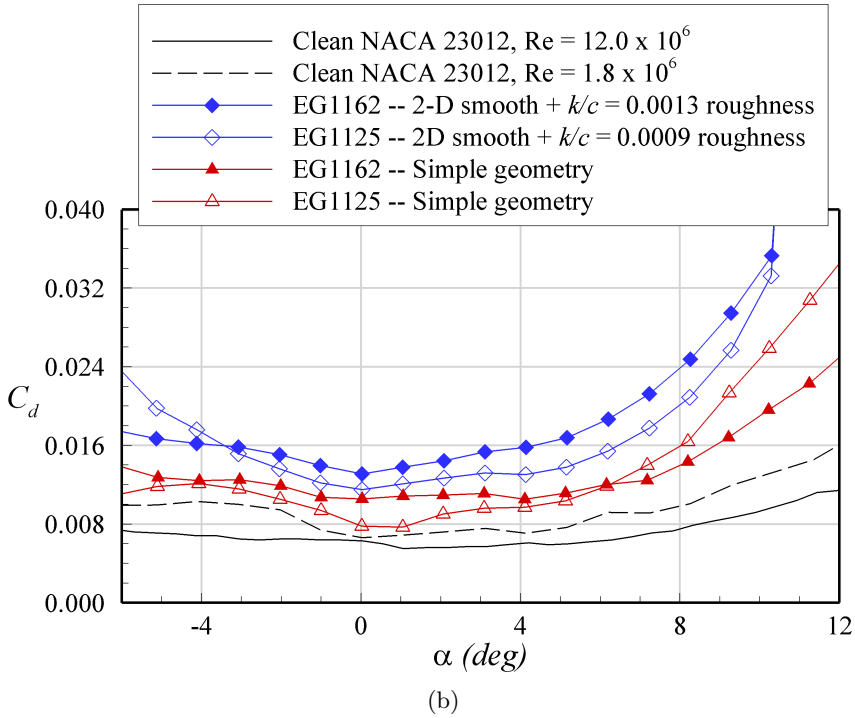

(b)

Fig. 4.17 Effect of gross leading-edge ice geometry of streamwise-ice simulations on NACA 23012 performance (balance data). $Re = 1.8 \times 10^6$ and $M = 0.18$.

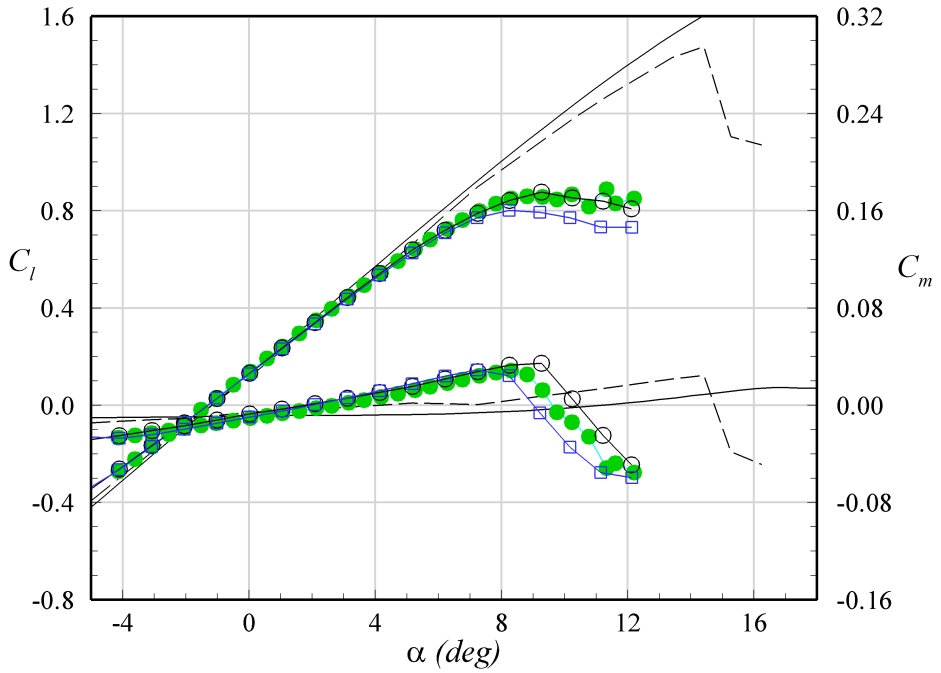

(a)

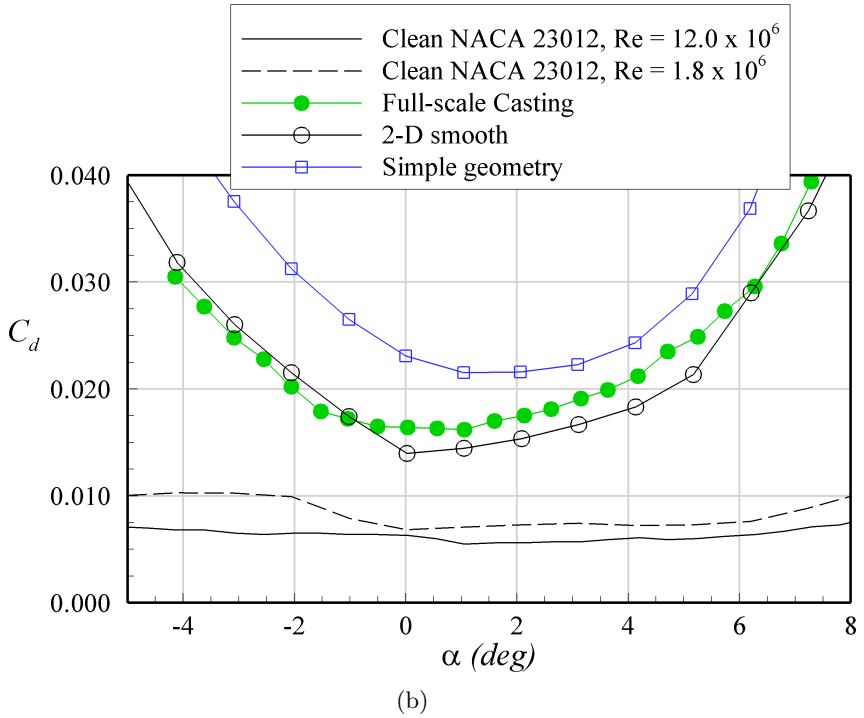

(b)

Fig. 4.18 Comparison of aerodynamic performance of sub-scale horn-ice simulations at Re = 1.8 x 10^6 and M = 0.18 with the corresponding full-scale casting at Re = 12.0 x 10^6 and M = 0.20.[11]

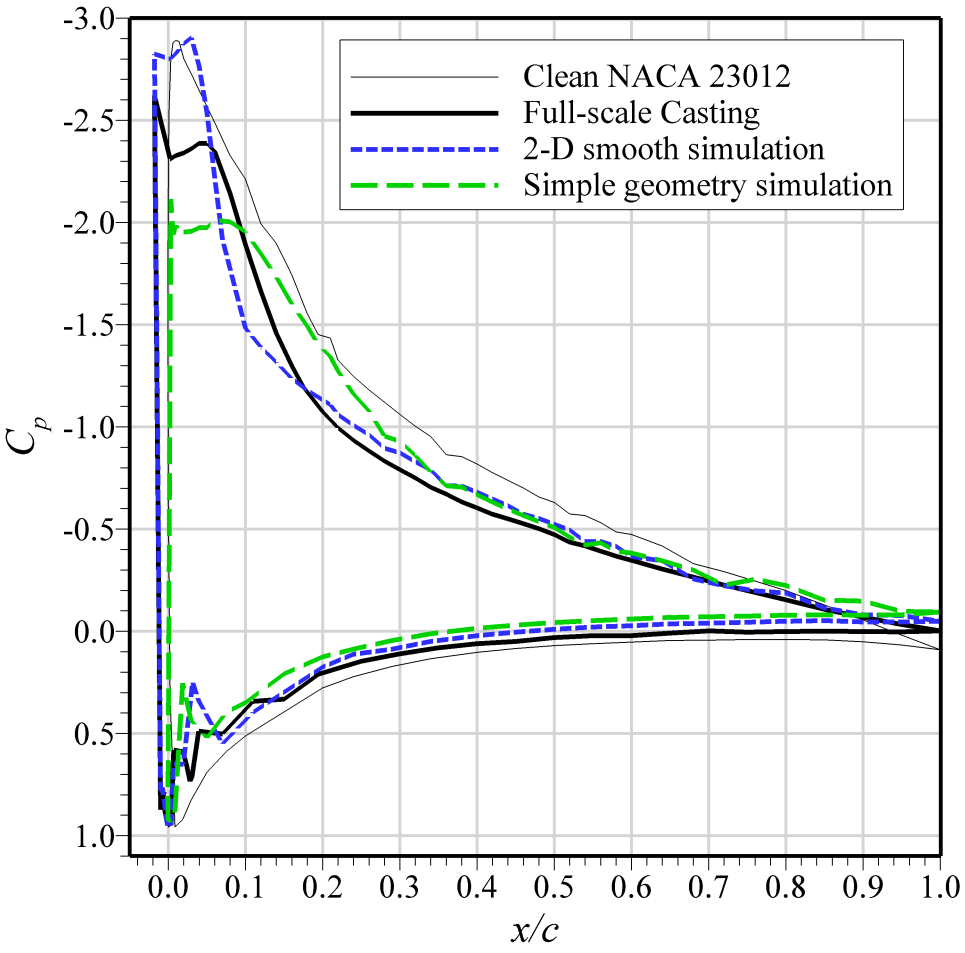

Fig. 4.19 Pressure distribution around EG1164 horn-ice simulations at $\alpha = 8$ deg.

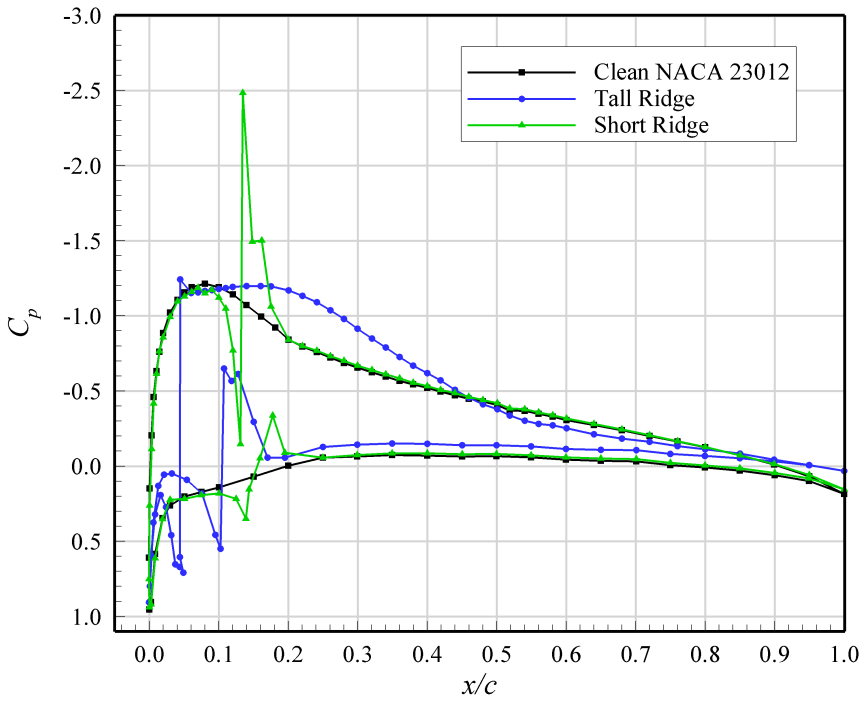

Fig. 4.20 Effect of tall and short ridges on pressure distribution of NACA 23012 airfoil at Re = 12.0 x 10^6 and M = 0.20 and a matched angle of attack of 3.0 deg. Data from Broeren.[29]

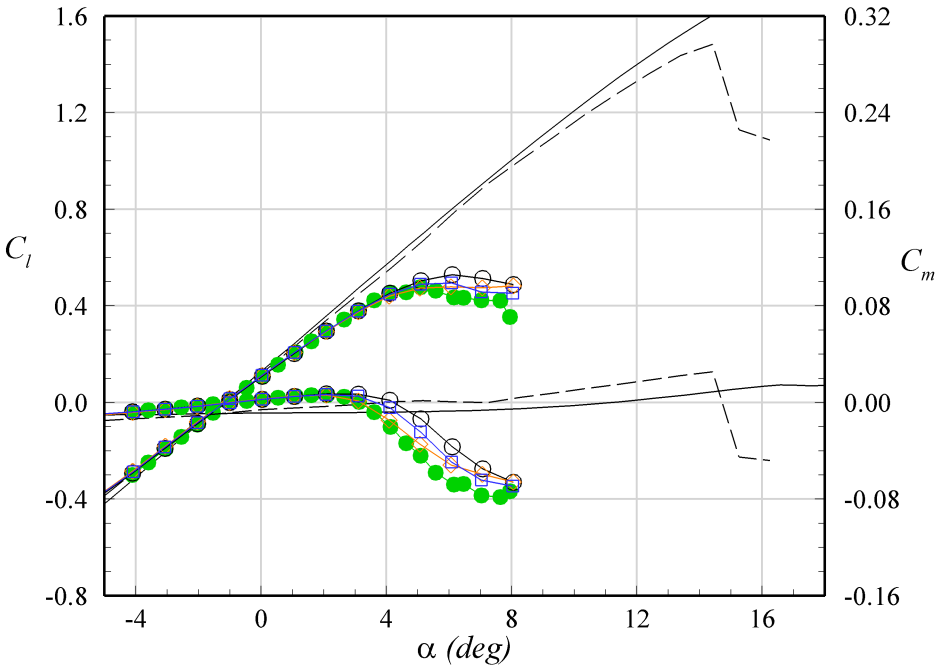

(a)

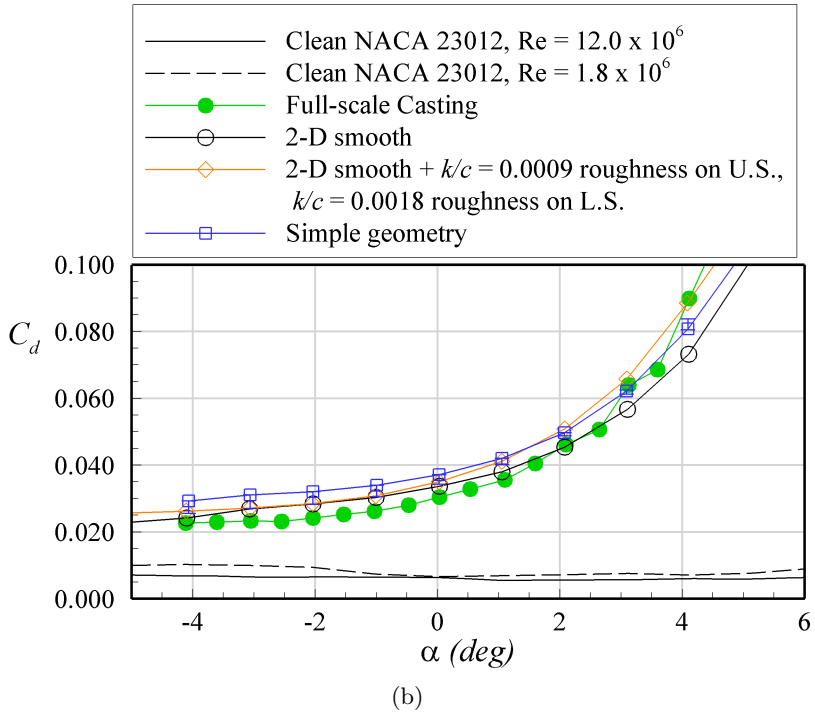

(b)

Fig. 4.21 Comparison of aerodynamic performance of sub-scale tall spanwise-ridge ice simulations at Re = 1.8 x 10^6 and M = 0.18 with the corresponding full-scale casting at Re = 12.0 x 10^6 and M = 0.20.[11]

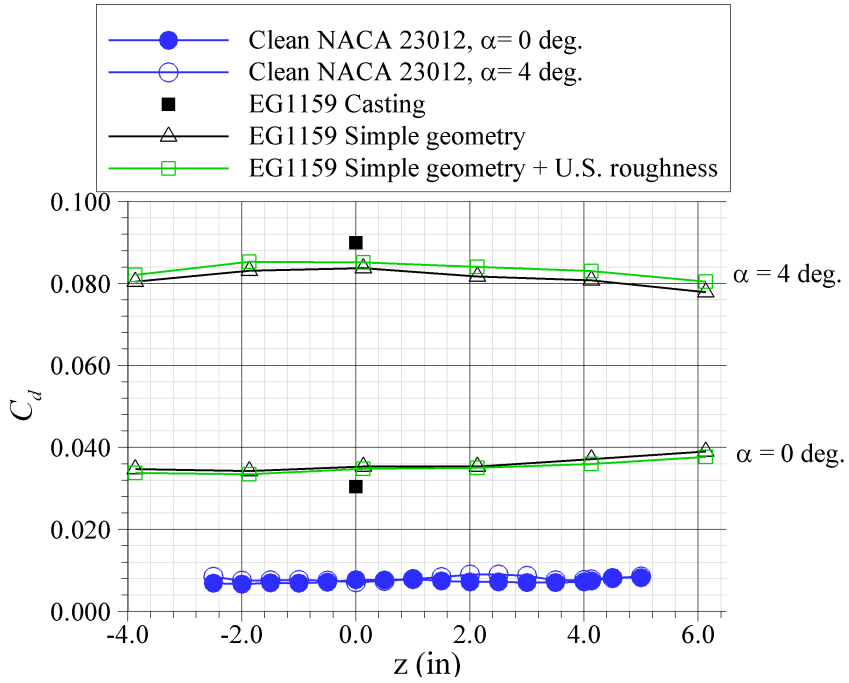

Fig. 4.22 Comparison of sub-scale simulation C_d at multiple spanwise stations for EG1159 tall-ridge ice simple-geometry simulations and casting. (Casting data at Re = 12.0 x 10^6 and M = 0.20, subscale simulation data at Re = 1.8 x 10^6 and M = 0.18.

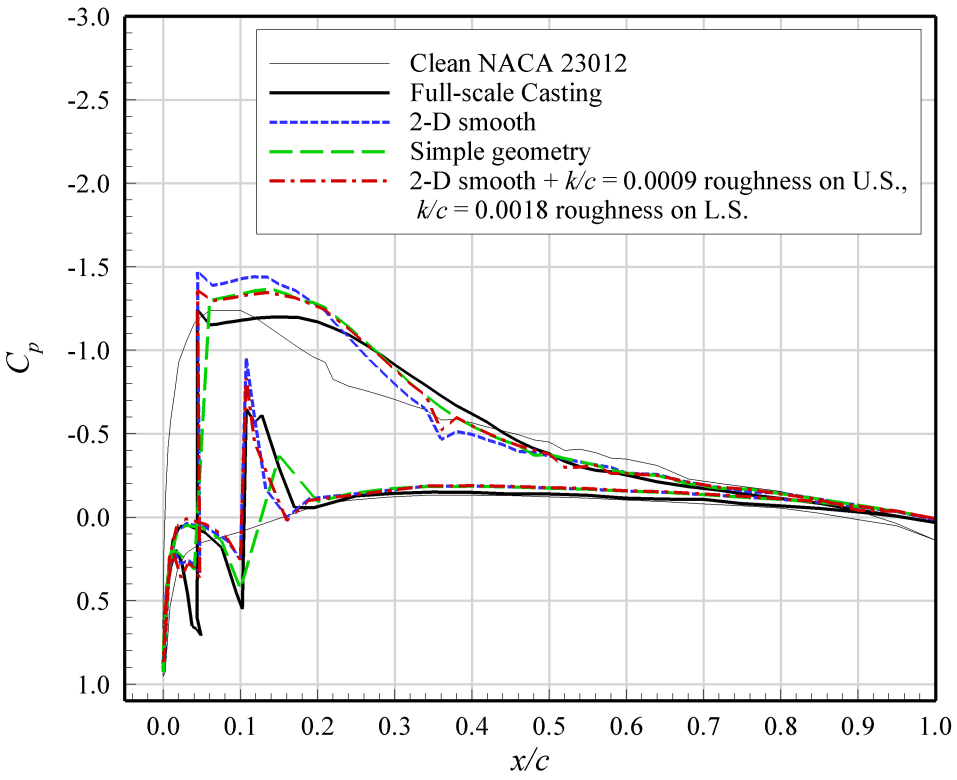

Fig. 4.23 Pressure distribution around EG1159 spanwise-ridge ice simulations at α = 3 deg.

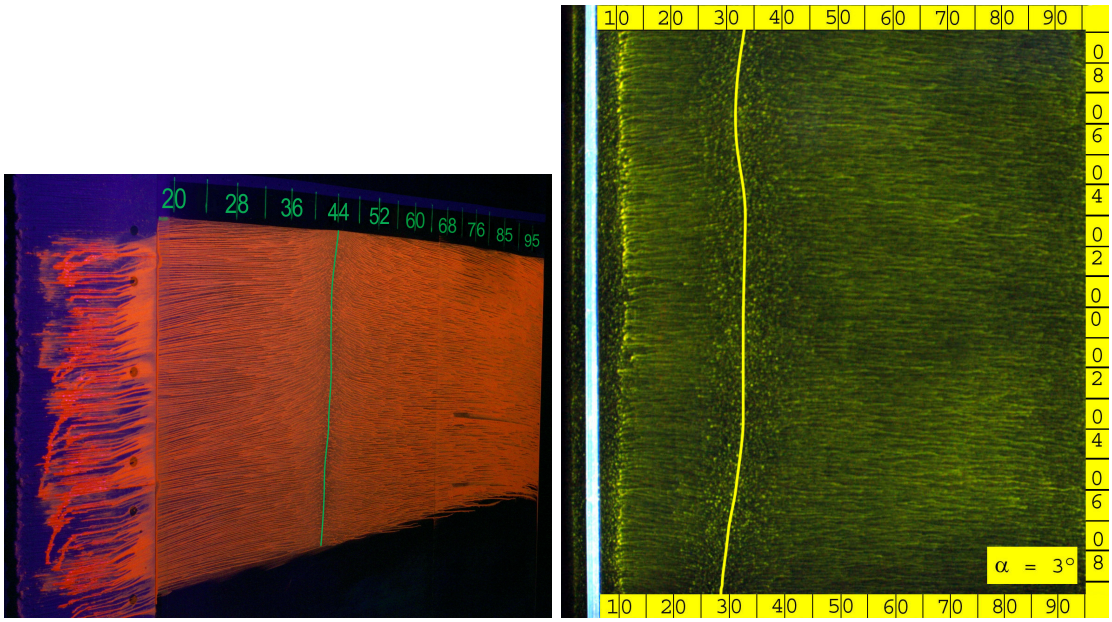

(a) (b)

Fig. 4.24 Surface oil-flow visualization images of EG1159 spanwise-ridge ice simulations on NACA 23012 airfoil at $\alpha = 3$ deg.: (a) Full-scale casting at $Re = 7.8$ x 10^6 and $M = 0.20$ and (b) sub-scale 2-D smooth simulation at $Re = 1.8$ x 10^6 and $M = 0.18$. In the photos, the flow is from left to right. The estimated mean separation bubble reattachment location has been highlighted in each case.

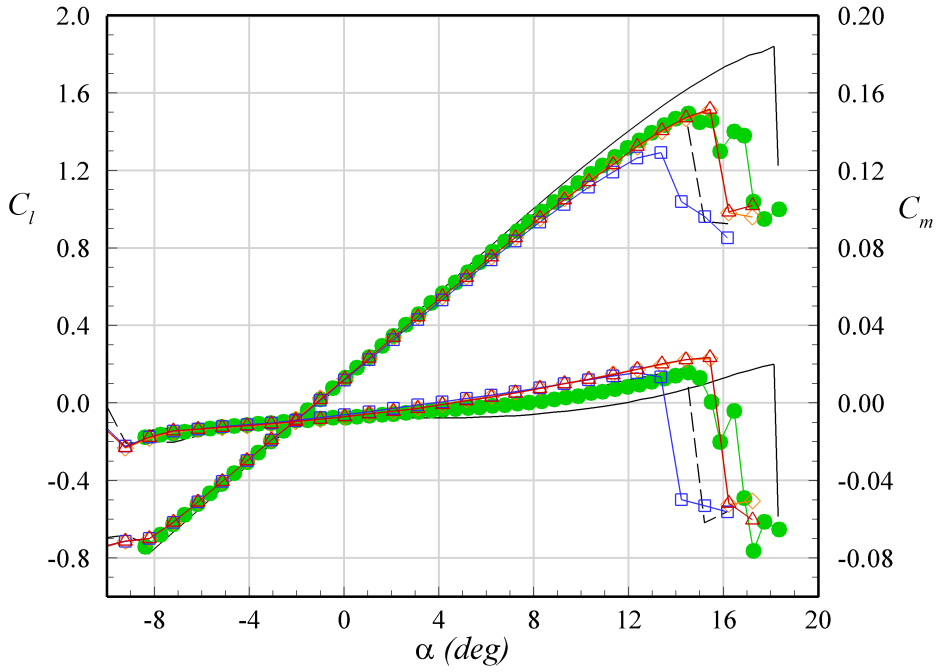

(a)

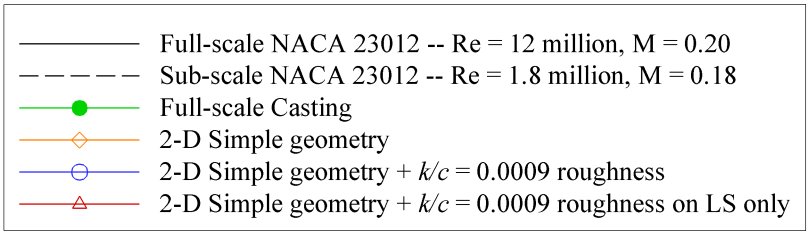

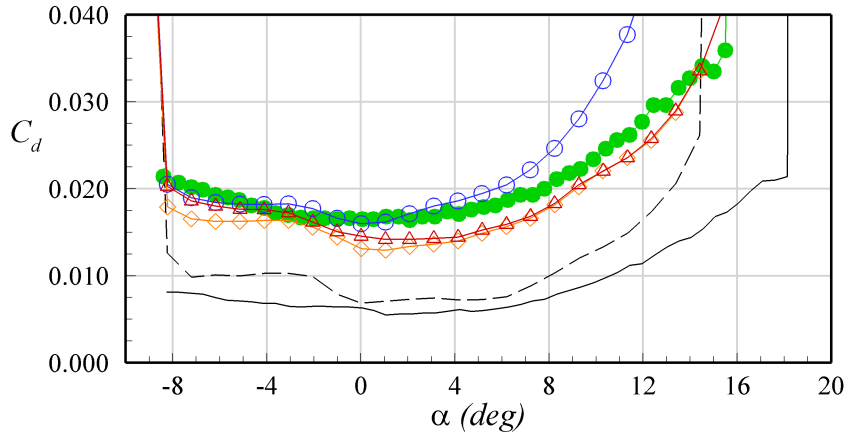

(b)

Fig. 4.25 Comparison of aerodynamic performance of 2D sub-scale NGO671 short spanwise-ridge ice simulations at $Re = 1.8$ x 10^6 and $M = 0.18$ with the corresponding full-scale casting at $Re = 15.9$ x 10^6 and $M = 0.20$.[15]

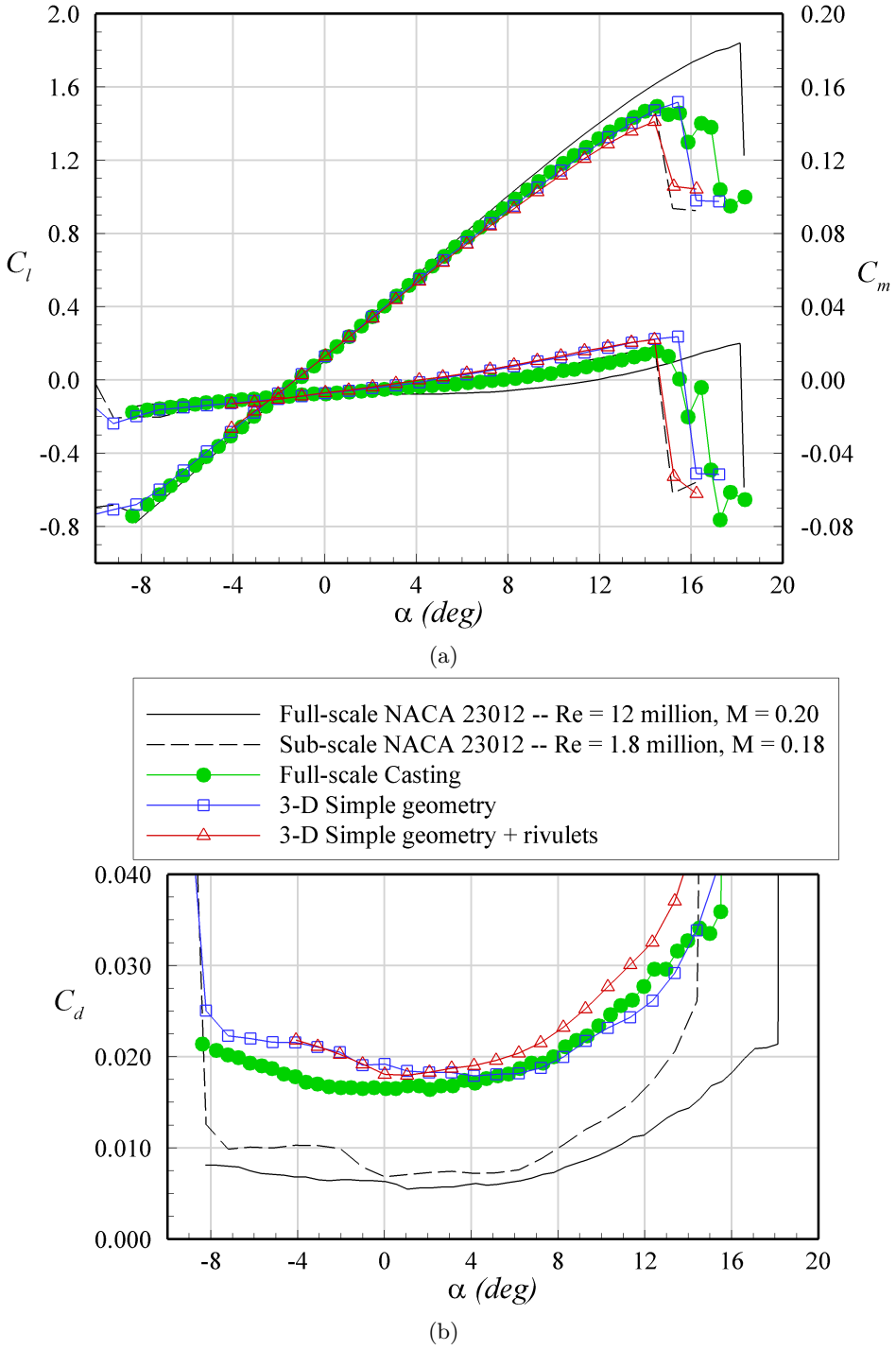

Fig. 4.26 Comparison of aerodynamic performance of 3D NGO671 sub-scale short spanwise-ridge ice simulations at $Re = 1.8$ x 10^6 and $M = 0.18$ with the corresponding full-scale casting at $Re = 15.9$ x 10^6 and $M = 0.20$.[15]

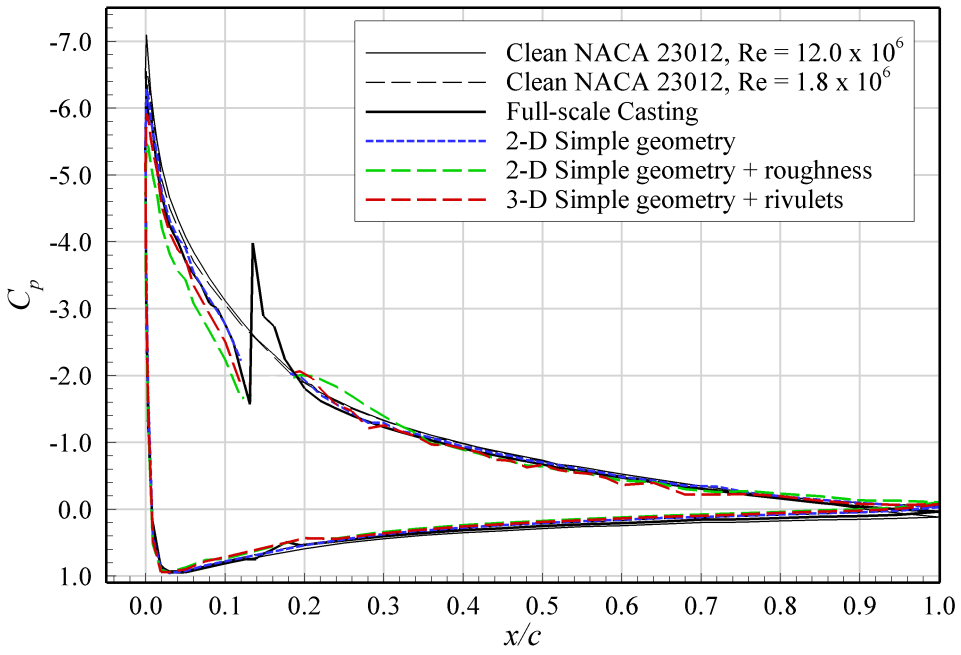

Fig. 4.27 Pressure distribution around NGO671 short ridge-ice simulations at $\alpha = 13$ deg.

References

[1] Busch, G., Broeren, A., and Bragg, M., "Aerodynamic Simulation of a Horn-Ice Accretion on a Subscale Model," *J. Aircraft*, Vol. 45, No. 2, 2008, pp. 604–613.

[2] Lynch, F. and Khodadoust, A., "Effects of Ice Accretions on Aircraft Aerodynamics," *Progress in Aerospace Sciences*, Vol. 37, 2001, pp. 669–767.

[3] Bragg, M., Broeren, A., Addy, H., Potapczuk, M., Guffond, D., and Montreuil, E., "Airfoil Ice-Accretion Aerodynamics Simulation," AIAA-2007-0085, *45th AIAA Aerospace Sciences Meeting & Exhibit*, Reno, NV, Jan. 2007.

[4] Bragg, M. B., Broeren, A. P., and Blumenthal, L. A., "Iced-Airfoil Aerodynamics," *Progress in Aerospace Sciences*, Vol. 41, July 2005, pp. 323–362.

[5] Busch, G., "Ice Accretion Aerodynamic Simulation on a Subscale Model," M.S. Thesis, University of Illinois at Urbana-Champaign, 2006.

[6] Busch, G., Broeren, A., and Bragg, M., "Aerodynamic Simulation of a Horn-ice Accretion on a Subscale Model," AIAA-2007-0087, *45th AIAA Aerospace Sciences Meeting & Exhibit*, Reno, NV, Jan. 2007.

[7] Broeren, A., Busch, G., and Bragg, M., "Aerodynamic Fidelity of Ice Accretion Simulation on a Subscale Model," SAE Paper 2007-01-3285, 2007.

[8] Broeren, A., Busch, G., and Bragg, M., "Aerodynamic Fidelity of Ice Accretion Simulation on a Subscale Model," *SAE 2007 Transactions: Journal of Aerospace*, Vol. 116, Aug. 2008, pp. 560–575.

[9] Broeren, A., Bragg, M., H.E. Addy, J., Lee, S., Moens, F., and Guffond, D., "Effect of High-Fidelity Ice Accretion Simulations on the Performance of a Full-Scale Airfoil Model," AIAA-2008-0434, *46th AIAA Aerospace Sciences Meeting & Exhibit*, Reno, NV, Jan. 2008.

[10] CassouDeSalle, D., Gilliot, A., Geiler, C., Monnier, J., Broeren, A., and H.E. Addy, J., "Experimental Investigations of Simulated Ice Accretions at High Reynolds Numbers in the Onera F1 Wind Tunnel," *AIAA-2009-4265*, 1st AIAA Atmospheric & Space Environments Conference, San Antonio, TX, Jun. 2009.

[11] Busch, G., Broeren, A., and Bragg, M., "Aerodynamic Fidelity of Sub-Scale Two-Dimensional Ice Accretion Simulations," AIAA-2008-7062, *26th AIAA Applied Aerodynamics Conference*, Honolulu, HI, Aug. 2008.

[12] Busch, G. and Bragg, M., "Experimental Study of Full-Scale Iced Airfoil Aerodynamic Performance Using Sub-Scale Simulations," AIAA-2009-4264, *1st AIAA Atmospheric & Space Environments Conference*, San Antonio, TX, Jun. 2009.

[13] Tani, I., "Low-speed Flows Involving Bubble Separations," *Progress in Aerospace Sciences*, Vol. 5, 1964, pp. 70–103.

[14] McCullough, G. and Gault, D., "Examples of Three Representative Types of Airfoil-Section Stall at Low Speed," *NACA TN 2502*, Sep. 1951.

[15] Broeren, A., Whalen, E., Busch, G., and Bragg, M., "Aerodynamic Simulation of Runback Ice Accretion," AIAA-2009-4261, *1st AIAA Atmospheric & Space Environments Conference*, San Antonio, TX, Jun. 2009.

[16] Papadakis, M., Alansatan, S., and Seltmann, M., "Experimental Study of Simulated Ice Shapes ona NACA 0011 Airfoil," *AIAA-1999-0096*, 37th AIAA Aerospace Sciences Meeting & Exhibit, Reno, NV, Jan. 1999.

[17] Kim, H., "Effects of Leading-edge Ice Accretion Geometry on Airfoil Performance," M.S. Thesis, University of Illinois at Urbana-Champaign, 2004.

[18] Lee, S., "Effects of Supercooled Large Droplet Icing on Airfoil Aerodynamics," Ph.D. Dissertation, University of Illinois at Urbana-Champaign, 2001.

[19] H. E. Addy, J. and Chung, J. J., "A Wind Tunnel Study of Icing Effects on a Natural Laminar Flow Airfoil," *AIAA-2000-0095*, 38th AIAA Aerospace Sciences Meeting & Exhibit, Reno, NV, Jan. 2000.

[20] Papadakis, M., Laflin, B. E. G., Youssef, G. M., and Ratvasky, T. P., "Aerodynamic Scaling Experiments with Simulated Ice Accretions," *AIAA-2001-0833*, 39th AIAA Aerospace Sciences Meeting & Exhibit, Reno, NV, Jan. 2001.

[21] Lee, S., Kim, H., and Bragg, M. B., "Investigation of Factors that Influence Iced-Airfoil Aerodynamics," *AIAA-2000-0099*, 38th AIAA Aerosapce Sciences Meeting & Exhibit, Reno, NV, Jan. 2000.

[22] Cummings, M., "Airfoil Boundary-Layer Transition Due to Large Isolated 3-D Roughness Elements in a Favorable Pressure Gradient," M.S. Thesis, University of Illinois at Urbana-Champaign, 1995.

[23] Brumby, R. E., "Wing Surface Roughness – Cause & Effect," *D.C. Flight Approach*, Vol. 41, Jan. 1979, pp. 2–7.

[24] Jackson, D. G., "Effect of Simulated Ice and Residual Ice Roughness on the Performance of a Natural Laminar Flow Airfoil," M.S. Thesis, University of Illinois at Urbana-Champaign, 1999.

[25] Papadakis, M., Yeong, H., Chandrasekharan, R., Hinson, M., and Ratvasky, T., "Effects of Roughness on the Aerodynamic Performance of a Business Jet Tail," *AIAA-2002-0242*, 40th AIAA Aerospace Sciences Meeting & Exhibit, Reno, NV, Jan. 2002.

[26] Wright, W., "Validation Results for LEWICE 3.0," AIAA-2005-1243, *43rd AIAA Aerospace Sciences Meeting & Exhibit*, Reno, NV, Jan. 2005.

[27] Kim, H. S. and Bragg, M. B., "Effects of Leading-Edge Ice Accretion Geometry on Airfoil Performance," *AIAA-1999-3150*, 17^{th} AIAA Applied Aerodynamics Conference, Norfolk, VA, Jun. 1999.

[28] Bragg, M. and Gregorek, G., "Aerodynamic Characteristics of Airfoils with Ice Accretion," AIAA-1982-0282, *20^{th} AIAA Aerospace Sciences Meeting*, Orlando, FL, Jan. 1982.

[29] Broeren, A., private communications, University of Illinois, Urbana, IL, 2007.

[30] Blumenthal, L. A., Busch, G. T., Broeren, A. P., and Bragg, M. B., "Issues in Ice Accretion Aerodynamic Simulation on a Subscale Model," *AIAA-2006-0262*, 44^{th} AIAA Aerospace Sciences Meeting & Exhibit, Reno, NV, Jan. 2006.

[31] Pan, J. and Loth, E., "Effect of Airfoil Geometry on Performance with Simulated Ice Accretions, Volume 2: Numerical Investigation," *DOT/FAA/AR-3/65*, Aug. 2003.

[32] Chung, J., Reehorst, A., Choo, Y., Potapczuk, M., and Slater, J., "Navier-Stokes Analysis of Flowfield Characteristics of an Ice-Contaminated Aircraft Wing," *J. Aircraft*, Vol. 37, No. 6, 2000, pp. 947–959.

[33] Gurbacki, H. M., "Ice-Induced Unsteady Flowfield Effects on Airfoil Performance," Ph.D. Dissertation, University of Illinois at Urbana-Champaign, 2003.

[34] Roberts, W., "Calculation of Laminar Separation Bubbles and Their Effect on Airfoil Performance," *AIAA Journal*, Vol. 18, No. 1, 1980.

[35] Lee, S., private communications, University of Illinois, Urbana, IL, 2008.

[36] Jacobs, J. J. and Bragg, M. B., "Particle Image Velocimetry Measurements of the Separation Bubble on an Iced Airfoil," *AIAA-2006-3646*, 24^{th} AIAA Applied Aerodynamics Conference, San Francisco, CA, Jun. 2006.

[37] Jacobs, J., "Iced Airfoil Separation Bubble Measurements by Particle Image Velocimetry," Ph.D. Dissertation, University of Illinois at Urbana-Champaign, 2007.

[38] Blumenthal, L., "Surface Pressure Measurement on a Three-Dimensional Ice Shape," M.S. Thesis, University of Illinois at Urbana-Champaign, 2005.

[39] Mabey, D., "Analysis and Correlation of Data on Pressure Fluctuations in Separated Flow," *Journal of Aircraft*, Vol. 9, No. 9, 1972, pp. 642–645.

[40] Farabee, T. and Casarella, M., "Measurements of Fluctuating Wall Pressure for Separated/Reattached Boundary Layer Flows," *Journal of Vibration, Acoustics, Stress, and Reliability in Design*, Vol. 108, 1986, pp. 301–307.

[41] Driver, D., Seegmiller, H., and Marvin, J., "Time-Dependent Behavior of a Reattaching Shear Layer," *AIAA Journal*, Vol. 25, No. 7, 1987, pp. 914–919.

[42] Lee, I. and Sung, H., "Characteristics of Wall Pressure Fluctuations in Separated and Reattaching Flows over a Backward-Facing Step: Part I: Time-mean Statistics and Cross-spectral Analyses," *Experiments in Fluids*, Vol. 30, 2001, pp. 262–272.

[43] Kiya, M. and Sasaki, K., "Structure of a Turbulent Separation Bubble," *Journal of Fluid Mechanics*, Vol. 137, 1983, pp. 83–113.

[44] Cherry, N., Hillier, R., and Latour, M., "Unsteady Measurements in a Separated and Reattaching Flow," *Journal of Fluid Mechanics*, Vol. 144, 1984, pp. 13–46.

[45] Feng, K., Ying-zheng, L., Han-ping, C., and Koyama, H., "Simultaneous Flow Visualization and Wall-pressure Measurement of the Turbulent Separated and Reattaching Flow over a Backward-Facing Step," *Journal of Hydrodynamics*, Vol. 19, No. 2, 2007, pp. 180–187.

[46] Liu, Y., Kang, W., and Sung, H., "Assessment of the Organization of a Turbulent Separated and Reattaching Flow by Measuring Wall Pressure Fluctuations," *Experiments in Fluids*, Vol. 38, 2005, pp. 485–493.

[47] Papadakis, M., Alansatan, S., and Wong, S., "Aerodynamic Characteristics of a Symmetric NACA Section with Simulated Ice Shapes," *AIAA-2000-0098*, 38^{th} AIAA Aerospace Sciences Meeting & Exhibit, Reno, NV, Jan. 2000.

[48] H. E. Addy, J., Broeren, A. P., Zoeckler, J. G., and Lee, S., "A Wind Tunnel Study of Icing Effects on a Business Jet Airfoil," *AIAA-2003-0727*, 41^{st} AIAA Aerospace Sciences Meeting & Exhibit, Reno, NV, Jan. 2003.

[49] Whalen, E., Broeren, A., and Bragg, M., "Aerodynamics of Scaled Runback Ice Accretions," *Journal of Aircraft*, Vol. 45, No. 3, 2008, pp. 1076–1088.

[50] Lee, S. and Bragg, M. B., "Investigation of Factors Affecting Iced-Airfoil Aerodynamics," *Journal of Aircraft*, Vol. 40, No. 3, May-Jun. 2003.

[51] Jacobs, E., "Airfoil Section Characteristics as Affected by Protuberances," *NACA Report 446*, 1932.

[52] Lee, S. and Bragg, M., "Effects of Simulated-Spanwise Ice Shapes on Airfoils: Experimental Investigation," *AIAA-1999-0092*, 37^{th} AIAA Aerospace Sciences Meeting & Exhibit, Reno, NV, Jan. 1999.

[53] Whalen, E., "Aerodynamics of Runback Ice Accretions," Ph.D. Dissertation, University of Illinois at Urbana-Champaign, 2007.

[54] Whalen, E., Broeren, A., and Bragg, M., "Considerations for Aerodynamic Testing of Scaled Runback Ice Accretions," *AIAA-2006-0260*, 44^{th} AIAA Aerospace Sciences Meeting & Exhibit, Reno, NV, Jan. 2006.

[55] Calay, R., Holdo, A., Mayman, P., and Lun, I., "Experimental Simulation of Runback Ice," *Journal of Aircraft*, Vol. 34, 1997, pp. 206–212.

[56] Botura, G., Sweet, D., and Flosdorf, D., "Development and Demonstration of Low Power Electrothermal De-icing System," AIAA-2005-1460, *43^{rd} AIAA Aerospace Sciences Meeting & Exhibit*, Reno, NV, Jan. 2005.

[57] Cook, D., "Unusual Natural Icing Encounters During Boeing 777 Flight Tests," AIAA-1997-0304, *35^{th} AIAA Aerospace Sciences Meeting & Exhibit*, Reno, NV, Jan. 1997.

[58] Broeren, A., H.E. Addy, J., and Bragg, M., "Effect of Intercycle Ice Accretions on Airfoil Performance," AIAA-2002-0240, *40^{th} AIAA Aerospace Sciences Meeting & Exhibit*, Reno, NV, Jan. 2002.

[59] Gurbacki, H. M. and Bragg, M. B., "Unsteady Aerodynamic Measurements on an Iced Airfoil," *AIAA-2002-0241*, 40^{th} AIAA Aerospace Sciences Meeting & Exhibit, Reno, NV, Jan. 2002.

[60] Gurbacki, H. M. and Bragg, M. B., "Unsteady Flowfield about an Iced Airfoil," *AIAA-2004-0562*, 42^{nd} AIAA Aerospace Sciences Meeting & Exhibit, Reno, NV, Jan. 2004.

[61] Pan, J. and Loth, E., "Reynolds-Averaged Navier-Stokes Simulations of Airfoils and Wings with Ice Shapes," *Journal of Aircraft*, Vol. 41, No. 4, 2004, pp. 879–891.

[62] Marongiu, C., Vitagliano, P., Zanazzi, G., and Narducci, R., "Aerodynamic Analysis of an Iced Airfoil at Medium-High Reynolds Number," *AIAA Journal*, Vol. 46, No. 10, 2008, pp. 2469–2478.

[63] Kumar, S. and Loth, E., "Detached Eddy Simulations of an Iced Airfoil," AIAA-2001-0678, *39^{th} AIAA Aerospace Sciences Meeting & Exhibit*, Reno, NV, Jan. 2001.

[64] Pan, J. and Loth, E., "Detached Eddy Simulations for Iced Airfoils," *Journal of Aircraft*, Vol. 42, No. 6, 2005, pp. 1452–1461.

[65] Mogili, P., Thompson, D., Choo, Y., and Addy, H., "RANS and DES Computations for a Wing with Ice Accretion," AIAA-2005-1372, *43^{rd} AIAA Aerospace Sciences Meeting & Exhibit*, Reno, NV, Jan. 2005.

[66] H. E. Addy, J. and Lee, S., "Icing Encounter Duration Sensitivity Study," *AIAA-2009-4263*, 1^{st} AIAA Atmospheric & Space Environments Conference, San Antonio, TX, Jun. 2009.

[67] Gonsalez, J. and Arrington, E., "Aerodynamic Calibration of the NASA Lewis Icing Research Tunnel (1997 Tests)," *AIAA-1998-0633*, 36^{th} AIAA Aerospace Sciences Meeting & Exhibit, Reno, NV, Jan. 1998.

[68] Racisz, S., "Effects of Independent Variations of Mach Number and Reynolds Number on the Maximum Lift Coefficients of Four NACA 6-Series Airfoil Sections," *NASA TN 2824*, Nov. 1952.

[69] Abbott, I., von Doenhoff, A., and L.S. Stivers, J., "Summary of Airfoil Data," *NACA ACR L5C05*, Nov. 1952.

[70] Yamauchi, G. and Johnson, W., "Trends of Reynolds Number Effects on Two-Dimensional Airfoil Characteristics for Helicopter Rotor Analyses," *NASA TM 84363*, Apr. 1983.

[71] Papadakis, M. and Gile Laflin, B. E., "Aerodynamic Performance of a Tail Section with Simulated Ice Shapes and Roughness," *AIAA-2001-0539*, 39^{th} AIAA Aerospace Sciences Meeting & Exhibit, Reno, NV, Jan. 2001.

[72] L.K. Loftin, J. and Smtih, H., "Aerodynamic Characteristics of 15 NACA Airfoil Sections at Seven Reynolds Numbers from 0.7 x 10^6 to 9.0 x 10^6," *NACA TN 1945*, 1949.

[73] Lee, S., Ratvasky, T., Thacker, M., and Barnhart, B., "Geometry and Reynolds-Number Scaling on an Iced Business-Jet Wing," AIAA-2005-1066, *43^{rd} AIAA Aerospace Sciences Meeting & Exhibit*, Reno, NV, Jan. 2005.

[74] McCroskey, W., "A Critical Assessment of Wind Tunnel Results for the NACA 0012 Airfoil," *NASA TM 100019*, Oct. 1987.

[75] Leishman, J. G., *Principles of Helicopter Aerodynamics*, Cambridge University Press, NY, 1st ed., 2002.

[76] Tsao, J. and Anderson, D., "Further Assessment of MVD Effects in SLD Applications," *AIAA-2005-0072*, 42^{nd} AIAA Aerospace Sciences Meeting & Exhibit, Reno, NV, Jan. 2005.

[77] Tsao, J. and Anderson, D., "Results of Scaling Tests for Large Model-Size Ratios," *AIAA-2006-0467*, 44^{th} AIAA Aerospace Sciences Meeting & Exhibit, Reno, NV, Jan. 2005.

[78] Vickerman, M. B., Choo, Y. K., Schilling, H. W., Baez, M., Braun, D. C., and Cotton, B. J., "Toward an Efficient Icing CFD Process Using an interactive Software Toolkit – SmaggIce 2D," *AIAA-2002-0380*, 40^{th} AIAA Aerospace Sciences Meeting & Exhibit, Reno, NV, Jan. 2002.

[79] Chung, J., Reehorst, A., Choo, Y., and Potapczuk, M., "Effect of Airfoil Ice Shape Smoothing on the Aerodynamic Performance," *AIAA-1998-3242*, 34^{th} AIAA-ASME-SAE-ASEE Joint Propulsion Conference & Exhibit, Cleveland, OH, Jul. 1998.

[80] Westphal, R. and Johnston, J. P., "Effect of Initial Conditions on Turbulent Reattachment Downstream of a Backward-Facing Step," *AIAA Journal*, Vol. 22, No. 12, 1984, pp. 1727–1732.

[81] Shin, J. and Bond, T., "Results of an Icing Test on a NACA 0012 Airfoil in the NASA Lewis Icing Research Tunnel," *AIAA-1992-0647*, 30^{th} AIAA Aerospace Sciences Meeting & Exhibit, Reno, NV, Jan. 1992.

[82] Shin, J. and Bond, T., "Repeatability of Ice Shapes in the NASA Lewis Icing Research Tunnel," *J. Aircraft*, Vol. 31, No. 5, 1994, pp. 1057–1063.

[83] Miller, D., Potapczuk, M., and Langhals, T., "Preliminary Investigation of Ice Shape Sensitivity to Parameter Variations," *AIAA-2005-0073*, 43^{rd} AIAA Aerospace Sciences Meeting & Exhibit, Reno, NV, Jan. 2005.

[84] H. E. Addy, J., Potapczuk, M., and Sheldon, D. W., "Modern Airfoil Ice Accretions," *AIAA-1997-0174*, 35^{th} AIAA Aerospace Sciences Meeting & Exhibit, Reno, NV, Jan. 1997.

[85] Campbell, S., Broeren, A., Bragg, M., and Miller, D., "Aircraft Performance Sensitivity to Icing Cloud Conditions," *AIAA-2007-0086*, 45^{th} AIAA Aerospace Sciences Meeting & Exhibit, Reno, NV, Jan. 2007.

[86] Campbell, S., Broeren, A., and Bragg, M., "Sensitivity of Aircraft Performance to Icing Parameter Variations," *Journal of Aircraft*, Vol. 44, 2007, pp. 1758–1760.

[87] Campbell, S., "Aerodynamic Performance Sensitivity to Icing Cloud Parameters," M.S. Thesis, University of Illinois at Urbana-Champaign, 2006.

[88] Irvine, T., Kevdzija, S., Sheldon, D., and Spera, D., "Overview of the Icing and Flow Quality Improvements Program for the NASA Glenn Icing Research Tunnel," *AIAA-2001-0229*, 39^{th} AIAA Aerospace Sciences Meeting & Exhibit, Reno, NV, Jan. 2001.

[89] Guglielmo, J. and Selig, M., "Spanwise Variations in Profile Drag for Airfoils at Low Reynolds Numbers," *J. Aircraft*, Vol. 33, No. 4, 1996, pp. 699–707.

[90] Althaus, D., "Drag Measurements on Airfoils," OSTIV Congress, Paderborn, Germany, 1981.

[91] Barlow, J. B., W.H. Rae, J., and Pope, A., *Low-Speed Wind Tunnel Testing*, John Wiley & Sons, Inc., NY, 3rd ed., 1999.

[92] Broeren, A. and Bragg, M., "Effect of Airfoil Geometry on Performance with Simulated Intercycle Ice Accretions," AIAA-2003-0728, *41st AIAA Aerospace Sciences Meeting & Exhibit*, Reno, NV, Jan. 2003.

[93] Broeren, A. P. and Bragg, M. B., "Effect of Airfoil Geometry on Performance with Simulated Intercycle Ice Accretions," *Journal of Aircraft*, Vol. 42, No. 1, Jan.-Feb. 2005.

[94] Broeren, A. P., Lee, S., LaMarre, C. M., and Bragg, M. B., "Effect of Airfoil Geometry on Performance with Simulated Ice Accretions Volume 1: Experimental Investigation," Report No. DOT/FAA/AR-03/64, Aug. 2003.

[95] Broeren, A., "An Experimental Study of Unsteady Flow over Airfoils near Stall," Ph.D. Dissertation, University of Illinois at Urbana-Champaign, 2000.

[96] Jones, B. M., "Measurement of Profile Drag by the Pitot-Traverse Method," Tech. Rep. 1688, British Aeronautical Research Council Reports & Memoranda, 1936.

[97] Allen, H. and Vincenti, W., "Wall Interference in a Two-Dimensional-Flow Wind Tunnel, with Consideration of the Effect of Compressibility," *NACA TR 782*, 1944.

[98] Ide, R. F. and Oldenburg, J. R., "Icing Cloud Calibration of the NASA Glenn Icing Research Tunnel," *AIAA-2001-0234*, 39th AIAA Aerospace Sciences Meeting & Exhibit, Reno, NV, Jan. 2001.

[99] Reehorst, A. and Richter, G., "New Methods and Materials for Molding and Casting Ice Formations," *NASA TM 100126*, Sep. 1987.

[100] Kline, S. and McClintock, F. A., "Describing Uncertainty in Single-Sample Experiments," *Mechanical Engineering*, Vol. 75, 1953, pp. 3–8.

[101] Coleman, H. W. and W.G. Steel, J., *Experimentation and Uncertainty Analysis for Engineers*, Wiley-Interscience, NY, 1989.

[102] Drela, M., "XFOIL: An Analysis and Design System for Low Reynolds Number Airfoils," Conference on Low Reynolds Number Airfoil Aerodynamics, University of Notre Dame, Jun. 1989.

[103] Abbott, I. and von Doenhoff, A., *Theory of Wing Sections*, Dover Publications, Inc., Mineola, NY, 1959.

[104] Schlichting, H., *Boundary Layer Theory*, McGraw-Hill, NY, 7th ed., 1979.

[105] Papadakis, M., Yeong, H., Chandrasekharan, R., Hinson, M., Ratvasky, T., and Giriunas, J., "Experimental Investigation of Simulated Ice Accretions on a Full-Scale T-Tail," *AIAA-2001-0090*, 39th AIAA Aerospace Sciences Meeting & Exhibit, Reno, NV, Jan. 2001.

[106] Schlichting, H., "Experimentelle Untersuchungen zum Rauhigkeitsproblem," *Ing.-Arch.*, Vol. 7, 1936, pp. 1–34, English translation: NACA TM 823.

[107] Nikuradse, J., "Laws for Flows in Rough Pipes," *VDI-Forchungsheft*, Vol. 4, Series B, 1933, English translation: NACA TM 1292.

[108] Bons, J. and Christensen, K., "A Comparison of Real and Simulated Surface Roughness Characterizations," *AIAA-2007-3997*, 37^{th} AIAA Fluid Dynamics Conference & Exhibit, Miami, FL, Jun. 2007.

[109] Boyle, R. and Senyitko, R., "Measurements and Predictions of Surface Roughness Effects on Turbine Vane Aerodynamics," *GT2003-38580*, Proceedings of ASME Turbo EXPO 2003, Jun. 2003.

[110] Fitzgerald, E. and Mueller, T., "Measurements in a Separation Bubble on an Airoil using Laser Velocimetry," *AIAA Journal*, Vol. 28, No. 4, 1990, pp. 584–592.

[111] Lee, S., Dunn, T., Gurbacki, H., Bragg, M., and Loth, E., "An Experimental and Computational Investigation of Spanwise-Step-Ice Shapes on Airfoil Aerodynamics," *AIAA-1998-0490*, 36^{th} AIAA Aerospace Sciences Meeting & Exhibit, Reno, NV, Jan. 1998.

[112] H.L. Morgan, J., Ferris, J., and McGhee, R., "A Study of High-Lift Airfoils at High Reynolds Numbers in the Langley Low-Turbulence Pressure Tunnel," *NASA TM 89125*, 1987.

[113] Vargas, M. and Tsao, J., "Observations on the Growth of Roughness Elements into Icing Feathers," *AIAA-2007-0900*, 45^{th} AIAA Aerospace Sciences Meeting & Exhibit, Reno, NV, Jan. 2007.

[114] Lee, S. and Bragg, M. B., "The Effect of Ridge-ice Location and the Role of Airfoil Geometry," *AIAA-2001-2481*, 19^{th} AIAA Applied Aerodynamics Conference, Anaheim, CA, Jun. 2001.

[115] H. L. Morgan, J., Ferris, J. C., and McGhee, R. J., "A Study of High-Lift Airfoils at High Reynolds Numbers in the Langley Low-Turbulence Pressure Tunnel," *NASA TM 89125*, Jul. 1987.

[116] Herman, E., "Goodrich Icing Wind Tunnel Overview, Improvements, and Capabilities," *AIAA-2006-0862*, 44^{th} AIAA Aerospace Sciences Meeting & Exhibit, Reno, NV, Jan. 2006.

[117] Drela, M., "XFOIL: An Analysis and Design System for Low Reynolds Number Airfoils," Jun. 1989.

[118] Broeren, A., Bragg, M., and Addy, H., "Flowfield Measurements About an Airfoil with Leading-Edge Ice Shapes," *Journal of Aircraft*, Vol. 43, No. 4, 2006, pp. 1226–1234.